PHOTOALIGNMENT AND SPATIAL PATTERNING OF LIQUID CRYSTALLINE CONJUGATED POLYMERS FOR POLARISED LIGHT EMISSION

YUPING SHI

St Cross College & Department of Engineering Science

University of Oxford

A thesis submitted for the degree of

Doctor of Philosophy

Michaelmas 2021

Acknowledgments

First and above all, I would like to express my deepest gratitude to my supervisors, Prof. Donal D.C. Bradley (CBE, FRS) and Prof. Stephen M. Morris for their unfailing guidance, prompt help and utmost encouragement through the years of my D.Phil. study and research. I am immensely grateful for the continuous support of the two vastly knowledgeable and enormously kind professors, whose superb patience and hard work has ensured that I make it to the end. I am also extremely fortunate to have joined probably the most prestigious university in the world.

I gratefully acknowledge the prestigious Hong Kong Jockey Club Graduate Scholarship at the University of Oxford for the full-cost financial support throughout my D.Phil. study. It is a privilege for me to have been a JC-Oxford scholar. I am also indebted to the Rank Prize Funds for awarding me the optoelectronic Covid-19 grant that is a great honour, which had been an indispensable financial source in support of the final half year of my research and thesis writing.

I sincerely thank the examiners of the present thesis, Prof. Steven Collins and Prof. Ji-Seon Kim, as well as all my collaborators whose constant efforts and valuable contributions have made this thesis possible - Dr. Patrick Salter for his long hours spent on laser direct writing fabrication; Profs. Henry Snaith, Robert Taylor, SeungNam Cha and Peter Bruce for kindly allowing me to use their research facilities; Profs. Steve Elston, Paul Stavrinou, Laura Herz, Dominic O'Brien, Martin Castell, Mischa Bonn, Henning Sirringhaus and Sir Richard Friend for the inspiring and fruitful discussions; Prof. Moritz Riede and his research group for help with my grazing-incidence wide-angle x-ray scattering measurements; last but not least, Prof. Ruidong Xia for hosting one of my major research visits to broaden my horizons and her wholehearted support of the subsequent collaborative experiments.

Thanks a lot to all members of the Soft Matter Photonics group in the Department of Engineering Science and the Physics and Application of Soluble Semiconductors research group in the Department of Physics. Special thanks go to Drs. Sungho Nam, Julian Fells, Hao Ye, Bernard Wenger, Jia-De Lin, Pabitra Nayak, Yiren Xia, Sofia Bekou, John Sandford O'Neill, Taimoor Ali, Chao He, Alice Smith, Nikol Lambeva, Kimberley Savill, Gregory Rees and Alberto Privitera, as well as Mr. Bingjun Wang, Xiuze Wang, Waqas Kamal, Ziyang Ning, Paul Giraud, Fubiao Gu and Grahame Faulkner, for their enormous help with stimulating and coordinating various experiments. On a personal note, frequent discussions about numerous topics with all my colleagues and friends have enriched my life in Oxford and future career.

Finally, I would like to dedicate this thesis to my beloved parents and sister. Without their incessant support I would not arrive at where I am, so I really hope I've made you all proud.

Abstract

Polymeric semiconductors have a number of benefits in the ease of processing and large-area production, tunability of the physical properties, low-cost, flexibility and biocompatibility. Although high-quality polymer alignment is highly favorable in terms of allowing access to fundamental optical/electrical anisotropy, the realisation of large-area extended uniform alignment and high-resolution spatial patterning of polymer chain-orientation remains a challenge. The purpose of this thesis is to investigate and optimise a non-contact photoalignment technique by exploiting the inherent long-range orientational ordering present in a liquid crystal (LC) mesophase to create highly aligned monodomains over cm^2 areas with submicron patterning in thermotropic liquid crystalline conjugated polymers (LCCPs). The solution (water)-processable photoalignment material, azobenzene sulphonic dye (SD1), is presented within this thesis to be optically rewritable and remain stable at >300 °C temperatures, ensuring that it is suitable for orienting LCCP overlying films.

Two different photoalignment processes are explored in this thesis: the first involves using macroscopic linearly polarised ultraviolet (UV) light illumination to trigger alignment whereas the second method uses two-photon femtosecond direct laser writing (DLW), for the first time, to align/pattern the SD1 thin layers. The alignment conditions are optimised to enable ~100% order parameters for SD1-aligned nematic glass films of light-emitting LCCP fluorene-benzothiadiazole alternating copolymer F8BT. Uniform alignment (>10 dichroic ratios) is obtained for F8BT monodomain films with thicknesses in the range of 100 to 300 nm. Indirect photoalignment is also showcased using a 90 wt% F8BT:10 wt% non-LC Red-F binary blend film, whilst the photo-masked UV-alignment leads to a spatial pattern resolution of 2 - 4 μm.

Fine control of the domain structure and SD1-aligned long-range orientational ordering has been employed to tailor the order parameter in three types of F8BT films in order to study the structure-property relationships. The spin-coated amorphous F8BT reference film was found to possess no long-range structural order and exhibit the lowest photoluminescence (PL) lifetime and quantum efficiency (PLQE) of ~30%. It is also shown that LC alignment itself is responsible for a smeared X-ray diffraction ring and extra lower-energy absorbing species in the nematic polydomain F8BT glass film, in line with the formation of a minor (~5%) fraction of the locally and spontaneously oriented polymeric nanocrystals embedded in an amorphous matrix. It is suggested that this bi-phasic polydomain texture resembles a self-doped host-guest system in which nonradiative host-to-guest Förster resonance energy transfer and intrachain radiative recombination gives rise to a high PLQE of >70%, a value that approaches the PLQE limit measured for F8BT solutions. Our micro-PL spectral mapping results support that efficient

radiative intrachain recombination most takes place in polymeric nanocrystals that act as low-energy acceptors and therefore dictates the PL behaviours in the self-organised F8BT nematic polydomain glass films. The SD1-aligned F8BT monodomain films have an order parameter of almost 1 and a >70% crystallinity, but show an intermediate PLQE of ~50% potentially due to the enhanced interchain conjugation length up to 20.5 nm and associated interchain PL emission.

Two-photon infrared laser writing using an ultrafast Ti:sapphire laser (785 nm, 250 fs, 80 MHz) has been utilised to inscribe bespoke photoalignment patterns with a resolution of 0.5 ~ 1 μm in F8BT monodomain glass films. Laser (re)writing enables a higher pattern resolution and integrated PL contrast of >15 than the polarised UV alignment. Laser writing and UV alignment induce different F8BT chain-conformations and interchain packing, as judged by the distinct polarisation-dependent vibronic transitions in the polarised micro-PL spectra. We elucidate that the efficient (>70% PLQE) and linearly polarised intrachain emission dominates the parallel-polarised $PL_{//}$ spectrum, whereas the red-shifted perpendicular-polarised $PL_{\perp}$ spectrum indicates an interchain emission character with a significantly reduced PLQE of ~10%.

The anisotropic structural and spectral information presented in this thesis complements previous studies on non-oriented light-emitting conjugated polymers. Bringing structural order and creating spatial alignment-pattern offers great potential for the fabrication or performance improvement of various devices such as polarised/micro-organic light-emitting diodes, flexible thin-film transistors, microcavity lasers, meta/quantum-materials, and integrated optical circuits.

Publications

1. **Yuping Shi**, Paul N. Stavrinou, Bingjun Wang, Robert A. Taylor, Stephen M. Morris, Donal D.C. Bradley, Fine-tuning the emission characteristics of fluorescent conjugated polymers using photoalignment and liquid-crystalline long range ordering, *Submitted*.
2. **Yuping Shi**, Patrick S. Salter, Mo Li, Robert A. Taylor, Steve J. Elston, Stephen M. Morris, Donal D.C. Bradley, Two-photon laser-written photoalignment layers for patterning liquid crystalline conjugated polymer orientation, *Advanced Functional Materials* **31**, 2007493 (2021).
3. Xiuze Wang, Julian A. J. Fells, **Yuping Shi**, Taimoor Ali, Chris Welch, Georg H. Mehl, Timothy D. Wilkinson, Martin J. Booth, Stephen M. Morris, Steve J. Elston, A compact full 2π flexoelectro-optic liquid crystal phase modulator", *Advanced Materials Technologies* **5**, 2000589 (2020).
4. Haoran Zhang, Lingling Ma, Qian Zhang, **Yuping Shi**, Yueting Fang, Ruidong Xia, Wei Hu, Donal D. C. Bradley, Azobenzene sulphonic dye photoalignment as a means to fabricate liquid crystalline conjugated polymer chain-orientation-based optical structures, *Advanced Optical Materials* **8**, 1901958 (2020).
5. Taimoor Ali, Jia-De Lin, **Yuping Shi**, Steve J. Elston, Stephen M. Morris, Developing flexible liquid crystal defect mode lasers, *Proceedings of SPIE* **11303**, Emerging Liquid Crystal Technologies XV, 113030Q (31 March 2020).
6. **Yuping Shi**, Patrick Salter, Mo Li, Robert Taylor, Steve Elston, Stephen Morris, Donal Bradley, High quality alignment of conjugated polymers using two-photon laser direct writing of photoalignment layers, accepted as a poster presentation for the International Conference on Science and Technology of Synthetic Metals (ICSM 2022).

Table of Contents

Chapter 1

Introduction and Background

1.1 Introduction and Motivation

As an indispensable complement to silicon-based semiconductor technologies, flexible organic semiconductors are able to generate and strongly interact with light. These soft semiconducting materials have a number of benefits in terms of the ease of processing, tunability of energy levels, large-area production, low cost and biocompatibility. These unusual properties have enabled an increasingly rich range of (opto-)electronic devices such as solid-state lighting and displays, organic solar cells, multi-sensing, and biomedical applications. In terms of organic semiconductors, π-conjugated polymers exhibit unusual light harvesting and energy conversion properties due to the facile tunability of the energy levels and π-electron delocalisation. This provides great flexibility for fine-tuning the desired properties by tailoring their intrinsic anisotropic physical structure such as the chain-conformation and orientation. However, polymeric semiconductors usually suffer from significant light/energy losses and only exhibit isotropic and unideal properties in the as-prepared state, due to the formation of an amorphous or polydomain texture with a significant degree of structural and energetic heterogeneities. This inherent disorder complicates the structure-property relationships in conjugated polymers, which limits the resulting device performance and defect tolerance.

The localised polymer chain orientations in the solution-processed conjugated polymer films are typically either completely disorderly distributed (i.e., an amorphous phase), or well

oriented within an individual domain yet randomly distributed amongst the different domains. As a result, the macroscopic physical properties for non-oriented conjugated polymers are spatially averaged over randomly oriented multi-domains/chains and, thus, limited in magnitude and are nearly isotropic when measured along different directions. The full exploitation of conjugated polymers therefore necessitates high-quality yet cost-effective polymer alignment in the form of extended monodomains over large areas. In this way, the highly oriented extended polymer monodomains would exhibit high degrees of structural order and allow access to fundamental anisotropies in the optical, electrical and optoelectronic properties. Despite the huge potential, realisation of high quality, uniform and large-area chain orientation in the otherwise highly disordered conjugated polymers remains challenging.

A lot of research has been conducted along this line, aiming to continually improve the polymer alignment quality and the length scale over which the chain orientation can be maintained so that the related device performance can be enhanced. Taking solution processable polymers as an example, deliberately aggregated solutions have been prepared for polymer film deposition, though the polymer aggregates typically only polydomain textures in the as-deposited film. Other existing polymer alignment methods can be categorised in terms of the application of external forces/fields (e.g., rubbing or a shearing force, electric or magnetic field, substrate confinement, and surface tension) into the solution processing steps. Nevertheless, the resultant alignment quality and length scale of the molecular/chain alignment are rarely both sufficient at the same time. Traditional alignment techniques also have several potential drawbacks in relation to the resulting surface roughness, the presence of debris and electrostatic charges, thermal stability, and a very limited ability to spatially pattern the oriented film.

The main objective of this thesis is to explore the use of a feasible and effective polymer alignment method in order to provide low-cost and high-quality chain orientation over a large

area. Moreover, the aim is to achieve high-resolution spatial patterning of the polymer chain-orientation in the aligned film. Highly oriented and spatially patterned polymer monodomains with submicron- to nano-scale features enable tailoring of the physical structures such as chain conformation, polymer interchain packing and domain texture. It also allows for easy modulation of the refractive index, anisotropy of the light emission polarisation, charge-carrier mobility anisotropy, and spatiotemporal coherence of the photon emission/amplification. Thus, realisation of these combined features is expected to facilitate the fabrication of novel photonic/optoelectronic devices, meta-surfaces, optical circuits, and polymer-based quantum-technology systems.

In this work, the feasibility of combining a non-mechanical photoalignment technique with the intrinsic long-range orientational ordering present in the liquid crystal (LC) mesophase of liquid crystalline conjugated polymers (LCCPs) is considered. Specifically, highly fluorescent LCCPs with a nematic LC phase at relatively high temperatures of ~200 °C - 300 °C are the subject of the work presented in this thesis. These mesophase temperatures far exceed the clearing temperature of commercial low molar mass LCs commonly used in the flat panel displays industry. Therefore, alignment techniques that have excellent high-temperature stability are required, which negates the use of standard mechanically-rubbed polyimide alignment layers that are normally used in the LC displays industry due to the insufficient thermal stability.

For the studies presented in this thesis, the photoalignment material, sulphonic azo-benzene dye (SD1), is employed. It is shown to be more robust to high temperatures compared with conventional rubbed polyimides, alongside being solution (and water)-processable, reversible photoalignment, and compatible with nonlinear two-photon absorption. While photoalignment layers such as SD1 are prone to photo-instabilities, this is not a limiting factor

for their use in orienting LCCPs. The polymer alignment is triggered in a high-temperature mesophase by interfacial interactions between the polymer layer and the photoaligned SD1commanding layer, which are then communicated through the bulk of the overlying LCCP film by chain-chain interactions. Upon rapid quenching to room temperature, the long-range nematic orientational order of the polymer chains is frozen into a nematic glass state that does not then require the presence of the photoalignment layer to maintain its order.

Using photomasks with polarised UV-alignment of the SD1 commanding layers could be used to create chain-orientation patterns, though this needs extra design steps and the fabrication of photomasks. However, pattern resolutions extending below the submicron lengthscale is challenging. In order to improve the pattern resolution and provide an alternative photoalignment approach, two-photon ultrafast direct laser writing (DLW) is utilised, for the first time, to inscribe bespoke alignment patterns with submicron features in the SD1 photoalignment layers. This process was used to orient both the chain-orientation and the optical transition dipole moment direction in overlying light-emitting LCCP films.

In the following Sections of this Chapter, the relevant background and theory is introduced. The thesis outline is then provided in the last Section.

1.2 Electron Delocalisation and Conjugated Polymers

The performance of optoelectronic devices based on soft organic semiconductors is dictated by the chemical, physical and energetic structures. Compared with their inorganic counterparts, which usually have a high crystallinity and dielectric permittivity that strongly screen the Coulomb interactions between the electrons and holes, organic semiconductors exhibit more complicated structure-property relationships. This is due to the synergic effects of their lower (1.5 - 3) dielectric constants, the hierarchy in terms of the inherent intra/inter-molecular

interactions, and the presence of various degrees of disorder [1]. These spatial structural heterogeneities induce significant light/energy losses and thus reduce the controllability in semiconducting organics. On the other hand, dielectric constants of insufficient magnitude would result in the dominance of electron-hole bound pairs (excitons) as the charge carriers in the optically or electrically excited states [2].

Organic compounds can be sub-divided into saturated and unsaturated categories. For the unsaturated type, there is at least one double or triple bond that is often utilised to tune: 1) the electronic wavefunction distribution and the energy bandgap, namely, the difference in energy between the highest occupied molecular orbital (HOMO) and the lowest unoccupied molecular orbital (LUMO); and 2) the optoelectronic properties by polymerisation or doping. The frontier *p* orbital of carbon acts as the main building block in organic semiconductors, which can be divided into two in-plane components, p_x and p_y, and an out-of-plane p_z component. Each orbital has the capacity to accommodate two external electrons with opposite spin. In carbon-based organic compounds, a carbon atom could form four bonds with adjacent atoms since the hybridisation of its *s* orbital and *p* orbital gives rise to an extra hybrid *sp* orbital. For instance, in the sp_2 hybridisation the 2s orbital is mixed with the $2p_x$ and $2p_y$ orbitals, leaving the $2p_z$ orbital unchanged; and the three new hybrid states are stabilised in an energetically equilibrium geometry by lying in the *x*-*y* plane at an angle of 120˚to each other [3]. The first carbon-carbon single bond is of the σ type, where the hybrid electron wavefunction of the pair of electrons exists in the *x*-*y* plane between the two nuclei. A carbon-carbon double bond results from a stronger rotational σ bond and a π bond arising from the overlapping of the $2p_z$ orbitals of the two nearest carbon atoms. Thus, the π bond is weaker and the associated two π molecular orbitals (a low-energy π-bonding orbital and a high-energy π^* anti-bonding orbital) are less spatially localised with a smaller energy splitting before and after excitation [3].

The enhanced delocalisation of the electronic wavefunction accompanying the formation of π molecular orbitals can be used to tune the HOMO/LUMO energy levels and the (sub-)bandgap states, hence engineering the optical, electrical and optoelectronic properties of organic semiconductors. The so-called π-conjugated double bonds refer to an alternating occurrence of the single and double carbon-carbon bonds in the molecular structure. In other words, in order to be considered conjugated, two or more π bonds must be separated by only one single bond. The corresponding conjugation length of a molecule is the length at which the π-orbitals of a unit are no longer conjugated with the π-orbitals at the origin. A prominent example of this conjugated bond structure is the benzene molecule, along with aromatics such as the biphenyl conjugated molecule and poly(para-phenylene) (PPP) conjugated polymer.

As depicted in **Figure 1.1**, the benzene molecule is a cyclic 6-electron system, where all six carbon atoms in the ring are sp^2-hybridised and, thus, the π electrons are delocalised in the cyclic array of six hybridised $2p_z$ orbitals that extend with no preferred direction around the planar ring, above and below the plane of the ring [4]. In this way, three π bonding orbitals and three unoccupied π^* anti-bonding orbitals are formed in the benzene ring. By using the plus and minus signs to represent the phase signs of the electron wavefunctions describing these π-bonding anti-bonding orbitals, Figure 1.1 shows six possible phase configurations (i.e., each corresponds to one molecular orbital) accommodating the six hybridised atomic $2p_z$ orbitals. When the phases of all six atomic $2p_z$-orbitals in the benzene molecule correspond and leave no "node" lying between orbitals themselves (a node is where there is a change in phase between adjacent *p*-orbitals), the atomic orbitals would overlap with each other to generate a molecular orbital (π_1) with the lowest energy and the greatest overlap/delocalisation of the π-electrons over the benzene molecule. In contrast, the highest energy molecular orbital (π_6^*) of benzene is generated when all the atomic orbital phases alternate and, thus, are separated by

three nodal planes (denoted by the blue dashed lines in Figure 1.1), leading to zero overlap between adjacent atomic *p*-orbitals and the minimum possible π-electron delocalisation [5].

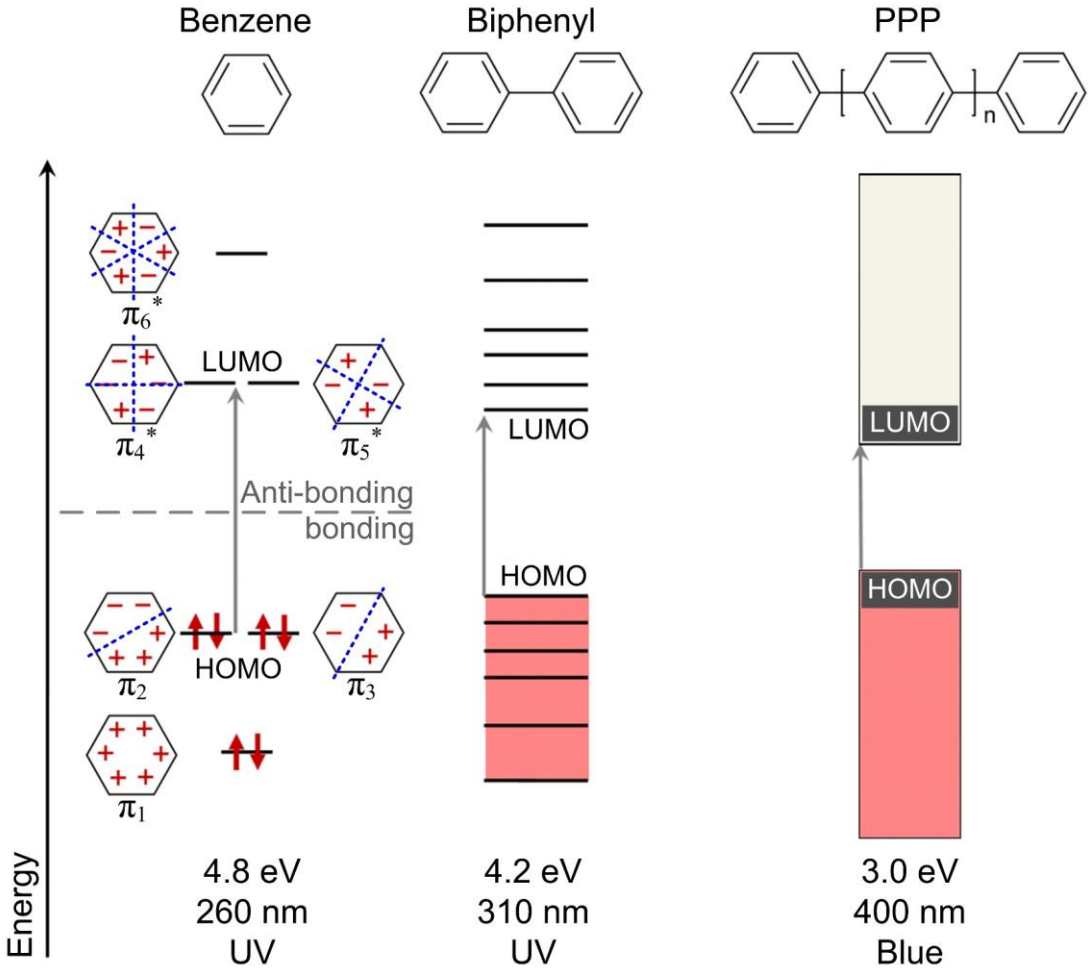

Figure 1.1: The π-orbitals and orbital energy levels of the benzene molecule, as well as the energy level splitting and reduction in the energy bandgap in biphenyl and PPP due to an enhancement in the effective conjugation length. Reproduced from [4].

For each of the two intermediate energy levels (i.e., the same number of nodal planes in the molecular orbital) of the benzene molecule, two degenerate molecular orbitals of the same energy level are included by considering the molecular symmetry and the type/numbers of the possible hybridised orbitals. The remaining carbon valence electrons then occupy the three π-bonding molecular orbitals in pairs according to their energy levels, which results in the π_1 molecular orbital being fully occupied (6 electrons) and the π_2 or π_3 orbital partially occupied by accommodating one or two pairs of electrons. This means that the HOMO orbital of benzene

is made up of two π-bonding (π_2 and π_3) orbitals whereas its LUMO orbital is either of the two unoccupied (π_4^* and π_5^*) anti-bonding orbitals.

When bringing two benzene monomers sufficiently close together so that the intermolecular coupling strength increases and a biphenyl molecule is produced, the frontier HOMO and LUMO molecular orbitals of biphenyl arise from the so-called energetic splitting of the overlapped orbitals of the two benzene monomers. This occurs due to the asymmetric interactions between the strongly coupled carbon atoms in the two monomers. A generic trend in this hybridisation is that the stronger the intermolecular interaction, the larger the degree of orbital energy splitting. Accordingly, the orbital overlap and effective conjugation length of the biphenyl molecule is enhanced. The bandgap is then reduced from 4.8 eV in benzene to 4.2 eV in biphenyl, although both values still correspond to UV wavelengths. As the number of benzene monomers increase, it is possible to produce π-conjugated polymers such as poly(para-phenylene) (PPP) shown in the right panel of Figure 1.1 [6]. In this case, the discrete energy levels of either the HOMO or LUMO molecular orbital have evolved into a continuum band and, concomitantly, the bandgap of the conjugated PPP reduces to 3.0 eV that is of the order of visible light. As an empirical rule of thumb, the optical/electronic bandgap of a conjugated polymer decreases with an increase in the so-called persistence length of the polymeric material (i.e., the chain-segment length between two broken-symmetry kinks along the conjugation path). This chain-segment length is determined by the polymer rigidity and rotational disorder.

1.3 Vibronic Transitions and Spectral Line Broadening in Polymeric Semiconductors

A typical conjugated polymer chain possesses >100 atoms and all of them are vibrating constantly. These atomic vibrations couple with the electronic transitions through a change in the length of the bonds due to dynamic variations in the electron density. Optically or electrically pumping a polymeric semiconductor with light/electrical current whose energy

exceeds the energy bandgap, brings the polymer into an electronically and vibrationally excited state (S_1) via an electronic transition from the ground state (S_0) to the S_1 state. This occurs simultaneously with a change in position of the nuclei before and after the excitation. The separation in energy between the vibrational sub-levels can be described as $E_{vib} = h\upsilon \times (n + 1/2)$, where h is Planck's constant and the order of vibrations is, $n = 0, 1, 2, 3, \cdots$. For the ground state and the excited electronic state, the difference in their vibrational energies is due to the vibration frequency (υ) in the two states being different.

An electronic transition leads to a non-equilibrium state (Frank-Condon state) that relaxes to the thermodynamic equilibrium state on the order of a few picoseconds. The Frank-Condon principle implies that the electronic transition is much faster (of the orders of 10^{-15} seconds) than nuclei vibrations (10^{-13} - 10^{-12} seconds). It is therefore reasonable to consider that the molecular geometry remains unchanged during an electronic transition as the nuclei that make up the molecule remain in a fixed position [7]. The absorption of a photon is an instantaneous process by promoting a valence electron from the lowest-lying energy sub-level of the ground state to a vibrational sub-level of the excited S_1 state within a time of the order of femtoseconds. Since light absorption involves only the spatial re-configuration of inertia-free electrons, this would leave an inadequate time for the nuclei to re-arrange their positions. Instead, the adjustment of a nuclei's position happens after the absorption process and ends with the formation of a new vibration state that is confined by a different potential energy.

This optical transition process is best demonstrated by the Frank-Condon energy diagrams, such as that shown in **Figure 1.2**(a). The two potential wells in Figure 1.2(a) show the nuclei-separation dependence of the molecular potential energy for the S_0 and S_1 states. Light absorption (and emission) can be denoted by a vertical arrow up (down) that strikes one of the low-lying vibrational sub-levels of the excited (ground) state. Within the lifetime of the

excited electronic state (~10^{-10} seconds to nanoseconds for typical light-emitting conjugated polymers), the molecule quickly releases any excess vibrational energy by means of going through thousands of vibrations and energy exchange with the surrounding molecules. In this way, the excited molecule reaches the lowest-lying sub-level (the 0^{th} order vibrational energy level) of the upper potential curve, from there it spontaneously decays to the ground state either radiatively via photon emission (i.e., fluorescence for the excited singlet state or phosphorescence for the excited triplet state), or nonradiatively through thermal relaxation and/or "intersystem crossing" to an excited lower-energy spin-forbidden triplet electronic state.

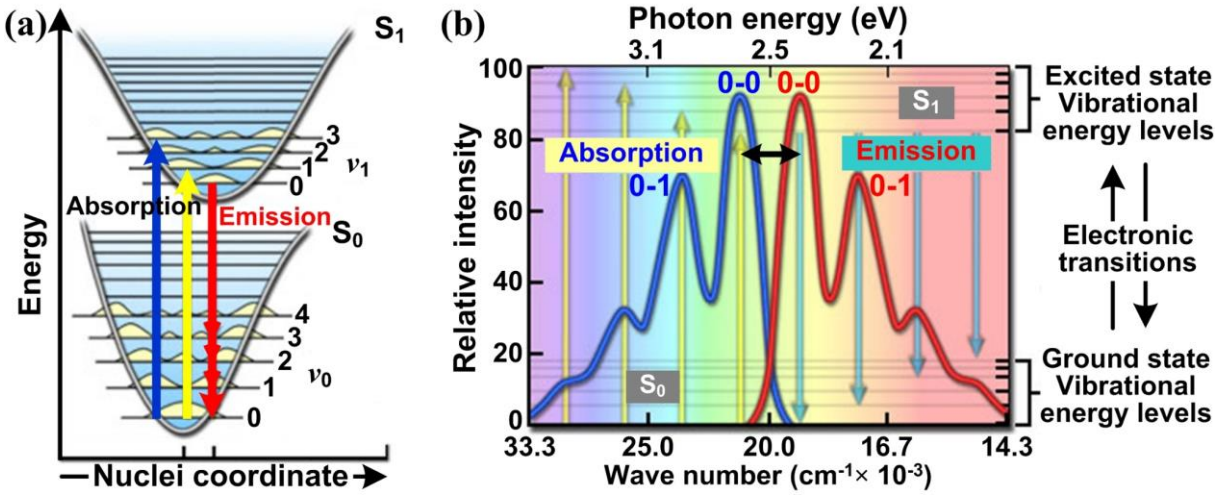

Figure 1.2: (a) The Frank-Condon energy diagram. (b) Vibronic structures of the optical absorption (the blue curve) and emission (the red curve) bands, along with the vibrational energy levels of the ground state (S_0) and the first excited electronic singlet state (S_1). The colours of the three single-headed arrows in (a) denote different wavelengths (red: long wavelengths; yellow: middle wavelengths; blue: short wavelengths) of light absorption and emission. The black double-headed arrow in (b) represents the Stokes shift. Images reproduced from [8].

The Franck-Condon principle applies equally to both absorption and emission, hence indicating an approximate mirror symmetry between the absorption and emission spectra, as illustrated in Figure 1.2(b). However, as there are two periods of vibrational energy relaxation involved in a cyclic absorption-emission process, the fluorescence emission always takes places at a lower energy than the light absorption. Such a red-shift of the wavelength of the maximum

of the fluorescence emission spectrum relative to that of the maximum of the first absorption band is called the Stokes shift, such as that illustrated in Figure 1.2(b). This shift can be seen in the separation of the two 0-0 vibronic transition centres in the absorption and emission spectra.

Within the Frank-Condon framework, the optical absorption and emission spectrum can be expressed as a progression of vibronic transition peaks rising from an initial frequency of ω', separated by ω_0 with a Poisson distribution of intensities [9]:

$$I_{abs}(\omega) \propto \sum_{j=0}^{\infty} \frac{e^{-D} D^j}{j!} \delta(\omega - \omega' - j\omega_0) \tag{1.1}$$

where ω is frequency and D denotes the Huang-Rhys parameter. In essence, this describes a vibrational progression that accompanies the electronic transitions and indicates that vertical electronic transitions take place most favourably (or are strongest) when the nuclear structures of the ground and excited vibronic states are closely matched. The normalized intensity of the 0-*n* vibronic transition peak is given by the Frank-Condon coefficients

$$|\langle 0|n\rangle|^2 = D^n/(n! \times e^D) \tag{1.2}$$

It can be seen from Equation 1.2 that the relative intensities of these vibronic peaks depend on the Huang-Rhys parameter, which is a dimensionless factor related to the mean square displacement of the nuclei upon excitation. Thus, the Huang-Rhys parameter often acts as a measure of the molecular rigidity and of the coupling strength between the nuclear and electronic degrees of freedom. In particular, the relative weight of the 0-0 vibronic absorption transition. This in turn is related to the electronic transition from the lowest-lying (0^{th}) vibrational energy level of the ground state to the lowest (0^{th}) vibrational level of the excited S_1 singlet state. The total absorption equals to e^{-D}. As a result, the Huang-Rhys enables a correlation to be made between the photophysical spectral information with the physical structure of the semiconducting polymer, such as the overall molecular rigidity and chain conformation.

The Huang-Rhys parameter is also the mean of the Poisson distribution in Equation 1.1 and 1.2, therefore we can equate D to the mean order number of the vibrational energy levels excited in the upper S_1-state potential curve upon photon absorption from the ground state [9]. In the case of $D \leq 1$, the maximum transition intensity occurs at ω' with $n = 0$ and the amplitude of the vibronic progression falls off according to D^n. For $D >> 1$ (strong coupling), the vertical transition with the greatest nuclear structure overlap and therefore the maximum transition intensity occurs at the $n \approx D$ vibronic peak. As a result, the Huang-Rhys parameter approximates the mean order number of the vibrational energy levels excited from the ground state.

At the most fundamental level, an electronic transition between the ground state and an excited state does not result in light absorption/emission of a single wavelength only. In most cases, the photophysical spectra (e.g., optical absorption spectrum and fluorescence emission spectrum) of typical semiconducting polymers continue across a range of wavelengths and include >1 vertical electronic transition bands that resembles the overall spectra. Each electronic transition band in a spectral curve often comprises a superposition of several allowed vibronic transitions from the lowest (0^{th}) vibrational energy level of the original state (e.g., the S_0 state for optical absorption) to one or more of the low-lying (i.e., 0^{th}, 1^{st}, 2^{nd}, ···) vibrational levels of the final state (i.e., the excited S_1 or a higher electronic states for light absorption).

Taking the optical absorption and fluorescence spectra of a conjugated polymer such as a poly(9,9-dioctylfluorene-co-benzothiadiazole) (F8BT) film as an example (**Figure 1.3),** we can see that the resolution of the vibronic structure of the transition bands in the spectroscopic measurements is reliant on the separation of the vibronic peaks and the degree of line broadening. Significant linewidth broadening of the individual vibronic transitions results in overlap with the neighbouring vibronic peaks that intersect the upper potential energy surface, resulting in a convoluted electronic transition band in the spectral curve. This tends to hide the finer features of the allowed vibronic transitions.

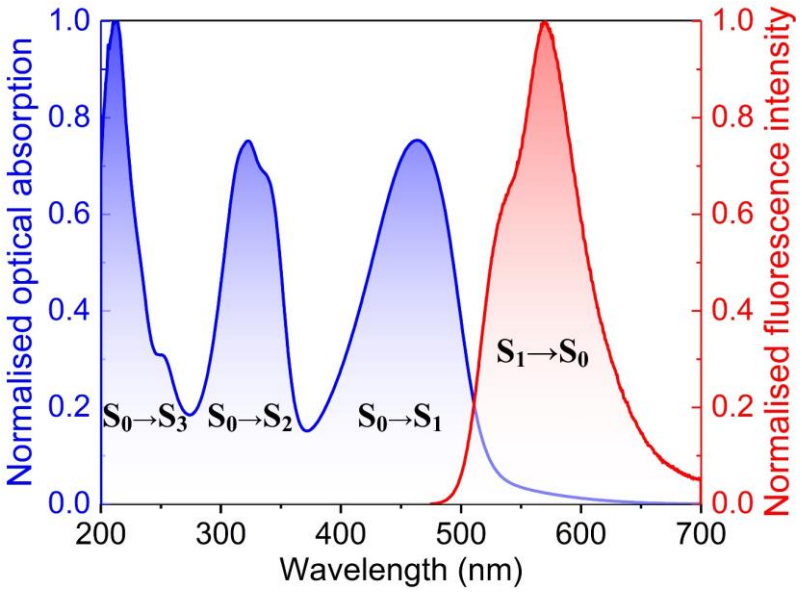

Figure 1.3: Optical absorption spectrum (blue) and fluorescence emission spectrum (red) of a spin-coated pristine film of the conjugated F8BT polymer. This absorption spectrum is shown with three transition bands resulting from the electronic transitions from the lowest-lying vibronic energy level of the ground state to the first ($S_0 \rightarrow S_1$), second ($S_0 \rightarrow S_2$), and third ($S_0 \rightarrow S_3$) excited electronic singlet states. The fluorescence spectrum, on the other hand, is generally dictated by a radiative $S_1 \rightarrow S_0$ decay. While the vibronic structures are clearly resolved for the three ($S_0 \rightarrow S_2$, $S_0 \rightarrow S_3$ and $S_1 \rightarrow S_0$) transition bands, the $S_0 \rightarrow S_1$ absorption band appears rather featureless and broad due to the formation of an amorphous texture.

The primary origin of line broadening in the photophysical spectral curves includes [10]: *i*) Natural line broadening as a result of Heisenberg's Uncertainty Principle - there is an uncertainty in the energy state of a molecule due to an uncertainty in the lifetime of its electronic states; *ii*) Collision/pressure broadening that results from molecules colliding and the associated perturbation of the energy states by neighbouring atoms; *iii*) Doppler broadening: the thermal motion of the molecules shifts the frequency of the emitter according to the Doppler effect, which depends on the inertia of the emitter, the frequency of the spectral line, and the temperature; and i*v*) Inhomogeneous broadening of the spectral linewidth induced by structural and energetic disorder. Inhomogeneous line broadening is usually related to the energy level of the light absorbing/emitting species of a molecule. In addition to the latter, the thermal Doppler broadening is also a type of inhomogeneous broadening, whereas the first two mechanisms are generally homogenous broadening, namely, they are the same for all the vibronic transitions.

Increasing the temperature results in a broadening of the photophysical spectra due to the combined effects of thermal Doppler broadening and collision broadening and, consequently, tends to blur the vibronic lineshape of the transition bands. In some cases, the occurrence of spectral line narrowing and super-irradiation have been observed for aggregated polymer chains that can be formed by dissolving the polymer in a "bad" solvent or concentrated solution [11]. Analogously, enhancing the structural order and overall crystallinity of conjugated polymer films through mitigation of the structural/energetic disorder is expected to facilitate a better understanding of their optoelectronic properties. This, in turn, would enable better control of these properties that are related to the vibronic electronic transitions and chain orientation in the otherwise disordered organic semiconductors.

1.4 Intrachain and Interchain Charge/Energy Transfer

Optical or electrical pumping of an organic semiconductor with an energy that is higher than its bandgap can promote the energy level of polymer chains to one or more excited electronic states. The Frank-Condon principle suggests that such excited states are not in thermodynamic equilibrium and that there exists a release of the excess vibrational energy prior to the final decay mechanism. In most cases, the dielectric constant of organic semiconductors is low (~1.5 - 3) and this only weakly screens the Coulomb interactions between the excited/injected holes and electrons in the conduction band, leading to a bounded state of the electron/hole pairs (i.e., excitons). These aspects point to the necessity of charge transfer/transport occurring between the absorption process and decay. Exciton transport from the initial light-absorption or charge-injection site to the ultimate decay site (see **Figure 1.4** (a)) is dictated by electronic coupling and electron-phonon (vibrational) coupling. For semiconducting polymers, these two fundamental coupling mechanisms are determined by the intrachain and interchain interactions.

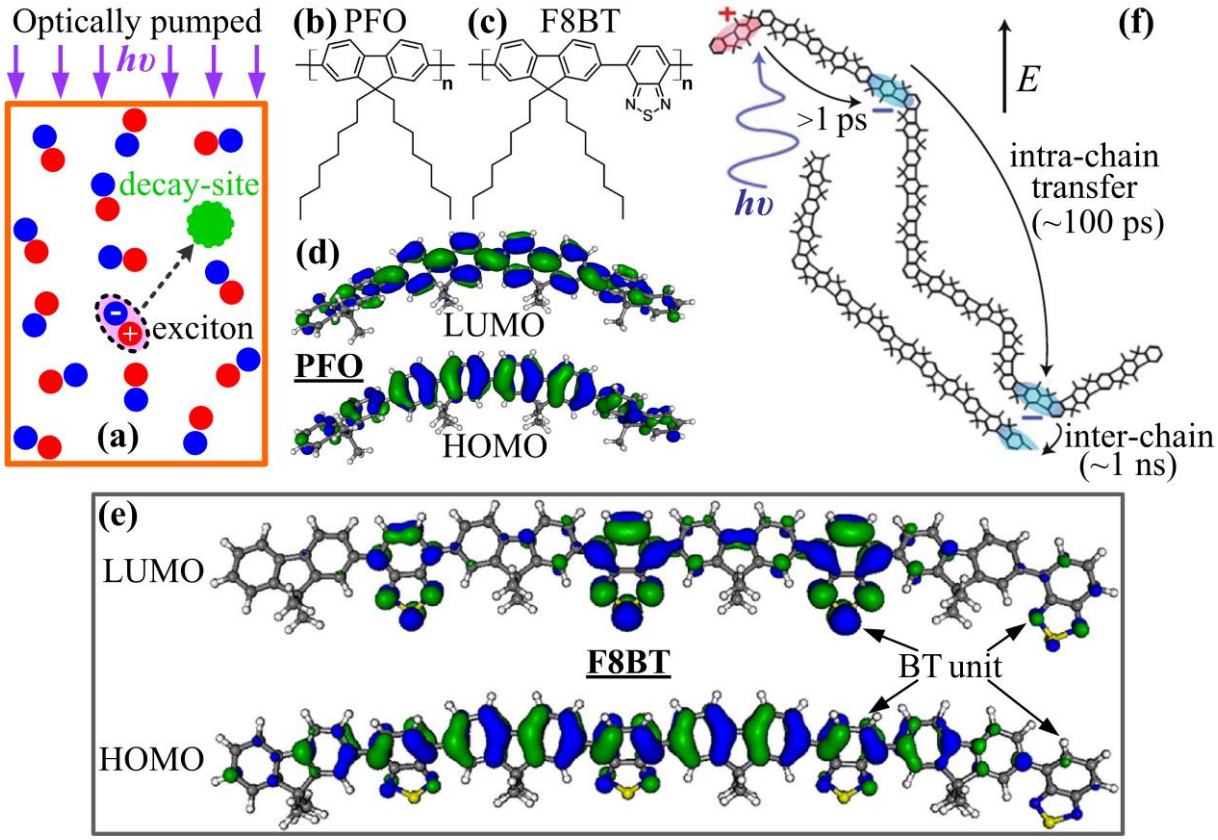

Figure 1.4: (a) Schematic illustrating the formation and transport of excitons (a bounded electron (blue sphere with a minus sign) and hole (red sphere with a plus sign) pair) toward the final decay site in an optically pumped organic semiconductor. Chemical structures of polyfluorene homopolymer PFO (or F8) (b) and the copolymer F8BT (c). Contour plots of the HOMO and LUMO orbitals of the PFO tetramer (d) and the F8BT tetramer (e). (f) Schematic demonstrating the intrachain and interchain electron transfer with characteristic times in an electrically (electrical field denoted by E) or optically (light frequency of υ) excited conjugated polymer. Images (d) and (e) were taken from [12], and (f) was taken from [13].

For conjugated polymer semiconductors, their intrinsic intra/inter-chain interactions as well as the associated delocalisation of π-electrons induce different electronic states, excitonic pathways and transfer/decay efficiencies. Highly fluorescent polyfluorenes such as the blue-light emitting poly(9,9-dioctylfluorene) (PFO or F8) homopolymer and the green-light emitting F8BT copolymer (chemical structures shown in Figure 1.4(b) and (c), respectively) have been found from density functional theory (DFT) calculations to exhibit different charge-carrier transporting properties, since they differ in terms of the LUMO and HOMO orbitals (Figure 1.4(d) and (e)) and therefore have distinct excitonic transfer [12]. Both the HOMO and LUMO

orbitals of the conjugated PFO homopolymer are uniformly distributed over the whole backbone due to the equally spaced single σ-bonds, whereas F8BT is characterised by a highly localised LUMO orbital on the benzothiadiazole (BT) units. The electronic states of the HOMO orbital, on the other hand, is more uniformly distributed across the conjugated backbone. This differentiation highlights a crucial influence of the additional BT motifs and resultant intrachain coupling on the charge-transport and photophysical properties of F8BT semiconductors. When the BT units are removed to form the highly conjugated planar polymer shown in Figure 1.4(f), electrons in the excited states are allowed to separate from the bounded exciton state and then propagate a longer distance (limited by the length of the Kuhn segments) along the backbone via intrachain charge transfer in ~100 picoseconds. This continues until interchain hopping takes place to transfer the electrons to the nearest neighbouring polymer chain [13].

The interchain migration of the electrons is far slower (of the order of a tenth of a nanosecond to several nanoseconds) than the intrachain transfer and, in most cases, dominate the overall charge/energy transporting properties of polymeric semiconductors. For the conjugated PFO homopolymer, the evenly distributed molecular HOMO and LUMO orbits would lead to a relatively fast interchain hopping rate. This is in contrast to the F8BT copolymer where the localisation of the LUMO orbit on the BT units results in a funnelling of the intrachain-transferred electrons via close/direct contact of the BT units in adjacent chains that leads to a longer interchain migration path/time.

In conjunction with the intrachain conjugation and energy/charge migration, the interchain electronic coupling/interactions in conjugated polymers provide additional energy transfer pathways. In this way, charge transport is navigated along two- or three-dimensions and, thus, is extremely sensitive to the interchain packing structure. As a result, the light-emitting/absorbing and charge transport/separation properties of semiconducting polymers can

be effectively tuned through design and tailoring of the physical structure. For example, this can be through the configuration of the motifs, the chain conformation and interchain alignment. It should be noted that the competition between the intrachain and interchain interactions, and the many degrees of conformational freedom in conjugated polymers may lead to a complex polymeric texture/network as a mixture of an amorphous phase and orientationally-ordered domains (see **Figure 1.5** for a schematic illustration).

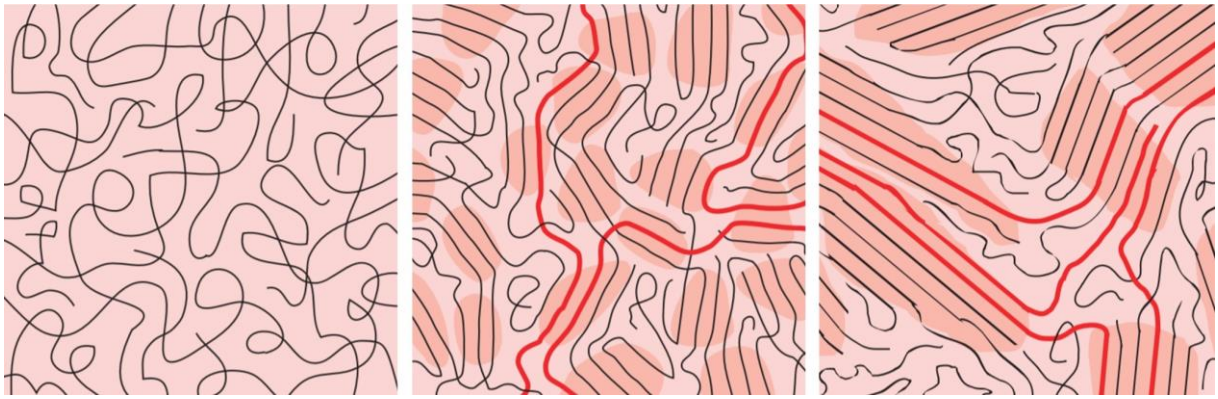

Figure 1.5: Schematics of the typical microstructures in conjugated main-chain polymer films (taken from [14]). Left) Amorphous phase, Middle) Aggregated, and Right) Semi-crystalline polymer films. The darker shadowed areas highlight well-oriented domains while the bright regions represent highly disordered regions. The thick red lines denote tie chains interconnecting the adjacent aggregated domains. When all semi-crystalline domains are oriented along a common direction and merge across the bulk, the most favourable monodomain texture can be generated and extended over a large area in the polymer film.

These different phases can exist at various length scales and with significant structural disorder [14]. The aggregated, locally ordered micro-domains have short-range ordering that is usually inherited from the solutions used for processing. The larger semicrystalline polymeric domains are thought to have a long-range periodicity in 3 dimensions and are enabled by the expansion or chain orientation of individual aggregated micro-domains. The highly disordered amorphous phase often has significant chain distortion and entanglement, alongside a larger energy bandgap than that observed for the ordered phase/regions [15]. This in turn leads to a higher energy barrier for the intrachain and interchain excitonic transfer. A substantial

improvement in the overall charge/energy transporting and other optoelectronic properties of polymeric semiconductors is therefore expected through the creation of percolation pathways, through which the charge carriers can migrate over the whole volume of the polymer film.

Percolating channels in a polymeric network can be generated by introducing sufficient amounts of long tie chains (the thick red lines in Figure 1.5) such that the locally ordered domains are interconnected through the amorphous matrix. An alternative engineering approach is to fabricate a more condensed/ordered polymer structure with a sufficiently suppressed disordered phase, via appropriate polymer alignment techniques. High quality ordering of polymeric chains generally enhances the effective intrachain conjugation by spatially restricting chain entanglements and rotational disorder. This would increase the average intrachain distance over which the charge carriers diffuse for each interchain hopping step between adjacent chains. This anisotropic enhancement can induce a twofold - threefold increase (decrease) in the charge-carrier mobility along the intrachain (interchain) direction when the polymer chains are aligned parallel to the transport direction [16-18], hence leading to considerable charge-carrier mobility anisotropies in the film plane. Other benefits associated with polymer alignment lie in the formation of a large-area monodomain and the removal or suppression of structural disorder of various kinds and, consequently, facilitate an improvement in the magnitude of most spatially-averaged physical properties in the aligned polymer films.

1.5 Molecular Alignment of Conjugated Polymers

Molecular alignment of conjugated polymers and the associated anisotropy in the physical structures and optoelectronic properties complement the benefits in terms of flexibility, mechanical strength, lightweight, easy processability and large-area fabrication. However, fabrication of highly oriented conjugated polymers, especially with an extended monodomain texture, remains challenging. In most film-processing cases, only polydomain films with small,

locally-oriented regions are fabricated using existing alignment techniques. For example, high-magnification scanning tunnelling microscopy (STM) images in **Figure 1.6** demonstrate well-oriented backbones of the conjugated NN1 [17] and TBIDT-BT [18] polymers (see the inserts for their chemical structures).

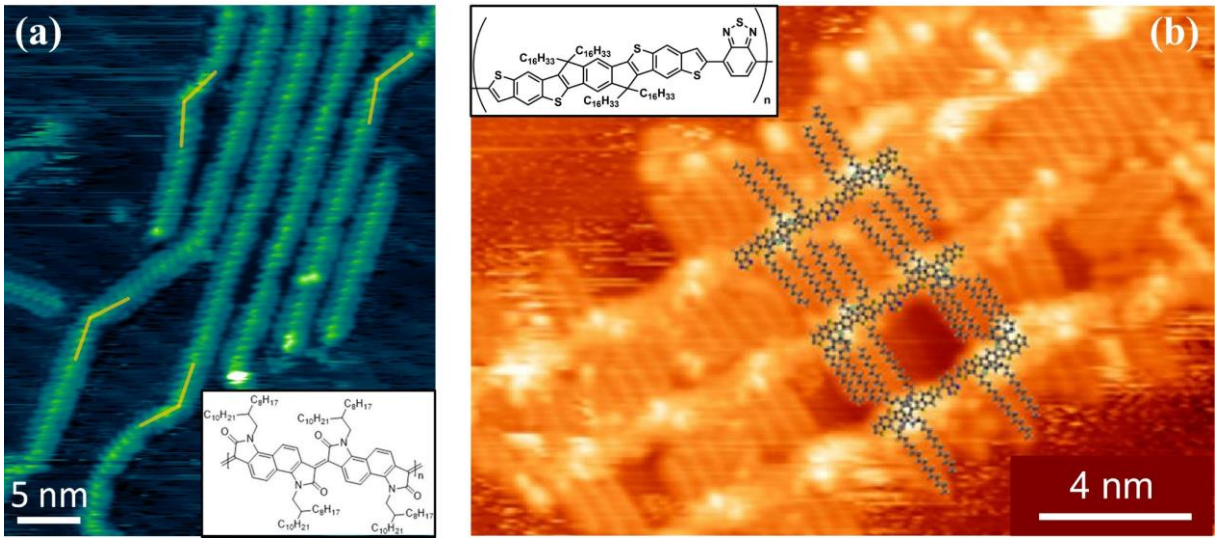

Figure 1.6: High-magnification STM images showing locally oriented backbones in sub-monolayer films of the conjugated NN1 (a) and TBIDT-BT polymers (b). The inserts in (a) and (b) show the chemical structures of NN1 and IDT-BT, respectively. The orange segments superposed on the STM image in (a) mark the occasional sharp bend in the oriented NN1 backbones. The calculated most stable molecular configuration of IDT-BT is superposed on the STM image in (b). Figures (a) and (b) was taken from [17] and [18], respectively.

The STM measurements were implemented for inspection of sub-monolayer films of NN1 and TBIDT-BT deposited on an Au(111) surface, with the backbones being oriented via solution-shearing and self-assembly, respectively. In contrast to a set of large scan STM imaging that confirms the absence of long-range order in amorphous films, high-resolution STM images reveal a high degree of backbone alignment at the local scale - the polymer strands in adjacent backbones were aligned parallel to each other. Occasionally, sharp bends were also observed in the oriented NN1 backbones. These bends in the backbone help to determine a typical Kuhn length of ~20 nm, which is a measure of how far a chain extends in a straight direction and thus provides information on the stiffness and coherent electronic transfer distance

of the polymer [16]. For the more closely packed molecular structures of TBIDT-BT, such as that induced by chain self-assembly, the long alkyl side chains were shown to interdigitate in-between the separation of adjacent parallel backbones and orient nearly perpendicular to the backbone [18]. The formation of this condensed configuration might be related with the fact that the van der Waals interactions between the side chains are maximised in this way and/or the sweep volume of the oriented polymer chains is minimised.

Although it remains challenging to realise, high-quality chain orientation over large-area extended monodomains of solution-processed conjugated polymers provides a variety of important opportunities: *i*) enhance polymer crystallinity as well as mitigate structural/energetic disorders and defects; *ii*) induce large anisotropies in the charge/energy transporting properties; *iii*) manipulate light emission polarisation for polarised polymer LEDs and laser applications; *iv*) modulate the spatial distribution of the refractive indices, enlarge the birefringence (i.e., refractive index difference along the parallel and perpendicular direction); and *v*) improve the spatiotemporal quantum coherence of energy transfer and photon emission in photonic devices. These potential benefits have been motivating researchers to explore more effective polymer alignment techniques to align the otherwise disordered conjugated polymers. The primary aim is to enable a significant improvement in the device performance and to realise new technologies based on highly oriented multifunctional conjugated polymers.

1.6 Liquid Crystalline Conjugated Polymers (LCCPs)

As for the chain alignment of conjugated polymers, liquid crystalline conjugated polymers (LCCPs) represent a unique family of organic semiconductors as they exhibit an inherent long-range orientational order in one- to three-dimensions. Furthermore, they provide an alternative route to the fabrication of highly ordered, large area extended monodomains through structural reorganisation with the application of various external stimuli. It is well known that the liquid

crystal (LC) phases of a material possess long range orientational and (in some cases) positional order compared with the completely disordered isotropic melt, but less order than in solids that have rigid positional and orientational ordering. For example, the molecules in a nematic LC phase do not have positional order, but long-range 1D orientational ordering of the molecular long axis.

LCs are generally comprised of anisotropic molecular structures. There are various types of materials exhibiting LC phases [19], which can be classified as either thermotropic or lyotropic LCs, which respond strongly to temperature or solution concentration changes, respectively. Specifically, thermotropic LCs self-organise into ordered domains in a mesophase (e.g., nematic, smectic A and C) that takes place in a particular temperature range between the solid and isotropic liquid states. Many thermotropic LCs exhibit a nematic phase when the material is heated (or cooled) from the solid (or liquid) state. As schematically shown in **Figure 1.7**, rod-like anisotropic LC molecules (e.g., conjugated polymer chains) tend to align along a preferred direction (known as the director $\hat{\boldsymbol{n}}$ and represented by the dashed red arrow) and are free to flow around each other in all three directions due to the absence of positional order. These features make the nematic phase the least ordered mesophase.

Homogeneous (in plane) and homeotropic (out-of-plane) alignments of the LC director can be induced by the application of sufficient external stimuli, such as the use of alignment layers on the substrate surfaces. The long-range orientational order of a thermotropic nematic LC mesophase [20] is promising for realising high-quality molecular alignment over a larger area, but for thermotropic LCCPs it can only be accessed at rather elevated temperatures ($\approx$ 200 - 300 ^{o}C) relative to conventional low molar mass nematic LCs. This demands special LCCP chain-orientation techniques that are still able to remain effective at these high temperatures.

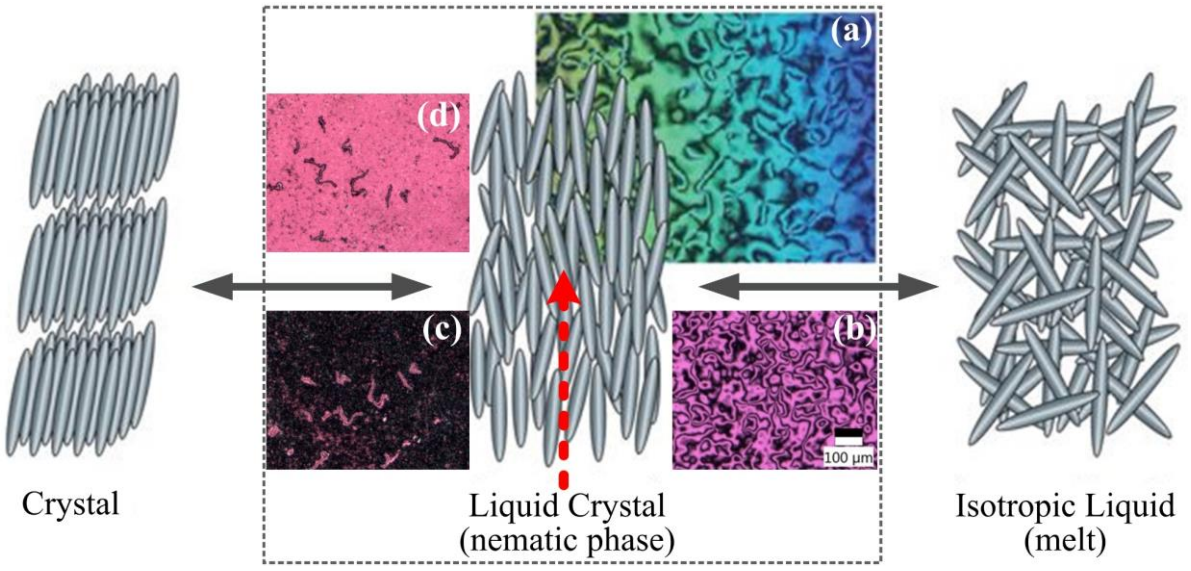

Figure 1.7: Heating a thermotropic nematic LC leads to a sequence of phase transitions from a solid 3D-ordered crystalline phase to an LC mesophase with long-range orientational order (i.e., the long-axes of the LC molecules tend to align along a common direction, namely, the director denoted by the dashed red arrow), and finally to the isotropic liquid phase. The polarising optical microscope images in the dotted rectangle highlight the typical textures formed in a nematic LC layer without ((a) and (b)) and with ((c) and (d)) a homogeneous alignment layer. The LC textures in (c) and (d) exhibit an improved ordering in the extended domains when viewed in the dark and bright state by rotating the sample by 45° relative to the crossed polarisers. For the non-aligned LC polydomain textures in (a) and (b), these resemble a Schlieren texture consisting of randomly oriented micro-domains.

So far, the most significant success of LC materials has been the application of nematic LCs in flat panel displays [21], thanks to the easy and fast electrical switching of the orientation of the LC director (between in-plane alignment and homeotropic alignment, for example) as well as the prominent birefringence, $\Delta n = n_{\parallel} - n_{\perp}$, which stems from two different indices of refraction and thus different speeds experienced by light polarised parallel ($n_{\parallel}$) and perpendicular ($n_{\perp}$) to $\hat{\boldsymbol{n}}$ (i.e., the LC director). Distinct phase retardation (depending on both the thickness of the LC layer and the spatial distribution of Δn) would change linearly polarised incident light to elliptically polarised light (unless the incident light polarisation is at 0° and 90° degrees with respective to $\hat{\boldsymbol{n}}$) when they exit the LC layer. The resultant retardance, where linearly polarised incident light that is blocked when propagating through two crossed

polarisers can be made to pass through (corresponding to the bright domains) the crossed polarisers between which a LC layer is placed.

Without experiencing any effect of alignment, the inherent long-range orientational order of nematic LC layers would lead to separate domains in the nematic phase, and the formation of a typical Schlieren texture. This texture is characterised by randomly oriented but locally ordered individual micro-domains, such as the polydomain LC textures shown in Figure 1.7(a) and (b) in a low molar mass nematic LC sandwiched between glass substrates. The colours in the crossed polarising optical microscopy (POM) images visualise the phase difference of the two non-aligned nematic LC layers (in this example the nematic LC is the well-known eutectic mixture E7) due to the different retardation and thicknesses. On the other hand, a homogeneous alignment layer can be used to orient the LC director to be along an in-plane direction defined by the commanding layer. This yields a highly oriented, large area extended monodomain LC texture (see Figure 1.7(c) and (d), respectively, for a dark-state and bright-state POM image, as well as visible thread-shape dislocation lines).

The degree of orientational order of the nematic LC director is often quantified by the orientational order parameter (*S*), which is a spatial average of the second-order Legendre Polynomial (P_2):

$$S = \langle P_2(\cos\theta)\rangle = \frac{1}{2}\langle 3\cos^2\theta - 1\rangle \tag{1.3}$$

where θ is the angle between the long axis of a LC molecule and the director $\hat{\boldsymbol{n}}$. For perfectly ordered LC phases with all molecules uniformly aligned along $\hat{\boldsymbol{n}}$, S = 1, while S = 0 in the isotropic liquid phase where the LC molecules are randomly oriented [22]. S can be experimentally determined in terms of anisotropies in the optoelectronic properties measured along a polarisation direction parallel and perpendicular to the LC alignment direction.

Prominent examples include optical absorption dichroism as well as anisotropy ratios of the photoluminescence (PL), electroluminescence (EL), and charge-carrier mobility.

As for both low molar mass LCs and LCCPs, the simplest anisotropic mesophase is the nematic phase where the long axis of the molecules exhibits long-range orientational order but there is no long-range positional order. As schematically illustrated in **Figure 1.8**, the distribution of the orientation about the director tends to be more restricted in the LCCPs thanks to their much larger molecular aspect ratios, which can then augment the quality of the alignment relative to low molar mass nematic LCs. However, a successful alignment of an LCCP requires overcoming the higher energy barrier since a greater number of atoms in the polymer chain are simultaneously re-oriented over a larger sweep volume. Moreover, there is normally a range of chain lengths for a LCCP material, namely, the polymer system is polydisperse. This would cause significant fractionation of the disordered amorphous phase and ordered phase of the LCCP chains, leaving the longer chains preferring to occupy the ordered phase, and the shorter chains, the amorphous phase [23].

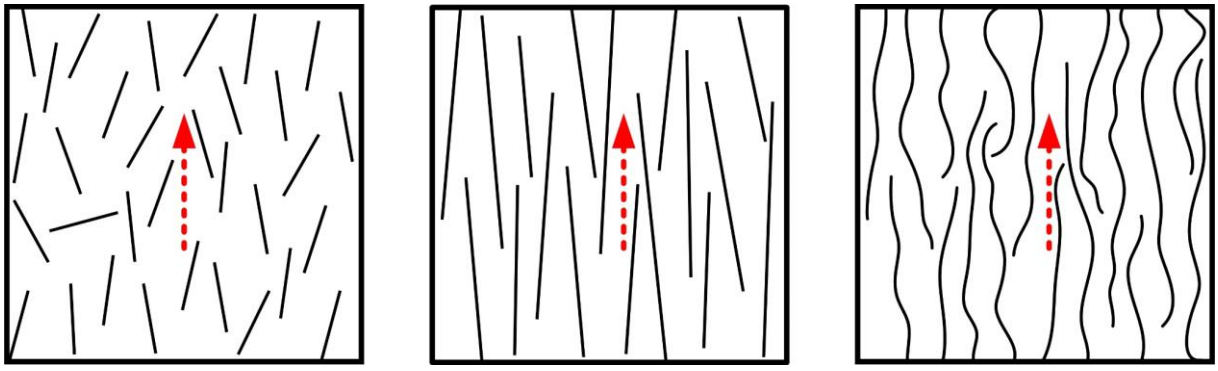

Figure 1.8: Schematic diagrams of a nematic LC organisation of the molecules: Left) low molar mass LC; A nematic LCCP with rigid chains (Middle) and semi-rigid chains (Right). The dotted red arrow denotes the director (or alignment direction) in each case.

The polymer chains that give rise to the nematic mesophase are rarely completely rigid and are best thought of as being semi-rigid chains. In other words, when the polymer chains are

too flexible, they should exhibit no LC phase [23]. Polymer chains with a sufficiently rigid backbone are expected to self-organise and align with each other (see the middle and right panels of Figure 1.8). Intuitively, the overall molecular alignment quality in an oriented LCCP film should be a positive function of the molecular weight and stiffness. A higher clearing temperature and a larger energy barrier for molecular re-orientation goes hand in hand with a greater molecular weight and/or stiffness. We can therefore expect that to successfully fabricate highly oriented, large-area extended LCCP monodomains, a commanding layer with a sufficiently high-temperature thermal stability and anchoring energy is required.

1.7 Existing Methods for Orienting LCCP Films

Realisation of high-quality LCCP chain-orientation and fabrication of large-area extended monodomains, ideally in a simple, cost-effective and scalable way, are urgently needed yet still remain a considerable challenge. Various polymer alignment methods have been developed that have attracted great attention from academia and industry, in terms of creating certain degrees of polymer chain orientation by making use of the low viscosity in the mesophase and coupling between the highly anisotropic polymer chains with applied stimuli such as mechanical, electrical and magnetic fields. The order parameter, length scale and uniformity of the polymer alignment in the correspondingly oriented polymer films, however, are rarely sufficient to meet the requirements for polymer-based (flexible) optoelectronic, electrical and optical applications.

The existing polymer alignment methods include mechanical alignment, use of pre-aligned commanding layers and substrate surface confinements, as well as orientation under flow, electromagnetic and surface tension effects. These chain-orientation techniques usually result in non-uniform alignment or polydomain textures formed in LCCP films, which are not ideal for a rich range of optoelectronic devices. There is thus a significant need for exploring new effective alignment methods for orienting multifunctional conjugated polymers.

1.7.1 Mechanical Alignment

Polymer chains can be oriented by mechanical alignment techniques such as polymer stretching, off-centre spin coating, and solution shear coating. In fact, the first polarised polymer LED was a product of mechanically aligned poly(3-(4-octylphenyl)-2,2'-bithiophene) (PTOPT) films by stretching the polyethylene substrates [24], which displayed an electroluminescent (EL) anisotropy ratio of 2.4 but a low external quantum efficiency of <1%. However, this polymer stretching alignment method suffers from issues associated with subsequent structural relaxation and soft-hard transition, unless the well-oriented polymer chains in the soft state can be converted during tensing or being locked in the solid state by a rapid quenching process [25].

In analogy to the mechanical force-enabled polymer alignment, off-centre spin coating exploits the centrifugal force of a conventional spin coating process. The molecular alignment by off-centre spin coating is reliant on a radial flow field or a directional shear friction at the liquid-ambient interface. Although this technique was first introduced to align small molecule semiconductors [26], its application has recently been extended to direct the film deposition of conjugated polymers and polymer blends [27], in which unidirectional chain alignment can be achieved in the pristine polymer films coated using aggregated solutions. In particular, high field-effect mobilities of 2.6 cm^2 V^{-1} s^{-1} were demonstrated in off-centre spin-coated P(NDI2OD-T2) films [28], compared with the mobility in normally spin-coated counterparts varied over a larger range from 0.1-0.6 cm^2 V^{-1} s^{-1}. Besides, a hole mobility of 7.3 cm^2 V^{-1} s^{-1} and mobility anisotropy of 37 between the radial and tangential direction of the offer-centre spin coating were shown in hole transporting poly[(E)-1,2,-(3,3'-dioctadecyl-2,2'-dithienyl)ethylene-alt-dithieno-(3,2-b:2',3'-d)thiophene] [29]. Nevertheless, off-centre spin coating usually produces non-uniform alignment across the substrate, since the centrifugal force exerted on the polymer solution/film are not mutually parallel due to the finite distance between the sample and the spin center [30].

Solution shear/bar coating has become another important mechanical alignment technique. This is a facile deposition process that can also induce uniaxial chain alignment, where the 1D motion of the solution meniscus with respect to the substrate generates a shear force on the fluid that triggers polymer chain re-orientation during the solvent drying process. It is favourable if the polymer has a rigid backbone structure. For instance, when solution shear coating was used to deposit and orient the chains of NN2 polymer films with extended linear conjugated backbones, an optical dichroic ratio of 6 and a saturation electron mobility anisotropy of ≈7 was observed in the resulting NN2 thin films [17].

1.7.2 Chain Orientation under Surface Tension and Electric Fields

Similar to the molecular alignment mediated by mechanical forces, surface tension has been utilised to orient polymer domains. One important technique in this category is direct inkjet printing, which uses droplet confinement from a solution surface tension gradient. Inkjet printing can locally align polymer chains in droplets and spatially pattern polymer chain-orientation [31]. When it comes to creating spatially patterned molecular alignment, inkjet printing has advantages such as allowing micron- to submicron pattern resolution on both rigid and flexible substrates. However, the distribution of the molecular alignment direction in inkjet-printed droplets is normally non-uniform in 2D or 3D when observed over finer length scales.

Application of a sufficient electric field offers extra mechanisms to orient polymer chains, which is exemplified herein by the electrospinning alignment of polymeric nanofibers. During an electrospinning process, a high voltage is applied to the precursor solution, which is then ejected from a syringe to form fibers due to interaction between the charged polymer chains and external electric field [32]. Electrospun polymer fibers could show high levels of chain orientation and mechanical strength along the fiber axis. When collected by a drum collector that rotates at a high speed, well-aligned polymeric fibres can be obtained, and the quality of

the fibre alignment increases with larger drawing forces from higher rotation speeds. Electrospinning alignment has advantages in terms of large-area polymer alignment. However, this process always results in highly porous films that have a relatively low filling factor due to the presence of nanopores. Although these nanoporous structures and subsequent carbonisation treatment of the electrospun polymer fibres are of great interest in energy conversion and storage devices [32] to act as a filtering membrane and conductive percolating networks, the high-density nano-voids become structural defects and are detrimental for the charge/energy transfer and light emission applications.

Langmuir-Blodgett (LB) deposition of stacked molecular layers is another method of molecular alignment using surface tension, in which polymer chains are aligned parallel to the substrate plane because of an anisotropic flow formed during the transfer/dip process. The LB-directed stacking of monolayers has enabled polarised light emission in organic LEDs. The LB-oriented thin films of rigid rod-like poly(p-phenylene) polymer [33] and shish-kebab-type lyotropic LCs [34] demonstrated good optical dichroic ratio and polarisation ratios for the EL/PL emission, compared with the non-aligned counterpart prepared using a spin coating deposition technique. Despite these encouraging anisotropic light-emitting properties, LB molecular alignment might be unrealistic for relatively thick polymer films since it would require multiple depositions of monolayers.

1.7.3 Substrate Surface Confinements

Alignment of both conjugated polymers and low molar mass LCs has been achieved by spatially confining polymer chains onto tailored/nanostructured surfaces prior to solvent removal or solidification. Periodic surface nano-confinements such as those created from corrugated or porous substrates can be effective in terms of converting the initially disordered polymer chains into a more regular fashion. This also restricts the orientational freedom of the polymer chains

in order to generate a longer-range structural ordering. Semicrystalline polymeric micro-colloids were observed by pre-aggregating polymer solutions [16] or confining conjugated polymers within nano-channels or nano-grooves fabricated in silica substrates [35,36]. In addition, nanoimprinted PMMA has also been shown to well-orient thermotropic LCs [37].

1.7.4 Rubbed Polyimide Commanding Layers for LC Alignment

Alignment has been exploited to enable facile and high-quality molecular alignment in LC displays (LCDs) thanks to the intrinsic fluidity, self-organisation and low-dimensional but long-range structural order. While preserving all the previously discussed chain orientation mechanisms, the unique rhetological and self-assembling behaviour of thermotropic LCCPs are expected to enable both better polymer chain alignment and facile fabrication of highly oriented large-area extended monodomains. Homogeneous and homeotropic alignment layers have been thoroughly explored to orient conventional low molar mass LCs. Usually, a pair of aligned commanding layers is assembled to form a glass cell with a gap in-between that is filled with the LC. This leads to the alignment of the LC layer into a monodomain due to the alignment/commanding layers (e.g., rubbed poly(vinyl alcohol) (PVA) or poly(imides) (PIs)-coated glass substrates). In addition to the homogeneous alignment of low molar mass LCs, rubbed high-temperature PI and PVA commanding layers were found to be effective for homogeneously aligning conjugated polymer layers, where good alignment requires a high rubbing strength [38]. An absorption dichroic ratio of ≈5 was reported for mechanically rubbed alignment of polyfluorene polymers [39].

Although such rubbing approaches are a well-established alignment technology in the LCD industry and can also yield reasonable alignment quality, they introduce various detrimental defects such as contaminations, electrostatic charges and scratches. It is also noteworthy that the various types of commanding layers employed in the previously discussed

chain orientation techniques are highly insulating, which greatly downgrades the potential of directly introducing them into the well-established architecture for OLED technologies and other electron-injection/extraction related organic electronics for molecular alignment.

1.7.5 Comparison of Various Polymer Alignment Methods

The advantages and disadvantages of the described existing polymer alignment methods and the photoalignment technique exploited in this Thesis are summarised in **Table 1.1**.

Table 1.1. Comparison of the advantages and disadvantages of the existing polymer alignment methods and the proposed photoalignment technique.

Alignment Technique	Alignment Quality	Advantage	Disadvantage
Polymer film stretching	Relatively low	Easy uniaxial alignment	Structural relaxation and soft-hard transition
Off-centre spin coating	Low - Moderate	Easy deposition	Non-uniform alignment
Solution shear coating	Low - Moderate	Facile process	Introduce contaminants and rough film surface
Direct inkjet print	Relatively low	Potential to enable micro-to-submicron pattern resolution	Non-uniform alignment in the printed droplets
Electrospinning	Low - Moderate	Produce free-standing/ nanoporous (conductive) nano-fibers (mats)	Operation with very high voltage; Polymeric nanofibers alignment
Langmuir-Blodgett deposition	Moderate - High	Alignment of mono-layers and stacks	Unrealistic for orienting polymer films
Nano-grooved/porous interfacial confinement	Low - Moderate	Well-established; Easy implementation	Require nanostructured substrates; Cause rough film surface
Rubbed alignment layer	Moderate	Well-established; Suitable for large-area unidirectional alignment	Introduce of various contaminants and rough film surface; Unstable at high temperatures
Photoalignment presented in this thesis	Record-high (~100%) order parameters	Non-contact operation; Uniform alignment and fine control over chain orientations in the same film; Fabricate extended polymer monodomain films with sub-micron spatial pattern resolution	A combination of macroscopic UV-light alignment and local ultrafast two-photo laser writing alignment can be required to enable fine patterning of LCCP chain-orientations

1.8 Photoalignment of Low Molecular Weight LCs

In contrast to the fabrication of only uniaxial polymer/LC alignment and the introduction of detrimental defects (e.g. electrostatic charges, scratches, voids, domain boundaries) arising from conventional mechanically-rubbing aligned commanding layers, photoalignment is emerging as a more promising molecular alignment technique. This is because it offers a contactless operation (i.e., no mechanical rubbing), easy fabrication process, most importantly, its capacity for enabling high spatial pattern resolution of the molecular alignment. Photoaligned commanding layers have already been used to generate homogeneous alignment and extended monodomains in some low molar mass LCs [41]. In addition, photoalignment using a mask can be effective in terms of creating fine-scale features in the LC alignment patterns. The long-range orientational order in photo-aligned/patterned nematic LC host is also feasible to orient functional molecular/nanostructured guests. Therefore, photoalignment is expected to hold the promise of easy and low-cost fabrication of uniformly aligned LCCP monodomains as well as submicron pattern resolution of LCCP chain-orientation.

1.8.1 Photoalignment Layer Used for LC alignment

The photoalignment technique has emerged as a versatile molecular alignment method by making use of photo-induced anisotropic absorption and molecular re-orientation. It can be dated back to 1988 when a partial ordering of molecular fragments was noticed in photo-responsive azobenzene thin films after a photo-selected *cis-trans* transformation [40], which has well oriented molecular configurations with the alignment direction defined by the excitation light polarisation. These photoaligned layers were then employed to initiate planar or vertical alignment of nematic, ferroelectric, lyotropic and discotic LCs based on LC-surface interaction in the mesophase [41]. Later, optical control over the LC alignment was realised by exposing other photoalignable layers (e.g., dye-doped polymers, light-sensitive polymers) to polarised light with or without the use of a photomask. These photoalignment materials have

demonstrated capacity of providing high-quality alignment of low molar mass LCs that were either sandwiched between or deposited on photo-aligned/patterned commanding layers.

Photoalignment technology has a number of advantages over the previously mentioned LC/polymer alignment techniques, which can be summarised as follows:

1. Cost-effective and contactless molecular alignment, which helps to avoid mechanically induced electrostatic charges, impurities, and structural damage;
2. Facilitating the fabrication of highly ordered, large-area extended monodomains and less rough command surfaces, which could significantly alleviate light/energy losses because of the absence of defects and domain boundaries formed in polydomain films;
3. Better/cheaper photo-patternablity and rewritability of the optically aligned regions;
4. High thermal stability and capacity of large-area monodomains on rigid/flexible substrates;
5. Huge potential for transforming a rich range of photonic and optoelectronic applications such as light and refractive index modulation, polarised polymer LEDs and multi-domain alignment on LCD pixels, and for enabling new LCs/LCCPs device configurations such as planar microcavity, holographic elements, meta-surfaces, and optical routing/circuits.

The mechanisms responsible for photoalignment include [41]: *i*) photochemically reversible *cis-trans* isomerisation; *ii*) pure molecular alignment of absorptive oscillators owing to the diffusive re-orientation excited by polarised light; *iii*) topochemical crosslinking; and *iv*) photo-degradation/destruction. The former two photoalignment mechanisms involve reversible structural transformations, whilst irreversible photochemical changes usually take place in the last two cases. When optically pumped by a polarised light beam, the anisotropic absorption of the molecules in the photoalignment layer such as rod-like azo-dyes could activate chromophores (along the long axis of the molecules) to thermodynamically re-orient and align parallel or perpendicular to the light polarisation. Among other attributes, some photo-oriented

azo-dye thin films have demonstrated high levels of photoalignment order and anchoring energies (e.g., azimuthal anchoring energy of ~10^{-4} J/m^2), voltage holding ratio (greater than 99% at 80 ^{o}C) and almost zero pretilt angle [42-43], which become comparable with, if not better than, that of the standard rubbed-PI commanding layers [44].

1.8.2 Uniform and Spatially Patterned Photoalignment of Low Molar Mass LCs

In addition to facilitating the manufacture of large-area extended uniform LC alignment, another prominent advantage of the photoalignment technology lies in the ability to generate spatial definition of the LC alignment using photo-masking or photopatterning of the polarised light exposure. In contrast to the facile and cost-effective photoalignment, other existing spatial pattern methods are expensive and involve difficult fabrication procedures. The maximum possible pattern resolution (i.e., the smallest size of the ordered domains) reported for the photo-alignment of LCs can be as high as 105 nm in Ref. [45] through the UV-alignment of a sulfonic dye, SD1, layer, where a two-step orthogonal SD1-alignment process was employed that involved using a Lloyd's mirror interference technique for the second step (see **Figure 1.9**).

While the direct photoalignment technique has enabled a variety of sophisticated optical elements such as photo-patterned polarisers, phase retarders, colour filters and optical security elements, an indirect photoalignment method is also needed to complement the direct photoalignment, in case anisotropic absorbers cannot be directly photoaligned by the application of an excitation light source [41]. In principle, it is possible to utilise the guest-host effect to photo-align an anisotropic molecular/nanostructured guest (or host) by photoaligning the host (or guest). For instance, after dispersing functional additives such as highly luminescent nanorods (NRs) into a photo-alignable LC host [46], it is possible to indirectly orient the initial spin-coated, disordered NRs in the NRs/LC composite film in the process of photo-aligning the LC host in the mesophase of the host LC.

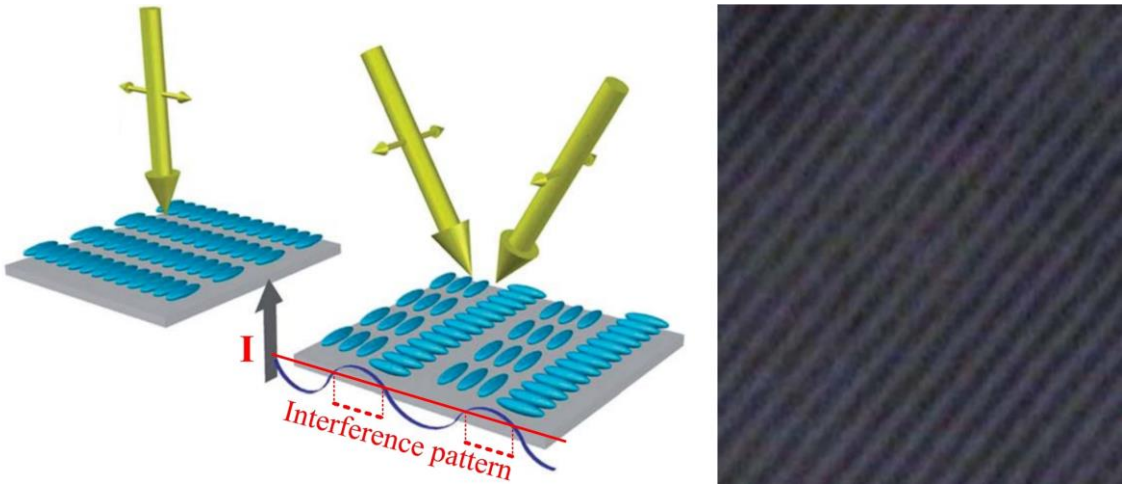

Figure 1.9: (Left) schematic illustration of the exposure procedure used to fabricate a unidirectional photo-aligned SD1 commanding layer. (Middle) Illustration of the process for forming a spatially patterned grating structure by exposing a uniformly oriented SD1 photoalignment layer to an optical interference pattern consisting of two parallel-polarised expanded UV-light beams (produced by a Lloyd's mirror) with polarisation perpendicular to that used in the left-hand panel for the uniform photoalignment step. (Right) the optical micro-photograph of the resulting 1D grating pattern formed in a ULC17 LC film, which was deposited on the photo-pattered SD1 commanding layer. The pitch of the grating was ≈2 μm. The SD1 molecules re-orient in the substrate plane and align perpendicular to the light polarisation when the intensity of the polarised excitation beam or optical interference pattern exceeds the energy barrier (denoted by the red horizontal line in the middle panel) for SD1 photoalignment. All images shown herein were taken from [45].

Figure 1.10 showcases photomasked photoalignment of a thin film of red-light emitting CdSe/CdS NRs dispersed in a photo-polymerisable LC host, which was spin-coated from a blend solution on a two-step photoaligned SD1 commanding layer. The photo-masked alignment patterns were created in the second irradiation step of SD1 with a polarisation that was at 90^{o} relative to the polarisation used in the first step to form a unidirectional uniform SD1-alignment [46]. Subsequently, the photoaligned NR/LC composite film was photo-cured to trigger polymerisation. The as-shown fluorescence images reveal that strongly polarised light emission was observed in the photoaligned NR/LC domains with a critical size of 2 - 10 μm.

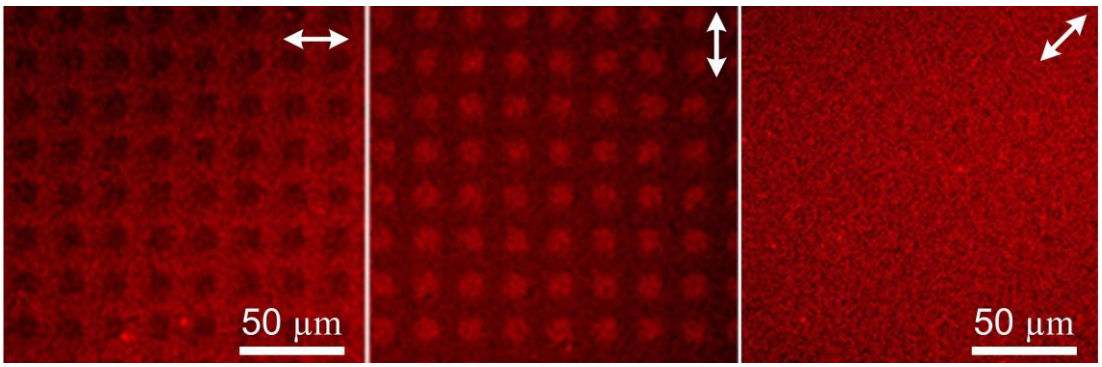

Figure 1.10: Fluorescence optical micrographs demonstrating that a 90 ° rotation of the analyser (denoted by the double-headed white arrows) from the horizontal (left) to vertical (middle) direction could switch between the bright and dark states of a 2D grating pattern. This grating had been generated in a photoaligned composite thin film of highly luminescent CdSe/CdS core-shell nanorods dispersed a photo-polymerisable LC host. The microscale alignment patterns were shown to completely disappear when the analyser polarisation angle was set at 45° to the direction of the nanorod alignment (middle), where the fluorescence intensity was uniform across the film. Images were taken from [46].

1.9 Scope and Outline of the Thesis

An introduction to conjugated polymers and the alignment of LC phases has been provided in the present Chapter. The delocalisation of π-electrons in organic molecules, conjugated polymers, and the associated energy levels and vibronic transitions are briefly described. In this thesis we emphasized that the optical, electronic and optoelectronic properties of polymeric semiconductors are dictated by their intrachain/interchain interactions and effective conjugation lengths. Both aspects are extremely sensitive to the configurations of the chemical motifs and physical structures such as the polymer alignment, chain conformation, domain pattern and structural/energetic defects. It is pointed out that the solution-processed polymer films and/or vacuum-deposited small molecule films usually exhibit an amorphous/polydomain structure and significant structural disorder, instead of the favorable highly ordered, large-area extended monodomains. This calls for realisation of high-quality orientation of the polymers at large length scales such as >cm, ideally in an easy and low-cost way. Among other benefits, well-oriented conjugated polymers could be shown to provide better control and greater anisotropy in the physical structure and a variety of highly sought-after properties, hence complementing

the existing studies on the complicated structure-property relationships in the technologically important conjugated polymers.

A combination of the inherent long-range orientational order present in low molar mass LCs and the comparatively recent photoalignment technology has been proposed to facilitate the manufacture of extended polymer monodomains (at a large length scale) and high-resolution spatial alignment pattern (at a fine scale) of widely-used liquid crystalline conjugated polymers (LCCPs). Photoalignment is demonstrated as a reversible process for optically rewritable and multiple alignment of LCCPs. Exposing photoalignment layers to polarised light with or without a photomask could enable highly ordered commanding layers with excellent high-temperature thermal stability and submicron LCCP pattern resolution. Other advantages and potential related to photo-aligned/patterned LCCPs have been highlighted in this Chapter.

In Chapter 2 a summary is provided on the experimental techniques for characterising the overall alignment quality and spatially-varied structure/properties in the photo-aligned/patterned LCCP films. The operating principle and benefits of each characterisation technique used in this thesis are discussed, which includes X-ray diffraction, crossed polarising optical microscopy, polarised optical spectral measurements, polarised confocal fluorescence microscopy and micro-photoluminescence spectral mapping.

In Chapter 3, the properties of the photoalignment layer material SD1 and the optimisation of the linearly polarised UV-mediated alignment process for the photoalignment layers is presented. The key photoalignment parameters optimised include the duration of the UV illumination, and the thickness of both the SD1 photoalignment layer and the photoaligned F8BT overlying film. The optimal UV-aligned SD1 commanding layers and SD1-oreinted F8BT film thickness are identified in order to specify the tunable range of the structural order and application scope of the photoaligned LCCPs. An experiment using photomasks and UV-

mediated alignment is also carried out to determine the best spatial pattern resolution that can be achieved using this photomasked photoalignment method. In addition, the effectiveness of the indirect photoalignment technique is showcased using a photo-aligned F8BT/Red-F binary blend film. It is indicated that the polymer chains of the non-LC Red-F guest could be oriented by the photoaligned F8BT host in its nematic mesophase.

In Chapter 4 we systematically study the microstructural and photophysical properties of a series of LCCP films that have different degrees of structural ordering via LC self-organisation and partial/full photoalignment in the nematic phase. Crossed polarising optical microscopy is used to observe the optical texture formed in the different types of F8BT films, while grazing-incidence wide-angle x-ray scattering (GIWAXS) measurements are implemented to determine their chain conformations, interchain packing structures, and coherence lengths along different directions. Polarised optical absorption spectra, polarised steady-state and time-resolved photoluminescence spectra are recorded to provide information about the chain-orientation quality, the polarisation and lifetime of the light emission, along with the strength/efficiency of the intrachain/interchain chromophoric and fluorophoric species. Polarised confocal fluorescence microscopy and micro-photoluminescence mapping measurements are carried out to resolve the spatial and angular variations in the intensity and spectral lineshape of the polarised light-emission components in selected locations in various F8BT films that are created from different fabrication and chain-alignment processes.

In Chapter 5 two-photon femtosecond infrared laser writing is used, for the first time, to locally align the molecules in an SD1 layer, with the aim of significantly enhancing the spatial pattern resolution in both the photoalignment layer and the SD1-oriented LCCP overlying films. This process takes advantage of the highly nonlinear two-photon absorption of the SD1 layer to create bespoke alignment patterns in the SD1-aligned LCCP films. The laser writing

parameters including the laser power, the writing speed and the numerical aperture of the focussing lenses are optimised in terms of enabling the best pattern resolution and the highest alignment quality/uniformity in the SD1-oriented F8BT nematic glass films. Two-photon laser rewriting is carried out on both nonaligned and UV-prealigned photoalignment layers using a range of different relative orientations between the pre-alignment direction and the laser-writing polarisation. Control of the light polarisation orientation leads to different LC textures and contrast in the polarised fluorescence light-intensity in the oriented LCCP films. The width of the laser-written lines generated in the oriented F8BT glass films is extracted as a measure of the two-photon direct laser writing pattern resolution.

In Chapter 6 we present a detailed comparison between the alignment obtained using the ultrafast two-photon infrared laser writing process and the macroscopic polarised UV-alignment of SD1. Anisotropies in the optical absorption strength and photoluminescence intensity are measured and analysed from the photoaligned F8BT glass films on the SD1 commanding layers that have been created using the two different fabrication approaches in order to compare the F8BT alignment quality and light emission character. Polarised micro-photoluminescence spectra mapping is implemented as well to extract information on the anisotropy in the localised light emission, which is then correlated with the overall crystallinity and possible chain conformations induced in the aligned F8BT films on the UV- and laser-aligned SD1 photoalignment layers. The polarised fluorescence spectra and efficiencies of emissive intrachain/interchain species are differentiated in the two-photon-laser and UV-aligned F8BT nematic monodomains.

Finally, in Chapter 7 the main achievements and conclusions are presented. This chapter also includes suggestions for future work, pointing to some new ideas and novel research frontiers of the high-quality photo-aligned and photo-patterned organic semiconductors.

References

[1] S. R. Forrest, The path to ubiquitous and low-cost organic electronic appliances on plastic, *Nature* **428**, 911 (2004).

[2] E. F. Valeev, V. Coropceanu, D. A. da Silva Filho, S. Salman, J. L. Brédas, Effect of electronic polarisation on charge-transport parameters in molecular organic semiconductors, *J. Am. Chem. Soc.* **128**, 9882 (2006).

[3] M. C. R. Lorente de No, 2005, Polymer dispersed dyes as gain media for optical amplifiers and lasers. PhD Thesis, Imperial College London, London.

[4] S. M. Menke, R. H. Friend, D. Credgington, *Organic semiconductors: fundamental aspects of materials and applications*, Wiley, Weinheim (2017).

[5] S. S. Shaik, P. C. Hiherty, J.-M. Lefour, G. Ohanessian, Is delocalization a driving force in chemistry? Benzene, allyl radical, cyclobutadiene, and their isoelectronic species, *J. Am. Chem. Soc.* **109**, 363 (1987).

[6] Y. Li, V. Coropceanu, J.-L. Brédas, The WSPC reference on organic electronics. Materials and energy series. Volume 2: organic semiconductors: fundamental aspects of materials and applications, Wiley, Weinheim (2017).

[7] P. F. Bernath, *Spectra of Atoms and Molecules (Topics in Physical Chemistry)*, Oxford University Press, Oxford UK (1995)

[8] B. Herman, J. R. Lakowicz, D. B. Murphy, T. J. Fellers, M. W. Davidson, (2004). Available at: http://www.olympusconfocal.com/theory/fluoroexciteemit.html.

[9] A. Tokmakoff. Lecture 6: Absorption lineshapes. In *Introductory Quantum Mechanics II - MIT Course No. 5.74*. Cambridge MA, 2009, MIT OpenCourseWare [Online]. URL: https://ocw.mit.edu/courses/chemistry/5-74-introductory-quantum-mechanics-ii-spring-2009/lecture-notes.

[10] G. Thomas, K. Stamnes, *Radiative Transfer in the Atmosphere and Ocean*, Cambridge University Press, Cambridge MA (2017).

[11] M. Grell, D.D.C. Bradley, X. Long, T. Chamberlain, M. Inbasekaran, E.P. Woo *et al.*, Chain geometry, solution aggregation and enhanced dichroism in the liquid crystalline conjugated polymer poly(9,9-dioctylfluorene), *Acta Polyme.* **49**, 439 (1998).

[12] L. L. G. Justino, M. L. Ramos, P. E. Abreu, A. Charas, J. Morgado, U. Scherf *et al.*, Structural and electronic properties of poly(9,9-dialkylfluorene)-based alternating copolymers in solution: An NMR spectroscopy and density functional theory study, *J. Phys. Chem. C* **117**, 17969 (2013).

[13] S. Fratini, M. Nikolka, A. Salleo, G. Schweicher, H. Sirringhaus, Charge transport in high-mobility conjugated polymers and molecular semiconductors, *Nature Mater.* **19**, 491 (2020).

[14] R. Noriega, J. Rivnay, K. Vandewal, F. P. V. Koch, N. Stingelin, P. Smith, M. F. Toney, A. Salleo, A general relationship between disorder, aggregation and charge transport in conjugated polymers, *Nature Mater.* **12**, 1038 (2013).

[15] W. F. Pasveer *et al.*, Unified description of charge-carrier mobilities in disordered semiconducting polymers, *Phys. Rev. Lett.* **94**, 206601 (2005).

[16] H. Sirringhaus *et al.*, Mobility enhancement in conjugated polymer field-effect transistors through chain alignment in a liquid-crystalline phase, *Appl. Phys. Lett.* **77**, 406 (2000).

[17] M. Xiao, B. Kang, S. B. Lee, L. M. A. Perdigão, A. Luci, D. A. Warr *et al.*, Anisotropy of charge transport in a uniaxially aligned fused electron-deficient polymer processed by solution shear coating, *Adv. Mater.* **32**, 2000063 (2020).

[18] H. Chen, A. Wadsworth, C. Ma, A. Nanni, W. Zhang, M. Nikolka *et al.*, The effect of ring expansion in thienobenzo[b]indacenodithiophene polymers for organic field-effect transistors, *J. Am. Chem. Soc.* **147**, 18806 (2019).

[19] E. B. Priestley, P. J. Wojtowicz, P. Sheng (Eds.), *Introduction to liquid crystals*, Plenum Press, New York (1974).

[20] R. Xia, G. Heliotis, D. D. C. Bradley, Fluorene-based polymer gain media for solid-state laser emission across the full visible spectrum, *Appl. Phys. Lett.* **82**, 3599 (2003).

[21] B. Bahadur (Ed.), *Liquid crystals: applications and uses*, World Scientific, Singapore, (1991).

[22] K. Takashi, T. Carsten, G. Helen, E. P. Raynes, *Handbook of liquid crystals*, Wiley, Weinheim (2014).

[23] A. M. Donald, A. H. Windle, *Liquid Crystalline Polymers*, Cambridge University Press, Cambridge, 1992.

[24] P. Dyreklev, M. Berggren, O. Inganäs, M. R. Andersson, O. Wennerström, T. Hjertberg, Polarized electroluminescence from an oriented substituted polythiophene in a light emitting diode, *Adv. Mater.* **7**, 43 (1995).

[25] M. Grell, D. D. C. Bradley, Polarized luminescence from oriented molecular materials, *Adv. Mater.* **11**, 11 (1999).

[26] Y. Yuan *et al.*, Ultra-high mobility transparent organic thin film transistors grown by an off-centre spin-coating method, *Nat. Commun.* **5**, 3005 (2014).

[27] H. Wang, L. Chen, R. Xing, J. Liu, Y. Han, Simultaneous control over both molecular order and long-range alignment in films of the donor-acceptor copolymer, *Langmuir* **31**, 469 (2014).

[28] R. Matsidik, H. Komber, A. Luzio, M. Caironi, M. Sommer, Defect-free naphthalene diimide bithiophene copolymers with controlled molar mass and high performance via direct arylation polycondensation, *J. Am. Chem. Soc.* **137**, 6705 (2015).

[29] N.-K. Kim *et al.*, High-performance organic field-effect transistors with directionally aligned conjugated polymer film deposited from pre-aggregated solution, *Chem. Mater.* **27**, 8345 (2015)

[30] D. Khim *et al.*, Uniaxial alignment of conjugated polymer films for high performance organic field-effect transistors, *Adv. Mater.* **30**, 1705463 (2018).

[31] H. Sirringhaus *et al.*, High-resolution inkjet printing of all-polymer transistor circuits, *Science* **290**, 2123 (2000).

[32] B. Zhang, F. Kang, J.-M. Tarascon, J.-K. Kim, Recent advances in electrospun carbon nanofibers and their application in electrochemical energy storage, *Prog. Mater. Sci.* **76**, 319 (2016).

[33] Dr. V. Cimrová, M. Remmers, D. Neher, G. Wegner, Polarized light emission from LEDs prepared by the Langmuir-Blodgett technique, *Adv. Mater.* **8**, 146 (1996).

[34] Z. Aliadip, K. Davison, H. Nooshin, R. H. Tredgold, Magnetic orientation of phthalocyaninato-polysiloxanes, *Thin Solid Films* **201**, 18 (1991).

[35] M. S. Chen *et al.*, Enhanced solid-state order and field-effect hole mobility through control of nanoscale polymer aggregation, *J. Am. Chem. Soc.* **135**, 19229 (2013).

[36] T.-Q. Nguyen *et al.*, Control of energy transfer in oriented conjugated polymer/mesoporous silica composites, *Science* **288**, 652 (2000).

[37] Z. Zheng *et al.*, Uniaxial alignment of liquid-crystalline conjugated polymers by nanoconfinement, *Nano Lett.* **7**, 987 (2007).

[38] D. D. C. Bradley, R. H. Friend, H. Lindenberger, S. Roth, Infra-red characterization of oriented poly (phenylene vinylene), *Polymer* **27**, 1709 (1986).

[39] M. Grell *et al.*, Blue polarized electroluminescence from a liquid crystalline polyfluorene, *Adv. Mater.* **11**, 671 (1999).

[40] K. Ichimura, Y. Suzuki, T. Seki, A. Hosoki, K. Aoki, Reversible change in alignment mode of nematic liquid crystals regulated photochemically by 'command surfaces' modified with an azobenzene monolayer, *Langmuir* **4**, 1214 (1988).

[41] V. G. Chigrinov, V. M. Kozenkov, H.-S. Kwok, *Photoalignment of liquid crystalline materials: physics and applications*, Wiley, Chichester (2008).

[42] V. Chigrinov, H.-S. Kwok, H. Takada, H. Takatsu, Photoaligning by azo-dyes: physics and applications, *Liquid Crystals Today* **4**, 1 (2005).

[43] B. Zhang, K. Li, V. Chigrinov, H.-S. Kwok, H. C. Huang, Application of photoalignment technology to liquid-crystal-on-silicon microdisplays. *Jan. J. App. Phys.* **44**, 3983 (2005).

[44] V. Chigrinov *et al.*, Diffusion model of photoaligning in azo-dye layers, *Phys. Rev. E* **69**, 061713 (2004).

[45] E. A. Shteyner, A. K. Srivastava, V. G. Chigrinov, H.-S. Kwok, A. D. Afanasyev, Submicron-scale liquid crystal photo-alignment, *Soft Matter* **9**, 5160 (2013).

[46] J. Schneider, W. Zhang, A. K. Srivastava, V. G. Chigrinov, H.-S. Kwok, A. L. Rogach, Photoinduced micropattern alignment of semiconductor nanorods with polarized emission in a liquid crystal polymer matrix, *Nano Lett.* **17**, 3133 (2017).

Chapter 2

Experimental Techniques for Photoaligned and Spatially Patterned LCCPs

The optical, electrical and optoelectronic properties of conjugated polymers are extremely sensitive to structural order and defects. Solution-processed polymers usually exhibit an amorphous or polydomain texture with randomly distributed local orientation and significant structural/energetic disorder, unless they experience an effective chain orientation process such as photoalignment. Polymer alignment can produce high degrees of structural order at large length scales, hence resulting in large anisotropies in the photophysical and optoelectronic properties. In particular, photoaligned LCCP films with photo-patterned chain orientation with high pattern resolution (μm - submicron) should also show a spatial variation in both the physical structure and optoelectronic properties. Measurements of the overall alignment quality and the spatially varied structure-properties in these photo-aligned/patterned LCCP films requires the use of specialised experimental techniques.

X-ray or electron diffraction is particularly powerful to investigate samples with some degree of preferential orientation and structural order and, thus, appropriate for characterising the order parameter and molecular/interchain packing structures in photoaligned LCCP films. Alternatively, polarised optical spectral measurements are useful to experimentally determine the chain-orientation quality in terms of the optical dichroic ratio and photoluminescence (PL) intensity anisotropy. Combining the polarised absorption and PL spectral information can be

used to reveal typical changes in the chromophoric or fluorophoric species accompanying the formation of the liquid crystal (LC) polydomains or photoaligned mesophase monodomains.

Crossed polarising optical microscopy is widely used to observe the bright and dark states of polydomain and monodomain LC textures, where the spatial resolution, however, is limited to be >1 μm. On the other hand, polarised super-resolution fluorescence microscopy is effective for directly resolving the fluorescence intensity profile of a LCCP film with submicron-to-nanoscale resolution. Micro-PL spectral mapping technique using polarised excitation and/or polarised emission collection is capable of clarifying the PL spectral lineshapes and anisotropy from either randomly oriented, yet locally ordered micro-domains, or photoaligned monodomains formed in a light-emitting LCCP film.

2.1 Crossed Polarising Optical Microscopy

The existence and optical texture of a LC mesophase can be visualised using polarising optical microscopy (POM). The basic configuration of a polarised optical microscope is shown in **Figure 2.1**, where the sample is placed between two crossed polarisers.

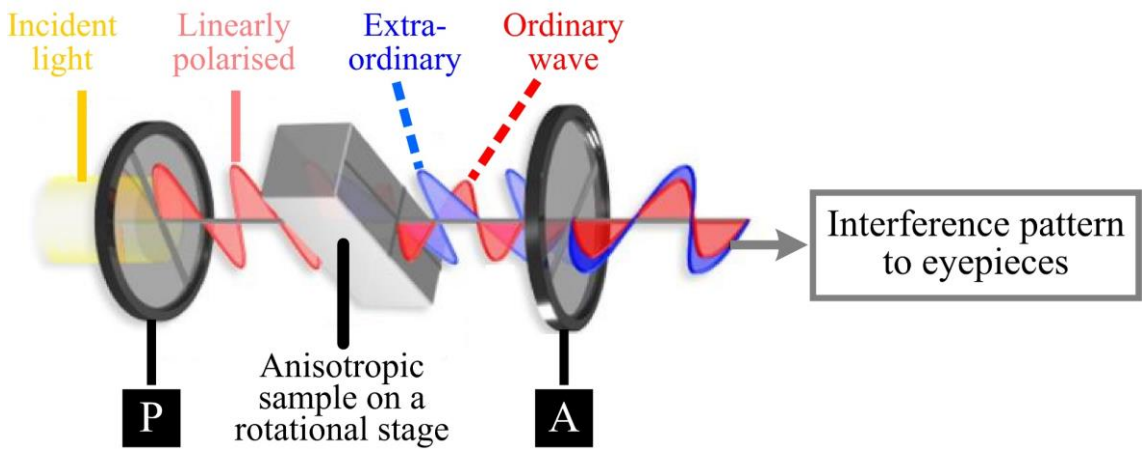

Figure 2.1: Basic configuration of a POM. P and A denotes the polariser and analyser, whose transmission axes are crossed. Copyright: Nikon Corporation.

For an isotropic sample such as the as-deposited amorphous LCCP film, the linearly polarised wave passing through the polariser is subsequently blocked by the analyser due to the orthogonal configuration of the transmission axes. An anisotropic sample with different refractive indices along different directions, on the other hand, can produce two orthogonal wave components, namely, the fast ordinary wave and the slow extraordinary wave. This is because the initial linearly polarised incident wave after the polariser splits into components that travel at different speeds resulting in a phase delay between the components. In other words, after exiting the birefringent sample the two light components become out of phase and recombine to result in either constructive (bright) or destructive (dark) interference when they pass through the analyser. This optical effect is known as retardation, which depends on the optical path difference of the sample and the wavelength of light. The contrasting interference enables different domains to be observed in the LC films where the molecules/chains in the different domains are oriented along different directions and separated by domain boundaries.

The retardation and resulting interference depend on the relative orientation between the LC director alignment and the transmission axis of the polariser/analyser. When fixing the crossed polariser and analyser pair, the resultant colour changes when the sample stage is rotated through 360 degrees in the film plane. The transmitted intensity for light of wavelength λ passing through a birefringent LC film of thickness d can be described as [1]:

$$I = I_0 \sin^2(2a_0) \sin^2(\pi d \Delta n / \lambda) \tag{2.1}$$

where a_0 is the angle between the LC director and the easy axis of the initial polariser, and Δn is the birefringence. Equation 2.1 emphasizes that the bright-state (maximum transmission) and dark-state POM images of the same LC film can be switched by rotating the sample by 45° in the plane of the film or by controlling the birefringence. All POM images included in this Thesis were recorded using a cross-polarised Olympus BX51 microscope with a QImaging Retiga R6 CCD camera.

2.2 X-ray and Electron Diffraction/Scattering Patterns

Diffraction is a powerful technique for revealing the internal structure of materials. Diffraction patterns are detected with incident radiation of a wavelength that is comparable to the intermolecular spacing and, thus, can provide information about the relative positions of the molecules, presence of long-range positional order, and the quality of the molecular alignment along a preferred orientation [2]. While diffraction has become an integral part of electron microscopy so as to directly correlate diffraction patterns with high-resolution microscopic images, X-ray is probably the most broadly used source for diffraction techniques. Depending on the relative orientation of the incident X-ray source with respect to the sample and detector, there exist various X-ray diffraction techniques such as grazing-incidence (incident angle α_I < 1° - 5°) X-ray diffraction (GIXD) and grazing-incident wide-angle (large azimuth angle, φ_F, and *z*-scanning angle, α_F) and X-ray scattering (GIWAXS), as schematically shown in **Figure 2.2**(a). The fundamental relation governing the diffraction behaviour is given by the Bragg equation

$$m\lambda = 2d \sin\theta_B \tag{2.2}$$

where m denotes the order of diffraction, λ the wavelength of the radiation, d the molecular spacing along the normal direction to the diffraction planes, and θ_B the diffraction angle.

Figure 2.2(b) illustrates a representative X-ray transmission diffraction pattern, which consists of a set of concentric circles measured from a polycrystalline sample where the local molecular alignment in different domains/grains is randomly oriented [2]. The radius of each diffraction circle satisfies the Bragg requirement and therefore provides the *d*-spacing of the spatially periodic diffraction planes. For samples that are non-crystalline or have only short-range positional order, their diffraction planes are not well-defined and lead to the observation of diffused diffraction peaks whose positions can be related to the mean molecular/chain spacing. We can see that diffraction is particularly useful for samples that have various degrees of molecular alignment in a preferred orientation relative to an external axis, such as non-

aligned and photo-aligned LCCP films. In order to assist in the interpretation of the transmission diffraction patterns, Figure 2.2(d) shows an example of a GIXD pattern recorded from a smectic C LC film (see Figure 2.2(c) for a schematic of its packing structure [2]), for which the molecular spacing/orientation, and the degree of positional/orientational order can be obtained.

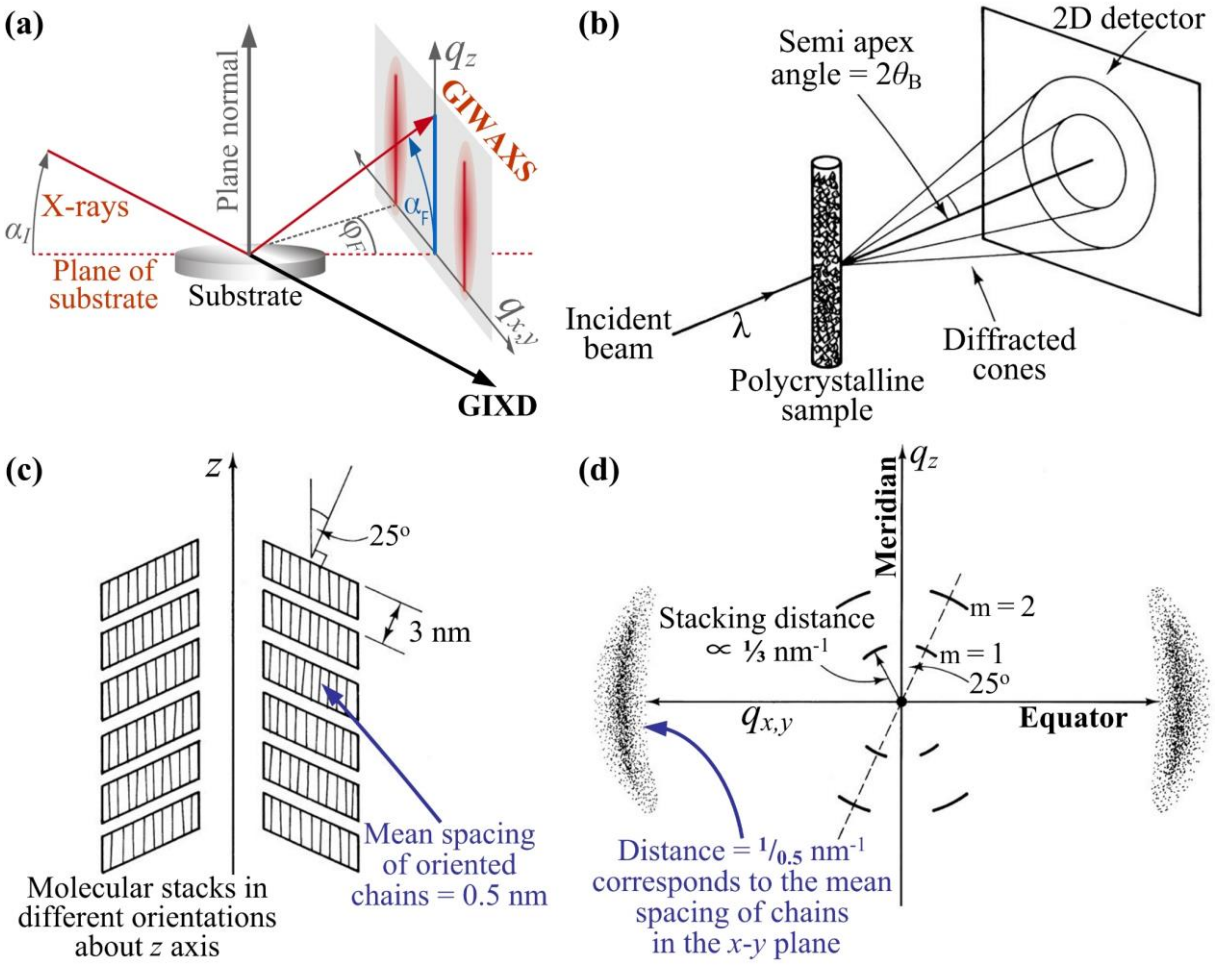

Figure 2.2: (a) Schematic of the basic configuration of GIXD and GIWAXS (the two red curves) measurements. (b) Illustration of a diffraction pattern detected from a polycrystalline sample with randomly oriented domains. A schematic diagram showing the relationship between a *smectic C* LC structure (c) and the various typical features of the corresponding diffraction pattern (d). In (d), the axis parallel to the rotation symmetry axis of the sample is known as the meridian (vertical) while that at right angles is the equator (horizontal). The diffused equatorial maxima indicates that the molecular packing are only short-range ordered in the *x-y* plane, whilst the arc length reflects the order parameter. On the other hand, the thin and short concentric diffraction arcs reveal positional order over a longer range along the *z* direction. Images (b - d) taken from [2].

The degree of orientational or positional order can be estimated according to the arc length of the diffraction pattern: the shorter the arc length, the higher the order parameter. However, it should be emphasized that the measured order parameter depends on the material volume sampled. This is particularly important for the electron diffraction recorded from polydomain/polycrystalline samples such as non-aligned nematic polydomain LCCP films where the polymer chains in an individual domain are highly ordered, but the local chain orientations in different LC domains are randomly distributed. As a result, this means that a much higher order parameter would be obtained if the incident beam could be focused onto a single LC micro-domain, compared with the value measured from a spatially-averaged diffraction pattern resulting from a larger sampling area or volume that encompasses multiple domains. This size effect can be insignificant for the photoaligned, highly oriented, large-area LCCP monodomains, which would result in an anisotropy in the diffraction patterns as well when the incident beam propagates along different directions or with distinct polarisations with respect to the LC alignment direction.

2.3 Polarised Optical Spectral Measurements and Charge-Transport Anisotropy

For the uniaxially-aligned polymer films, the order parameter is often quantified by the optical dichroism, which involves measurements of both the parallel and perpendicular polarised optical absorption spectra using a spectrometer and a high-quality polariser. For this thesis, the polarised UV-vis absorption spectroscopy was carried out using a PerkinElmer Lambda 1050 where a common beam depolariser (CBD) is built-in to generate a randomly polarised common incident beam in both the sample optical path and the blank reference arm.

A Glan-Thompson polariser (or a Thorlabs WP25M-UB broadband wire-grid polariser) was mounted in front of the LCCP films (or a photoalignment layer) to generate a linearly polarised incident beam, while the other reference arm remains empty and without a polariser

in order to enable 100% transmission (see **Figure 2.3** for a schematic of the setup). The relative orientation of the polymer chains with regard to the incident light polarisation could be varied by rotating the LCCP sample in the *x*-*y* plane on a rotation stage.

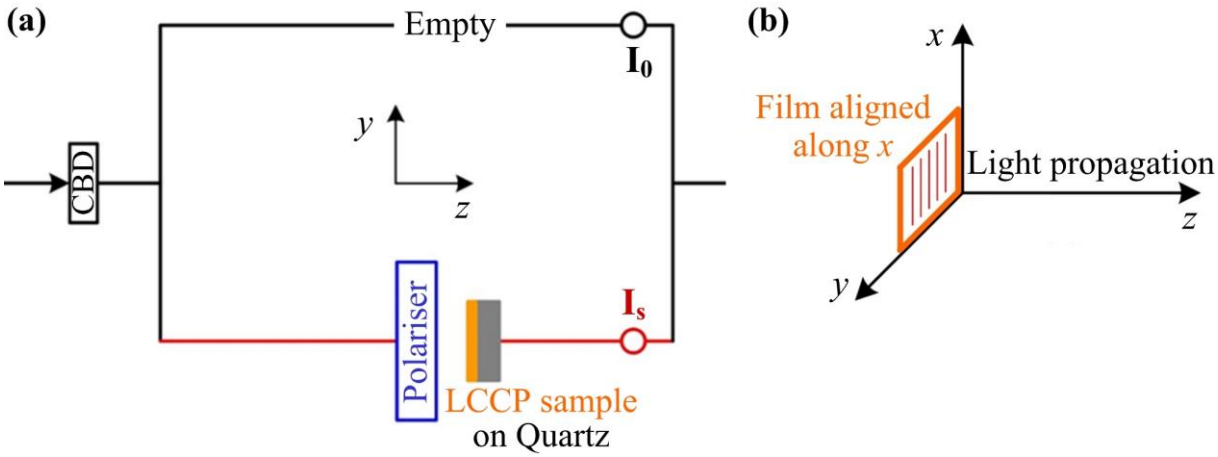

Figure 2.3: (a) Schematic illustrating the optical setup used for polarised optical absorption spectral measurements of an oriented LCCP film coated on a quartz substrate. CBD represents a built-in common beam depolariser. (b) shows that the polymer chain orientation (along the *x* axis shown herein) can be adjusted with respect to the transmission axis of the polariser by rotating the LCCP sample in the *x*-*y* plane.

The parallel (∥) and perpendicular (⊥) polarised UV-*vis* transmission (%*T*) spectra of an LCCP film, $T_{\parallel}$ and $T_{\perp}$, were calibrated based on

$$T_{\parallel \text{ or} \perp} = \frac{I_S/I_0}{\%T_{pol.}} = \frac{\%T_{LCCP+Qtz}}{\%T_{pol.} \times \%T_{Qtz}} \tag{2.3}$$

where I_o and I_s denotes the transmitted light intensity from the blank reference arm and the sample arm after the polariser, respectively. The ratio between the two becomes the transmission attenuated by the LCCP film and the quartz substrate, $\%T_{LCCP+Qtz}$. Therefore, the transmission spectra of the polariser ($\%T_{pol.}$) and a quartz substrate ($\%T_{Qtz}$) are also needed for calibration in order to yield the transmission of only the LCCP film.

The parallel ($A_{\parallel}$) and perpendicular ($A_{\perp}$) polarised absorbance spectra of the LCCP film are readily calculated based on the well-known Beer-Lambert law: $A = 2 - \log(\%T)$. Correspondingly, the dichroic ratio (*DR*) of the LCCP film is given as

$$DR = A_{\parallel} / A_{\perp} \tag{2.4}$$

It is assumed herein that the strongest optical absorption or the optical transition dipole moment is along the long axis of the molecules/chains. The order parameter, *S*, can be calculated from

$$S = (A_{\parallel} - A_{\perp})/(A_{\parallel} + 2A_{\perp}) = (DR - 1)/(DR + 2) \tag{2.5}$$

In the case of the optical transition dipole moment lying non-parallel to the molecular long axis [3], even for perfect chain alignment the optical dichroic ratio would be limited to a finite value when measured along the long axis of molecules. In this situation, the order parameter given in Equation 2.5 needs to be updated as S/S_{op} in order to reveal the real alignment quality, where $S_{op} = 1/2\ (3\cos^2\beta - 1)$ represents the maximum order parameter achievable when measured along the long axis of the molecules as a direct result of the presence of a deviation angle (β) between the direction of the molecular dipole moment and the LCCP chain-orientation (i.e., along the long axis of the molecule) [4]. A combination of polarised Raman and optical dichroism measurements has demonstrated the possibility of determining the values of β in some unidirectionally-aligned LCCP thin films [4].

It should be emphasized that polarised Raman spectroscopy itself is a complementary technique used to determine the order parameter. Raman spectroscopy detects changes in the laser-induced dipole moment or polarisation on the excited surface of the sample, which produces Raman scattering. Raman spectral measurements are typically operated in a reflection geometry and it is thus feasible to characterise the molecular stretching modes of organic film samples that are not transparent or have been built into a device architecture such as in polymer

LEDs and field-effect transistors [5]. Polarisation dependent spectra could be recorded by rotating the sample in the film plane perpendicular to the incident beam and then used to calculate the order parameter based on Equations 2.4 and 2.5.

The introduction of a preferential polymer chain orientation in LCCP films provides an effective method to remarkably enhance the charge transport along a specific direction. Charge-carrier mobility anisotropy measurements in field-effect transistors (FETs) utilising an aligned polymer film as the active charge transporting layer becomes another useful technique to experimentally determine the order parameter [6,7]. The electron and hole mobility anisotropy could be acquired by fabricating the FET channels with the width direction fabricated to be parallel and perpendicular the polymer chain orientation.

2.4 Photoluminescence Polarisation Ratio and Decay Lifetime

Polymer alignment is bound to alter the emissive excited species. High-quality orientation of polymer chains is able to direct the inherent intrachain excitonic propagation and optical transition dipole moment of LCCPs, which then fundamentally dictate the polarisation and vibronic spectral lineshape of the resulting luminescence. Molecular alignment circumvents the significant structural and energetic defects observed in disordered LCCP films. It can also lead to a refinement of the chain conformation, the effective conjugation and interchain packing. Combined, these synergic effects are expected to produce highly polarised luminescence, polarisation-dependent luminescence spectra and the possibility of generating new emissive intrachain or interchain species.

Polarised steady-state PL spectral measurements help to reveal polarisation-dependent light-emitting characteristics, whilst time-resolved PL spectra for different polarisation directions are useful for understanding the radiative PL decay lifetime and to provide insight

regarding the luminescent mechanisms in different types of LCCP films. Our polarised PL spectra were recorded in a reflection geometry using a Jobin Yvon Horiba Fluoromax-3 spectrofluorometer equipped with two polarisers for generating linearly polarised excitation beam and polarised collection of emission. As a result, four combinations of polarisation can be used to acquire the polarised PL spectra of the LCCP film and correlate the PL spectral lineshape with the structural characteristics. Similarly, polarised, time-resolved PL spectra measurements can adopt four polarisation configurations with respect to the polymer alignment direction. A monochromator grating and streak-camera were employed to collect time-resolved PL spectra in a time range of tens - hundreds of nanoseconds. The collected PL transients are ready to be integrated to record the kinetic traces of different photoemission regions and simultaneously estimate the lifetime and rate constants for radiative and nonradiative decays.

2.5 Polarised Confocal Fluorescence Microscopy

As an essential source of major discoveries in cell biology, fluorescence microscopy has demonstrated its capacity of revealing the steady state and dynamic internal organisation of a cell. Unlike relying on incident light from a bulb and only achieving micrometre-scale resolution in the optical microscopy apparatus, fluorescence microscopy is typically operated with laser light that is focused by the objective lens to a tight diffraction-limited spot. Implementation of wavefront correction and a tight excitation focus, using confocal pinholes or selective detection/excitation enabled by the introduction of adaptive optics, has enabled fluorescence microscopy to approach the diffraction-limited resolution (i.e., $0.61\lambda / NA$, where λ is the wavelength of light and *NA* the numerical aperture of the focus lenses). It even allows for super-resolution (tens of nanometres to submicron) imaging of light-emitting patterns by coupling other specialised excitation/emission selection techniques [8].

Coupling with a polariser in order to select the polarisation of emission, polarised confocal fluorescence microscopy is a powerful technique to directly resolve the fluorescence polarisation and intensity contrast, as well as the shape/size of polydomains or monodomain formed in the light-emitting LCCP films as the entire field at once. In addition, it provides opportunities for in-situ observation of the formation and dynamics of LCCP domains in the nematic phase. These measurements can be performed for either the spontaneous LC self-organisation or the alignment imposed by a commanding (alignment) layer.

2.6 Polarised Micro-Photoluminescence Spectral Mapping

Micro-PL (μ-PL) spectral characterisation resolves both the PL intensity and spectrum at a given scanning pixel. The μ-PL spectral maps of LCCP films presented in this thesis were recorded at room temperature with linearly polarised 405 nm, 100 fs, and 76 MHz excitation from a frequency-doubled Ti: sapphire laser, using the schematic setup illustrated in **Figure 2.4**. The excitation laser was focused on the top surface of an LCCP film by a 100× objective with a numerical aperture of $NA = 0.7$. The spot size of the incident laser beam focused on the sample was $\approx$1 μm in diameter. The polarisation of the incident light and the collected PL spectra were controlled using a combination of linear polarisers and half-wave plates in front of the objective and the spectrometer, respectively. The excited PL emission was collected by the same objective, dispersed by a 0.3-m-long spectrometer with a 300 lines/mm grating and detected by a thermoelectrically cooled charge-coupled device (CCD).

For alignment purposes, the sample was illuminated by a broadband visible light source (yellow path) and an image of the sample was then collected by a CCD camera. A 430 nm long pass filter was used to remove the excitation laser. The samples were held on a piezo-electric controlled platform with a maximum scanning area of 100 μm × 100 μm and a scanning step size of 200 nm to 1 μm in both *x* and *y* axes.

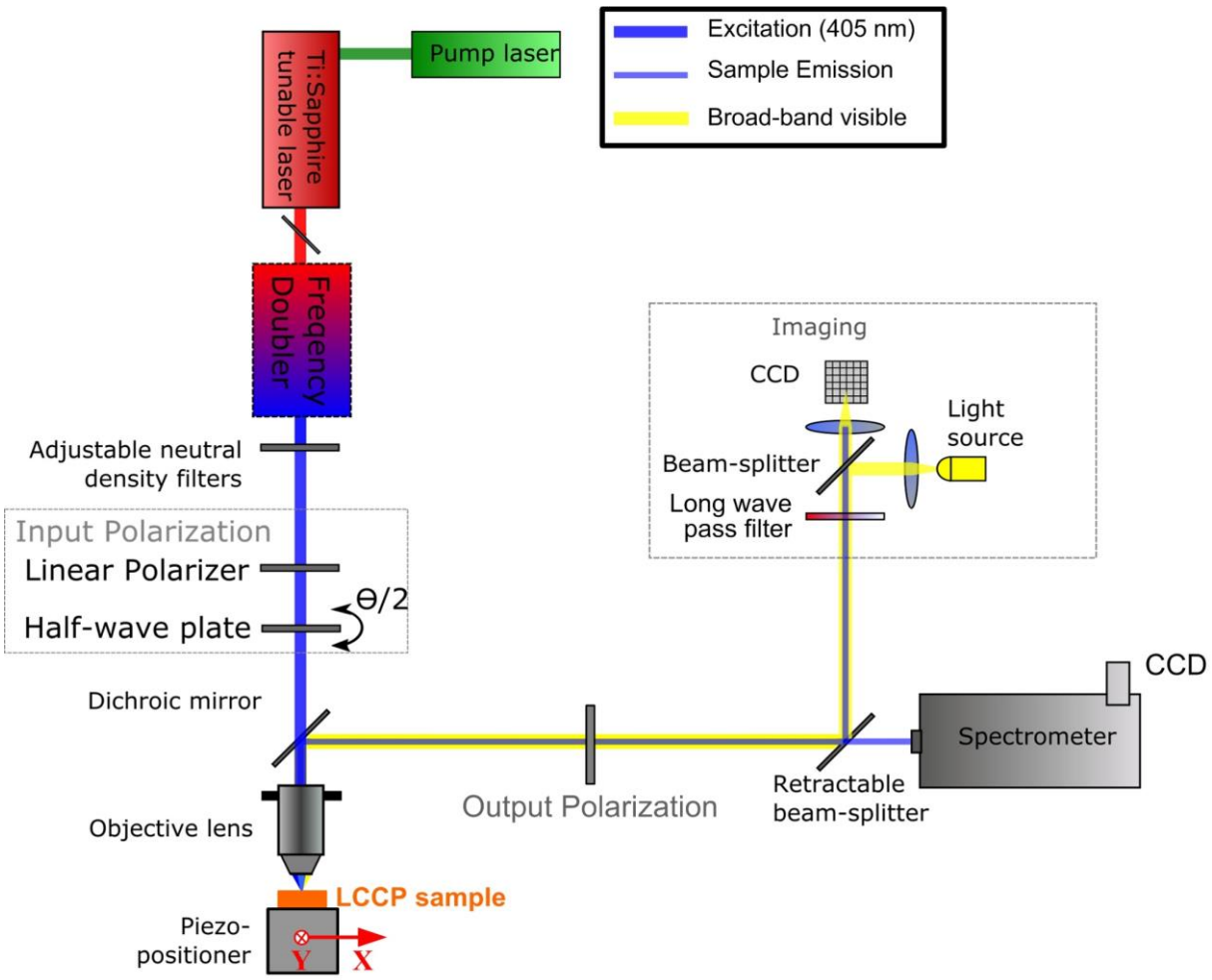

Figure 2.4: Experimental arrangement for mapping the micro-PL from the photo-aligned LCCP film.

2.7 Summary

The optical, electrical and diffraction experimental techniques used to obtain the data and results presented in this thesis have been introduced in this Chapter, along with a detailed discussion about the operating principle and benefits of each technique in terms of revealing either the uniform or spatially varying structures/properties of LCCPs.

X-ray and electron diffraction patterns measured with parallel and perpendicular propagation relative to the polymer alignment direction are powerful methods to provide information about the order parameter, mean interchain/interchain spacing, interchain packing structure, effective conjugation length and overall crystallinity in different types of LCCP

samples. This includes nonaligned polydomain and photoaligned monodomain glass LCCP films. Crossed polarising optical microscopy is widely used for imaging the LC optical texture with ≈1 μm resolution and for estimating the polymer alignment quality based on the transmitted/reflected light-intensity for the bright- and dark-states. Polarised optical spectral measurements such as absorption and PL have also been briefly introduced. It has been discussed how these methods can be used to determine the order parameter of the molecular alignment and to investigate the intrachain/interchain chromophoric and emissive species. Moreover, polarised super-resolution fluorescence microscopy is effective in terms of resolving the polarisation components of the fluorescence and the contrast in the intensity for light emitted from polydomains or monodomain formed in a light-emitting LCCP film. In addition, μ-PL mapping can provide spectral information about both the PL intensity and spectrum at a given point on the film and thus enables the PL spectral information to be collected at different locations in a photo-patterned LCCP film.

References

[1] K. Takashi, T. Carsten, G. Helen, E. P. Raynes, *Handbook of liquid crystals*, Wiley, Weinheim (2014).

[2] A. M. Donald, A. H. Windle, *Liquid Crystalline Polymers*, Cambridge University Press, Cambridge, 1992.

[3] M. Grell, D. D. C. Bradley, X. Long, T. Chamberlain, M. Inbasekaran, E. P. Woo, M. Soliman, Chain geometry, solution aggregation and enhanced dichroism in the liquid crystalline conjugated polymer poly (9,9-dioctylfluorene), *Acta Polym.* **49**, 439 (1998).

[4] H. M. Liem, P. Etchegoin, K.S. Whitehead, D. D. C. Bradley, Raman anisotropy measurements: An effective probe of molecular orientation in conjugated polymer thin films. *Adv. Funct. Mater.* **13**, 66 (2003).

[5] M. Grell, D. D. C. Bradley, Polarized luminescence from oriented molecular materials, *Adv. Mater.* **11**, 11 (1999).

[6] H. Sirringhaus, R. J. Wilson, R. H. Friend, M. Inbasekaran, W. Wu, and E. P. Woo, M. Grell, D. D. C. Bradley, Mobility enhancement in conjugated polymer field-effect transistors through chain alignment in a liquid-crystalline phase, *Appl. Phys. Lett.* **77**, 406 (2000).

[7] M. Xiao, B. Kang, S. B. Lee, L. M. A. Perdigão, A. Luci, D. A. Warr *et al.*, Anisotropy of charge transport in a uniaxially aligned fused electron-deficient polymer processed by solution shear coating, *Adv. Mater.* **32**, 2000063 (2020).

[8] N. Ji, Adaptive optical fluorescence microscopy, *Nature Methods* **14**, 364 (2017)

Chapter 3

Polarised UV Alignment of Photoalignment Layers for Orienting LC Devices and LCCP Films

The photoalignment technique allows for contactless alignment and spatial patterning of the liquid crystal (LC) director in both low molar mass LC devices and liquid crystalline conjugated polymer (LCCP) films. The inherent long-range orientational order present in the nematic mesophase of LCs and LCCPs is utilised in this Chapter to induce long-range LC/chain-orientation ordering. However, for LCCPs the nematic phase is only entered at rather elevated temperatures (≈200 - 300℃) before being subsequently "frozen-in" into a *glass* solid-state upon rapid quenching to room temperature. The necessity to withstand high temperatures requires the photoalignment layers to exhibit a good thermal stability at these mesophase high temperatures. In this Chapter, the use of linearly polarised UV illumination of SD1 photoalignment layers is explored and optimised in terms of the alignment quality achieved in uniaxially oriented LCCP glass films. Specifically, the study involves systematically varying the UV-alignment parameters and the thickness of both the SD1 and LCCP layers. A USAF target has also been employed as a photomask to spatially define the polarised UV illumination of the SD1 photoalignment layers in order to create patterns in the LCCP layer on top of the SD1 layer. This study investigates the spatial pattern resolution and demonstrates the optical rewritability of the SD1 photoalignment layer. In addition, this chapter compares the thermal stability and alignment quality in low molar mass nematic LC cells that are homogeneously aligned using either conventional rubbed-polyimide alignment layers or UV-aligned SD1

commanding layers. Where relevant, we also highlight the advantages of the photoalignment technique for orienting and patterning both LCs and LCCPs.

3.1 The SD1 Photoalignment Layer

3.1.1 Chemical Structure and Photoalignment Mechanism

SD1 is a versatile photo-alignable sulfonic azo dye with a rod-like anisotropic molecular structure (see **Figure 3.1** for the chemical structure and two different conformations of SD1). When exposed to polarised light, SD1 molecules undergo diffusive re-orientation and/or *cis-trans* photoisomerisation [1,2] involving a change in the molecular configuration in relation to one or two of the nitrogen double bonds. The inclusion of sulfonic, carboxylic and hydroxyl groups promotes hydrophilic behaviour and strong anchoring with commonly used substrates (e.g., glass, quartz, silicon, metals and plastics). Moreover, SD1 is water/alcohol-processable and allows for easy deposition (e.g., by spin-coating) into ultrathin alignment layers for orienting a LC device or a LCCP overlying film in a mesophase. The co-existence of electron-donating and electron-withdrawing groups in the SD1 molecules can be beneficial for the electron pull-push effect for two-photon absorption, charge-carrier mobility and ionic conductivity [3]. The feasibility of creating spatially defined alignment patterns in the ultrathin SD1 films might also allow for precise control of the occurrence of direct electron tunnelling/injection.

Under the excitation of linearly polarised UV light, the molecular anisotropy of SD1 leads to anisotropic optical absorption. In this case, the probability/strength of the SD1 absorption is proportional to $cos^2\theta$, where θ is the angle between the SD1 absorption oscillator (i.e., along the long molecular axis) and the UV-light polarisation direction, as shown in Figure 3.1(c). This highly asymmetric absorption drives the initially randomly oriented optical oscillators in a neat non-aligned SD1 photoalignment layer to rotate in the film plane and align along a direction

that is perpendicular to the UV-excitation polarisation. This is a thermodynamically equilibrium position for all photo-aligning SD1 molecules since the UV-activation drops to zero at $\theta = 90^{o}$ [1,4]. Following illumination with polarised UV light, the SD1 molecules in the photoalignment layer become aligned perpendicular to the polarisation direction. This alignment of the SD1 layer also results in the chain-orientation direction of the LCCP film deposited directly onto the UV-aligned SD1 photoalignment layer.

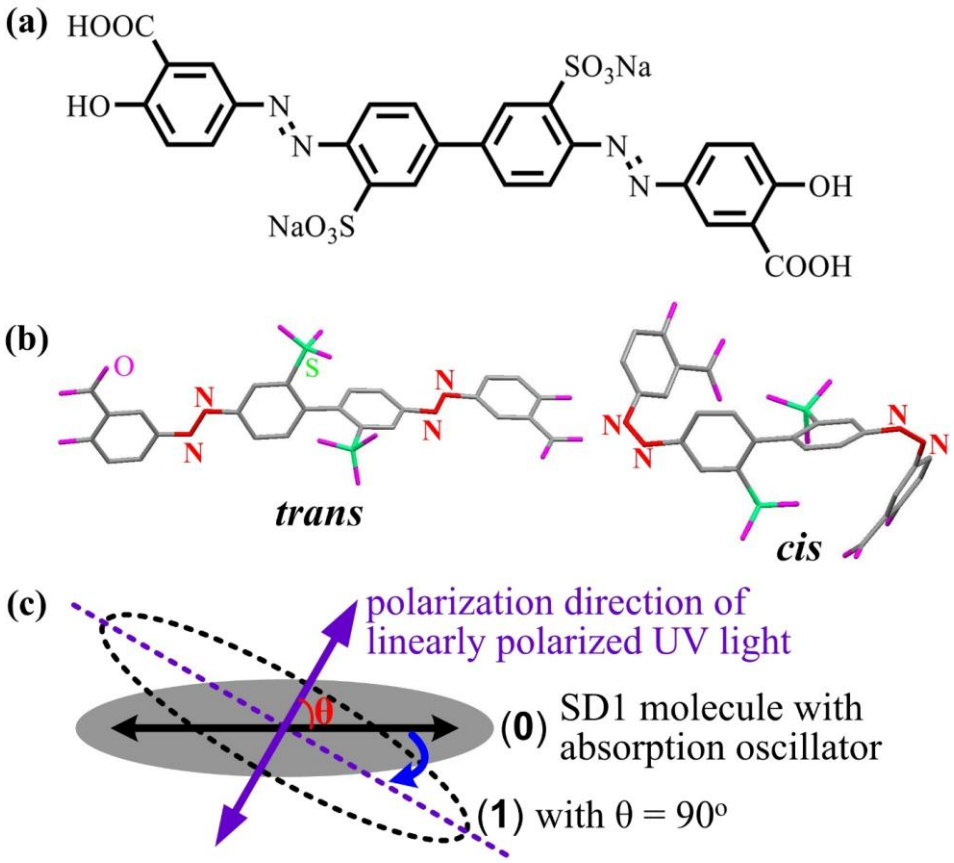

Figure 3.1: (a) Chemical structure of the SD1 photoalignment material. (b) Configuration for the *trans*- and *cis*-conformations of an SD1 molecule; the hydrogen and sodium atoms were omitted herein for clarity. (c) Schematic demonstrating the SD1 molecular reorientation process photo-aligned by linearly polarised UV light. The absorption oscillator of the SD1 molecule is parallel to the long molecular axis. When exposed to the polarised UV illumination, the absorption oscillator of all SD1 molecules comprising a photoalignment layer tends to rotate from a random direction in the initial (0) state to align perpendicular to the UV-light polarisation in the equilibrium (1) position.

3.1.2 Characterisation of SD1 Layers

The photoalignment layer material, SD1, was provided by DIC Corporation Japan and used as received. The SD1 alignment layers were spin-coated from different concentrations of SD1 solutions in anhydrous 2-methoxyethanol (≥ 99.8%) onto pre-cleaned polished Spectrosil substrates at 500 rpm for 5 seconds then 2000 rpm for 20 seconds. The SD1-coated substrates were then annealed at 110 °C for 10 minutes in ambient conditions to ensure solvent removal. **Figure 3.2**(a) shows the non-polarised absorption spectra of a typical SD1 alignment layer in the as-prepared state. The long wavelengths of the SD1 absorption band exist mainly in the UV range and peak at ~370 nm. Furthermore, it has been confirmed by separate photoluminescence measurements that the SD1 photoalignment layers remain non-luminescent when being excited with 300 nm - 500 nm light, which is in accord with the as-shown H-aggregated absorption feature of the SD1 photoalignment layer in Figure 3.2 - an asymmetrical broadening of the longer-wavelength (> 370 nm) half side of its optical transition band. Our measured absorbance results from the non-aligned SD1 layer were then used to calibrate the thickness of the spin-coated SD1 layers used in this study based on the reported values [1,2]. These results point to a nearly linear dependence of the spin-coated SD1 film thickness on the concentration of SD1 for solutions ranging from 1 mg/mL to 10 mg/mL (see Figure 3.2(b)).

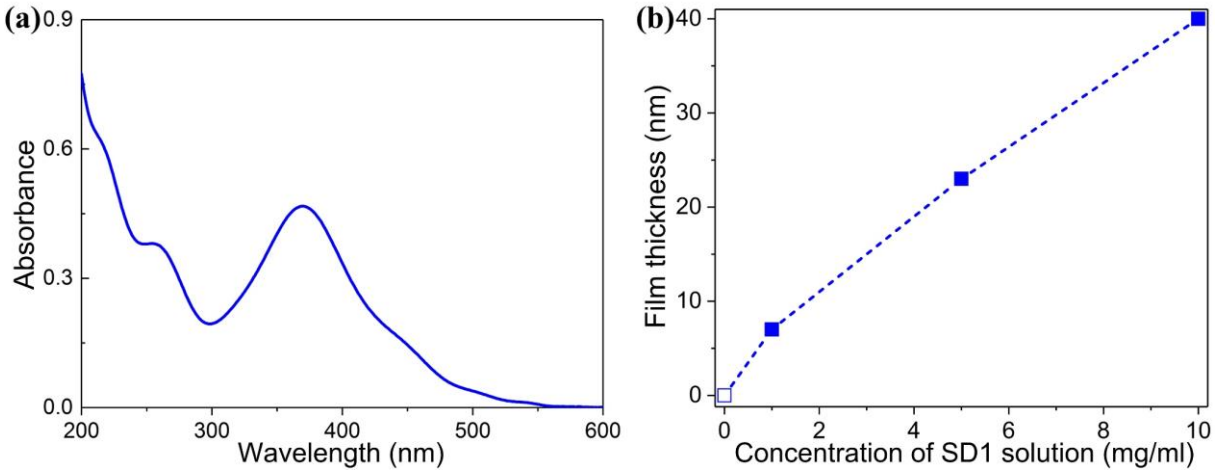

Figure 3.2: (a) Absorbance spectrum for an SD1 layer spin-coated from 10 mg/mL solution onto a quartz substrate. (b) Thickness of the spin-coated SD1 films vs SD1 solution concentration.

In order to characterise the energy levels of SD1, air photoemission spectra (APS) measurements were performed to estimate the HOMO level of the SD1 photoalignment layers that had been spin-coated using 2 mg/mL solution on an indium tin oxide (ITO)-coated glass substrate. **Figure 3.3**(a) illustrates the corresponding APS profile, from which the HOMO level of SD1 was estimated to be 5.79 eV based on a cube-root fitting of the photoemission intensity as a function of the excitation energy because SD1 is non-conductive [5]. Indeed, this ASP-deduced HOMO level is rather deep, a result consistent with the observed non-luminescent characteristic of the SD1 layers. Moreover, a variation in the thickness (controlled by the concentration of SD1 solutions ranging from 1 mg/mL to 10 mg/mL) of the spin-coated SD1 photoalignment layers was found not to alter the HOMO value, hence confirming the HOMO value is an essential material property of the photoalignable SD1 that we have explored.

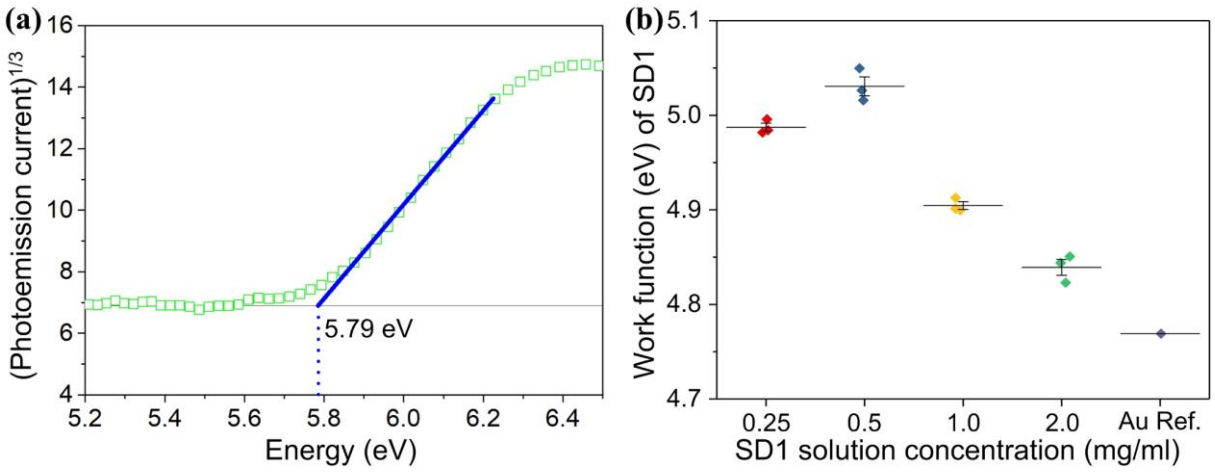

Figure 3.3: (a) Air photoemission spectra (APS) of an SD1 photoalignment layer spin-coated from 2 mg/mL solution on an ITO-coated glass. (b) Kelvin probe measurements of the work function in the spin-coated SD1 films on gold-coated glass substrates vs the concentration of SD1 in solution. The gold-coated glass substrates were also measured for direct comparison. For each type of measured SD1 sample, the Kelvin probe measurements were performed on three different regions of three SD1 samples, and the average work-function is indicated by the horizontal lines. The work function values were calibrated using the work function of the standard highly oriented pyrolytic graphite, ϕ = 4.65 eV.

Also, Kelvin probe measurements have been carried out to determine the work function (ϕ) of the SD1 photoalignment layers. These tests were performed in ambient conditions on a set of spin-coated SD1 films from various concentrations of the SD1 solution (e.g., 0.25 mg/mL, 0.5 mg/mL, 1.0 mg/mL, and 2.0 mg/mL) on glass substrates that were pre-coated with a vacuum-evaporated gold layer of 10 nm thickness. The obtained ϕ results are plotted in Figure 3.3(b) as a function of SD1 solution concentration. For a direct comparison, the ϕ of the gold-coated glass sample without an SD1 film on top was measured as well. For all of the Kelvin probe measurements, highly oriented pyrolytic graphite (HOPG) was used as a reference electrode to calibrate the ϕ results [6]. The SD1 layer deposited using the 0.5 mg/mL solution demonstrated the highest work function of ϕ = 5.03 eV, whereas the ϕ value for the SD1 layers coated from 1.0 mg/mL and 2.0 mg/mL solution decreased to 4.90 eV and 4.84 eV, respectively. It should be noted that the work function of the SD1 layer spin-coated from the 0.25 mg/mL solution is shown to be 30 meV lower than that from the 0.5 mg/mL SD1 solution, which can be ascribed to a discontinuous coverage of the spin-coated SD1 layer on the substrate due to the low concentration of SD1 solution (see Section 3.4.2 for more details). Considering ϕ = 4.77 eV for the evaporated gold and 4.7 eV for the standard ITO-coated glass substrates, the SD1 photoalignment layers can be regarded as a promising interlay candidate for efficient hole injection/extraction, in addition to homogeneously aligning the overlying LCCP film.

3.2 Polarised UV Alignment Process

3.2.1 Linearly Polarised UV-Illumination of SD1-Coated Substrates

The long molecular axis of the SD1 molecules in a spin-coated *pristine* SD1 layer are initial randomly oriented in the plane of the substrate. As demonstrated in **Figure 3.4**, the SD1 photoalignment layers were aligned in the present study by irradiating the samples in air with linearly polarised 365 nm light (close to the absorption peak of SD1) at normal incidence from a Thorlabs CS2010 UV-curing LED system equipped with a Thorlabs WP25M-UB broadband

wire-grid polariser [7]. The polarised UV illumination, of a sufficient duration, results in the long molecular axis of SD1 orienting in the plane of the substrate along a direction that is orthogonal to the excitation polarisation. This SD1 molecular alignment direction can be manipulated in practice by an azimuthal rotation of the polariser transmission axis relative to the SD1 photoalignment layer.

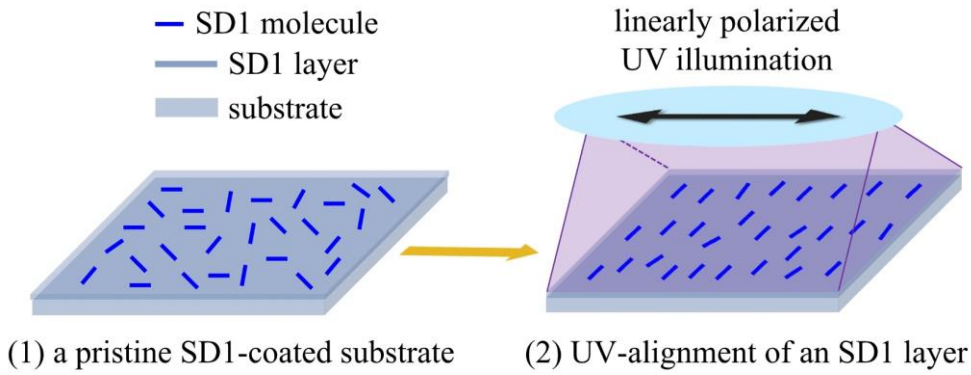

Figure 3.4: Schematic illustration of (1) randomly oriented SD1 molecules in a pristine SD1 layer coated on a precleaned substrate and (2) the polarised UV-illumination process used to induce homogeneous alignment in the SD1 photoalignment layer.

The SD1 alignment quality achieved through the use of linearly polarised UV illumination depends on the exposure time [1,4]. The power density of the UV light source at the SD1 layer after the polariser was held constant at 5 mW/cm^2. It should be emphasized that the resultant UV-aligned SD1 films have been found to possess >10^{-4} J/m^2 anchoring energies, which approaches that of standard rubbed polyimide (PI) layers [2], whilst also exhibiting excellent thermal stability since the intermolecular interaction in the new oriented state cannot be easily destroyed by thermal motion [1,2,4]. Contactless photoalignment of the SD1 commanding layers that has been explored here is a rewritable process, which, together with the insertion of a photomask in the optical path of the polarised UV light source, allows for the precise spatial definition of the alignment patterns in the same SD1 layer. Furthermore, a multi-step photoalignment process is also possible by adjusting the direction of the polarisation of the UV-light source during each step of the process.

3.2.2 Alignment Quality in UV-Aligned SD1 Layers

The alignment quality arising from the oriented state in a UV-aligned SD1 layer is quantified in terms of the birefringence, anisotropic dichroism and/or order parameter. The latter two parameters are correlated according to $S = (A_{//} - A_{\perp})/(A_{//} + 2A_{\perp}) = (DR - 1)/(DR + 2)$, where S and $DR = (A_{//} / A_{\perp})$ denote the order parameter and the optical dichroic ratio, respectively, and $A_{//}$ and $A_{\perp}$ represent the absorption strength (optical density) for parallel and orthogonal polarised light relative to the SD1 alignment direction. Unless otherwise stated, the alignment quality achieved in an oriented film has been experimentally measured from the dichroic ratio calculated at the low-energy absorption peak wavelength.

Figure 3.5 shows the typical non-polarised absorption spectrum of a non-aligned SD1 film that was spin-coated from a 1 mg/mL solution and the polarised absorption spectra of the same SD1 layer but after linearly polarised UV illumination for 10 mins. Before UV irradiation, the optical absorption of the spin-coated pristine SD1 film does not depend on the polarisation of the incident light, corresponding to a random distribution of the SD1 molecular orientation and a *DR* value of ~1 in the non-aligned SD1 film. After UV-alignment, the optical intensity for the parallel polarised spectrum ($A_{//}$) significantly increases (solid blue curve, Figure 3.5) while that of the $A_{\perp}$ spectrum decreases (blue dashed curve, Figure 3.5). The *DR* of the UV-aligned SD1 film at 370 nm was determined to reach a high value of 3.6.

As a direct comparison, the absorbance obtained from the same UV-aligned SD1 layer that had been subsequently erased by randomly-polarised UV light (365 nm) for 10 min prior to the absorption spectral measurement was found to be slightly attenuated relative to that of the pristine SD1 film. This slight lowering of the absorbance in the UV-erased SD1 layer implies that the UV-alignment process may result in oxidation in the photoalignment layer.

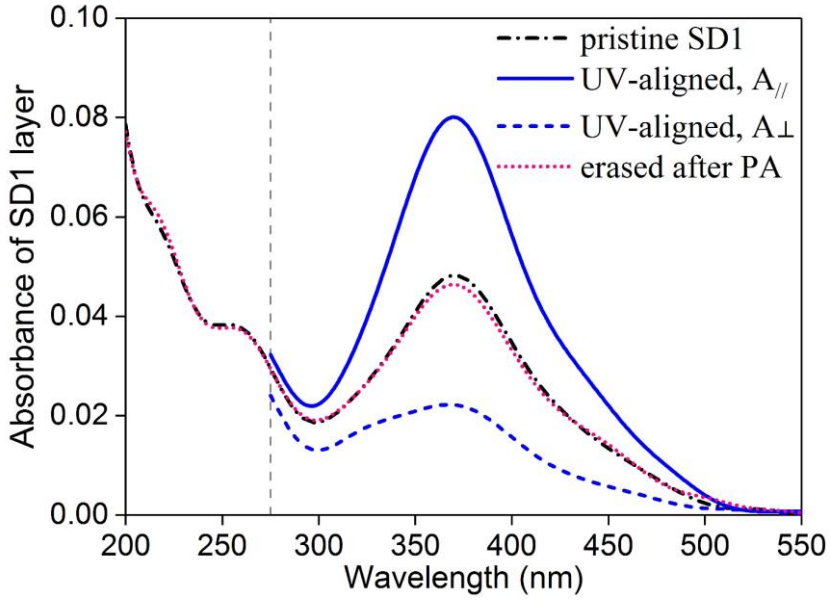

Figure 3.5: Non-polarised (for both the pristine SD1 and photo-erased SD1) and Polarised (for the UV-aligned SD1) optical absorbance spectra of an SD1 photoalignment layer that was spin-coated from 1 mg/mL solution on a Spectrosil substrate but had undergone a series of treatments. The black dash-dotted line denotes the non-polarised absorption spectrum of the spin-coated pristine (non-aligned) SD1 layer, which was then excited by unpolarised light. The two blue lines were measured for the same SD1 layer that, however, was subsequently photoaligned (PA) using 365 nm polarised UV-light for 10 min and measured with the SD1 orientation direction (i.e., the long molecular axis) being aligned parallel ($A_{//}$) and perpendicular ($A_{\perp}$) to the polarisation direction of linearly polarised excitation; the pink dotted line was recorded from the identical UV-aligned SD1 film which was finally erased with 365 nm randomly-polarised UV light for 10 min prior to the absorption measurement. The dichroic ratio (*DR*) value of the UV-aligned SD1 film at the absorption peak wavelength of 370 nm was determined to be $DR = A_{//} / A_{\perp} = 3.6$. The two polarised absorption spectra of the UV-aligned SD1 layer were cut off at 275 nm due to the wavelength limit of the WP25M-UB polariser placed in front of the sample to generate linearly polarised excitation.

Alternatively, provided that the SD1 molecules in the spin-coated pristine film are in the form of *trans*-conformers (according to our calculation results using time-dependent density functional theory) and remain in the plane of the substrate, then the photo-induced reorientation may stabilise the SD1 molecules with a small pretilt angle in the photo-aligned layer and/or a greater fraction of the *cis*-conformers. All these possibilities point to certain degrees of degradation in the overall alignment quality achieved with an SD1 layer after a multi-step

photoalignment process. This is also in accord with our findings that either a too long UV-alignment process or multi-step photoalignment process of an SD1 layer lowers the order parameter in both the resultant UV-aligned SD1 films (see **Figure 3.6**) and the corresponding LCCP glass film deposited onto the SD1 alignment layer (Section 3.4.3.2).

In order to optimise the UV-alignment quality of the photoaligned SD1 layers, the duration of the linear polarised UV-LED illumination was varied from 3 mins to 20 mins while the thickness of the SD1 films was tuned by spin-coating using 1 mg/mL and 5 mg/mL solutions. The dichroic ratios in the correspondingly UV-aligned SD1 layers are shown in Figure 3.6.

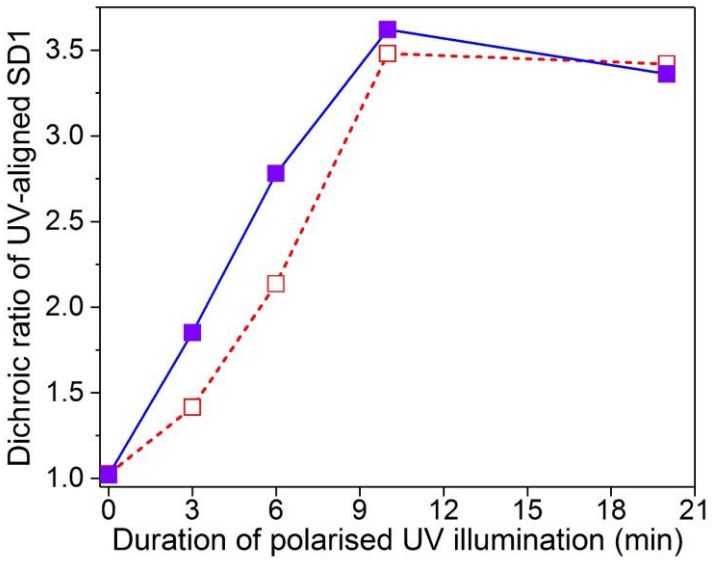

Figure 3.6: Dichroic ratio of the UV-aligned SD1 layers as a function of the duration of the linearly polarised UV illumination. The filled (open) boxes are for the SD1 films of ~7 nm (23 nm) thickness that were spin-coated from 1 mg/mL (5 mg/mL) solution on Spectrosil substrates.

A general trend for the two photoaligned SD1 films lies in that there exists an optimal UV-illumination time (e.g., 10 mins for the two measured thickness of the as-prepared SD1 layers) that maximises the UV-alignment quality in the SD1 films of the same thickness. Also, it is noteworthy that all the *DR* values obtained for the thinner (e.g., fabricated from 1 mg/mL solution) SD1 layers that had been UV-aligned for the first three selected durations were

constantly greater than those achieved in the thicker (from 5 mg/mL) SD1 films. However, the maximum *DR* value in the 1 mg/mL- and 5 mg/mL-coated SD1 films is estimated to be 3.6 and 3.5, respectively. The difference between these two DR maximum is small and within error, suggesting that the best SD1-alignment quality should be independent of the film thickness [1-2] as long as they are exposed to UV illumination for an appropriate time. As discussed above, the *DR* decreases with long UV illumination exposure times, which is probably due to a UV-activated oxidation and/or tilt of the SD1 molecules.

3.3 Comparing Photoalignment and Mechanically-Induced Alignment in LC Cells

Following the initial study in the previous sections, the UV-aligned SD1 films are now ready to function as the alignment layers for orienting LC devices and LCCP films. The UV-aligned SD1 commanding layers described in the previous section, namely, the SD1-coated glass substrates deposited from 1 mg/mL solution and then exposed to linearly polarised UV illumination for 10 mins, were used to induce a homogeneous alignment in low molar mass nematic LC mixtures (the eutectic nematic mixture E7 from Synthon Chemicals Ltd.) filled in glass cells. The E7-filled glass cells using either the non-aligned SD1 layers or the standard rubbed PIs as the alignment layers were fabricated in order to compare the resulting LC alignment quality and the thermal stability of the rubbed PIs and the UV-aligned SD1 layers. It is demonstrated in this Section that the UV-aligned SD1 photoalignment layers exhibit better high-temperature thermal stability and can induce higher LC alignment quality than the rubbed-PI alignment layers after processing at high temperatures.

3.3.1 Alignment of LC Devices Using UV-Aligned SD1 Commanding Layer

3.3.1.1 Assembly Process and Different Types of Nematic LC Cells

In order to investigate the LC alignment ability of the UV-aligned SD1, the SD1-coated (deposited from 1 mg/mL solution) glass substrate films that had been exposed to polarised UV

illumination for 10 minutes were employed for the LC glass cells with a sandwich architecture. As schematically shown in **Figure 3.7**, each of the assembled nematic LC cells consist of a pair of alignment layers (e.g., the UV-aligned SD1 or rubbed PIs) coated onto glass substrates with the gap between the two substrates capillary filled with the nematic E7 mixture, which exhibits a nematic phase at room temperature and a clearing temperature of ~70 °C.

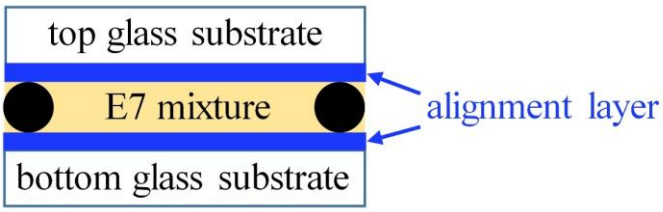

Figure 3.7: Schematic illustration of a LC device with two alignment layers and filled with the nematic LC mixture, E7. The thickness of the LC cell was controlled by the diameter of micro-particles (the two black spheres herein) dispersed as the spacer in a UV-curable glue.

The whole LC cell assembling process starts with the dispersion of TiO_2 micro-particles of a selected diameter (ranging from several to tens of μm) as the spacer bead into a UV-curable glue (No.61, Merck) in order to control the thickness of the cell (gap). This is then transferred to a pneumatically-driven syringe and written as thin lines close to the edges of the bottom substrate. Subsequently, the two glass substrates coated with the UV-aligned SD1 layers were assembled with the SD1 layers placed facing each other to form a gap inside the glass cell, which was followed by UV-curing the glue lines with 365 nm non-polarised light (7.5 mW/cm^2 for 3 minutes). Throughout the UV-curing process, the area inside the glue lines of the top substrate was completely shaded to avoid UV illumination of the SD1 commanding layers, otherwise the randomly polarised UV curing would erase the SD1 alignment that had already been written. Finally, the thermotropic E7 nematic LC mixture was capillary filled into the gap of the glass cells in the isotropic liquid state above its clearing temperature.

By tailoring the SD1-alignment direction on the top and bottom glass substrates, two types of homogeneously aligned E7 glass cells were fabricated using a pair of the UV-aligned SD1 commanding layers. These are the *Freedericksz* cell in which the SD1 alignment direction of the two glass substrates are aligned antiparallel to each other and a *twisted nematic* (TN) cell assembled with orthogonal SD1-alignment directions on the two glass substrates. Additionally, E7-filled commercially available glass cells were prepared using conventional rubbed PIs as the two homogeneous alignment layers. Cells with two bare glass substrates or two glass substrates coated with a non-aligned SD1 film were also fabricated as reference samples. These additional cells enabled the LC alignment for the mechanically rubbed-PI alignment layers to be compared with the UV/non-aligned SD1 commanding layers.

3.3.1.2 LC Alignment for Different SD1-coated Substrates

Figure 3.8 shows a direct comparison of the resulting LC textures formed in the layer of nematic E7 filled in three types of glass cells assembled using the same 10 μm spacers but different alignment layers. This includes two pristine (non-aligned) SD1 layers, two UV-aligned SD1 commanding layers fabricated with parallel SD1 alignment directions in the two SD1 layers in the cell (i.e., a Freedericksz cell), and two bare glass substrates. The last type exhibits a polydomain LC texture with high alignment non-uniformity and a Schlieren texture. The polydomain feature and shape irregularity of the typical Schlieren texture are found to remain during a 360^{o} azimuthal rotation of the bare glass cell. This is because of a random distribution of the LC director orientation in the cell since the bare glass substrates have no macroscopic alignment effect on the nematic LC layer. A similar trend also holds for the E7 layer aligned by the two non-aligned SD1 layers, though larger LC domains with certain interconnectivity were observed to exist over small regions (see Figure 3.8(a) and (d)). However, these seemingly interconnected domains were shown to be further divided into smaller polydomains using higher-magnification POM imaging (Figure 3.8(g)).

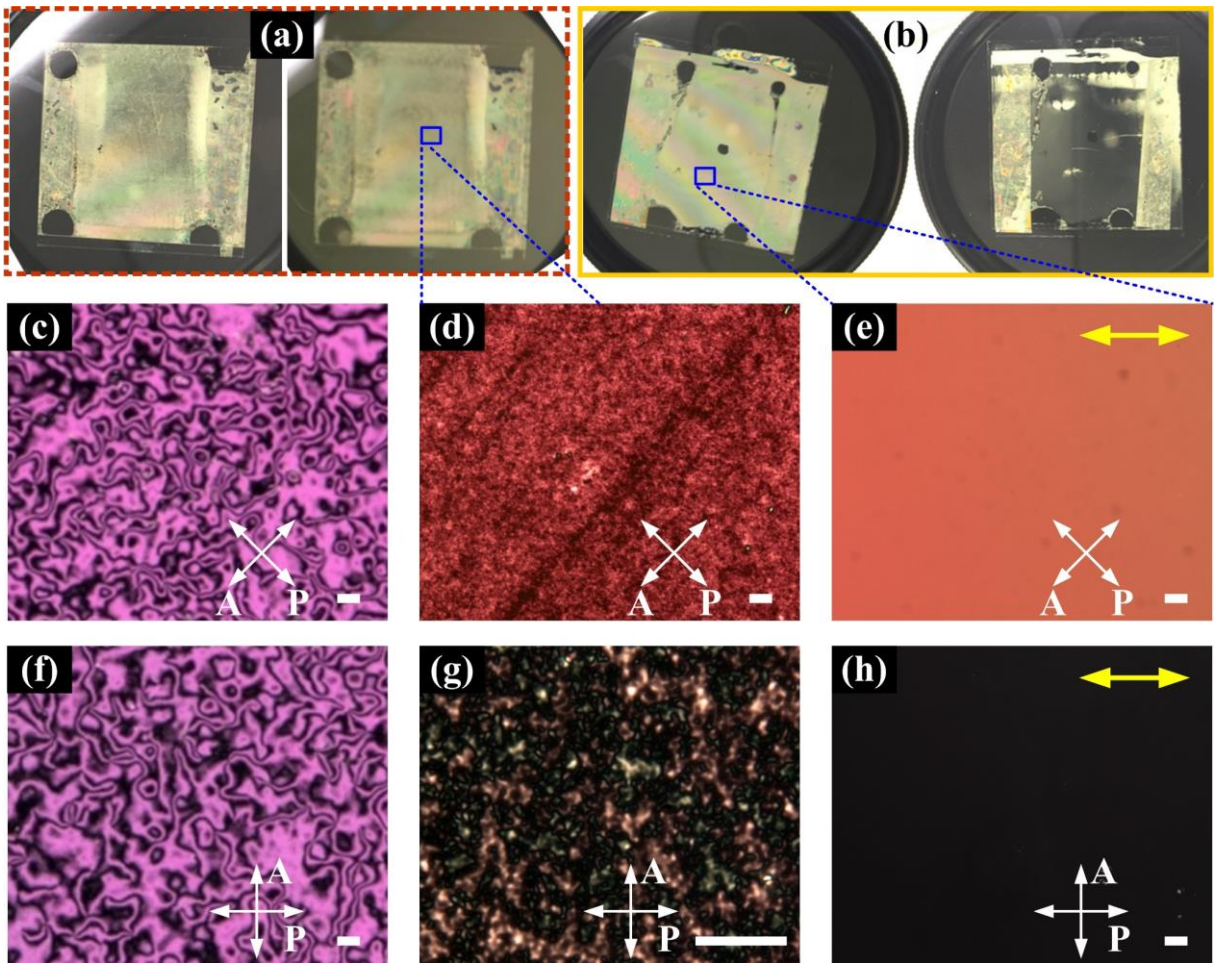

Figure 3.8: Nematic LC for different alignment conditions. The results are for the nematic LC filled in glass cells using three different pairs of alignment layers, namely, two non-aligned SD1 layers (a, d, g), two parallel UV-aligned SD1 commanding layers (b, e, h), and two bare glass substrates (c, f). (a - b) Bright-state and dark-state photograph of the E7 cell (25 mm × 25 mm in size) assembled with the non-aligned SD1 (a) and the UV-aligned SD1 (b); the images were recorded by placing the E7 glass cell between two crossed polarisers when illuminating with a white lightbox. (c - f) Enlarged polarised optical micrographs (POMs) demonstrating the distinct LC textures formed in a representative region (located at the solid blue rectangle in (a) and (b)) of the three different E7 LC cells at bright state (c - e) and dark state (f, g, h). The solid yellow double-headed arrows in (e) and (h) indicate the UV-aligned uniaxial orientation of SD1 in the two SD1 alignment layers in the Freedericksz cell. (g) is a higher-magnification POM in order to better resolve the dark-state LC texture formed in the nematic E7 layer that was sandwiched by the two nonaligned SD1 layers. All the bright-state images ((d - e) and the left panel of (a, b)) were recorded by rotating the E7 glass cell by 45° in the plane of the substrate with respect to the position used for recording the dark-state image whilst keeping the polariser and analyser pair crossed. The double-headed solid white arrows in (c - h) denote the orientations of the transmission axes of the polariser and analyser; the white solid scale bars in the bottom right of (c- f) are 50 µm.

These POM observations tend to exclude the existence of long-range orientational order in the as-prepared E7 cells and imply that the nonaligned SD1 films have a weak orienting effect on the LC. This observation can be explained by the possibility of localised self-organisation of the deposited SD1 molecules during the solvent removal process and/or orientational ordering triggered by the centrifugal force in the spin-coating process. On the contrary, an extended monodomain texture (feature size ranging mm - cm) was confirmed in the nematic LC Freedericksz cell. This uniform monodomain formed in the homogeneously SD1-aligned E7 layer displays a large bright/dark contrast for a 45^{o} cell rotation and thus significant birefringence, which showcases the LC-alignment capacity of the UV-aligned SD1 layer for fabricating high quality, uniform LC monodomains over a large area.

3.3.2 Alignment Quality and Thermal Stability

In addition to the orientation of low molar LCs at temperatures below 100 °C (e.g., the nematic E7 mixture at <70 °C), high-quality chain-orientation of LCCPs requires much higher temperatures to access the nematic LC phase (e.g., F8BT has a nematic phase in a temperature range of 235 °C - 265 °C). As a result, this necessitates that the alignment layers have excellent thermal stability at these high temperatures. For the UV-aligned SD1 layers, a subsequent thermal treatment (e.g., pre-annealing the UV-aligned SD1 layers at certain temperatures for a period of time) before they are assembled to form an LC glass cell could provide information about the thermal stability of the UV-aligned SD1 layers.

In order to experimentally study the thermal stability of SD1 photoalignment and compare with conventional rubbed PI layers, the uniformly UV-aligned SD1 layers coated on glass substrates (from 1 mg/mL SD1 solution and after polarised UV illumination for 10 mins) were annealed at 250 °C, 300 °C and 350 °C for 30 minutes. These substrates were then used to build three LC glass cells (10 µm spacers). The cells were assembled by employing a pair of parallel

aligned SD1-coated glass substrates as the homogeneous alignment layers. Additionally, commercially available glass cells with conventional rubbed-PI layers as the alignment layers were annealed at 250 °C, 300 °C and 350 °C in for 30 minutes before they were capillarity filled with the E7 LC mixture. All heat treatments were carried out in a nitrogen atmosphere. For direct comparison, the E7-filled glass cells with the same thickness but using a pair of the bare glass substrates or the non-aligned SD1 coated glass substrates were fabricated as reference samples.

The LC cells using different alignment layers were experimentally examined for both the UV-aligned SD1 and rubbed-PIs, and their thermal stability was assessed based on the optical textures formed in the nematic phase. The alignment quality for the SD1 photoalignment layers treated in different ways and for the standard rubbed-PI layers were quantified by the transmitted light intensity contrast (and the extracted greyscale contrast ratio) between the bright-state and dark-state POM images. A dark-state POM image is observed when the LC director orientation is parallel to either the polariser or analyser transmission axis, whereas a bright-state image is observed when it is at 45° to the axes of the polariser/analyser.

The bright/dark-state contrast ratio [8] is defined as $(T_{\text{bright}} - T_{\text{background}})/(T_{\text{dark}} - T_{\text{background}})$ where $T_{\text{background}}$ denotes the transmitted light intensity recorded when it is blank between the crossed polarisers, and T_{bright} and T_{dark} represent the transmitted light intensity detected for the bright-state and dark state when the LC is placed between the crossed polarisers. A photodiode connected to an oscilloscope was integrated into our crossed polarising optical microscope to detect the transmitted light intensity for the dark and bright states of each LC cell. The optical texture used to measure the contrast ratio of the E7 LC glass cells were viewed at a low (×10) magnification in order to average the transmitted light signals over a sufficiently large area. The bright/dark-state contrast ratios of the seven E7-filled glass cells are plotted in **Figure 3.9**(a)

with their alignment layers listed in the legend. The contrast ratio for the glass cell with two bare glass substrates (Cell No.1) and two non-aligned SD1 coated glass substrates (Cell No.2) is identified to be very low, i.e., 1.2 and 4.3, respectively. As expected, the two contrast ratios are relatively close to 1 because both the bare glass and the non-aligned SD1 should have no or very weak effect on the LC alignment. In contrast, a value of 720 was determined for the Freedericksz glass cell (Cell No.3) that had been aligned by two anti-parallel rubbed-PI commanding layers without any thermal annealing treatment and had no glass spacer beads dispersed inside the gap of the cell.

Among all the measured glass cells, the Freedericksz glass cell with two anti-parallel UV-aligned SD1 commanding layers without thermal annealing treatment (Cell No.4) shows the highest bright/dark-state contrast ratio of 816, a value even greater than the contrast ratio determined for the cell using two anti-parallel rubbed-PI alignment layers (Cell No.3). This trend is consistent with the previously measured higher voltage-holding ratios for SD1-aligned ferroelectric LC cells than those aligned by rubbed-PI layers [4]. We can see that thermal treatment of the UV-aligned SD1 layers reduces the bright/dark-state contrast ratios in the resulting glass cells. The UV-aligned SD1 layers annealed at higher temperatures ranging from 250 °C to 300 °C resulted in a reduction in the contrast ratio in the corresponding cells, though this decreasing trend is moderate as the contrast ratios for all the cells assembled with the thermally annealed UV-aligned SD1 layer pairs still remain considerably high (above 200). Such a reduction in the alignment quality for the thermally treated UV-aligned SD1 layers is in accord with the corresponding microscope images as well, as illustrated in Figure 3.9(b). The uniformly aligned nematic monodomains in the E7 layers remained when the annealing temperature of the UV-aligned SD1 increases from room temperature to 250 – 300 °C (see also **Figure 3.10** for the bright/dark state for two parallel UV-aligned SD1 layers without any annealing treatment).

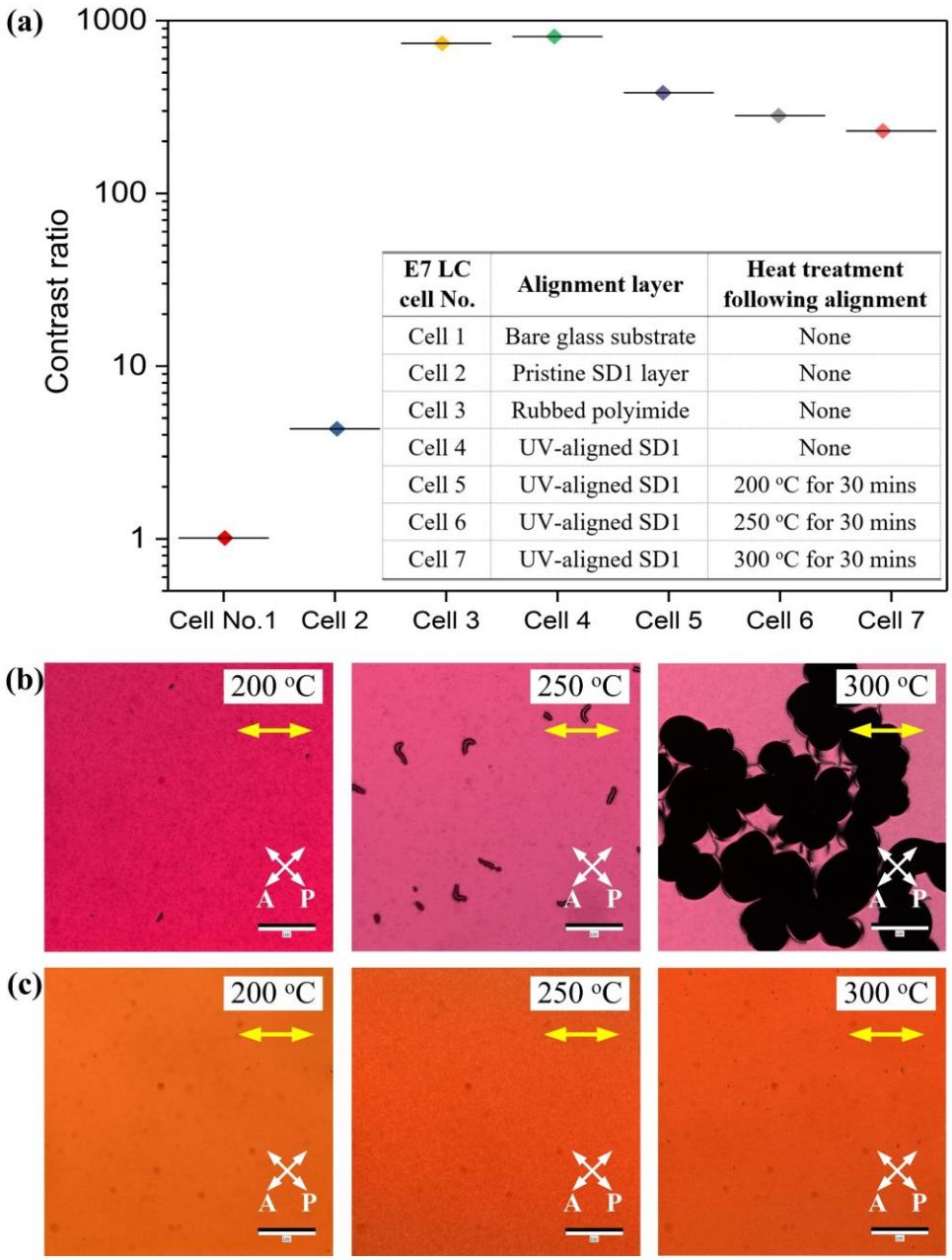

E7 LC cell No.	Alignment layer	Heat treatment following alignment
Cell 1	Bare glass substrate	None
Cell 2	Pristine SD1 layer	None
Cell 3	Rubbed polyimide	None
Cell 4	UV-aligned SD1	None
Cell 5	UV-aligned SD1	200 °C for 30 mins
Cell 6	UV-aligned SD1	250 °C for 30 mins
Cell 7	UV-aligned SD1	300 °C for 30 mins

Figure 3.9: Comparison of the LC alignment and the thermal stability in various nematic E7 glass cells using different alignment layers that were subjected to different annealing temperatures. This includes the SD1 photoalignment layer and the standard rubbed-PI alignment layer. (a) Bright/dark-state contrast ratio measured at room temperature for the seven E7-filled glass cells, with their alignment layers listed in the legend and the camera exposure settings kept the same. (b - c) Bright-state POM texture observed for the E7 glass cells using anti-parallel UV-aligned SD1 layers (b) and rubbed-PI alignment layers (c); all the commanding layers in the glass cells of 10 µm thickness (alignment direction denoted by the yellow arrows) observed in (b) and (c) have been pre-annealed at the selected temperatures (the numerical values in (b) and (c)) for 30 mins in a nitrogen atmosphere. The panel from left to right in (c) demonstrates the bright-state POM in Cell Nos.5, 6 and 7, respectively. The scale bars in (b - c) are 100 µm. The images in (b) and (c) were recorded at room temperature. The irregular black dots in (b - c) are from some dust in the objective lens, not in the cells.

The results for the contrast ratios and optical textures in the SD1-aligned E7 glass cells highlights the excellent thermal stability of the SD1 photoalignment layer. It is shown that, even at temperatures as high as ≥300 °C, which exceeds the nematic transition temperatures for most LCCPs, the photo-aligned SD1 alignment layer is able to create a uniform alignment. These experimental results demonstrate the feasibility of photoaligned SD1 for orienting a wide range of LC polymeric and small-molecular films.

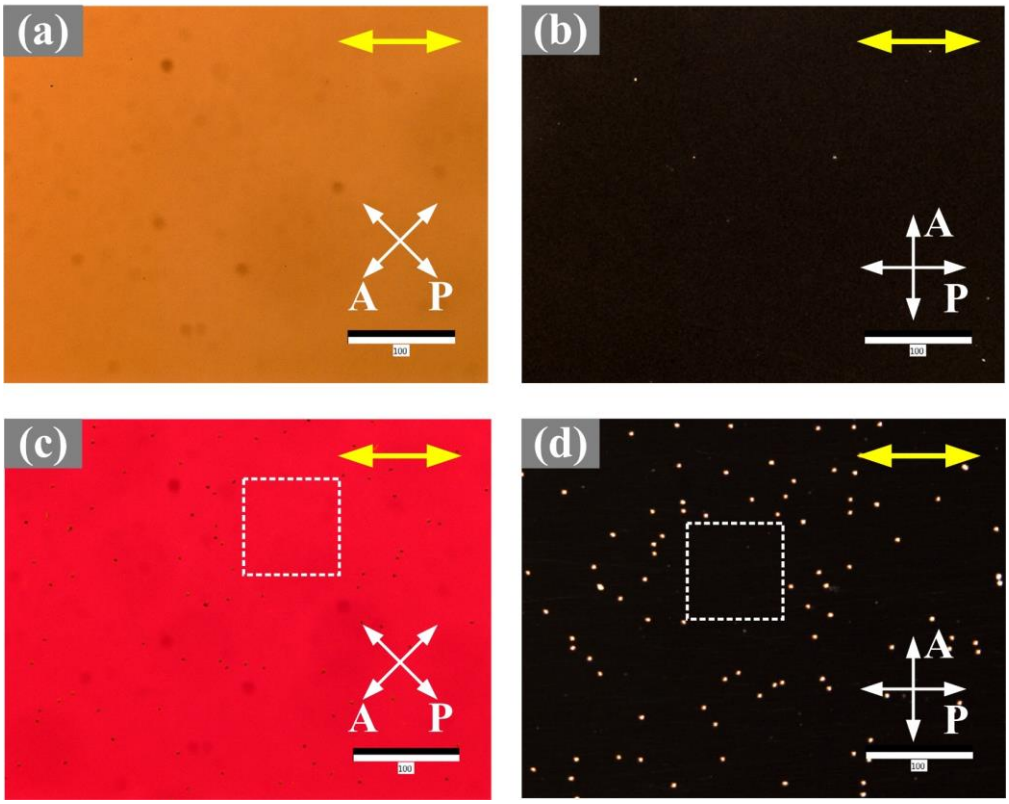

Figure 3.10: (a, c) Bright-state and (b, d) Dark-state POM images demonstrating the LC texture observed in the E7 glass cells (same thickness) using a pair of parallel UV-aligned SD1 layers (a - b) and rubbed-PI layers (c - d). All images were taken at room temperature. The solid yellow double-headed arrows indicate the alignment direction (i.e., the UV-aligned SD1 alignment direction or the PI-rubbing direction) of the alignment layers. The double-headed solid white arrows in each image denote the orientations of the transmission axes of the polariser and analyser; Scale bars: 100 µm. Note that the larger black spots in (a) and (c) should come from some dust in the microscope (not the E7 cell). The smaller black and white dots in (c) and (d) were induced by the dispersed beads in the commercial glass cells. The extracted greyscale contrast ratio of (a) and (b) is calculated to be 8.5 whilst that of the selected bead-free region in (c) and (d) is 5.6.

As a direct comparison, the standard mechanically rubbed PI alignment layers lead to a lower alignment quality in the resulting LC cells and also insufficient thermal stability at high temperatures of >200 °C. Two antiparallel aligned rubbed-PI layers are able to induce the formation of large-area extended nematic monodomains in the concomitantly oriented LC layer in the glass cell (see Figure 3.10(c - d)). For the increase in the annealing temperature of the rubbed-PI alignment layers to 200 °C, however, LC defects and/or non-aligned regions with irregular shapes appear in the LC cell (Figure 3.9(b)). The size and/or number density of these non-aligned spots/defects substantially increase as the temperature increases up to 250 °C. The worst alignment (and therefore the greatest thermal degradation of alignment layers) in the E7 cells occurs when the two anti-parallel rubbed-PI alignment layers had been pre-annealed at 300 °C for 30 mins. In this case, the LC defects and/or non-aligned regions could merge together, leading to the formation of polydomain LC textures and a rather high, uncontrollable degree of alignment non-uniformity in the resulting LC devices.

Even for the rubbed-PI and UV-aligned SD1 alignment layers that had not experienced any thermal annealing treatment, the photo-aligned SD1 in Cell No. 4 was shown in Figure 3.9(a) to produce higher LC alignment quality. The transmitted light intensity contrast ratio between the bright state and dark state of the E7-filled glass cells aligned by two rubbed-PI layers that had not experienced thermal annealing is still lower than (by ~100) the contrast ratio induced by the two antiparallel UV-aligned SD1 commanding layers without pre-annealing treatment (Cell No. 4). This finding is also supported by the extracted greyscale contrast ratios for the two cases: the greyscale contrast ratio in the nematic E7 layer homogeneously aligned by the two anti-parallel mechanically rubbed PIs in the glass cell is determined to be 5.6 ± 0.8, compared with a greyscale contrast ratio of 8.5 ± 0.6 in the same-thick Cell No. 4 that was assembled with two anti-parallel UV-aligned SD1 commanding layers without thermal annealing treatment.

3.3.3 Photopatterning and Rewritablity of SD1-Alignment Using Photomasks

In contrast to the difficulty associated with creating high-resolution spatial definition of alignment patterns in the mechanically rubbed PI layers, the excellent rewritability of the SD1 photoalignment is showcased in this Section by employing a US air force (USAF) target [9] as a photomask, along with many other photomasks [1,2,4,10], to spatially pattern (i.e., *rewriting*) the already uniformly UV-aligned SD1 commanding layers. A facile UV-rewriting process with respect to the uniformly pre-aligned SD1 alignment layers (by polarised UV illumination for 10 mins, spin-coated from 1 mg/mL SD1 solution) that has been coated on glass substrates, was implemented by placing a USAF mask on the SD1-coated glass substrates and then rotating the polariser by 90^{o} (from the direction used for the uniform UV-prealignment of SD1) such that polarised UV light with a 90^{o} orientation is generated to activate the *SD1 rewriting* process. Subsequently, each photo-masked UV-rewritten SD1 substrate was paired with another uniformly UV-aligned SD1 coated glass substrate to assemble and align E7 LC glass cells (5 μm spacer). In these E7 glass cells the UV-prealigned SD1 orientations in the two alignment layers can be either parallel or perpendicular to each other. The POM images of the as-assembled E7 glass cells were recorded and shown in **Figure 3.11** to illustrate the LC textures and birefringence, which confirms excellent texture/alignment uniformity and high colour contrast as proof of the unusual rewritability of the SD1 photoalignment.

By varying the SD1-alignment directions in the uniformly aligned SD1 layer and the (first-step) UV-prealigned background in the rewritten SD1 commanding layer, the as-assembled E7 LC cells can be aligned into either a parallel-aligned configuration by the top and bottom photoalignment layers or the orthogonal-aligned twisted nematic (TN) configuration. The main difference between the two differently configured LC cells lies in that the pre-aligned background in the parallel-aligned cell, when placed between the crossed polariser/analyser pair, turns into a black dark-state (the black background in Figure 3.11(a) and (c)) during a >90^{o}

azimuthal rotation of the cell sample, whereas the pre-aligned background in the TN cell does not exhibit black color at the dark state, instead of a green optical texture in Figure 3.11(e).

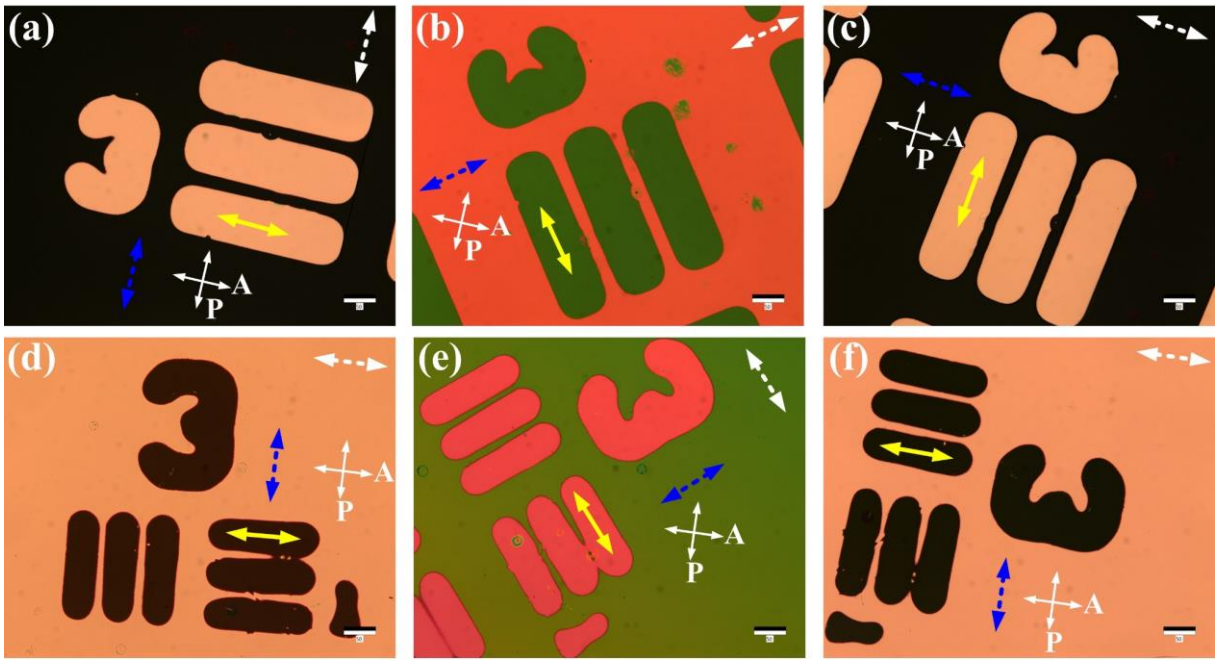

Figure 3.11: Rewritability illustration of the SD1 photoalignment based on a two-level UV alignment process, in which an orthogonal polarisation direction was used between the first-step uniform pre-alignment of SD1 by linear polarised UV illumination (alignment direction denoted by the dashed blue arrows), and the second-step photo-masked UV rewriting process using the USAF target (with the alignment direction denoted by the solid yellow arrows). A photo-masked UV-rewritten SD1 coated glass substrate was paired with another uniformly UV-aligned SD1 coated glass substrate (the alignment direction marked by the dashed white arrows) to build a glass cell (using 2 µm spacers), in which the UV-prealigned SD1 orientations in the two alignment layers can be either parallel (a - c) or perpendicular (d - f) to each other. The LC textures in the resultant nematic E7 cells placed between crossed polarising polariser (P) and analyser (A) were observed with an anti-parallel (a - c) or twisted nematic configuration (d - f). (a, b, c) and (d, e, f) show the E7-alignment pattern masked, respectively, by the 3rd element in the 2nd group and the 1st element in the 3rd group in the used USAF target. (b, e) and (c, f) were recorded by rotating the cell from (a, c) by 45^{o} and 90^{o}. The scale bars are 50 µm.

Analogously, due to the orthogonality of the SD1-alignment directions in the locally rewritten regions and the uniformly UV-prealigned background in the two-step UV-aligned

SD1 commanding layers, each of the resulting LC cells is made up of either parallel-aligned or TN sub-domains. The high-quality nematic E7 alignment in the photo-masked patterns, in terms of high ordering, small colour fluctuations, large-area uniformity of the nematic orientation, together with the as-shown sharp boundaries separating the rewritten region and pre-aligned background in all the images of Figure 3.1, can be indicative of a high-quality uniform LC alignment and potentially very high pattern resolution of the photoaligned SD1.

3.4 Optimisation of the UV-Alignment Process for Orienting LCCP Films

The UV-aligned SD1 commanding layers have been experimentally verified in the previous Sections with excellent rewritablity, facile patternablity, and high thermal stability at temperatures as high as >300 °C. These unique advantages of the SD1 photoalignment endow the feasibility of utilising the photo-aligned SD1 to uniaxially orient an LCCP exhibiting an LC mesophase at a temperature of <300 °C and to spatially define the chain-orientation patterns in LCCP-based structures and devices. However, the photo-pattern resolution of the SD1 alignment was found to only achieve 5 - 10 μm in the nematic E7 LC cells (Figure 3.11) due to the thickness of the assembled glass cells (several μm). Solution processed LCCPs, on the other hand, allow easy deposition into thin-films (tens to hundreds nm in thickness), which are supposed to significantly reduce the length scale of the elastic deformation in SD1-aligned LC layers and, therefore, offer the opportunity to substantially enhance the pattern resolution.

Our experimental study on the dependence of dichroic ratio of the UV-aligned SD1 films on the polarised-UV exposure time and SD1 film thickness in the previous Sections of this Chapter has revealed that for an SD1 alignment layer spin-coated from a specific concentration of SD1 solution, there indeed exists an optimal UV-illumination time that could optimise the SD1-alignment quality (i.e., prolonged UV exposure could lower the order parameter in the resulting SD1 films). Although the SD1-film thickness does not appear to alter the ultimate

photoalignment quality in the UV-aligned SD1 layers, the orientation effect of the LC director may still vary in the mesophase, as the elastic properties might differ when the UV-aligned SD1 layers are of different thicknesses. There is thus a need to optimise the UV-alignment process of the SD1 alignment layers in order to maximise the alignment quality in the overlying LCCP films. This Section involves systematically varying the duration of the linearly polarised UV illumination, and the thickness of both the SD1 photoalignment layer and the SD1-orinted overlying LCCP film.

3.4.1 Nematic LC Phase Alignment of the LCCP Film

Solution processable LCCPs can be deposited onto the UV-aligned SD1 layers by means of spin-coating or other coating techniques. The thickness of a deposited LCCP overlying film was tuned from tens of nanometres to hundreds of nanometres, through systematically varying the spin-coating speed and duration and using the same filtered solution such as either a 30 mg/mL F8BT solution or a 15 mg/mL PFO solution in anhydrous toluene, in order to minimise the uncertainties associated with the whole fabrication process. The LCCP films were vacuum-dried for >1 hour to remove excess solvent and then subjected to heating to raise the LCCP into the nematic LC phases to align the polymer chains.

The polymer chains in a single LCCP layer or an SD1/LCCP bilayer were heated into a melt of the LCCP (e.g., ~268 °C for F8BT, ~190 °C for PFO), which was followed by slowly cooling (at a rate of 3 ^{o}C/min) the film sample to a temperature that sits in the middle of the nematic-phase temperature range of the deposited LCCP (e.g., 247 °C - 250 °C for F8BT and 160 °C - 165 °C for PFO) before it is then held at this temperature for 10 minutes. The whole thermally-induced alignment process was completed by rapidly quenching the SD1-oriented nematic LCCP layer to room temperature (e.g., by transferring the sample from the hot stage onto a copper bar) to finally form a solid nematic glass state. The quenching step prevents

crystallisation and thereby locks in the LC director configuration formed in the nematic mesophase [10,11], namely, a self-organised polydomain LC texture for a single layer of LCCP directly coated on a substrate or an SD1-oriented monodomain for the LCCP film coated on a polarised UV illuminated SD1 alignment layer.

The fabrication of the LCCP monodomain glass films that can extend over a large area and possess favourable anisotropies in the physical properties can be mediated by the inherent long-range orientational ordering present in the nematic mesophase, via direct molecular interaction between the UV-aligned SD1 layer and the LCCP polymer chains at the SD1/LCCP interface. Subsequently, chain orientation is communicated through the bulk of the overlying LCCP film by chain-chain interactions and π-π stacking. The highly oriented director in the SD1-aligned LCCP layers in the mesophase can be preserved by the rapid quenching to form the nematic glass films that are then used for our structural and photophysical characterisations.

3.4.2 Polydomain and Monodomain LC Textures

POM images were recorded when the SD1-aligned and long-range self-organised LCCP glass films were placed between a crossed polariser and analyser pair to observe the resultant optical textures therein. A highly-oriented monodomain LCCP glass film aligned on a polarised UV-illuminated SD1 alignment layer shows a dark (bright) state in the POM image when the direction of the chain orientation (which defines the optic axis) is parallel (at 45°) to the transmission axis of either the polariser or analyser. **Figure 3.12** shows the bright-state and dark-state POM images recorded from three types of quenched F8BT nematic glass films of the same thickness of 160 nm (F8BT was purchased from ONE-Material Inc with a molecular weight of M_w = 55,000 and polydispersity index, PDI = 2.3). Results are presented for 1) a non-aligned F8BT polydomain nematic glass film that had been spin-coated and aligned/quenched on a bare glass substrate (Figure 3.12 (a) and (d)); 2) a fully-aligned F8BT monodomain nematic

glass film that had been spin-coated on a polarised UV-illuminated SD1 alignment layer (with continuous and uniform coverage on the substrate) (Figure 3.12 (b) and (e)); and 3) a partially-aligned F8BT polydomain nematic glass film (Figure 3.12 (c) and (f)) that was spin-coated and aligned on a polarised UV-illuminated discontinuous SD1 alignment layer (here with a discontinuous coverage on the substrate due to the spin-coating using ≤ 0.1 mg/mL concentration of SD1 solution).

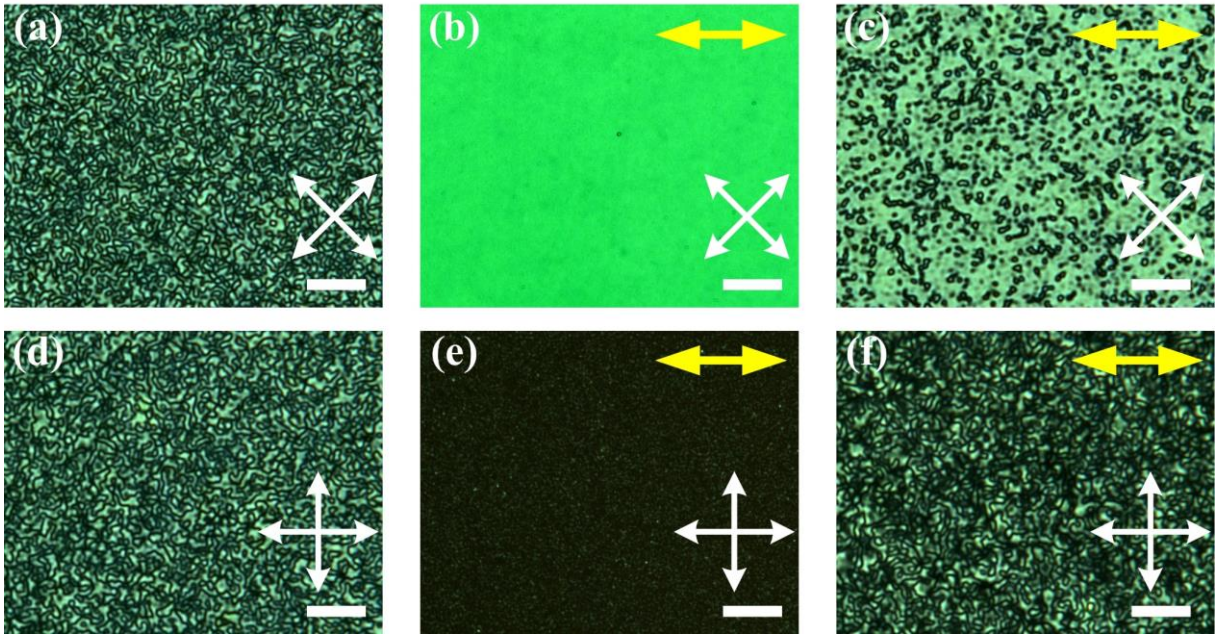

Figure 3.12: Polarised optical micrographs (viewed between the crossed polariser and analyser with the transmission axis denoted by the white double-headed arrows) of an F8BT film aligned and subsequently quenched on 1) (a, d) a bare glass substrate; 2) (b, e) a polarised UV-illuminated continuous SD1 alignment layer (spin-coated from 1 mg/mL SD1 solution and then photoaligned by polarised UV illumination for 10 mins), and 3) (c, f) a polarised UV-illuminated discontinuous SD1 alignment layer (spin-coated from 0.1 mg/mL SD1 solution and exposed to the polarised UV light source for 5 mins). The chain-orientation directions in the SD1-aligned F8BT nematic films in (b - f) are indicated by the thick yellow double-headed arrows. All the measured F8BT nematic glass films herein are 160 nm in thickness. The horizontal white solid scale bar in the bottom right of each image is 20 μm.

The typical Schlieren LC texture [12] is observed for the nonaligned F8BT polydomain nematic glass films, which can be ascribed to the spontaneous self-organisation taking place in

the nematic F8BT layer (without SD1-alignment) before quenching. In this case, the F8BT polymer backbones in each locally self-organised nematic micro-domain were well-oriented as well, due to the intrinsic long-range orientational ordering present in the nematic mesophase. The overall chain orientations among the nematic micro-domains are randomly distributed, as evidenced by a continuous transmitted-light intensity variation in each of the locally self-organised, irregularly-shaped nematic micro-domains when the F8BT glass film was rotated by 360° in the plane of the substrate.

High-quality and uniform chain orientation in larger-area extended nematic monodomains is illustrated in the bright-state and dark-state POMs recorded for the fully-aligned F8BT nematic glass film. There are still some distinguishable not-well-aligned regions appearing in the dark state POM (Figure 3.12(e)). However, as shown in the next Section, further optimisation of the UV-illumination parameters and the thickness of the SD1 and F8BT layers can eliminate these defects and/or nonaligned regions. On the contrary, for the discontinuous SD1 commanding layers, the UV-aligned SD1 molecules are expected to take the form of isolated islands on the substrate. Consequently, the UV-aligned discontinuous SD1 layers induce a polydomain nematic LC texture in the quenched F8BT glass films (see the nonaligned dark domains in Figure 3.12(c) and the bright regions in Figure 3.12(f)) as the separation distance among the isolated SD1 islands was larger than the characteristic lengthscale of the long-range orientational order of the nematic F8BT. Altogether, these POM images recorded from the different F8BT nematic glass films reveal that the partial (and full) alignment of F8BT nematic domains takes place with chain re-orientation and the associated increasing (or complete) elimination of the polydomain boundaries in the SD1-covered regions, which initially form with cooling from the isotropic F8BT melt into the nematic phase before the films are aligned in the nematic phase and rapidly quenched to form the glass state.

3.4.3 Optimisation of the Alignment Quality

In this Section, the alignment quality achieved in the aligned LCCP glass films that were coated and then oriented on a polarised UV-illuminated SD1 alignment layer is experimentally determined from the optical dichroic ratio, $DR = A_{//} / A_{\perp}$, where $A_{//}$ and $A_{\perp}$ denotes the optical density for the parallel and orthogonal polarised light components relative to the chain-orientation direction in a quenched LCCP glass film. As a result, the determination of the DR value in an LCCP glass film involves carrying out polarised optical absorption spectral measurements of the film sample. The SD1 commanding layers of various thicknesses, which had been aligned by polarised UV illumination for different durations, were then used to uniaxially orient the overlying F8BT nematic glass films of the same thickness. The UV alignment process and SD1 film thickness can be optimised in terms of the best alignment quality in the correspondingly oriented overlying F8BT glass films. Subsequently, the optimised UV-aligned SD1 alignment layers could be utilised to orient the overlying F8BT nematic glass films with different thicknesses so as to maximise the DR value achievable for SD1-aligned nematic F8BT.

3.4.3.1 Polarised Optical Absorption Spectral Measurements

Polarised UV-vis absorption spectroscopy was performed using a PerkinElmer Lambda 1050. A Thorlabs WP25M-UB broadband wire-grid polariser (wavelength range 275 nm - 1000 nm) was mounted in front of an LCCP film sample to generate a linearly polarised incident beam. As schematically demonstrated in the insert of **Figure 3.13**, the relative orientation of the polymer chains formed in an LCCP glass film to the polarisation direction of the normal incident light (propagating along the *z*-axis) was varied through rotating the LCCP film in the vertical (*x*-*y*) plane on a rotation stage in order to record the $A_{//}$ and $A_{\perp}$ spectra of the LCCP film. The parallel and perpendicular polarised UV-vis (percent) transmission (*%T*) spectra of an LCCP film sample, alongside the polarised *%T* spectrum of a quartz substrate ($\%T_{quartz}$) after

the polariser, were initially acquired and subsequently calibrated to give the corresponding parallel ($A_{//}$) and perpendicular ($A_{\perp}$) polarised optical absorbance spectra of the LCCP film based on the Beer-Lambert law: $A = 2 - \log(\%T / \%T_{quartz})$.

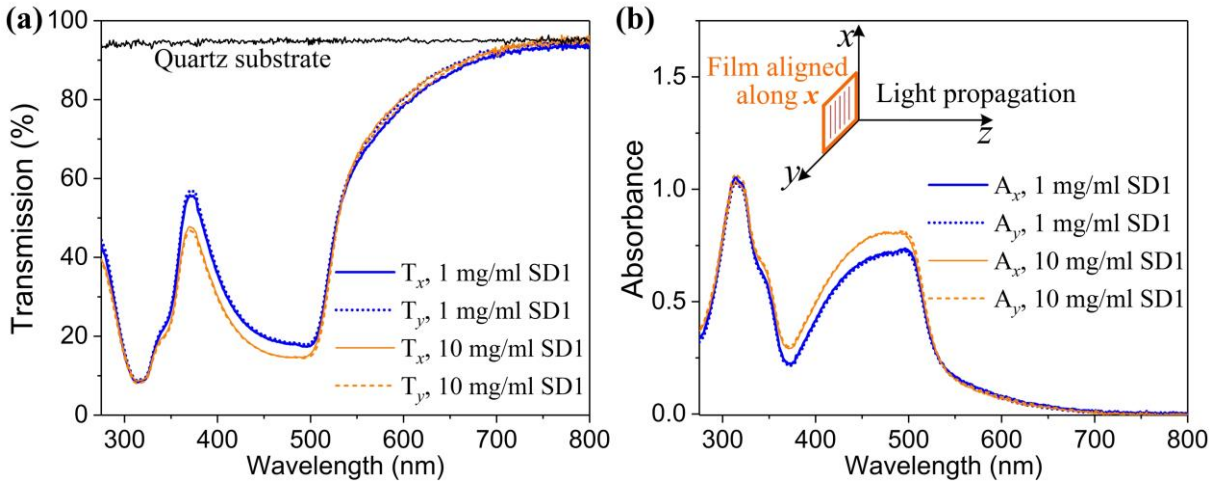

Figure 3.13: (a) Polarised UV-vis transmission (*%T*) spectra and (b) corresponding polarised optical absorbance spectra of two F8BT glass films deposited on a non-aligned SD1 photoalignment layer that had been spin-coated on a quartz substrate (12 mm × 12 mm in size) from 1 mg/mL (blue curves) and 10 mg/mL (orange curves) SD1 solution. The T_x spectra of the F8BT/SD1 bilayers in (a) and the A_x spectra in (b) were recorded by aligning one edge of the substrate to the *x*-axis shown in the insert in (b), while their T_y and A_y spectra were measured by rotating the film by 90° in the *x*-*y* plane (i.e., the edge of the substrate was aligned parallel to the *y*-axis). The black curve in (a) shows the polarised transmission spectrum of a quartz substrate. All the quenched F8BT glass films that were measured herein have the same thickness of ~160 nm.

Figure 3.13(a) and (b) shows the polarised UV-vis transmission spectra and the calibrated optical absorbance spectra recorded from two F8BT nematic glass films (160 nm in thickness) coated on a non-aligned SD1 photoalignment layer that was spin-coated on a 12 mm × 12 mm quartz substrate using either a 1 mg/mL (blue curves) or 10 mg/mL (orange curves) SD1 solution before the deposition and thermal alignment of the F8BT overlying film. Also shown is the polarised *%T* spectra of a quartz substrate (represented by the black curve in Figure 3.13(a)), which reaches *T%* of 93% - 94% at the longer wavelengths and converges with the

polarised *T*% spectral curves of the two F8BT film samples. Due to the amorphous nature of the quartz glass substrates, the polarised *%T* spectrum of the quartz substrate displays no orientation dependence when the substrate was rotated in the vertical (*x*-*y*) plane with respect to the incident polarisation that was fixed to align along the *x*-axis during all the following polarised UV-vis spectral measurements. For the SD1/F8BT bilayers, the polarised UV-vis transmission/absorbance spectra are acquired when one edge of the substrate was aligned parallel (the T_x spectra in Figure 3.13(a) and the A_x spectra in Figure 3.13(b)) and perpendicular (the T_y and A_y spectra) to the incident polarisation (along the *x*-axis). The convergence of the polarised %*T* spectrum of the quartz substrate with the ones of the quenched SD1/F8BT bilayers at the longer wavelengths makes the bilayer films demonstrate no absorption at >700 nm wavelengths. For each SD1/F8BT bilayer sample, the $A_{//}$ and $A_{\perp}$ spectra exhibit no clear difference in the spectral lineshape and absorption strength at the two peak wavelengths since the SD1 photoalignment layer had not been exposed to the polarised UV illumination.

Given that the measured F8BT nematic glass films have the same thickness, the as-shown spectral difference between the A_x (or A_y) spectra of the two types of SD1/F8BT bilayers should arise from the different thicknesses of the non-aligned SD1 layers. By assuming the contribution of other optical effects such as interface reflection/scattering is trivial, such a spectral intensity difference leads to the approximation of the absorbance of a 33 nm-thick SD1 layer to be ~0.1 at the wavelength of 450 nm - 460 nm (i.e., spin-coated from 9 mg/mL SD1 solution; see also Figure 3.2(b) for a linear relationship between the thickness of the spin-coated SD1 films and the concertation of SD1 solution). This absorption level is also found to be close to the proportionally projected non-polarised absorbance shown in Figure 3.2(a) for the pristine SD1 layer spin-coated using the 10 mg/mL solution. Accordingly, the absorption coefficient of the non-aligned SD1 was estimated to be ~70% of that of the quenched non-aligned nematic F8BT (M_w = 55,000) at 450 nm - 460 nm.

3.4.3.2 SD1 Film Thickness and UV-Exposure Time

Polarised UV-vis optical absorption measurements were performed to experimentally quantify the alignment quality in the quenched F8BT nematic glass films that had been spin-coated with the same thickness of ~160 nm and then aligned on different UV-illuminated SD1 alignment layers. The aim is to optimise the chain-orientation effect of the photoaligned SD1 by engineering the thickness of the UV-aligned SD1 layers (achieved by spin-coating different SD1 solutions with the concentration varying from 0.1 mg/mL to 10 mg/mL) and the duration of the linearly polarised UV illumination (e.g., 5 mins -30 mins). Accordingly, the typical $A_{//}$ and $A_{\perp}$ spectra of the quenched F8BT nematic glass films that had been oriented by the UV-aligned *continuous* (fabricated from 1 mg/mL SD1 solution) and *discontinuous* (from 0.1 mg/mL solution) SD1 alignment layers are shown in **Figure 3.14**(a) and (b), respectively.

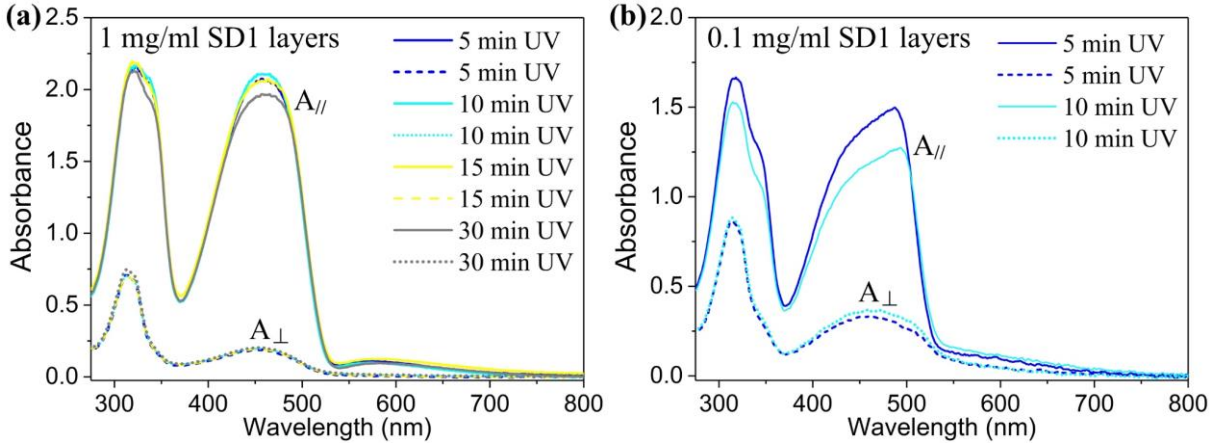

Figure 3.14: Polarised optical absorption spectra for different types of the SD1-aligned F8BT nematic glass film with the same thickness of 160 nm. Polarised absorbance spectra for an F8BT aligned on an SD1 photoalignment layer that was spin-coated using (a) 1 mg/mL or (b) 0.1 mg/mL SD1 solution and then exposed to polarised-UV-light for the selected duration (the numerical values of 5 mins, 10 mins, 15 mins, and 30 mins) before the deposition of the F8BT overlying films. Spectra are shown for both parallel ($A_{//}$) and perpendicular ($A_{\perp}$) incident polarisations, relative to the polymer chain-orientation direction. The SD1 photoalignment layers spin-coated using the 1 mg/mL solution result in a continuous and uniform coverage of the quartz substrate; whereas the ones fabricated from the 0.1 mg/mL SD1 solution yield a discontinuous coverage on the quartz substrate.

The polarised UV-illuminated continuous SD1 photoalignment layers result in the formation of extended monodomain LC textures in the fully-aligned F8BT nematic glass films (see Figure 3.12), while polydomain nematic textures appear to form for the alignment from the UV-illuminated discontinuous SD1 layers from the lower solution formulation. The difference in the LC textures has been found to induce distinct lineshapes in the polarised absorption spectra between the fully-aligned and partially-aligned F8BT nematic glass films. Compared with the broad optical transition band (located at wavelengths of >375 nm) of the nonaligned nematic F8BT (see Figure 3.13), the $A_{//}$ spectra of the partially-aligned polydomain F8BT glass films are narrowed but with enhanced absorption strength and also show a better-resolved absorption peak with a blue-shifted wavelength. The fully-aligned monodomain F8BT glass films, on the other hand, exhibit a larger enhancement (attenuation) in the optical density of the optical transition bands in the $A_{//}$ ($A_{\perp}$) spectra, alongside an increasingly narrow low-energy absorption band and a further blue-shift of its peak wavelength. For all the quenched F8BT nematic overlying films oriented by the UV-aligned continuous SD1 photoalignment layers (i.e., using1 mg/mL solution), the SD1-alignment by polarised UV illumination for 10 mins appears to give rise to the greatest F8BT absorption coefficient (i.e., absorbance/thickness) at the $A_{//}$ spectral peak wavelength λ_{max} of ~460 nm, which is followed in order by the 5 min, 15 min and 30 mins UV-alignment. In contrast, the $A_{\perp}$ spectra in Figure 3.14(a) appears to show very little difference for the different illumination times. These $A_{//}$ and $A_{\perp}$ spectra point to the conclusion that, for the SD1 photoalignment layers fabricated from the 1 mg/mL solution, the optimised UV-alignment duration is 10 mins in terms of the highest dichroic ratio ($DR = A_{//} / A_{\perp}$) at λ_{max} among the four SD1-aligned F8BT glass films. As for the discontinuous SD1 layers, as shown in Figure 3.14(b), the best UV-alignment time decreases to 5 mins due to the reduced SD1 material content. The optimal UV-alignment durations for other SD1 film thicknesses are also identified from the detailed DR results summarized in **Figure 3.15**(a).

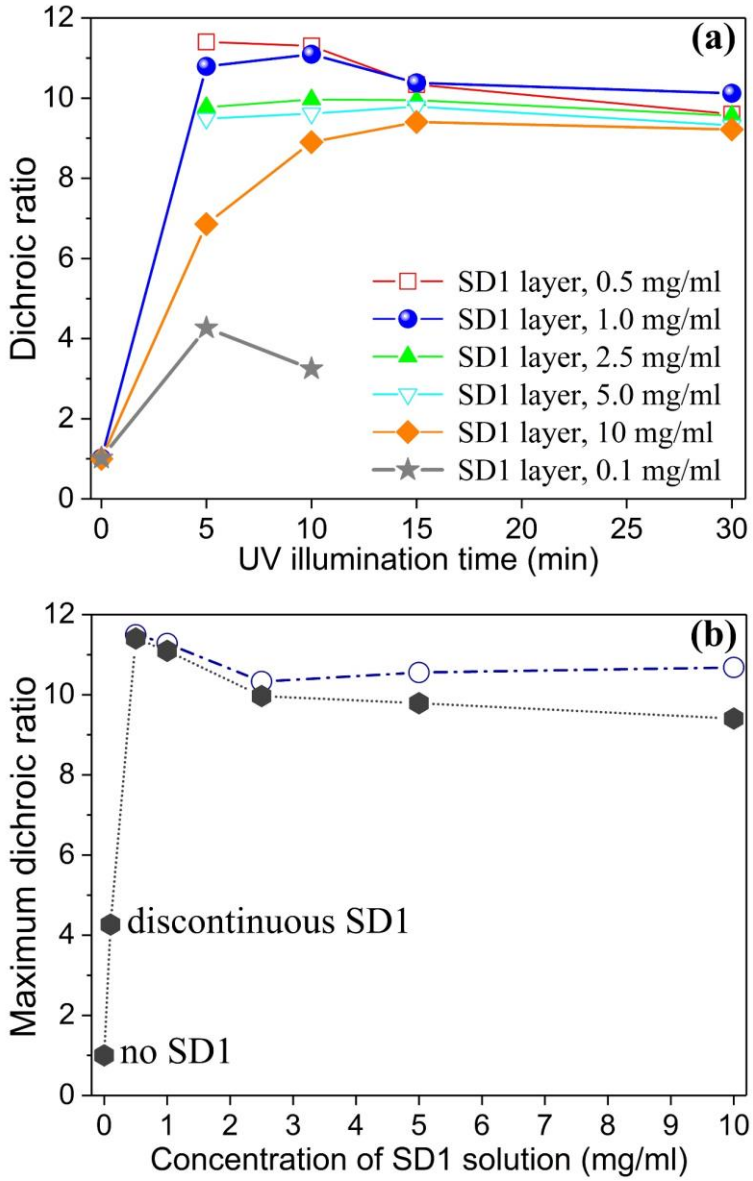

Figure 3.15: The dichroic ratios calculated at λ_{max} for the quenched 160 nm-thick F8BT glass overlying films that had been aligned by different UV-illuminated SD1 alignment layers. The thickness of the SD1 photoalignment layers was tailored by varying the SD1 solution concentration (the numerical values in the legend of (a)), whilst the F8BT alignment of the UV-illuminated SD1 photoalignment layers was tuned by changing the duration of the polarised UV illumination. (a) Dichroic ratios of the SD1-aligned F8BT nematic glass films as a function of the UV illumination time for different concentrations of the SD1 solutions used to deposit the SD1 layers. (b) The maximum dichroic ratio achieved in the SD1-aligned F8BT nematic glass films as a function of the SD1 solution concentration that had been exposed to polarised UV alignment for the optimised duration in (a). The concentration for the quartz substrate (no SD1) and UV-aligned discontinuous SD1 layer was plotted as 0 and 0.1 mg/mL. The filled black hexagon denotes the dichroism maxima calculated based on the parallel and perpendicular polarised absorbance of the quenched SD1/F8BT bilayers, while the open blue circle represents the data calibrated only for the correspondingly oriented F8BT nematic layers.

Analogous to our previous demonstration of an optimised UV exposure time to ensure the highest order parameter in the UV-aligned SD1 layers with a specific thickness (e.g., 10 mins for the SD1 layers spin-coated from 1 mg/mL solution, as shown in Figure 3.6), Figure 3.15(a) shows that, for each of the six different thicknesses of the measured UV-aligned SD1 photoalignment layers (corresponding to the six concentrations of SD1 solutions used to deposit the SD1 layers on quartz substrates), there also exists an optimal UV-illumination time that maximises the dichroic ratio achieved in the resulting oriented F8BT nematic glass films (160 nm in thickness): 5 mins for the SD1 layers fabricated from 0.1 mg/mL and 0.5 mg/mL solutions, 10 mins for the ones from 1 mg/mL and 2.5 mg/mL solutions, and 15 mins for the ones from 5 mg/mL and 10 mg/mL. Therefore, the higher the concentration of SD1 solution, the longer exposure time of the SD1 layers is needed. It should be noted that the optimal UV-aligned SD1 commanding layer thickness (3 - 4 nm) identified hereby for enabling the best chain orientation in the oriented F8BT nematic glass films, coincides with the reported optimal SD1 layer thickness of 3 - 5 nm in terms of providing the highest multiplex operation steadiness and contrast ratio in SD1-aligned ferroelectric LC display cells [13]. A shorter period of the polarised UV illumination would cause incomplete orientational ordering of the SD1 molecules in the photoaligned SD1 layer, whilst prolonged UV-exposure appears to reduce the ordering. This could be a result of the possible occurrence of a certain degree of SD1 oxidation in ambient conditions and/or an increased mixing/tilting of the *trans*- and *cis*-conformations of the SD1 molecules in the over-exposed SD1 layers.

The ordering in the non-optimally photoaligned SD1 alignment layers/surfaces can be transferred to the F8BT overlying films in the nematic phase, which therefore degrades the overall F8BT alignment quality (by 2% - 16% *DR* decreases depending on the thickness of the UV-aligned SD1 layers) in the resulting quenched F8BT glass films. As demonstrated in the first row and the second row of **Figure 3.16**(a) and (b), the over-exposure of the SD1 layers

leads to a decrease in the long range LCCP ordering, which is in accord with the increasing size/density of the non-aligned regions appearing in the bright-state and dark-state POM images.

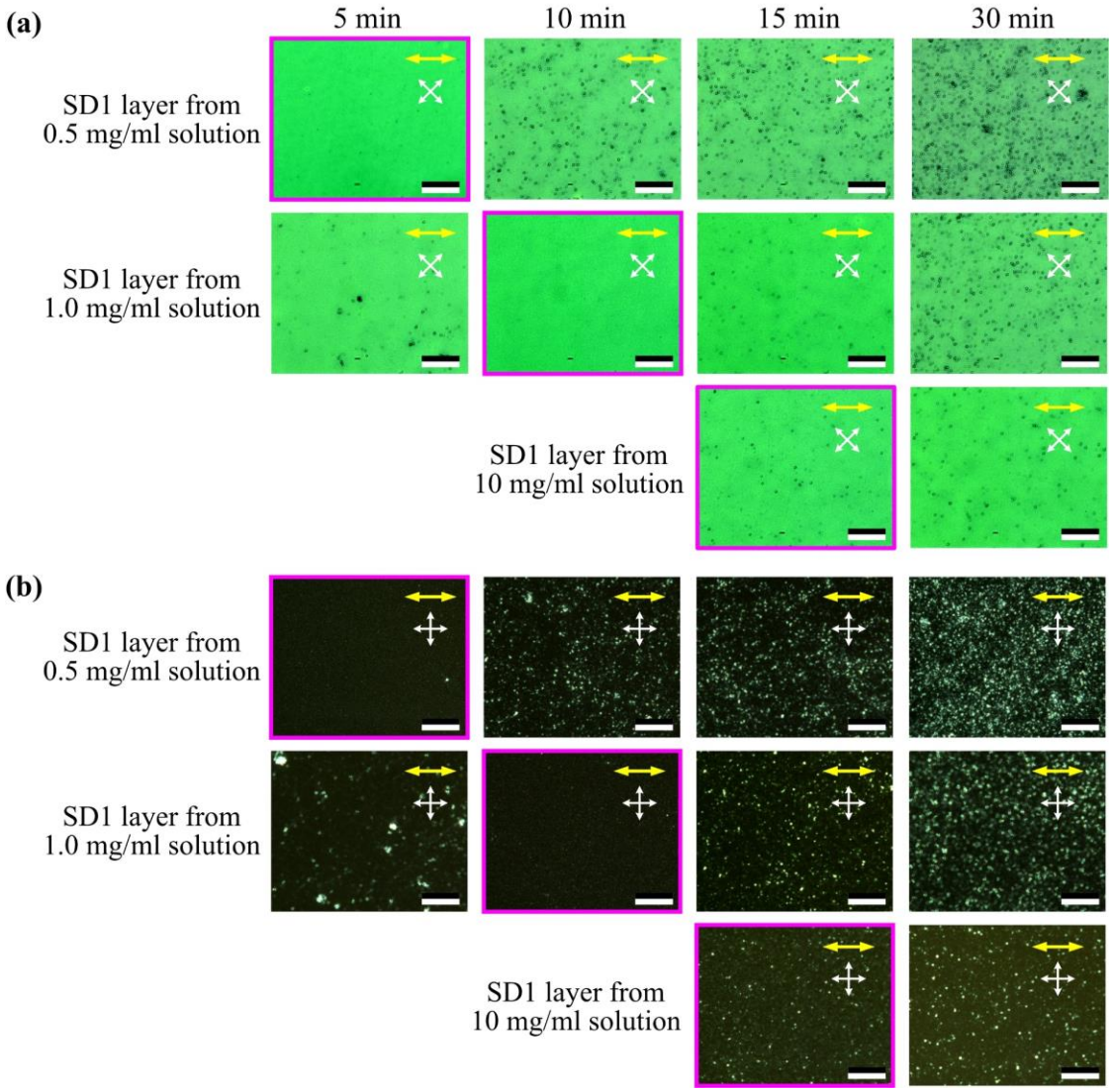

Figure 3.16: (a) Bright-state and (b) dark-state POM images illustrating the LC textures in the 160 nm-thick F8BT nematic glass films homogeneously aligned by the SD1 photoalignment layers, which had been spin-coated from 0.5 mg/mL (the first row), 1 mg/mL (the second row) and 10 mg/mL SD1 solution and subsequently exposed to the polarised UV illumination for 5 mins (the first column), 10 mins (the second column), 15 mins (the third column) and 30 mins (the fourth column). The oriented F8BT samples (the alignment direction denoted by the yellow arrows) were placed between a crossed polarised polariser/analyser pair (denoted by the crossed white arrows). The dark (bright) state POM images were recorded when the samples were rotated in the plane of the substrate to align the polymer chain-orientation parallel (at 45°) to the transmission axis of the polariser/analyser. The panels highlighted by the pink outline shows the LC textures with the optimised F8BT alignment quality among all the SD1-aligned nematic F8BT glass films shown in each row of (a) and (b). The horizontal scale bar in the bottom right of each image is 50 μm in length.

It is crucial to point out another generic trend seen in Figure 3.15(a) and (b): the oriented F8BT glass film on a thinner UV-aligned continuous (i.e., fabricated with a lower SD1 solution concentration ranging from 0.5 mg/mL to 10 mg/mL) SD1 commanding layer that had been exposed to the polarised-UV illumination for one of the coordinated durations always exhibits a larger dichroic ratio and thus higher F8BT alignment quality. Among all the 160 nm-thick SD1-aligned F8BT nematic glass films that have been investigated herein, the maximum dichroic ratio of 11.5 occurs in the F8BT monodomain glass film homogeneously aligned by the thinnest photoaligned continuous SD1 commanding layers, namely, the ones that had been spin-coated using the 0.5 mg/mL SD1 solution and UV-aligned for 5 min. For comparison, the maximum dichroic ratio decreases to 11.1, 10, 9.4, and 4.3 for the F8BT nematic glass films (160 nm in thickness) that were oriented by the optimally UV-aligned SD1 commanding layer fabricated from 1 mg/mL, 2.5 mg/mL, 10 mg/mL and 0.1 mg/mL SD1 solutions, respectively.

It should be noted that the dichroism maxima have been calculated using the $A_{//}$ and $A_{\perp}$ values at λ_{max} measured for the bilayers consisting of the UV-aligned SD1 layer and the SD1-oriented F8BT nematic glass film. A small increment in these maxima (the *DR* difference between the black hexagon and the blue circle shown in Figure 3.15(b)) for an SD1 solution concentration is sensible by calibrating the $A_{//}$ and $A_{\perp}$ values in order to exclude the contribution arising from the UV-aligned SD1 commanding layers. The calibration was performed by subtracting the $A_{//}$ and $A_{\perp}$ values at λ_{max} of the UV-aligned SD1 layers (with different thicknesses) from the ones of the corresponding SD1/F8BT bilayers. In doing so, the dichroic ratio of the optimally UV-aligned SD1 layers was chosen to be 3.5 - 3.6 (see Figure 3.6), whilst the average of ($A_{//}$ + $A_{\perp}$) at λ_{max} for the UV-aligned SD1 layer fabricated using a specific concentration of SD1 solution is fixed and projected proportionally according to the solution concentration by referring to the absorbance of the nonaligned SD1 (see Figure 3.13(b), that is, 0.1 equals to the absorbance of a non-aligned SD1 layer coated from a 9 mg/mL solution).

Although the non-aligned and partially-aligned F8BT nematic polydomain glass films exhibit ~1 and <5 dichroic ratios, respectively, the calibrated dichroism maxima at λ_{max} confirm that high-quality chain-orientation (>10 dichroic ratios) has been achieved in all the measured F8BT nematic monodomain glass films, which had been homogeneously aligned by the photoaligned continuous SD1 layers of different thicknesses (as the SD1 solution concentration was varied over a range of 0.5 mg/mL to 10 mg/mL). ***The optimised UV-illuminated SD1 photoalignment layer*** has been identified as the ones that are spin-coated using the 0.5 mg/mL SD1 solution (3 - 4 nm in thickness) and then UV-aligned for 5 min, judged by providing the best F8BT alignment quality so far (*DR* = 11.5) in the SD1-oriented F8BT nematic glass films with the same thickness of 160 nm. Even though the origin of a thinner UV-aligned continuous SD1 alignment layer (fabricated from a lower solution concentration) giving rise to a higher DR value (than the thicker counterparts) in the resultant oriented F8BT glass film is not very clear, it may be related to the following: 1) a reduction in the orientational ordering across a thicker photoaligned SD1 layer, and/or 2) an associated elastic relaxation/deformation of the UV-aligned SD1 molecules at the SD1/F8BT interface that occurs in the process of the LC alignment of F8BT polymer chains at the high temperatures of nematic mesophase F8BT.

3.4.3.3 Optimising the Dichroic Ratio

Another deciding factor for the polymer chain-orientation quality induced by a photoaligned SD1 layer is the thickness of the SD1-aligned LCCP glass films. The optimised UV-aligned SD1 photoalignment layer has been used to orient the overlying F8BT nematic films for a set of different thicknesses. The thickness of the SD1-aligned F8BT nematic glass films was tuned from 40 nm to 480 nm (measured using a Dektak profilometer) by only varying the speed of the spin-coating deposition with the 30 mg/mL F8BT solution in anhydrous toluene. The thickness dependence of the F8BT dichroic ratio and the LC textures of these F8BT glass films are shown in **Figure 3.17**.

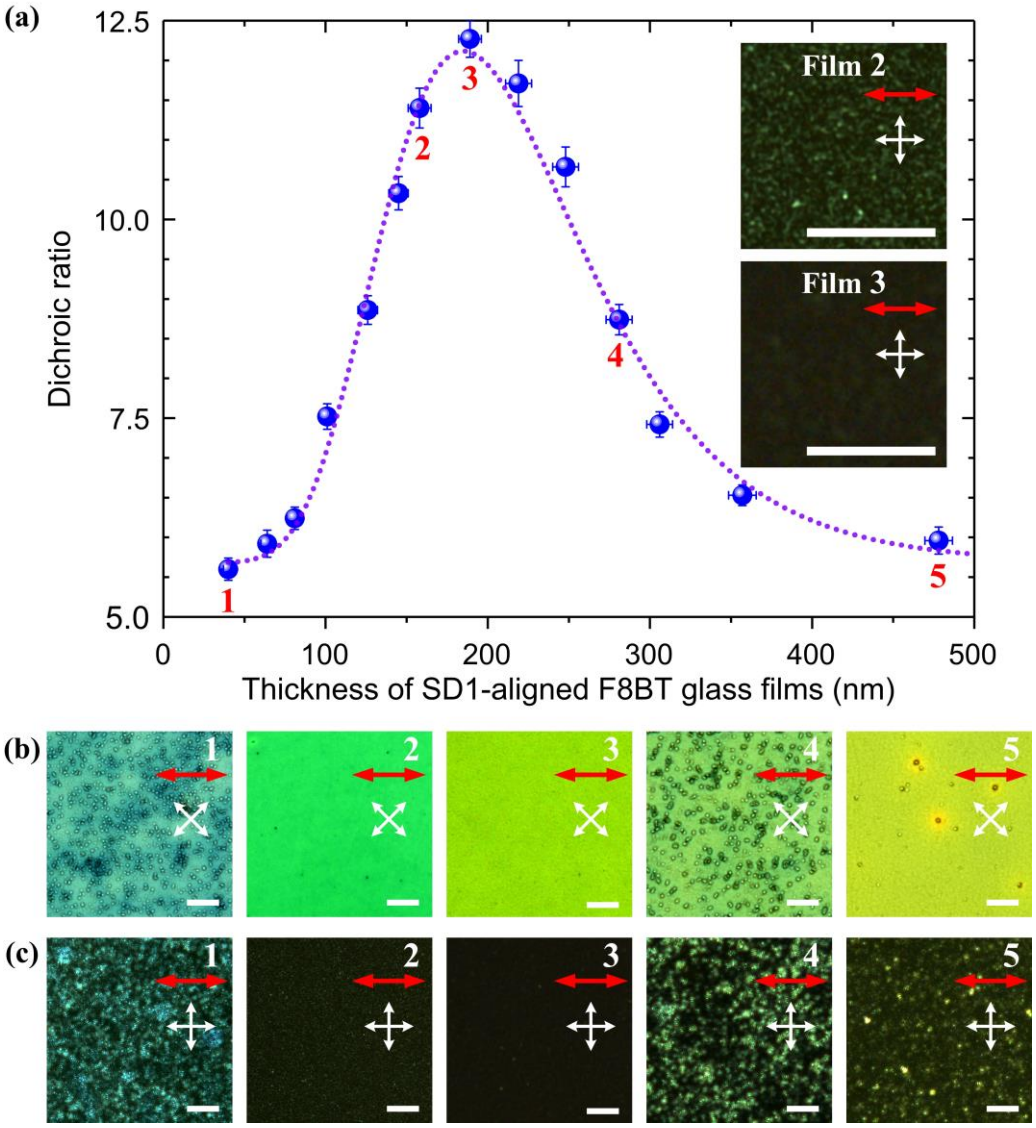

Figure 3.17: (a) Dichroic ratio at λ_{max} as a function of the thickness of the SD1-oriented nematic F8BT glass overlying films that had been uniaxially oriented by the optimised UV-illuminated SD1 photoalignment layers (from 0.5 mg/ml solution and UV-aligned for 5 mins). The dotted curve is a guide for the eye. (b) Bright-state and (c) Dark-state POM images illustrating the LC textures observed in the SD1-oriented F8BT nematic films with one of the F8BT film thicknesses at the five points labelled in (a), that is, from left to right: 40 nm (1), 160 nm (2), 190 nm (3), 280 nm (4) and 480 nm (5). The oriented F8BT samples (chain orientation denoted by the thick double-headed red arrows) were placed between a crossed polarised polariser/analyser pair (the crossed thin white arrows). All the dark (bright)-state POM images were recorded using the same imaging settings when the samples were rotated to align the polymer chain-orientation parallel (at 45°) to the transmission axis of one of the crossed polarisers. The colour change from (1) to (5) in (b) corresponds to the increase in retardation in the thicker films. The two inserted dark-state POM images in (a) were recorded from the oriented nematic F8BT films of 160 nm (2) and 190 (3) nm in thickness but using a larger magnification and exposure time. The horizontal scale bar in each image in (b) and the two inserted POM images in (a) is 20 μm.

The influence of the LCCP film thickness on polymer chain-orientation quality was carefully studied using F8BT as the model material so as to better understand the scope for the alignment quality optimisation. It is evident that polymer chain orientation arising from the same SD1 alignment layers is favoured for the F8BT glass films with thicknesses in the range ~100 to 300 nm, in terms of >10 dichroic ratios. The maximum dichroic ratio is 12.3 at a film thickness of ~190 nm, which, as a matter of fact, reaches the theoretical upper-limit of *DR* by considering a deviation angle of 20° - 22° between F8BT chain axis and the direction of transition dipole moment [14,15]. Although a further increase in F8BT film thickness can constantly lower the overall F8BT alignment quality averaged across the whole thickness of the quenched glass films, it reassuringly demonstrates that the best chain-orientation occurs for film thicknesses similar to those commonly used in a rich range of device structures [16-18]. This optimised optical dichroism for the photoaligned nematic F8BT in the solid glass nematic state is larger than the DR values reported for the oriented F8BT films by rubbed high-temperature PI alignment layer (*DR* = 8.2) [15,19] and by surface confinement (*DR* = 7) [20], as well as for the oriented F8BT nanofibers by an electrospinning process (*DR* = 2 -3) [21].

The polymer chains in the mesophase behave in a cooperative manner with the SD1 commanding layer acting to direct their long-range orientational ordering, most desirably into an extended monodomain state. It is expected that the interplay between chain-chain and chain-SD1 interactions facilitates the polymer chain ordering. As for a thicker F8BT film, the aligning effect/force of the optimised SD1 commanding layer will decrease with an increasing distance between the polymer chains and the alignment surface; this tends to magnify the effect of the self-organisation in the nematic phase before quenching. This could explain the emergence of the non-aligned or not-well-aligned regions in the LC textures of the 280 nm-thick Film 4 and 480 nm-thick Film 5 shown in Figure 3.17(b). On the other hand, the nematic mesophase polymer chains in a sufficiently thin F8BT glass film may experience a different yet strong

surface effect during the SD1-orienting process. This is due to the significantly reduced separation distance between the SD1 alignment surface and the free surface of the nematic F8BT, which would limit the re-orientation of the polymer chains [22,23] and result in the formation of not-well aligned regions and/or a polydomain texture. For example, the 40 nm-thick SD1-oriented F8BT glass film (Film 1) with its bright-state and dark-state POM images illustrated in Figure 3.17(b) reveals the presences of poorly aligned regions.

This thickness variation in the polymer chain-orientation quality in the SD1-aligned F8BT nematic glass films and associated LC textures provide insight into the SD1-directed LCCP chain ordering, which is discussed in more detail in the next Chapter. In addition to the polydomain LC textures formed in the homogeneously aligned F8BT glass films by the optimised UV-illuminated SD1 photoalignment layer, the enlarged dark-state POM images of Film 2 and Film 3 in the inserts of Figure 3.17(a) distinguish the highly-oriented nematic monodomains as well (see Figure 3.17(b)). There still remain unoriented polymeric nanocrystals [12] embedded in a well-aligned polymer matrix in the 160 nm-thick SD1-aligned F8BT nematic glass films, until the optimised film thickness of ~190 nm is used, at which point completely black images were observed throughout the dark-state POM, substantiating the generation of the high order chain-orientation and excellent monodomain LC texture.

3.4.4 Determination of the Spatial Pattern Resolution

A patterning resolution test using a standard 1951 US Air Force (USAF) Resolving Power Test Target [9,10] as a photo-mask to spatially pattern the polarised UV illumination of the optimised UV-aligned SD1 commanding layer (i.e., spin-coated from 0.5 mg/ml solution and UV-aligned for 5 mins) was carried out. The pattern results shown in **Figure 3.18** demonstrate that 2 - 4 μm feature sizes (Group 7 in the USAF Target mask [9]) are readily generated in the photo-masked chain-orientation patterns against a non-aligned background in the

correspondingly SD1-oriented F8BT nematic glass film (160 nm in thickness). Such high-resolution spatial control of the chain-orientation patterns offers the possibility to fabricate a variety of photonic structures with on-demand definition of the in-plane chain/molecular orientation distributions and associated refractive index modulation.

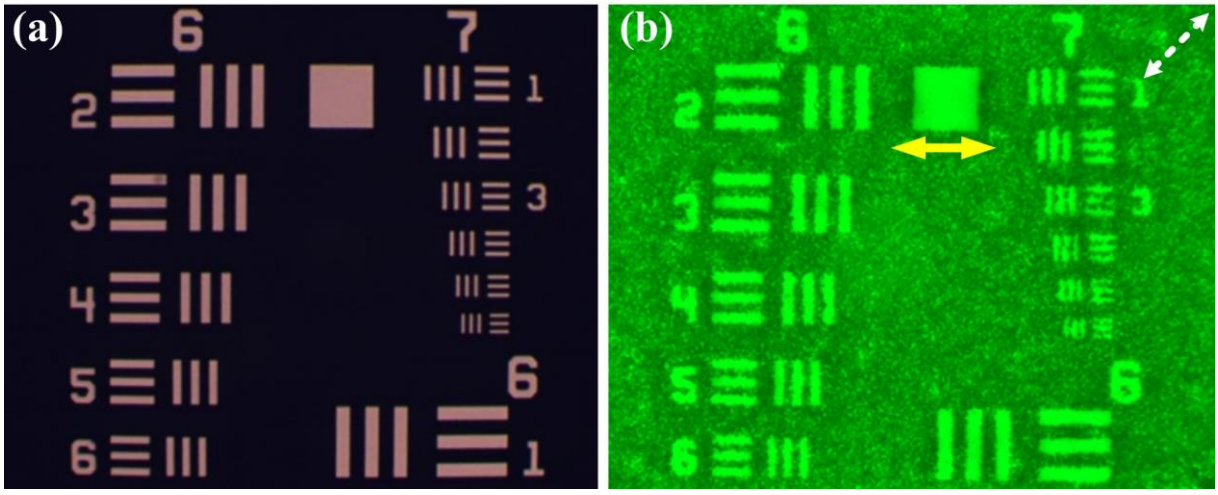

Figure 3.18: (a) Optical image of the Standard 1951 USAF Resolving Power Test Target that was used as a mask to create SD1 alignment patterns against a non-aligned background in the optimised UV-aligned SD1 commanding layer. (b) Polarised confocal fluorescence image of an F8BT glass film (160 nm in thickness) with the chain-orientation patterns generated by the optimised UV-aligned SD1 commanding layer using masked UV illumination. The fluorescence was photoexcited with randomly polarised light at 450 nm but collected with a polariser at 45° (denoted by the dashed white arrow) relative to the chain-orientation direction in the photo-masked patterns (the horizontal solid yellow arrow). It is clear that < 4 μm (Group 7) features are resolved in (b).

3.5 Photoalignment of Polymer Blend Films

So far, we have focused on using the UV-aligned SD1 commanding layers to directly orient mesophase LCCP F8BT chains. This is because F8BT has been widely deployed as the emission layer in polymer LEDs, a laser gain medium [24,25], and as a resonance energy transfer host for red-light emission guest gain polymers [26,27] such as the copolymer Red-F that comprises 9,9-dioctylfluorene [50%], benzothiadiazole [40%], triarylamine [5%], and

thiophene-benzothiadiazole-thiophene [5%] moieties (see **Figure 3.19**(a) for the chemical structure of Red-F). The large spectral overlap between the emission spectrum of F8BT and the absorption spectrum of Red-F enables efficient Förster resonance energy transfer from F8BT to Red-F[10] and polarised red-light emission from the blend films of F8BT and Red-F. While Red-F is not itself an LCCP, indirection photoalignment of Red-F is showcased by an SD1-oreinted 90 wt% F8BT host:10 wt% Red-F guest binary blend film. The alignment of Red-F guest stems from the SD1-oriented polymer chains of the F8BT host in its nematic phase.

Red-F was supplied by the Sumitomo Chemical Company Ltd and used as received. Chain oriented F8BT/Red-F blend films were fabricated using the UV-aligned SD1 as the commanding layer. The process for generating patterned chain-orientation structures for the F8BT/Red-F blend films (spin-coated as 305 nm-thick overlying films using a 90 wt% F8BT/10 wt% Red-F 30 mg/mL solution mixture) on the SD1-coated Spectrosil substrates was similar to that previously used to fabricate the chain-orientation (patterns) in the quenched F8BT glass films. The UV-alignment of SD1 was photo-masked in order to create alignment patterns in the SD1 commanding layers, prior to deposition of the F8BT/Red-F blend films. The blend/SD1 bilayers were first heated on the hot stage at 265 °C for 3 min under nitrogen, followed by slow cooling at 1 °C min^{-1} to 235 °C and then rapid quenching to room temperature. The polarised photoluminescence (PL) image in Figure 3.19(b) illustrates the resultant chain-orientation pattern formed in the quenched SD1-oriented F8BT/Red-F blend film. The letters correspond to the SD1-aligned regions and are resolved by viewing the PL intensity of the sample in a microscope equipped with crossed polarisers. The significantly enhanced emission intensity in the masked chain-orientation pattern should result from well-oriented Ref-F polymer chains in the quenched blend film. The dichroic ratio of the same quenched blend film homogeneously aligned by a uniformly UV-aligned SD1 layer is found to be 3.5 (Figure 3.19(c)) and the PL intensity anisotropy of 5.1 at the peak wavelength of 635 nm.

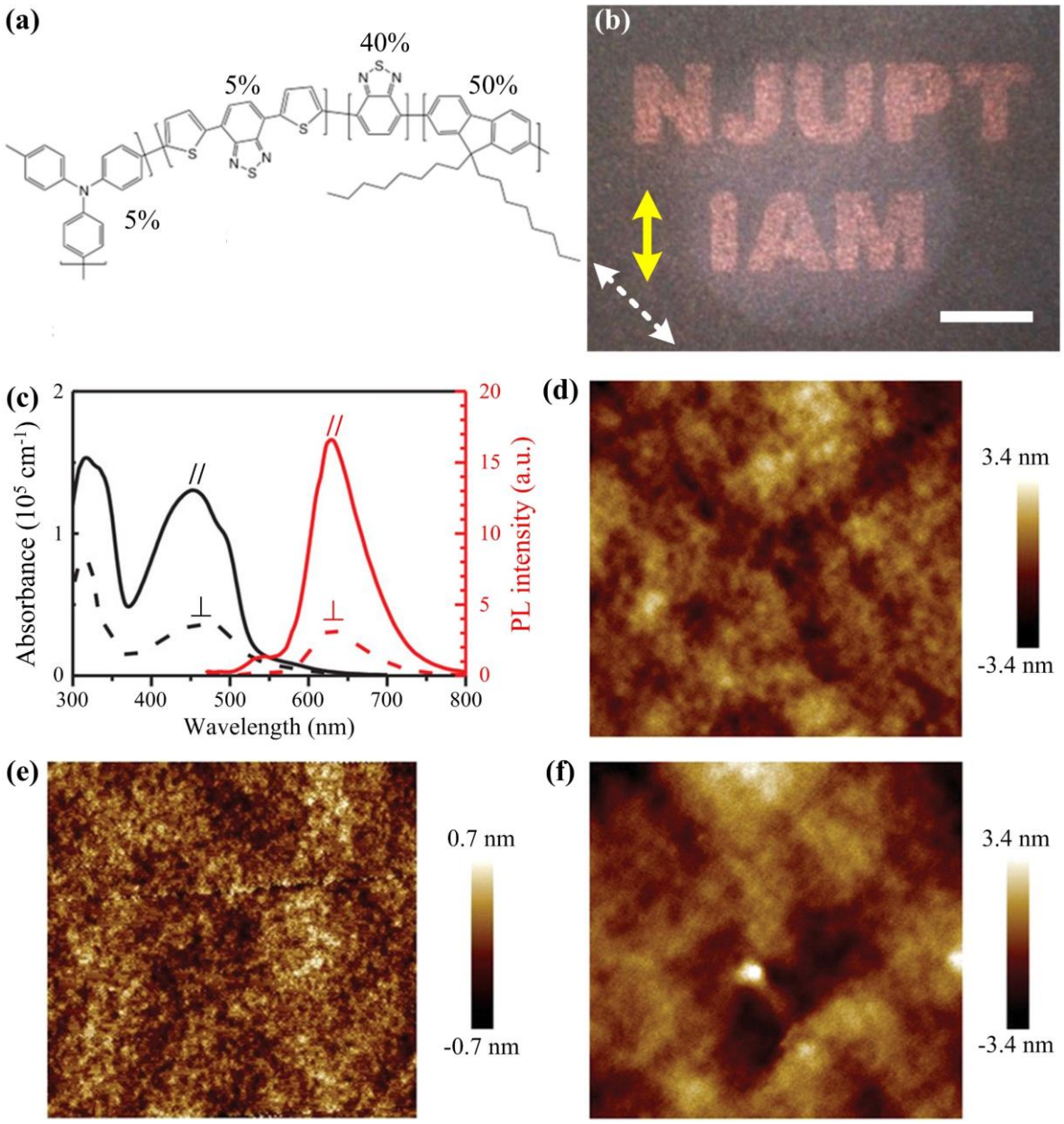

Figure 3.20: (a) Chemical structure of Red-F. (b) PL emission pattern generated for an F8BT/Red-F blend film (305 nm thickness), observed with a crossed polarizing microscope (*c.f.* bar for pattern scale). The double-headed solid yellow arrow represents the chain orientation and the double-headed dashed white arrow denotes the polarisation direction of the excitation light. (c) Polarised absorption (left ordinate) and PL (right ordinate) spectra for an SD1-aligned F8BT/Red-F blend film (305 nm thickness). Spectra are shown for both parallel (//) and perpendicular (⊥) incident (absorption)/analyser (PL) polarisations, relative to the polymer chain-orientation direction. (d - f) Atomic force microscope (AFM) film surface topography images (3 × 3 μm^2 area) for: (e) UV-aligned SD1 (23 nm thickness), (d) F8BT/Red-F blend (200 nm thickness) and (f) F8BT (250 nm) aligned on top of uniformly UV-aligned SD1 commanding layers. The results presented herein resulted from a collaboration with Prof. Ruidong Xia's group at Nanjing University of Posts and Telecommunications (NJUPT) [10].

Figure 3.19 shows atomic force microscope (AFM) images of surface topographies for e) a UV-aligned SD1 commanding layer (~23 nm thickness), d) an SD1-oriented F8BT glass film (250 nm thickness), and f) the SD1-aligned F8BT/Red-F blend film (305 nm thickness). These film surface topographies were measured using a Bruker Dimension Icon AFM equipped with Scanasyst-Air peak-force tapping mode tips. The deduced root-mean-square (RMS) roughness values are 0.41± 0.05 nm for SD1, 0.7 ± 0.1 nm for F8BT, and 0.7 ± 0.1 nm for F8BT/Red-F, confirming good uniformity in all the three types of films despite the extensive processing required for the fabrication.

3.6 Summary

In this Chapter, SD1 has been shown as a solution (water)-processable, extremely effective, high-temperature stable (>300 °C), rewritable photoalignment material for providing high-quality uniform chain-orientation and high-resolution spatial definition of long-range LC/chain-orientation patterns. The prominent examples include the LCCP overlying films of the green-light emission from F8BT and red-light emission from a 90 wt% F8BT host:10 wt% Red-F guest binary blend. The linearly polarised UV illumination process has been explored and optimised to align the SD1-coated substrates that are employed as highly effective homogeneous alignment layers. As a comparison, orienting nematic F8BT or F8BT/Red-F blend films is not feasible with the standard rubbed-PI alignment approach as the rubbed-PIs are demonstrated to remain thermally stable only up to temperatures of <200 °C, which is below the nematic-phase temperature range for F8BT (i.e., 235 °C - 265 °C). The UV-aligned SD1 commanding layers enable higher order parameters in the nematic E7 glass cells than the standard rubbed-PI alignment layers, in terms of >800 bright/dark-state transmitted-light intensity contrast of the SD1-aligned E7 glass cells and the extracted greyscale contrast of 8.5 between their bright-state and dark-state LC textures.

The HOMO level and work-function of the H-aggregated SD1 layers is identified to be ~5.8 eV and ~5 eV, respectively, which would make SD1 non-luminescent and also a promising interlayer candidate. The thickness of spin-coated SD1 photoalignment layers can be easily tuned by varying the concentration of the SD1 solution based on a linear relationship between the two. Continuous SD1 layers are fabricated when the concentration of the SD1 solution used for spin-coating SD1 films is not less than 0.5 mg/mL, whereas SD1 molecules discontinuously cover the substrate when SD1 solution concentrations of <0.1 - 0.25 mg/mL are used. The UV-aligned continuous SD1 photoalignment layers give rise to highly-oriented F8BT monodomain nematic glass films whilst the UV-aligned discontinuous SD1 layers lead to polydomain LC textures formed in the quenched F8BT glass films. Without any alignment, the LC-phase self-organised F8BT polydomain glass films exhibit the typical Schlieren LC textures.

Polarised absorption spectral measurements were performed to experimentally quantify the alignment quality of an oriented film based upon the optical dichroic ratio. The SD1-film thickness does not affect the ultimate photoalignment quality achieved in the UV-aligned SD1 commanding layers as long as they are UV-aligned for an optimal time. Analogously, the UV-alignment process of the SD1 photoalignment layers has also been optimised so as to maximise the F8BT alignment quality, via systematically varying the polarised UV illumination duration as well as the thickness of both the SD1 commanding layers and the quenched SD1-aligned F8BT nematic glass films. The optimised UV-aligned SD1 commanding layer has been identified as the ones that are spin-coated using 0.5 mg/mL SD1 solution (3 - 4 nm in thickness) and then UV-aligned for 5 min, which gives rise to an F8BT dichroic ratio at λ_{max} as high as 12.3 and an order parameter of 100% at an F8BT film thickness of ~190 nm. Such a high optical dichroism approaches the theoretical upper-limit of F8BT. Also, we showed that the SD1-aligned polymer chains are favoured (>10 dichroic ratios) for the F8BT nematic glass films with thicknesses in the range 100 to 300 nm, which are similar to the film thicknesses

commonly used in a rich range of device structures. Our AFM images of surface topographies confirm good uniformity in the UV-aligned commanding layers and the SD1-aligned glass films of the nematic F8BT and F8BT/Red-F blend despite the extensive processing required.

One of the specific advantages of using a photoalignment approach is the ability to generate spatial patterns in the LCCP orientation by masking the exposure of the SD1 films to the linearly polarised UV illumination. Our patterning resolution test using a standard 1951 US Air Force Resolving Power Test Target as the mask shows that 2 - 4 μm features are generated in the correspondingly SD1-aligned chain-orientation patterns in the F8BT nematic glass film. No smaller LCCP structures have been fabricated by a photo-masking method at this time but we note that an earlier study of SD1 showed that ≈100 nm orientation patterning can be achieved in the SD1 layers under specific conditions [28]. The ability to write polymer chain-orientation patterns offers the possibility to fabricate novel photonic structures, meta-surfaces and optical circuits.

References

[1] V. G. Chigrinov, V. M. Kozenkov, H. S. Kwok, *Photoalignment of Liquid Crystalline Materials: Physics and Applications*, John Wiley & Sons, West Sussex, England, 2008.

[2] V. Chigrinov, H. S. Kwok, H. Takada, H. Takatsu, Photo-aligning by azo-dyes: Physics and applications, *Liquid Crystals Today* **14**, 1 (2005).

[3] M. Pawlicki, H. A. Collins, R. G. Denning, H. L. Anderson, Two-photon absorption and the design of two-photon dyes, *Angew. Chem. Int. Ed.* **48**, 3244 (2009).

[4] V. G. Chigrinov, H.-S. Kwok, H. Hasebe, H. Takatsu, H Takada, Liquid-crystal photoaligning by azo dyes, *Journal of the SID* **16**, 900 (2008).

[5] J. R. Harwell, T. K. Baikie, I. D. Baikie, J. L. Payne, C. Ni, J. T. S. Irvine, G. A. Turnbull, I. D. W. Samuel, Probing the energy levels of perovskite solar cells via Kelvin probe and UV ambient pressure photoemission spectroscopy, *Phys. Chem. Chem. Phys.* **18**, 19738 (2016).

[6] J. A. Hutchison, A. Liscio, T. Schwartz, A.e Canaguier-Durand, C.Genet, V. Palermo, P. Samorì, T. W. Ebbesen, Tuning the work-function via strong coupling, *Adv. Mater.* **25**, 2481 (2013).

[7] Available at: https://www.thorlabs.com/newgrouppage9.cfm?objectgroup_id=5510.

[8] D. D. Huang, E. P. Pozhidaev, V. G. Chigrinov, H. L. Cheung, H. S. Kwok, Optimization of photo-aligned ferroelectric liquid-crystal display under passively addressed driving, *Journal of the SID* **12**, 455 (2004).

[9] https://en.wikipedia.org/wiki/1951_USAF_resolution_test_chart.

[10] H. Zhang, L. Ma, Q. Zhang, Y. Shi, Y. Fang, R. Xia, W. Hu, D. D. C. Bradley, Azobenzene sulphonic dye photoalignment as a means to fabricate liquid crystalline conjugated polymer chain-orientation-based optical structures. *Adv. Optical Mater.* **8**, 1901958 (2020).

[11] M. Grell, D. D. C. Bradley, Polarized luminescence from oriented molecular materials, *Adv. Mater.* **11**, 895, (1999).

[12] A. M. Donald, A. H. Windle, *Liquid Crystalline Polymers*, Cambridge University Press, Cambridge, 1992.

[13] D.D. Huang, E.P. Pozhidaev, V.G. Chigrinov, Y.L. Ho, H.S. Kwok, Effect of aligning layer thickness on photo-aligned ferroelectric liquid crystal displays, *Proceedings of the Sixth Chinese Optoelectronics Symposium (IEEE Cat. No.03EX701)*, 231 (2003).

[14] Y. Li, J. B. Lagowski, A multi-step simulation of electron mobility in fluorine-benzothiadiazole conjugated polymer - Case study. *Comput. Theor. Chem.* **977**, 157 (2011).

[15] H. M. Liem, P. Etchegoin, K.S. Whitehead, D. D. C. Bradley, Raman anisotropy measurements: An effective probe of molecular orientation in conjugated polymer thin films. *Adv. Funct. Mater.* **13**, 66 (2003).

[16] R. Xia, C. Cheung, A. Ruseckas, D. Amarasinghe, I. D. W. Samuel, D. D. C. Bradley, Wavelength conversion from silica to polymer optical fibre communication wavelengths via ultrafast optical gain switching in a distributed feedback polymer laser, *Adv. Mater.* **19**, 4054 (2007).

[17] C. I. Wilkinson, D. G. Lidzey, L. C. Palilis, R. B. Fletcher, S. J. Martin, X. Wang, D. D. C. Bradley, Enhanced performance of pulse driven small area polyfluorene light emitting diodes, *Appl. Phys. Lett.* **79**, 171 (2001).

[18] T. Virgili, D. G. Lidzey, M. Grell, D. D. C. Bradley, S. Stagira, M. Zavelani-Rossi, S. De Silvestri, Influence of the orientation of liquid crystalline poly (9, 9-dioctylfluorene) on its lasing properties in a planar microcavity, *Appl. Phys. Lett.* **80**, 4088 (2002).

[19] R. Xia, M. Campoy-Quiles, G. Heliotis, P. Stavrinou, K. S. Whitehead, D. D.C.Bradley , Significant improvements in the optical gain properties of oriented liquid crystalline conjugated polymer films, *Synth. Met.* **15**, 274 (2005).

[20] Z. Zheng, K.-H. Yim, M. S. M. Saifullah, M. E. Welland, R. H. Friend, J.-S. Kim, W. T. S. Huck, Uniaxial alignment of liquid-crystalline conjugated polymers by nanoconfinement, *Nano Lett.* **7**, 4, 987 (2007).

[21] S. Pagliara, A. Camposeo, E. Mele, L. Persano, R. Cingolani, D. Pisignano, Enhancement of light polarization from electro spun polymer fibers by room temperature nanoimprint lithography, *Nanotechnology* **21**, 215304 (2010).

[22] N. Lee, D. Diddens, H. Meyer, A. Johner, Local chain segregation and entanglements in a confined polymer melt. *Phys. Rev. Lett.* **118**, 067802 (2017).

[23] A. Milchev, K. Binder, Linear dimensions of adsorbed semiflexible polymers: What can be learned about their persistence length? *Phys. Rev. Lett.* **123**, 128003 (2019).

[24] Q. Zhang, Q. Wei, X. Guo, G. Hai, H. Sun, J. Li, R. Xia, Y. Qian, S. Casado, J. R. Castro-Smirnov, J. Cabanillas-Gonzalez, Concurrent optical gain optimization and electrical tuning in novel oligomer: polymer blends with yellow - green laser emission, *Adv. Sci.* **5**, 1801455 (2018).

[25] Q. Zhang, J. Liu, Q. Wei, X. Guo, Y. Xu, R. Xia, L. Xie, Y. Qian, C. Sun, L. Lüer, J. Cabanillas-Gonzalez, D. D. C. Bradley, W. Huang, Lasing: host exciton confinement for enhanced Förster-transfer-blend gain media yielding highly efficient yellow - green lasers, *Adv. Funct. Mater.* **28**, 1705824 (2018).

[26] R. Xia, P. N. Stavrinou, D. D. C. Bradley, Y. Kim, Efficient optical gain media comprising binary blends of poly(3-hexylthiophene) and poly(9,9-dioctylfluorene-co-benzothiadiazole), *J. Appl. Phys.* **111**, 123107 (2012).

[27] Y. Xu, G. Hai, H. Xu, H. Zhang, Z. Zuo, Q. Zhang *et al.*, Efficient optical gain from near-infrared polymer lasers based on Poly[N-9′-heptadecanyl-2,7-carbazole-alt-5,5-(4′,7′-di-2-thienyl-2′,1′,3′-benzothiadiazole)], *Adv. Opt. Mater.* **6**, 1800263 (2018).

[28] E. A. Shteyner, A. K. Srivastava, V. G. Chigrinov, H.-S. Kwok, A. D. Afanasyev, Submicron-scale liquid crystal photo-alignment, *Soft Matter* **9**, 5160 (2013).

Chapter 4

Fine-tuning the Emission Characteristics of LCCPs using Photoalignment Layers

This Chapter was prepared mainly based on the first journal paper in the publication list, but with more analyses and discussions. The use of liquid crystalline (LC) alignment is reported in the present Chapter as a mechanism to fine-tune the molecular packing structures and photophysical properties in light-emitting liquid crystalline conjugated polymers (LCCPs). We show that the intrinsic long-range structural ordering in the LC mesophase is effective for biomimetic energy transfer optimisation and photoluminescence quantum efficiency (PLQE) enhancement, via the formation of a self-doped host-guest system in the quenched LCCP polydomain films of highly fluorescent poly(9,9-dioctylfluorene-co-benzothiadiazole) (F8BT). The long-range LC orientational ordering in the nematic mesophase of F8BT is revealed to stabilise a small fraction (~5%) of highly oriented polymeric nanocrystals that act as the low-energy guest inclusions dispersed in a disordered amorphous-phase host and dictate the light emission behaviours of the nematic polydomain glass film through nonradiative host-to-guest Förster resonance energy transfer (FRET). Such LC-phase self-organised bi-phase texture gives rise to a new band-edge absorption state and the highest PLQE up to >70% among all types of the measured F8BT films. Based on our systematic PLQE, polarised micro-PL spectral and PL lifetime measurements, we then elucidate that such high PLQE values reach the PLQE limit of F8BT solutions and can be ascribed to a synergic effect of the occurrence of nearly coherent, non-radiative spatial FRET energy funnelling and associated domination of radiative intrachain

recombination that most favourably takes place in the highly oriented fluorophoric polymeric nanocrystals. In this respect, domain boundary regions, in which a slightly higher fraction of chromophoric amorphous F8BT is generally incorporated, are identified to be more favourable than the domain interiors for PLQE enhancement.

In addition, a combination of high-temperate stable UV-illuminated photoalignment layer and LC long-range structural ordering has been utilised to induce large-area extended F8BT nematic monodomain films with a ≈100% order parameter. Compared with the spin-coated amorphous F8BT films in the as-prepared state, these photoaligned monodomains were found to have a rather condense interchain packing structure and significant enhancement in both intrachain and interchain conjugation lengths based on the grazing-incidence wide-angle X-ray scattering (GIWAXS) patterns. These structural ordering features give rise to >70% overall crystallinity and polarisation-dependent PL spectral separation of two orthogonal excited emissive states. The micro-PL spectral lineshape of the parallel-polarised PL spectra recorded from the photoaligned F8BT region appears similar to that from the nonaligned polydomain background in the same quenched F8BT glass film, which is consistent with the purported dominant PL contribution of the highly oriented polymer nanocrystals to the PL emission from the nonaligned F8BT nematic polydomain glass film.

4.1 Biomimetic Tailoring of Physical Structures in LCCPs

4.1.1 Templated Microstructures and Coherent Energy Transfer in Natural LHCs

Nature is a constant source of inspiration for molecular and morphological optimisation. Green plants as well as some bacteria make efficient use of physical tuning of protein-templated pigment chromophores that form a light-harvesting complex (LHC) to undergo highly efficient photosynthesis [1]. As such, the absorbed excitation energy is spatially and efficiently funnelled within and between LHCs to ultimately reach an energetically expensive reaction centre (c.f.

Figure 4.1) for charge separation and photochemical transformation [2,3]. Consecutive FRET events between these chemically similar yet differently-sized LHCs are highly desirable in terms of funnelling the excitation energy in a nearly quantum coherent manner from minor chromophoric light-harvesting complexes (LH2) to a structurally identical but larger acceptor complex (LH1) [4,5]. The elegant molecular packing structures with precisely positioned/stacked pigment molecules have evolved naturally to be the multichromophoric LH1 and LH2 complexes in the ubiquitous photosynthetic system [1-5] and these serve as a useful guide for the design and construction of synthetic light-harvesting antennas and energy-conversion structures through fine-tuning of the physical size, spatial energy landscape and molecular arrangement. An optimal number of minor amorphous phase chromophores peripheralize and electronically couple with a highly ordered larger acceptor. In this way, the randomly-oriented peripheral chromophores help to increase the photon absorption for all light polarisation states [6], while the appropriate energy landscape and electronic coupling strength between the chromophores and the acceptor core can give rise to efficient excitation energy transfer via three-dimensional coherent FRET [7,8].

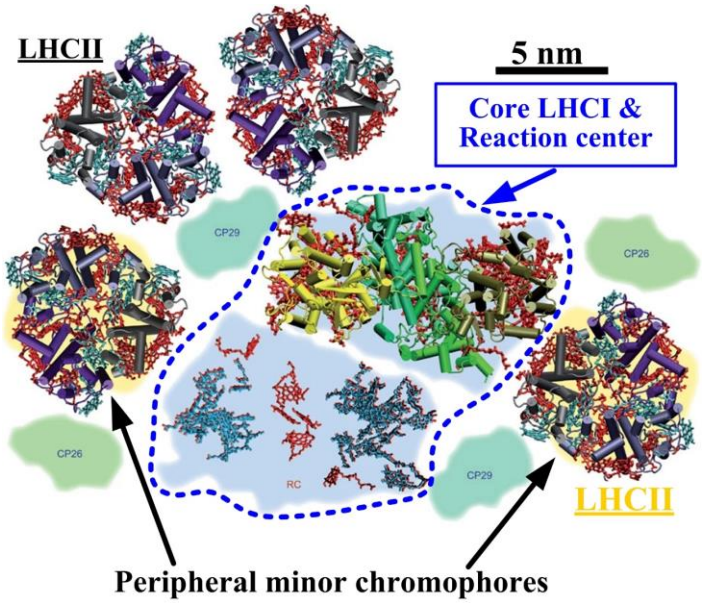

Figure 4.1: Illustration of the protein-templated structural organisation of photosynthetic LHCs and reaction centres in plants and green algae. The figure has been adapted from Ref. 1 but with further edits.

4.1.2 Fine Tuning of Physical Structures in Multichromophoric LCCPs

Organic semiconductors are inherently disordered, particularly π-conjugated polymers. Significant structural disorders are present in solution-processed conjugated polymers due to the spatially varying chain conformations, intermolecular torsions along the polymeric backbone, chain-entanglements, domain/grain boundaries, and other types of structural defects [9]. These features can exacerbate the difficulties associated with fine-tuning of the chemical and physical structures in technologically important but structurally disordered polymeric semiconductors. With respect to the engineering of chemical structure, the concept of nonradiative FRET and biomimetic excitation energy funnelling have been applied by careful matching of the energy levels in donor-acceptor systems to technologies such as organic LEDs, solar cells, polymer lasers, and thin-film transistors [10-15].

In contrast to the adoption of chemically similar LHCs in natural light-harvesting antennas, the use of chemically distinct species in a wide range of organic semiconductor devices has often resulted in significant energetic losses and photo-degradation, due to the intrinsic energy-gap mismatch as well as the presence of donor/acceptor interface and morphology mixing [16-19]. As a result, undoubtedly there is plenty of room for improvement in the performance and efficiency of these functional devices, which may be achieved by making best use of fine-tuning of the physical structures of the same active chemical species.

High-quality spatial definition of the physical structures such as the chain conformation, interchain packing, aggregation state, and domain pattern should be explored for fine-tuning of the physical structures in conjugated polymers [20-25]. Fluorescent conjugated polymers can be considered as a multi-chromophoric system with a spatially repeated chemical structure and tunable physical structure, since the extended intrachain conjugation is usually interrupted incoherently or broken up along a highly twisted and bended backbone [6,26]. In turn, this

allows each planar chain segment to act as a separate chromophoric or fluorophoric unit depending on its electronic state. The conjugated polymers are then able to resemble a 'self-doped' guest-host system and mimic the spatial optimisation of the number ratio between the active minor chromophoric LHCs and the larger fluorophoric LHCs. In this respect, fine-tuning of the polymer chain conformation and interchain packing can help to facilitate the spatial and energetic optimisation of the competitive chromophoric and fluorophoric species by using only one chemical species [6].

4.1.3 Liquid-Crystalline Alignment and Self-Doped Polymeric Nanocrystals

Molecular self-organisation by virtue of the intrinsic long-range orientational order present in the nematic LC phase of fluorescent LCCPs [27,28], such as the light-emitting polyfluorene F8BT, renders the possibility of better mimicking the fascinating light-harvesting properties of natural photosynthetic LHCs. In this respect, highly efficient F8BT films with close interchain packing and tunable electronic coupling strength were targeted by making use of the long range order present in the nematic LC phase. A unique, highly efficient self-doped host-guest system can be created from LC self-organisation, which, as shown in this Chapter, leads to a substantial PLQE enhancement through promoting the highly efficient non-radiative FRET and optimising the relative weighting of fluorophoric polymeric nanocrystals in the F8BT films.

High-quality photoalignment of the polymeric chain-orientation, in terms of order parameter $S \approx 0.98$, high PL intensity anisotropies [27], and engineering of the nematic domain size were also employed to showcase the benefits of tailoring the relative fraction of the disordered amorphous-phase chromophoric host. Besides, spatially patterned, highly oriented F8BT nematic monodomain films were fabricated to directly compare the photophysical properties of well-aligned F8BT vs nonaligned nematic glass background in the sample film. This Chapter therefore presents an investigation of the molecular structure-property

relationships in light-emitting conjugated polymer semiconductors with distinct microstructural packing structures, electronic coupling characteristics and energy transfer mechanism.

4.2 Fabrication Methods

The photoalignment layer material, SD1, was provided by DIC Corporation Japan and used as received. The F8BT polymer with molecular weight, M_w = 55,000 and polydispersity index, PDI = 2.3 was purchased from ONE-Material Inc. The photoalignment layers were spin-coated from SD1 solutions in anhydrous 2-methoxyethanol (≥ 99.8%) onto pre-cleaned Spectrosil substrate at 500 rpm for 5 seconds and then 2000 rpm for 20 seconds using SD1 solution concentrations of 0.5 mg/mL and 0.1 mg/mL for the fabrication of *continuous* and *discontinuous* SD1 layers, respectively. These discontinuous SD1 films were adopted to induce partial domain alignment in the overlying F8BT films in the nematic phase while the continuous SD1 layers were employed to fully align the overlying F8BT nematic films. After spin-coating, the SD1 photoalignment layers were annealed at 110 °C for 10 minutes in ambient conditions to ensure solvent removal, which was followed by molecular alignment performed via irradiating the samples in air with 5 mW/cm^2 linearly polarised 365 nm light from a Thorlabs CS2010 UV-curing LED system equipped with a WP25M-UB broadband wire-grid polariser. The polarised UV illumination results in the long molecular axis of the SD1 molecules being oriented in the plane of the substrate along a direction that is orthogonal to the polarisation of the LED light source [27-29]. The duration of the polarised UV irradiation for aligning both the continuous and discontinuous SD1 layers was varied over a range of 3 - 20 mins so as to produce varying levels of structural order in the SD1 layers which were then utilised to produce various dichroic ratios in the overlying F8BT nematic films.

F8BT was then spin-coated onto the UV-aligned continuous or discontinuous SD1 layers using the same filtered 30 mg/ml solution in anhydrous toluene. The thickness of the F8BT

films was tuned over a range of 40 nm - 480 nm by systematically varying the spin-coating speed and duration. The F8BT films were vacuum-dried for >1 hour to remove excess solvent and then subjected to thermotropic LC alignment and chain-orientation: the polymer chains in an F8BT film or SD1/F8BT bilayer were heated into a melt (~268 ^{o}C), followed by slowly cooling (at a rate of 3 ^{o}C/min) the sample to a temperature (e.g., 250 ^{o}C) that sits in the middle of the nematic temperature range of F8BT and maintaining this temperature for 10 minutes. The polymer chain-orientation process was completed by rapidly quenching the sample to room temperature to finally form a nematic glass film. This quenching step prevents crystallisation and thereby locks-in the LC director configuration that is formed in the nematic mesophase: *i*) a polydomain LC texture for a single layer of F8BT that is directly coated onto a substrate with no alignment layer (termed as *nonaligned* (NA) F8BT nematic glass film; labelled as *Film I*); and *ii*) a highly-oriented monodomain for the F8BT film coated on a UV-aligned SD1 photoalignment layer (termed as *fully aligned* (FA) F8BT nematic films; labelled as *Film II*).

The fabrication of these nematic monodomain F8BT films is mediated by the long-range orientational ordering in the nematic phase via molecular interaction between the UV-aligned continuous SD1 layer and the F8BT polymer chains at the commanding interface, which is then communicated through the bulk by chain-chain interactions and π-π stacking [27]. In addition, *partially-aligned* (PA) F8BT nematic films (labelled as *Film III*) were prepared by heating and quenching an overlying F8BT film coated on a UV-aligned *discontinuous* SD1 layer that resulted from spin-coating on a quartz substrate using a low concentration of SD1 solution. Finally, *spin-coated-only* (SC) F8BT films on quartz substrates without any treatment through the LC mesophase were used as non-LC (amorphous) reference and control samples (denoted as *Film 0*) for the subsequent microstructural and photophysical measurements. **Figure 4.2** provides an illustration of the configuration for the four different F8BT films.

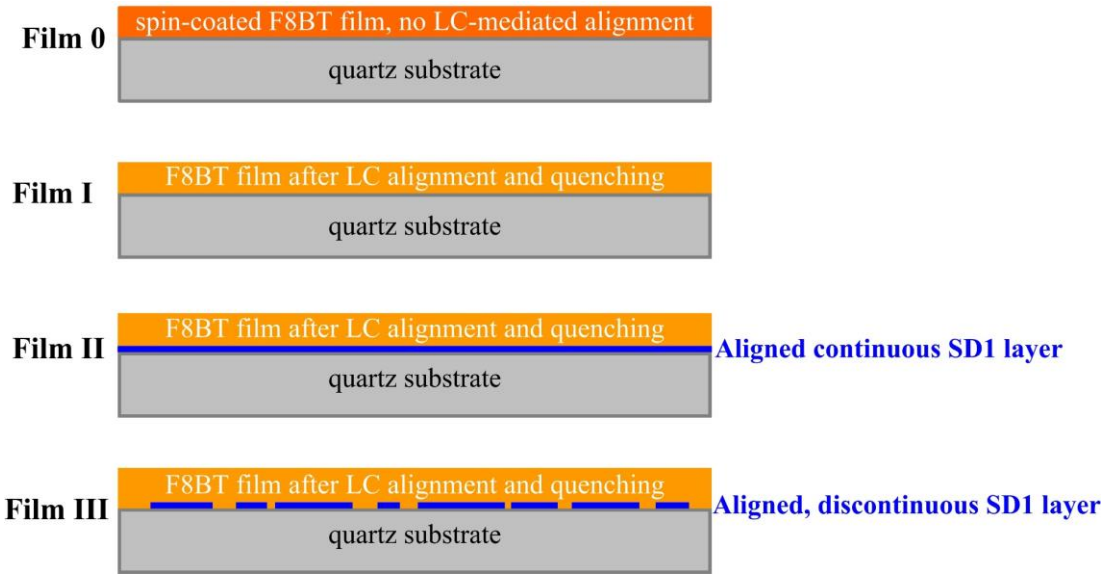

Figure 4.2: Illustration of the layer structure of the four different F8BT films.

4.3 GIWAXS Results and F8BT Packing Structures

4.3.1 2D GIWAXS Images and Crystallised/Amorphous Phase F8BT

To characterise the microstructure and interchain packing in the F8BT films created from the different fabrication processes, grazing-incidence wide-angle X-ray scattering (GIWAXS) measurements of the three types of F8BT films - the spin-coated non-LC F8BT film (*Film 0*) as well as the non-aligned (*Film I*) and fully-aligned (*Film II*) F8BT nematic films - were carried out using the Surface and Interface Diffraction beamline (I07) at the Diamond Light Source (DLS) with a beam energy of 20 keV (0.62 Å) and a Pilatus2M area detector. The samples were probed while inside a vacuum chamber at a pressure of around 10^{-3} mbar. The sample-to-detector distance was 41.8 cm as determined via AgBeh calibration. The images were converted to 2D reciprocal space using the DAWN software package. The raw GIWAXS data was plotted in **Figure 4.3** as 2D diffraction intensity images, while the 2D GIWAXS images in **Figure 4.4** was obtained after subtracting the GIWAXS images from the spin-coated reference sample (*Film 0*) as the background in order to uncover the effect of self-organisation in the nematic LC phase and chain-orientation over long-range (small *q*) orientational ordering. The

corresponding 2D GIWAXS patterns for both the nonaligned and fully-aligned F8BT nematic films are shown in Figure 4.4 (a)-(c).

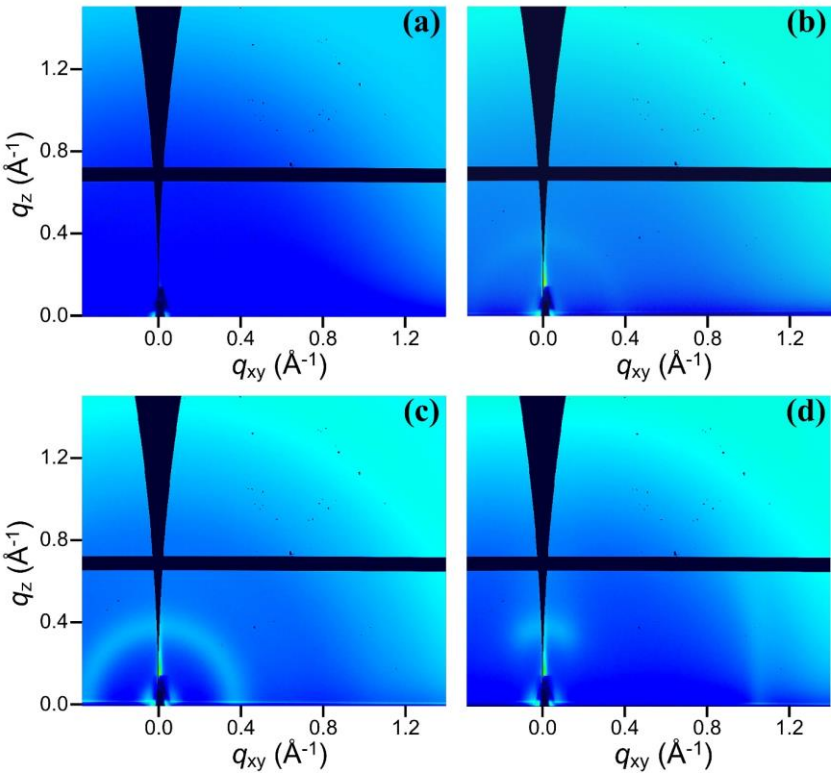

Figure 4.3: Raw GIWAXS data (i.e., before background and baseline subtraction) recorded from (a) a spin-coated-only non-LC F8BT film (*Film 0*), (b) a non-aligned F8BT nematic glass film (*Film I*), as well as (c) - (d) from a fully-aligned F8BT nematic film (*Film II*) when the propagation of the incident X-ray beam is either aligned parallel (c) or perpendicular (d) to the chain alignment direction in the F8BT film on a UV-illuminated SD1 photoalignment layer. All F8BT films measured herein were ~160 nm in thickness. These GIWAXS measurements were carried out and the raw data was converted to images with the help of Prof. Moritz Riede's group in the Department of Physics at the University of Oxford.

The GIWAXS data clearly shows that the F8BT films processed in different ways exhibit different polymer crystallinity levels, molecular packing, and structural anisotropy. For example, for the spin-coated non-LC reference film (*Film 0*) there is no clear evidence of long-range ordering, evidenced by the absence of a characteristic diffraction peak in Figure 4.3(a). The non-aligned F8BT nematic glass film (*Film I*), on the other hand, exhibits a faint smearing of the diffraction ring (see Figure 4.4(a) and also the insert in Fig. 5.4(d)) as a result of a random

distribution of the chain-orientation in a small proportion of highly localised crystalline regions, hence indicating the existence of well ordered "polymeric nanocrystal" inclusions in a disordered amorphous-phase matrix [30]. It is likely that these polymeric nanocrystals are similar to the previously observed crystalline "nano-platelets" or "aperiodic crystals" in other main-chain LCCPs, which have been proposed to stem from localised molecular sequence-matching of adjacent backbones within a LC mesophase [30].

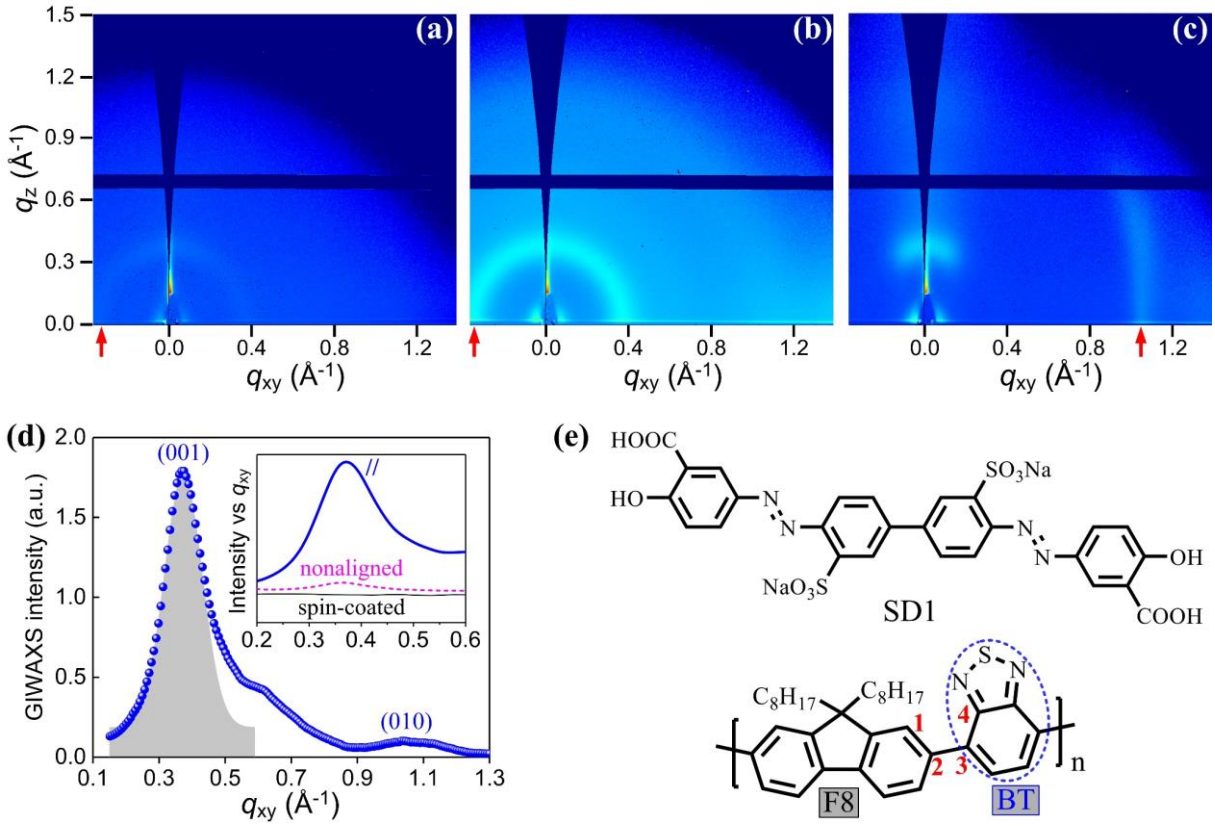

Figure 4.4: (a - c) 2D GIWAXS images of (a) a nonaligned F8BT nematic glass film (*Film I*), and (b - c) a fully-aligned F8BT nematic film (*Film II*) when the incident X-ray beam propagated in the aligned film along a direction parallel (b) or perpendicular (c) to the chain alignment direction. The vertical red arrows on the bottom of (a) - (c) mark the q_{xy} position of the characteristic scattering peaks. (d) In-plane linecut GIWAXS profile (blue dot) for *Film II* recorded from the parallel (//) configuration after subtracting a second order baseline; the inset shows the raw scattering intensity (offset for clarity) of the spin-coated non-LC F8BT film (*Film 0*) as well as the fully-aligned (// configuration) and nonaligned F8BT nematic films. (e) Chemical structures of SD1 and F8BT. The blue dashed ellipse encloses the BT unit and the four carbons labelled by the red numbers resemble a dihedral angle (i.e., intermolecular torsion angle) that links the F8 and BT units via a single C-C bond around which the F8 and BT units have a certain degree of freedom to rotate relative to each other.

The spontaneous LC self-organisation process that occurs in *Film I* involves stabilizing and expanding the highly-ordered, lower-energy polymeric nanocrystal nuclei within a mixture of amorphous-phase nematic F8BT chains that still have a polydispersity-defined variation of the main-chain length. These highly localised crystallization events of the polymeric nanocrystals initialize through LC self-organisation and chain-extension associated with the planar chain-sections on the longest straight sections in the backbone. The process then continues to selectively incorporate the next longest/extended chains in the mesophase into the already crystallized cores [30]. For the fully-aligned F8BT nematic films (*Film II*), it is possible that the same LC-alignment process proceeds in the nematic mesophase via further expansion and aggregation of the crystallised polymeric nanocrystals until all the accessible F8BT chains with spatially varying chain lengths are incorporated and then oriented along the SD1-alignment direction before quenching.

Noticeably higher diffraction signals and distinct GIWAXS patterns were collected from the fully-aligned F8BT nematic film, which implies a substantially enhanced crystallinity and structural anisotropy. The results show a rather strong diffraction ring for the parallel incident configuration but two different diffraction arcs for the perpendicular configuration, namely, a short, less-smeared (100) arc and a sharper (010) arc at q_{xy} = 1.055 Å^{-1}. The former arc indicates that the F8BT backbones are highly oriented and the relative rotation between the F8 and BT units is effectively restricted by largely aligning both units parallel to the substrate plane. The other (010) diffraction arc corresponds to an interchain repeat distance of 6.0 Å. Considering the length of the long alkyl side chains, this is a very small interchain periodicity and infers a prevalence of BT to BT close or direct contact between adjacent F8BT chains, together with the ensuing enhancement in interchain electronic coupling strength. The nearly identical q_z value of the three (100) characteristic diffraction peaks observed for both the nonaligned and fully-aligned F8BT nematic films implies a common lamellar stacking and a repeat distance of

≈16 Å along the out-of-plane direction, which is thought to be either four times the value of the characteristic π-stacking spacing of 4.2 Å at $q \approx 1.5$ [31] or the average projected length of the reoriented alkyl side-chains in the film thickness direction according to our calculation results.

Our time-dependent density-functional theory (TD-DFT) calculations predicted that there are two equally favourable chain conformations, namely, alternatingly kinked or concavely bent backbone segments, which have nearly the same minimum energy and also vertically orientated alkyl side-chains as well (see **Figure 4.5** for the two most probable chain confirmations of F8BT). During the DFT calculations, it was assumed that F8BT adopts a planar conformation (i.e., corresponding to the effect of the SD1-alignment and the mesophase-induced long-range ordering that restricts the dihedral angle of F8BT to be $\Phi = 0^o$ or 180^o). This prediction of the vertical ordering of the insulating long alkyl side-chains along the film thickness direction tends to minimise out-of-plane excitonic migration and to facilitate the formation of a condensed interchain packing structure and even direct BT-to-BT contacts between adjacent F8BT chains in the film plane. Concomitantly, such a prediction of the co-existence of kinked and concavely bent F8BT backbones in the fully-aligned nematic film can be used to explain the observation of the diffraction ring in Figure 4.4(b) and the two short but extended arcs in Figure 4.4(c).

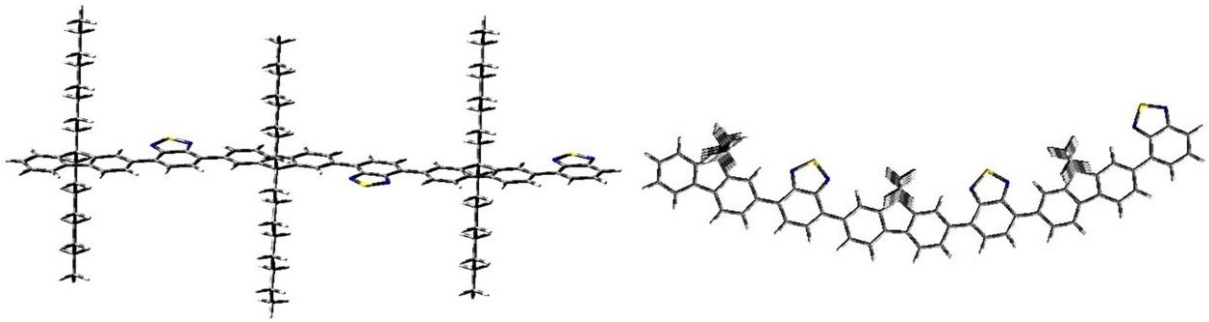

Figure 4.5: Schematic of an alternatingly kinked (left, side view) and bent (right, top view) backbone of a planar F8BT trimer, alongside well-aligned side chains along the vertical direction. Based on time-dependent DFT calculations, the as-shown two structural organisations were the most probable and energetically favourable chain-conformations when the dihedral angle of F8BT is relatively small (assuming a planar conformation: $\Phi = 0^o$ or 180^o) because the F8BT chains are subjected to the strong alignment imposed by the combination of the SD1 photoalignment layer and the LC nematic phase.

4.3.2 *d*-Spacing Distances, Coherence Lengths and Crystallinity Levels

The q values of the characteristic diffraction peaks, the corresponding d-spacing distances (determined based on $d = 2\pi / q$) as well as the coherence lengths were extracted from the GIWAXS data and are listed in **Table 4.1**. **Figure 4.6** presents the normalized diffraction peak profiles in both the nonaligned F8BT nematic film (*Film I*) and the fully-aligned F8BT nematic film (*Film II*). These diffraction data suggests that the self-organised polymeric nanocrystals embedded in the nonaligned F8BT nematic film were locked in a more extended planar chain-confirmation with a longer (by 3%; a smaller q_{xy} value of the diffraction peak) repeat distance along the backbone direction and larger (i.e., a narrower diffraction peak profile) but isotropic coherence lengths (141.7 - 149.6 Å).

The highly oriented F8BT chains in the fully-aligned F8BT nematic film work collectively to exhibit highly anisotropic coherence lengths of 120.8 Å, 205.1 Å, and 101.0 Å along the chain alignment, interchain, and film thickness directions, respectively. This substantial increase in the interchain coherence length in the fully aligned nematic film (*Film II*) tallies with its very small (6.0 Å) interchain d-spacing extracted from the sharper (010) diffraction peak.

The degree of crystallinity, i.e., the areal ratio of the (001) and (010) peaks to the total diffraction intensity, was calculated to be 73% for the fully-aligned F8BT nematic film when taking the shaded region under the Gaussian peak fitting curve in Figure 4.4(d) as the effective area of the (001) diffraction peak. In addition, the volume fraction of the polymeric nanocrystals in the nonaligned nematic film was estimated to be ~5 % based on the faint (100) ring, yielding the number ratio between the minor amorphous-phase chromophores and the well-aligned fluorophoric polymeric nanocrystals to be ~20.

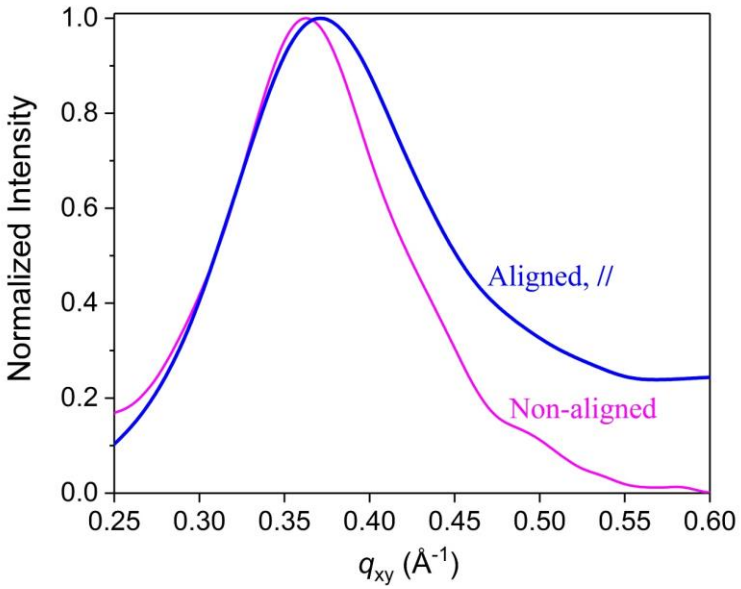

Figure 4.6: Plot of the normalized intensity profile of the first diffraction peak vs q_{xy} for the nonaligned F8BT nematic film (*Film I*) and the fully-aligned F8BT nematic film (*Film II*) measured using a parallel (//) configuration.

Table 4.1. The extracted *d*-spacing distances and coherence lengths from the 2D GIWAXS images recorded from the nonaligned and fully-aligned F8BT nematic films.

F8BT Sample	Direction	Peak	q (Å^{-1})	d-spacing (Å)	Coherence length (Å)
Nonaligned	In-plane	(100)	0.365	17.3	141.7
Aligned, //	In-plane	(001)	0.374	16.8	120 .8
Aligned, ⊥	In-plane	(010)	1.055	6.0	205.1
Nonaligned	Out-of-plane	(100)	0.394	15.9	149.6
Aligned, //	Out-of-plane	(100)	0.385	16.3	98.4
Aligned, ⊥	Out-of-plane	(100)	0.387	16.2	103.5

4.3.3 Proposed Distinct Packing Structurers in the Four F8BT Films

On the basis of the GIWAXS results presented above, an F8BT packing structure model has been proposed and is illustrated in **Figure 4.7** to explain the distinct scattering patterns and the different photophysical properties recorded from the three types of F8BT films. For the spin-coated non-LC F8BT films (*Film 0*), the BT units exhibit a relatively random distribution, but high degrees of intermolecular torsion with respect to the F8 units along the backbone direction

(the *a*-axis), as inherited from the significant structural disorder in the F8BT solution. The backbones are adjacent to each other in neighboring polymer chains in order to minimise steric hindrance. This molecular packing structure elucidates a prevalence of the highly disordered amorphous phase in these spin-coated non-LC reference films, as evidenced by the absence of a characteristic scattering ring in its GIWAXS image (Figure 4.3(a)).

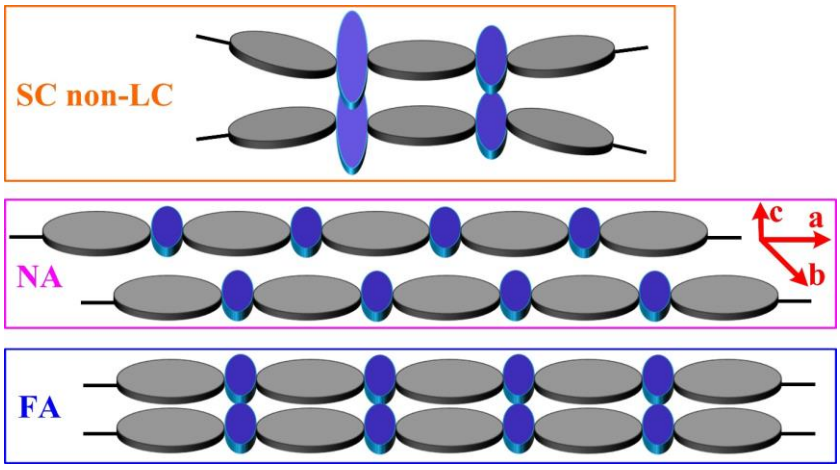

Figure 4.7: Schematic illustrations of the proposed microstructure model for the F8BT interchain packing structures in the spin-coated (SC) non-LC films (*Film 0*), as well as the nonaligned (NA, *Film I*) and fully-aligned (FA, *Film II*) F8BT nematic films. The grey ellipses and blue ellipses denotes the F8 and BT units along an F8BT backbone, respectively. The *a*, *b*, and *c* axes shown in the middle panel are along the backbone, interchain, and out-of-plane direction, respectively. The side-chains and backbone kinks are omitted herein for clarity.

The long-range LC orientational order in the nematic mesophase allows the polymeric nanocrystals, which are self-organised in the nonaligned nematic polydomain glass films, to arrange themselves in a more energetically favorable structure by adopting a more planar/extended chain-conformation and reducing dramatically the torsion angles. In this case, the BT units in one chain prefer to occupy positions adjacent to the F8 units in the neighboring chain ("alternating structure"), driven by the repulsive force between inter-chain BT dipoles [31-34]. Similarly, the fully-aligned F8BT nematic films (*Film II*) would still adopt an extended rigid chain-confirmation, but their highly oriented chains have translated relative to each other by ~half a repeat unit along the backbone direction, which could induce significantly more BT-

to-BT close or direct contact between adjacent chains, alongside a strong interchain electronic coupling and very limited out-of-plane energy transfer. The occurrence of such interchain translations in the nematic phase can be facilitated by the strong alignment imposed by the UV-illuminated SD1 layer and the interfacial molecular interaction between the UV-aligned SD1 molecules and the F8BT polymer chains.

4.4 LC Optical Textures and Orientational Ordering

4.4.1 Polarising Optical Micrographs and Polarised Confocal Fluorescence Images

Polarised optical micrographs (POMs) were recorded when the F8BT films were placed between a crossed polariser and analyser pair. The films show a dark (bright) state in the POM birefringence pattern in **Figure 4.8**(a) when the direction of the chain orientation (which defines the optic axis) is parallel (at 45^{o}) to the transmission axis of either the polariser or the analyser.

A Schlieren LC texture (*i* and *ii* in Figure 4.8(a)) is observed for the nonaligned F8BT nematic films. F8BT backbones in each locally self-organised nematic micro-domain were well oriented due to the long-range orientational order in the nematic mesophase, as identified by the highly polarised fluorescence from the polydomains (Figure 4.8(b)), although the overall chain orientations among the nematic micro-domains are randomly distributed as seen in the varying fluorescence intensity in Figure 4.8(b). High-quality chain alignment in the larger-area extended nematic monodomains is illustrated in the bright-state and dark-state POMs of the fully-aligned F8BT nematic film (*Film II*) (*v* and *vi* in Figure 4.8(a)). Partial (or full) alignment of the nematic domains in the F8BT films is found to take place with an increasing (or complete) elimination of the polydomain boundaries, which initially form during the heat treatment when cooling from the high-temperature isotropic F8BT melt into the nematic phase before the films are quenched.

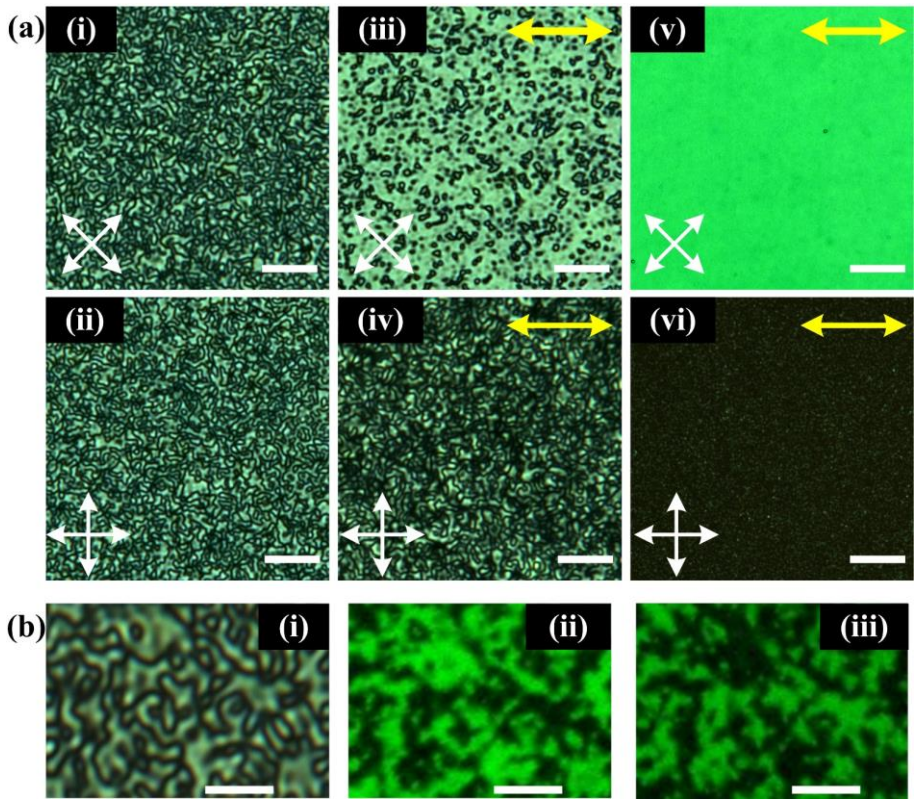

Figure 4.8: (a) Polarising optical micrographs (POMs) demonstrating a polydomain LC texture (*i* - *iv*) in both the nonaligned (*Film I*) (*i* , *ii*) and partially-aligned (*Film III*) (*iii*, *iv*) nematic films and a monodomain LC texture in the fully-aligned nematic film (*Film II*) (*v*, *vi*), viewed between crossed polarisers (labelled by the two crossed white double-headed arrows). The uniaxial chain-orientation direction is indicated by the double-headed yellow arrows in (*iii*) - (*vi*); scale bars: 20 µm. **(b)** POM images at a higher magnification showing (*i*) a typical Schlieren texture in the nonaligned nematic glass film, and the corresponding polarised confocal fluorescence images (*ii*, *iii*) recorded when the emission was photoexcited with randomly polarised light at 450 nm and collected with the analyser aligned to the two orthogonal (i.e., horizontal and vertical) polarisation directions. Scale bars: 5 µm.

4.4.2 Orientational Ordering of the F8BT Polymer Chains

From inspection of the polydomain LC texture recorded from the partially-aligned F8BT nematic films and the extended monodomains from the fully-aligned nematic films, we speculated that the LC alignment process involved in F8BT chain-orientation might take place by a gradual expansion of the locally crystallised polymeric nanocrystals, at the expense of domain boundaries and then re-orientation of the newly incorporated F8BT chains or domain regions towards a common direction that is defined by the pre-aligned SD1 layer.

The planar chain segments of the higher-molecular-weight backbones (i.e., longer chains with stronger intrachain conjugation and, thus, a lower energy bandgap and a red-shifted absorption peak, as demonstrated in the optical absorption spectra in the next Section) are most probably nucleated at the beginning of the LC self-organisation process as a crystalline core associated with a localised polymeric nanocrystal. The nucleated, highly-oriented core can continue to absorb and assemble the neighboring shorter unaligned polymer chains until the boundary of the well-oriented domains reaches the edge of the substrate regions covered by the UV-illuminated SD1 molecules. In the absence of SD1 photoalignment, such as in the case of the nonaligned F8BT nematic glass films (*Film I*), this proposed LC alignment process could only stabilise a minor fraction of highly ordered, low-energy polymeric nanocrystals consisting of a small portion of higher molecular-weight chains, which are well separated and dispersed in the remaining disordered, high-energy amorphous matrix. This situation can indeed resemble a 'self-doped' host-guest system in the quenched nonaligned F8BT nematic glass films (*Film I*) [26, 27]. Under electrical or optical pumping, the disordered, high-energy amorphous-phase host is believed to act as the chromophoric constituent and the localised low-energy polymeric nanocrystals as the fluorophoric units. As a result, fine-tuning of the relative weight, spatial distribution, and electronic coupling strength of the two components offers an intriguing means to optimise PLQE and imitate the ability of natural light-harvesting antennas to adapt to the change in the sunlight density by adjusting the number ratio of LH1 to LH2 complexes [1,5].

4.4.3 UV-Vis Absorption Spectra

The optical absorption spectra of F8BT is found to be composed of three transition bands as a result of the presence of benzene rings (band 1 labelled in **Figure 4.9**), π-π stacking between benzene rings (band 2), and inter/intra-chain charge transfer (band 3), respectively [31,34]. The absorption spectrum for the nonaligned F8BT nematic films (the thick solid pink curve in Figure

4.9) shows a significant broadening of band 3 toward longer wavelengths. This would indicate the emergence of a new lower-energy absorption species, consistent with the formation of the self-doped polymeric nanocrystals based on our GIWAXS results. The wavelength of the sharp peak of the band 3 associated with this new band-edge absorption state is revealed to blue-shift to 486 nm in the partially aligned F8BT film (*Film III*) from 498 nm in the nonaligned nematic film (*Film I*). This implies the existence of a lower energy, more extended chain conformation formed in the polymeric nanocrystals that are well dispersed in the nonaligned nematic polydomain glass films (*Film I*).

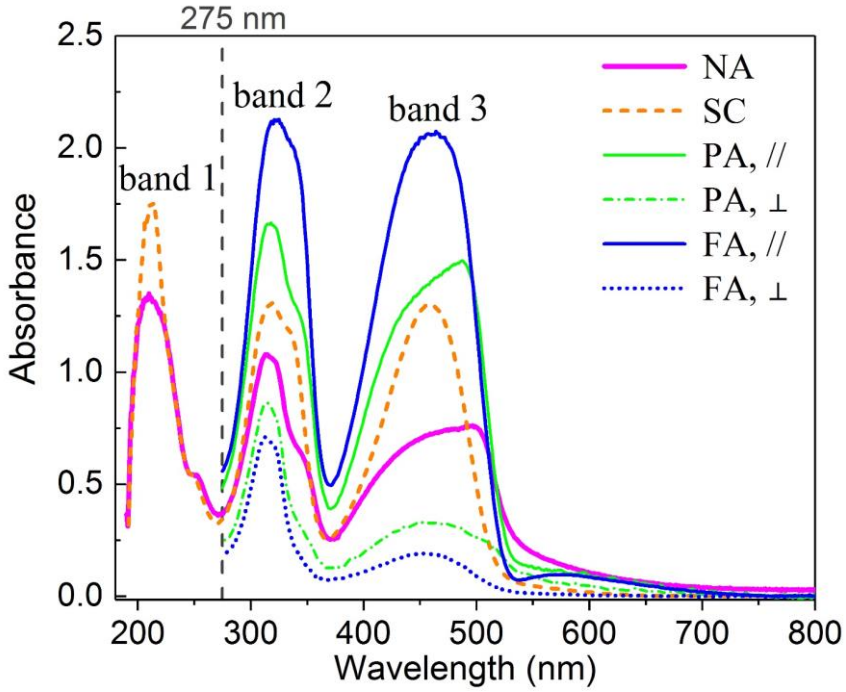

Figure 4.9: UV-vis absorbance spectra of the spin-coated (SC) amorphous F8BT film (*Film 0*) and of the nonaligned (NA, *Film I*), fully-aligned (FA, *Film II*) and partially-aligned (PA, *Film III*) F8BT nematic films. The parallel (//) and perpendicular (⊥) polarised spectra for the PA and FA films were recorded by aligning the excitation polarisation parallel and perpendicular to the chain alignment direction, respectively. All polarised spectra were cut off at 275 nm below which the transmission of the polariser drops rapidly, whereas the non-polarised spectra for both the non-LC film and NA glass film extends to 190 nm (as the wavelength limit of the UV-vis absorption spectroscopy). All measured F8BT films are 160 nm in thickness. It is confirmed that the absorption data presented herein did not saturate the spectrometer.

Compared with the non-LC F8BT film (*Film 0*), in which the majority of the F8BT backbones are confined by the spin-coating to face parallel to the film plane, the peak strength of the absorption band 1 in the nonaligned F8BT nematic glass film (*Film I*) with the same thickness is significantly attenuated due to the tilt of the backbones away from the film plane in the LC mesophase before quenching. This finding agrees with the observation of the smeared (100) diffraction ring in the 2D GIWAXS image of *Film I*, and the randomly distributed chain-orientations among the polymeric nanocrystal inclusions and in the amorphous phase matrix.

The peak wavelength of the longer-wavelength absorption band 3 further reduces to 464 nm in the highly-oriented monodomains in the fully-aligned F8BT nematic films (*Film II*), but this time the absorption strength has been remarkably enhanced in comparison with the spin-coated non-LC films and the nonaligned nematic film with the same thickness. This absorption enhancement tallies with the microstructures identified for the different types of F8BT nematic films (Figure 4.7). The backbones in the fully-aligned F8BT films are largely aligned in the plane of the substrate, whereas the backbones in both the polymeric nanocrystals and disordered amorphous-phase matrix in the nonaligned polydomain nematic films are randomly oriented and hence demonstrate an attenuated oscillation strength when measured along the film thickness direction. Domain boundaries presented in the nematic polydomain films are expected to play a similar role in terms of structural disorder and reduction in the absorption strength. The long-wavelength spectral tail for the nonaligned nematic films potentially results from light scattering arising from non-negligible inhomogeneous interfacial regions between the randomly-oriented, highly-ordered polymeric nanocrystals and the amorphous-phase matrix.

The polarised optical absorption spectra recorded from the fully-aligned F8BT nematic films (*Film II*) highlight the quality of the uniaxial chain-orientation and monodomain LC texture, in terms of the noticeably high optical dichroic ratio (i.e., the absorbance ratio between

parallel ($A_{//}$) and perpendicular ($A_{\perp}$) polarised spectra to the chain alignment direction) of 11.4 at the peak wavelength of the absorption band 3 and, thus, an order parameter of $S \approx 0.98$ [27]. Both the highly oriented backbones and the elimination of clear domain boundaries in the fully-aligned nematic films are crucial to inducing such large values of the dichroic ratio. The uniformity of the fully-aligned F8BT monodomains is also evident from the long-wavelength interference fringes seen in the parallel polarised spectrum.

The absorption peak intensity ratio between the transition band 3 to band 2 is found to increase in the non-LC and fully-aligned F8BT films up to $\approx$1, relative to the nonaligned nematic glass film. The higher the dichroic ratio becomes (i.e., the better the chain-orientation quality is), the greater the enhancement in the peak strength of the charge-transfer transition band. Considering that more BT-to-BT contacts have been proposed in both the non-LC and fully-aligned F8BT films, such an enhancement in the absorption peak strength ratio tends to indicate that the occurrence of charge transfer in the F8BT films indeed involves BT units through intrachain π-conjugation and/or interchain BT-to-BT interaction.

The absorption spectra in Figure 4.9 from the different types of F8BT films are also in accord with their packing structures proposed in Figure 4.7. In all cases, the π-π stacking absorption band 2 consists of two transition constituents centered at 316 nm and 340 nm exhibits distinct vibronic structures. The proposed alternating interchain packing structure for the nonaligned F8BT nematic film (*Film I*) is characteristic of the lowest number of BT-to-BT direct/close contacts, and demonstrates the greater misalignment of F8BT π-π stacking and the lowest relative weight of the 340 nm vibronic sub-band in the whole spectral area of band 2. The highly disordered packing structure in the spin-coated-only non-LC F8BT film (*Film 0*) shows a moderate relative weight of the 340 nm vibronic sub-band, due to the significant BT-to-BT direct contacts between adjacent chains. Among all types of F8BT film that we

investigated, the fully-aligned F8BT nematic film (*Film II*) has been found to have the greatest relative weight of the 340 nm vibronic sub-band in the $A_{//}$ spectrum, alongside the lowest relative weight in the $A_{\perp}$ spectrum. This absorption behaviour is consistent the suppressed torsion angles as well as the improved polymer crystallinity and interchain BT-to-BT contact.

4.4.4 Influence of Chain-Length Distribution and Film Thickness on Alignment Quality

Generally, the length of the LCCP main-chains follows a distribution that is dictated by the molecular weight and polydispersity of the polymer backbones. The F8BT polymer used herein has a molecular weight of M_w = 55,000 and polydispersity index of PDI = 2.3, which means that the F8BT backbone length varies from 79 nm to 182 nm, as calculated based on the extracted repeating distance of 1.73 nm in the highly oriented polymeric nanocrystal inclusions. As discussed in Section 4.4.2, the F8BT chain orienting process in the nematic LC mesophase is most probably triggered by the fractionation of all nonaligned polymeric chains into one portion of longer F8BT chains nucleated as the well-oriented cores of polymeric nanocrystals and the other portion of unaligned, shorter amorphous-phase polymeric chains. When subjected to the alignment imposed by the UV-illuminated SD1 photoalignment layers, a gradual elimination of the domain boundaries and the formation of an extended nematic monodomain would proceed with the re-orientation of newly incorporated amorphous-phase chains. This kind of F8BT fractionation and re-orientation necessitate 3-D diffusion/rotation of the mobile chains throughout the film in the nematic mesophase and should therefore be dependent on the competition between the main-chain length distribution and the real film thickness.

Intuitively, an insufficiently thick F8BT film would impose certain restrictions on the lateral/vertical diffusion and rotation of the polymeric chains in the nematic phase, which further limits the elimination of domain boundaries and ultimate formation of an extended monodomain alignment. This leads to a retention of the unaligned regions (c.f. Figure 4.16) and

lower chain-orientation quality in the quenched nematic glass film. However, when the nematic F8BT film becomes very thick, the influence of the alignment imposed by the UV-illuminated SD1 photoalignment layer reduces and there is an increasing risk of chain misalignment across the whole thickness. Therefore, this behaviour tends to degrade the overall chain-orientation quality spatially averaged across the quenched glass films. Therefore, it can be expected that there does exist an optimum thickness for the LCCP films in order to enable the best chain-alignment quality in the SD1-aligned nematic glass films.

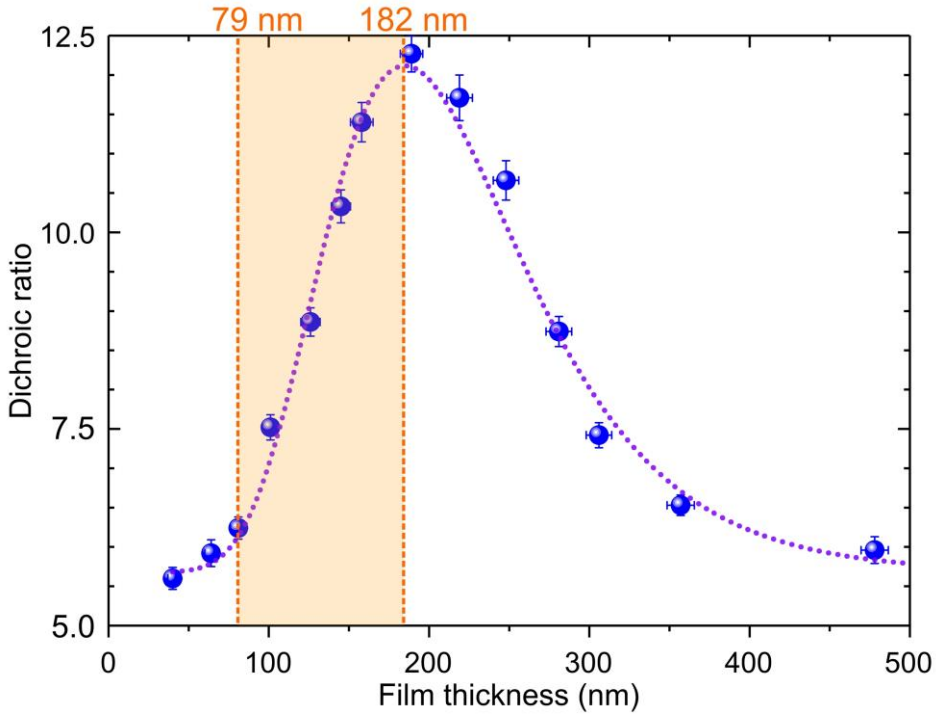

Figure 4.10: Dichroic ratio as a function of thickness for the fully-aligned F8BT nematic films (*Film II*). The shaded rectangle highlights the varying range of the backbone length of the F8BT polymer used in this study. The dotted curve is a guide for the eye.

The experimental results presented in **Figure 4.10** show the film thickness dependence of the dichroic ratio for various SD1-aligned F8BT nematic films. The results confirm an optimum film thickness of 180 nm - 200 nm. Also, such an optimum F8BT film thickness of 180 nm - 200 nm, which corresponds to the best chain-orientation quality and ~100% order parameter, is factually close to the length of the longest backbones of the polydisperse F8BT polymer. When the film thickness is smaller than the minimum length of the F8BT backbones,

the dichroic ratio in the SD1-aligned F8BT films reduces slowly with the film thickness. On the contrary, the dichroic ratio is found to grow more rapidly as the film thickness increases over the range of the F8BT backbone length (i.e., from 79 nm to 182 nm). Nevertheless, when the film thickness exceeds the optimum value, the spatially averaged chain-alignment quality in the SD1-aligned F8BT nematic films gradually decrease to ~50% of the peak value due to an increasing fraction of imperfectly oriented chains and/or nematic polydomains.

4.5 Photophysical Measurements

It is commonly thought that the lowest unoccupied molecular orbital (LUMO) of the F8BT polymer is highly localised on the BT units while the highest occupied molecular orbital (HOMO) tends to delocalise over the whole backbone [31,34]. The migration of charge carriers and excited states in an F8BT film therefore depends strongly on the intrachain conjugation and interchain transport events. As discussed, the various interchain packing structures and LC morphologies give rise to different X-ray scattering and optical absorption performance. In addition, they are also responsible for their distinct photophysical properties with prominent examples being the photoluminescence (PL), photoluminescence quantum efficiency (PLQE) and decay lifetime, as well as the amplified spontaneous emission (ASE) and lasing properties.

4.5.1 PL and PLE Spectral Lineshapes

The lineshapes of both the non-polarised (i.e., using an unpolarised excitation source and an unpolarised detection system) PL spectra in **Figure 4.11**(a)-(b) and PL excitation (PLE) spectra in Figure 4.11(d) are further supportive of the different F8BT packing structures formed in the four types of F8BT films. All F8BT films show a well-resolved 0-0 vibronic PL peak at ~538 nm and the 0-1 vibronic peak at ~570 nm. However, the relative PL intensity ratio of the 0-0 to 0-1 vibronic peak, $P_{(0\text{-}0)/(0\text{-}1)}$, clearly differs for the four types of F8BT films (see also Figure 4.11(b) for their normalized PL spectra). The nonpolarised PL spectra from both the nonaligned

(*Film I*) and partially-aligned F8BT nematic films (*Film III*) are dominated by the first allowed, high-energy (0-0) vibronic transition band, whereas the fully-aligned F8BT nematic film shows a relatively lower but still >1 $P_{(0\text{-}0)/(0\text{-}1)}$. On the contrary, the spin-coated only non-LC reference film (amorphous *Film 0*) demonstrates a much stronger 0-1 vibronic transition.

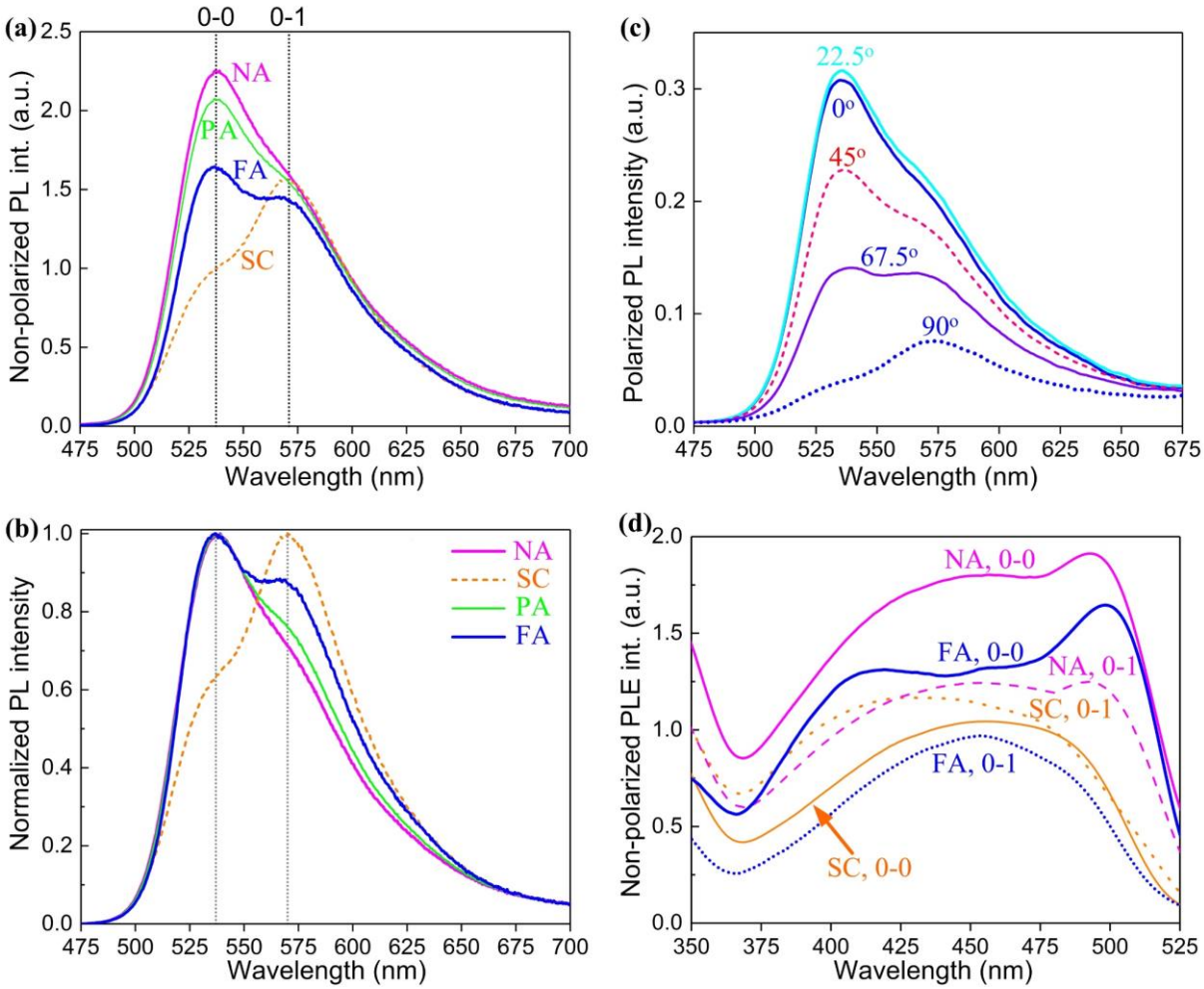

Figure 4.11: (a) Non-polarised PL spectra and (b) corresponding normalized PL spectra of the spin-coated (SC) non-LC F8BT film (*Film 0*) and of the nonaligned (NA, *Film I*), fully-aligned (FA, *Film II*) and partially-aligned (PA, *Film III*) F8BT nematic films. The two PL peaks marked by the vertical dotted lines in (a)-(b) were assigned to the center of the 0-0 and 0-1 vibronic transition bands. (c) Polarised PL spectra of the fully-aligned F8BT nematic film (*Film II*), probed under fixed parallel polarised light and with emission collected using a polarisation aligned at different angles relative to the chain alignment direction. (d) Nonpolarised PL excitation (PLE) spectra in the four types of F8BT films, with all the solid curves acquired for emission at the 0-0 vibronic PL peak and the dotted curves at the 0-1 vibronic peak. The PL and PLE spectra were measured using the same randomly polarised light source at 450 nm. All measured films are 160 nm in thickness.

These distinct $P_{(0\text{-}0)/(0\text{-}1)}$ results and PL peak intensities from all four types of F8BT films correspond with their PLE spectra recorded for the emission centered at the 0-0 and 0-1 vibronic PL peaks (Figure 4.11(d)). The non-LC F8BT films (*Film 0*) exhibit a disordered amorphous phase and, consequently, highly localised electronic wavefunctions on the BT units and no long-range exciton pathways. Entering and locking-in the LC mesophase, on the other hand facilitates the photo-excitation of the 0-0 vibronic transition in all F8BT nematic films, via microstructural self-organisation in the nematic phase into the dense F8BT in-plane packing structures in which the intrachain and interchain coherence length can be augmented considerably due to the long-range orientational order of the nematic phase. Such increased conjugation would greatly delocalise the energy transfer process and may also allow access to more emissive intrachain/interchain species, which indeed coincides with the emergence of a new longer-wavelength PLE band in both the nonaligned and fully-aligned F8BT nematic films.

A short-wavelength PLE band for the 0-0 vibronic PL emission is also collected for the highly oriented F8BT nematic monodomain glass film, whereas the corresponding PLE spectra for the 0-1 vibronic transition, however, is relatively featureless and lower in intensity. These PLE results measured for the fully-aligned F8BT nematic films (*Film II*) could indicate different origins of the 0-0 and 0-1 vibronic PL components. This can also be seen from the polarised PL spectra of the fully aligned nematic films (Figure 4.11(c)). There is a gradual shift in the relative PL intensities of these two vibronic components, and the 0-0 vibronic transition becomes more intense as the emission was collected with a polarisation that was at a smaller angle relative to the chain alignment direction. In contrast, the 0-1 emission component maximizes its fraction when the emission was collected at an orthogonal polarisation direction.

By assigning the primary origin of the 0-1 vibronic emission transition to the emissive interchain excited state of BT units [27,31], the proposed model for F8BT interchain packing

structures in Section 4.3.3 (Figure 4.7) could explain the distinct relative weights of the two vibronic PL components in the different F8BT films. For the non-LC F8BT films (*Film 0*), highly twisted chain-conformations and extremely localised BT-to-BT interchain interactions in adjacent chains give rise to the dominance of the 0-1 vibronic transition band and, concurrently, low PLQE values. The separated BT units in neighboring chains with the alternating interchain packing structure in the nonaligned nematic films could make interchain energy transfer become more difficult and therefore the energy transfer would rely more on intrachain migration, enabling the dominance of a high-energy 0-0 vibronic transition in the PL spectra and the highest PLQE among all the measured F8BT films.

4.5.2 Dependence of PLQE on F8BT Film Type and Alignment Quality

Nonpolarised solid-state PLQE measurements were performed using a Horiba Quanta-Phi diffusely-reflecting integrating sphere attached to a Horiba FluoroMax-4 with randomly-polarised 450 nm excitation. Three film samples were measured for each type of F8BT films we investigated, and for each sample two PLQE measurements were carried out with the second test performed by rotating the film by 90^{o} in the horizontal plane relative to the first measurement so as to study the effect of polymer chain alignment direction on PLQE. PLQE values were then calculated using the methodology detailed in Ref. [37].

Enhanced PLQE up to 70% is demonstrated in the self-doped host-guest system of the F8BT polydomains formed in the nonaligned nematic films (*Film I*, **Figure 4.12**(a)), compared with the PLQE of 35% ± 5% determined for the spin-coated-only non-LC F8BT reference film (*Film 0*) and 29% ± 4% for the annealed spin-coated pristine F8BT film at 80 ^{o}C for 30 mins in a N_2 atmosphere. The PLQE values obtained herein for the non-LC F8BT films are similar to previously published PLQE results [31,35]. The LC polydomains in either the nonaligned (*Film I*) or the partially-aligned F8BT nematic films (*Film III*) show larger PLQE than that of 49% -

53% measured for the fully-aligned monodomain films. This varying trend of the PLQE observed in all four types of F8BT films are further supported by the obtained non-polarised PL spectra and PL excitation (PLE) spectra in Figure 4.11, in terms of a good agreement between their PL/PLE peak intensities and the corresponding PLQE values.

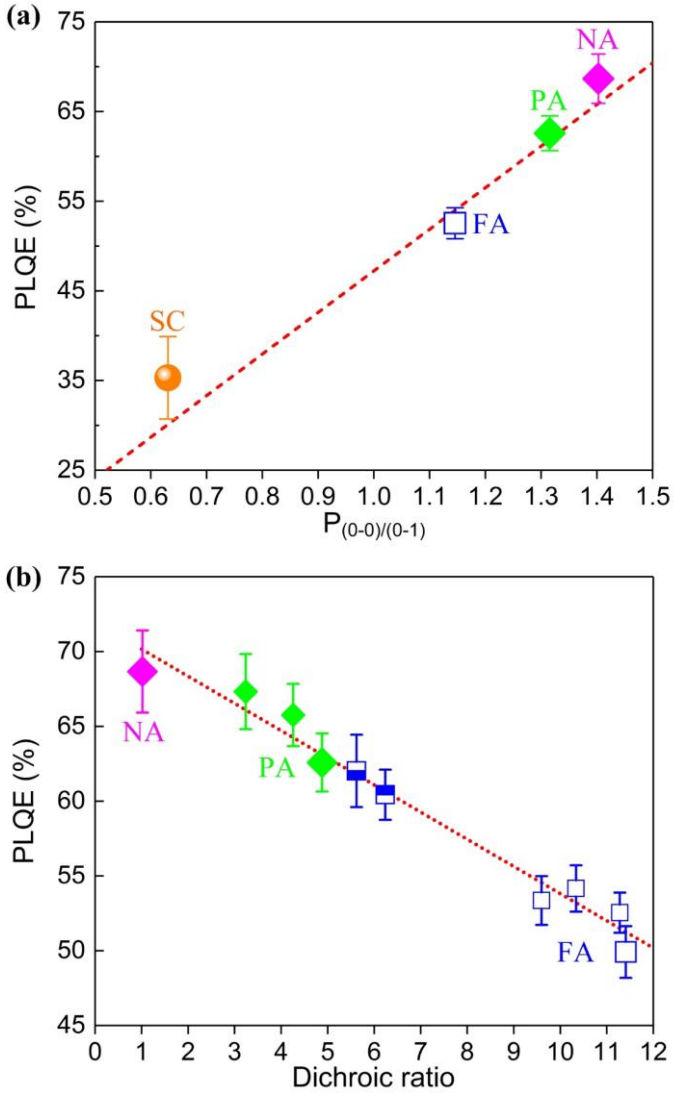

Figure 4.12: A plot of PLQE as a function of (a) the PL intensity ratio at the 0-0 vibronic peak to the 0-1 vibronic peak, $P_{(0\text{-}0)/(0\text{-}1)}$, and (b) the optical absorption dichroic ratio at 450 nm for the four different F8BT nematic films: the spin-coated (SC) non-LC F8BT film (*Film 0*) and of the nonaligned (NA, *Film I*), fully-aligned (FA, *Film II*) and partially-aligned (PA, *Film III*) F8BT nematic films. The four blue open squares in (b) are the data from the fully-aligned F8BT monodomain films, whilst the fully-filled diamonds are for the nematic polydomain films of either the nonaligned (NA) or partially-aligned (PA) film type; the two half-filled boxes represent data for fully-aligned but thin overlying F8BT films with 40 nm and 80 nm in thickness. The error bars denote a variation in the corresponding data determined from four film samples for each dichroic ratio.

The overall trend from Figure 4.12(b) is that the PLQE of the F8BT nematic films decreases nearly linearly with chain-alignment quality and order parameter (quantified by the optical dichroic ratio determined in the F8BT films), alongside a concomitant enhancement in the interchain electronic coupling strength and associated interchain fluorescence.

Taking all of the POM and photophysical spectral information into account leads to the conclusions: *i*) that the LC-phase self-organised host-guest system formed in the nonaligned nematic polydomain films (*Film I*) manifest itself in the formation of a small fraction of low-energy polymeric nanocrystal inclusions dispersed in a disordered amorphous-phase host, and in the effectiveness for enabling the non-radiative host-to-guest FRET funnelling and the obtained record-high PLQE value for F8BT solid-state films; *ii*) that analogous PL spectral lineshapes exist between the emission spectrum observed from the non-aligned nematic polydomains that observed for the fully-aligned monodomains with when the polarisation orientation used to collect the light is parallel to the chain alignment direction; and *iii*) that a combination of the dramatically enhanced polymer crystallinity, BT-to-BT close/direct contact in adjacent chains, and interchain coherent length in the highly-oriented nematic monodomain films results in distinct emissive excited states, which are fundamentally responsible for the measured lower PLQE and PL spectral separation of the two orthogonal emission components.

For all of the types of F8BT films, π-conjugation anisotropy and interchain excitonic transfer/decay could act as a key PLQE-limiting factor. Specifically, highly localised interchain BT-to-BT excitonic couplings in the amorphous film would restrict energy transfer to the most energetically favorable emissive sites, hence predominantly triggering the low-energy (0-1) emission transition and lowering the overall PLQE. Nonetheless, the extremely ordered in-plane packing and substantial BT-to-BT close/direct contacts in the fully-aligned monodomain films have induced a large anisotropy in the conjugation and electronic coupling strength, which

may spatially concentrate the energy transfer events in the film plane to significantly more non-emissive defects and, thus, is still not an ideal situation for maximising the overall PLQE. As a result, an appropriate relative weighting between the chromophoric to fluorophoric units in the F8BT films and a medium strength/lengthscale of interchain electronic coupling appears to be more favourable in terms of optimising the FRET and PLQE, a prominent example being the self-doped host-guest system that is self-organised in the nonaligned F8BT nematic films.

4.6 Polarised μ-PL Spectra

High-resolution spatial patterning of the chain-orientation, microstructural anisotropy, and concomitant interchain electronic coupling strength could dictate the photophysical properties of the different types of F8BT films. In order to elucidate the effect of high-quality chain alignment and self-organised nematic microstructures on the localised photophysical properties, systematic polarised micro-PL (μ-PL) measurements (c.f. Figure 2.4 for the experimental setup) were carried out on SD1-aligned, spatially-patterned alignment patterns against the nonaligned nematic polydomain background in the same F8BT nematic film.

4.6.1 Fabrication of Photomasked F8BT Alignment Pattern

Spatial patterning of the chain-orientation in the F8BT sample was created using photomasked UV-alignment of continuous SD1 layers before accessing the nematic LC phase of F8BT to induce an alignment of the polymer chains in the overlying F8BT film. For spatial definition of the alignment pattern in an SD1 alignment layer, polarised UV exposure was used in combination with a specially made photomask placed on the SD1-coated substrate (with spatially patterned silver surface of a photomask facing the top surface of the SD1 layer). The spatially defined photomask pattern was fabricated based on a standard photolithography technique for spatially patterning a silver-coated (150 nm thickness) glass substrate (see the fabricated silver pattern on the photomask and an illustration of the sample fabrication in **Figure**

4.13). There were five groups of well-aligned 4 × channels with linewidths of 3.0 μm, 5 μm, 10 μm, 25 μm, and 50 μm that were spatially patterned, as confirmed by the bright-state polarised optical micrograph in Figure 4.13(b). In particular, the UV-illuminated 3 μm-thick F8BT channel against its nonaligned nematic glass background have been systematically investigated using polarised μ-PL measurements to directly compare the localised PL emission properties (e.g., polarised PL spectra and vibronic spectral lineshape, PL intensity anisotropy) measured at different locations in the same F8BT nematic glass film.

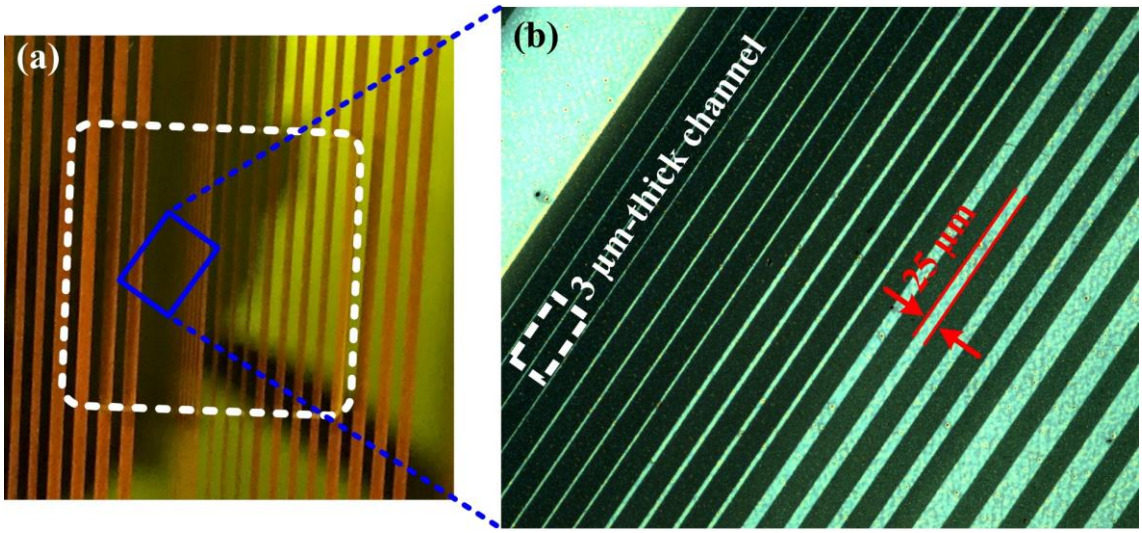

Figure 4.13: Illustration of the photo-masked UV-alignment method used to spatially define a bespoke alignment pattern in the SD1 alignment layer and consequently the overlying F8BT film. (a) A photograph of a large photomask placed on a SD1-coated quartz substrate (denoted by the dashed white square; size: 25 mm × 25 mm) during the process of polarised UV illumination of the SD1 layer. (b) Bright-state polarised optical micrograph of the resulting LC optical texture in a selected region, as labelled by the blue rectangle in (a), in the quenched overlying F8BT nematic film.

4.6.2 Micro-PL Spectra and Anisotropy Mapping in Aligned vs Nonaligned Regions

All polarised μ-PL spectra were acquired at room temperature with a linearly polarised 405 nm, 150 fs, 76 MHz laser excitation source (see the schematic setup in Figure 2.4) with fixed beam polarisation parallel to the chain-orientation direction in the photoaligned line (along the *y*-axis

in the 3D rendered maps in **Figure 4.14**). The emission from the F8BT nematic film was separated using an analyser with polarisation parallel ($PL_{//}$) and perpendicular ($PL_{\perp}$) to the transition dipole moment direction of the highly oriented F8BT chains in the patterned line region. The spot size at the sample was ≈ 1 μm diameter; the scanning step of the high precision *x*-*y* positioning stage was set as 200 nm in both *x* and *y* scanning directions.

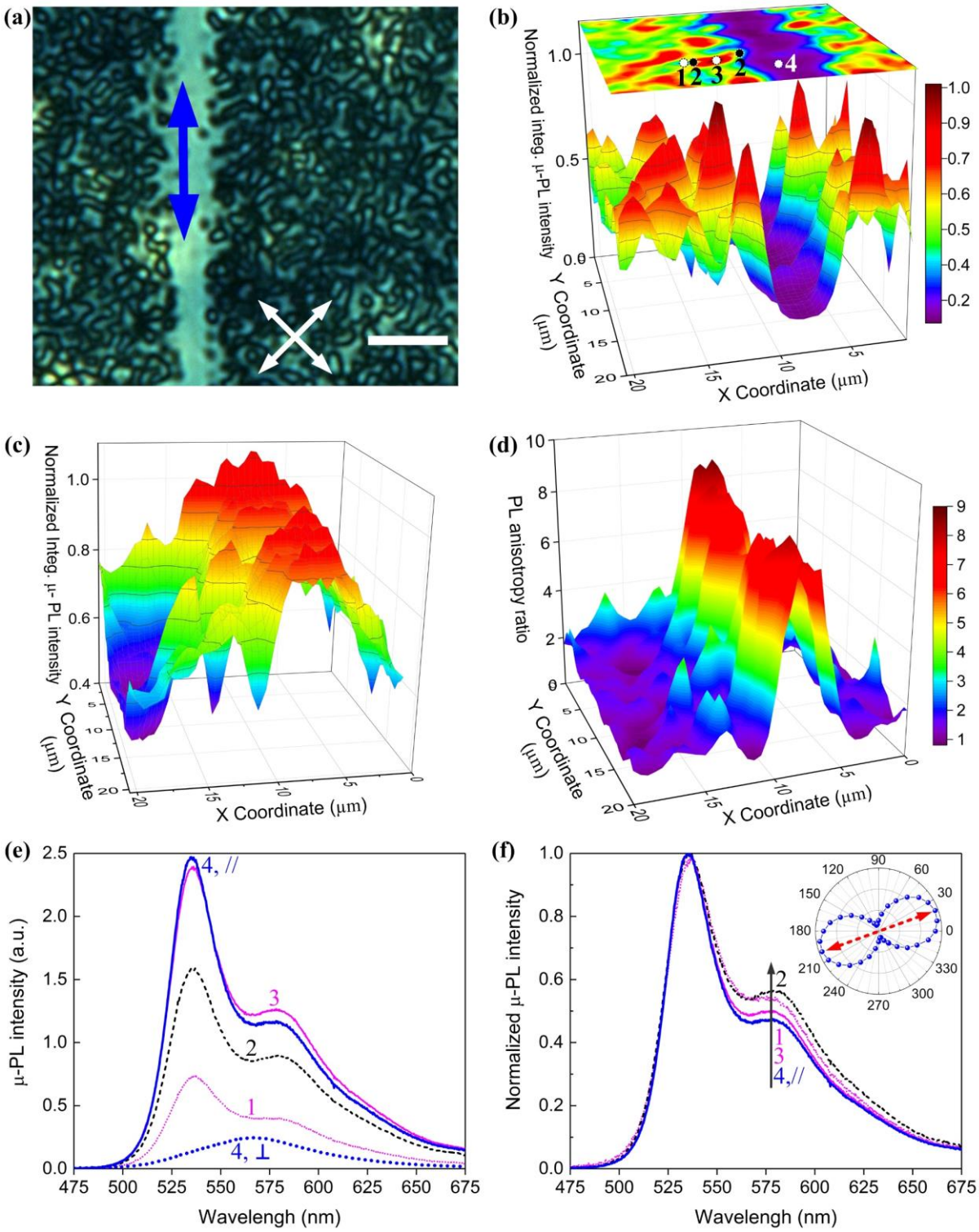

Figure 4.14: Polarised μ-PL spectral and mapping results for an F8BT nematic film (160 nm thickness) oriented by a spatially-patterned SD1-photoalignment layer. (a) Crossed POM image with the chain-orientation direction indicated by the double-headed blue arrow; horizontal scale bar: 6 μm. (b) - (c) 3D colour-coded μ-PL integrated intensity map measured with the fixed excitation polarisation parallel to the chain-orientation direction (along the *y*-axis) and F8BT emission collected with polarisation perpendicular (b) or parallel (c) to the transition dipole moment of the oriented F8BT chains in the SD-aligned channel region. A contour plot of the normalized total μ-PL intensity as a function of the in-plane location were plotted as well in (b) and (c). (d) Corresponding 3D map of the spatial variation of the integrated PL anisotropy in the same area plotted in (a) and (b). Polarised μ-PL spectra (e) and the corresponding normalized μ-PL spectra (f) recorded at the four locations labelled in (b) when the F8BT emission was collected with polarisation *perpendicular* to the direction of the transition dipole moment of the UV-aligned F8BT chains. For the scanning point #4 in the aligned line region, its perpendicular (⊥) and parallel (//) polarised μ-PL spectra were acquired with emission collection polarisation being perpendicular and parallel, respectively, to the transition dipole moment of aligned F8BT. The inset in (f) is a polar plot of the normalized total μ-PL intensity recorded from location point #4 as a function of the angle between the analyser polarisation and the chain alignment direction in the photoaligned region (with 0^o defined when the two become parallel to each other). It is confirmed that the transition dipole moment of the highly oriented F8BT chains in the SD1-aligned line region, which corresponds to a μ-PL intensity from the aligned F8BT line that is maximised under the fixed excitation (marked by the red dashed arrows), is at an angle of ~20^o relative to the chain-orientation direction.

A 3D rendered map (bottom of Figure. 14(b)) and a 2D colour-coded contour plot (top of Figure 4.14(b)) demonstrate the spatial variation of the integrated $PL_{\perp}$ spectral intensity in both the aligned line and the nonaligned nematic polydomain background (emission from the latter was collected with the same excitation and analyser polarisation used to record the $PL_{\perp}$ spectra from the region that was aligned). The corresponding 3D mapping of the integrated $PL_{//}$ intensity from the same region in the F8BT nematic film sample is shown in Figure 4.14(c). The nonaligned polydomain background displays an irregular variation in both the domain size/shape and μ-PL intensity along the *x*-axis and *y*-axis in the film plane, in accordance with a random distribution of the chain orientation across the nematic polydomains.

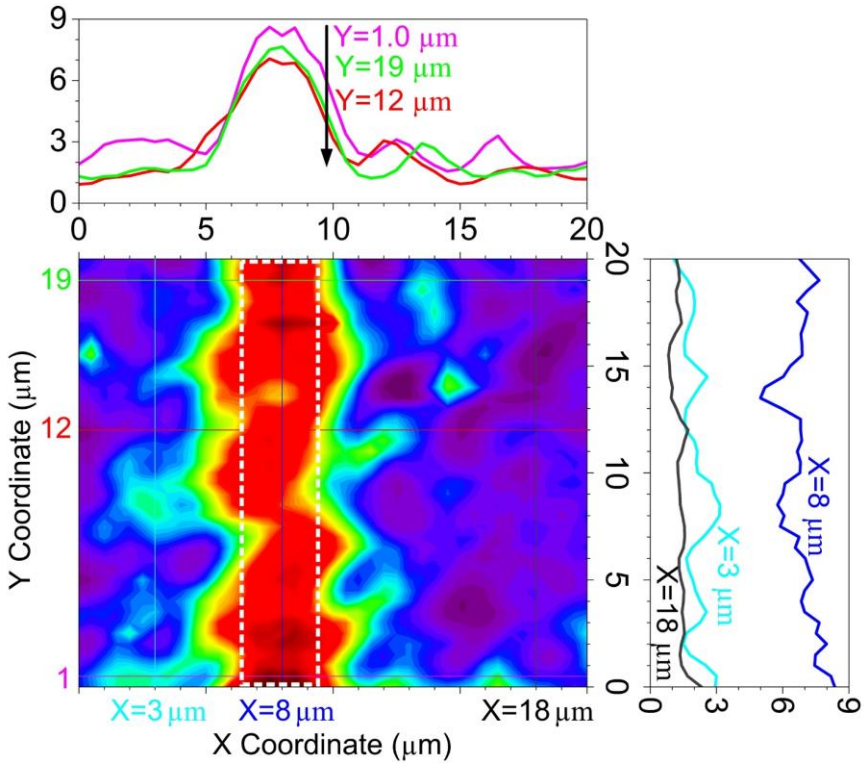

Figure 4.15: Colour-coded contour plot and linecut profiles of the integrated PL anisotropy ratio in the six labelled lines along the *x*-axis and *y*-axis (i.e., *x* = 3 µm, 8 µm, and 18 µm; *y* = 1 µm, 2 µm, and 19 µm). The white dashed box represents the shape and position of the photomask employed to pattern the polarised UV alignment of the 3 µm-thick line in the photoalignment layer.

Figure 4.14(d) further demonstrates relatively small values of the integrated PL anisotropy, i.e., $= \int PL_{//} / \int PL_{\perp}$, from the nonaligned nematic polydomain background. Inspection of the spatial variation of this anisotropy across the background (see also **Figure 4.15**) leads to an estimation of the average domain size to be 3.5 - 5 µm, which highlights a 90° difference between the chain orientation formed in adjacent domains and, thus, agrees with the irregular polarised confocal fluorescence images shown in Figure 4.8. For comparison, the spatially averaged domain size of ~2 µm based on the POM images of the polydomains relies on a 45° difference in the F8BT chain orientation between the bright- and dark-states. The photo-patterned F8BT exhibits much larger yet uniform PL anisotropy ratios, e.g., an anisotropy of 8.9 calculated from the $PL_{//}$ and $PL_{\perp}$ spectra in Figure 4.14(e), as a result of the noticeably reduced interchain $PL_{\perp}$ intensity but slightly enhanced intrachain $PL_{//}$ intensity.

The polarised μ-PL spectra recorded from different locations around a typical domain in the nonaligned nematic background (location #1 - #3) and in the aligned channel (location #4), as labelled in Figure 4.14(b), are presented in Figure 4.14(e)-(f) and **Figure 4.16**. The three locations in the nonaligned polydomain background have similar spectral lineshapes in both the $PL_{//}$ and $PL_{\perp}$ spectra, except that the domain boundary (location #2) exhibits the best resolved 0-1 vibronic PL peak at ~580 nm and the biggest relative intensity ratio between the 0-1 and 0-0 vibronic peak, $P_{(0\text{-}1)/(0\text{-}0)}$. A general correlation between $P_{(0\text{-}1)/(0\text{-}0)}$ and μ-PL intensity appears in that the higher the μ-PL intensity from a recorded location, the more reduced the $P_{(0\text{-}1)/(0\text{-}0)}$ value in the $PL_{//}$ and $PL_{\perp}$ spectra. Among the polarised μ-PL spectra collected from the four recorded locations, the $PL_{//}$ spectra from location #4 in the aligned channel is found to have the highest PL intensity at the 0-0 vibronic peak but the lowest $P_{(0\text{-}1)/(0\text{-}0)}$. These μ-PL spectra also correspond well to the general trend of $P_{(0\text{-}1)/(0\text{-}0)}$ as a function of the PL intensity extracted based on the non-polarised macroscopic PL spectral results (Figure 4.11(a)-(b)) for the nonaligned (*Film I*), partially-aligned (*Film III*), and fully aligned (*Film II*) F8BT nematic films.

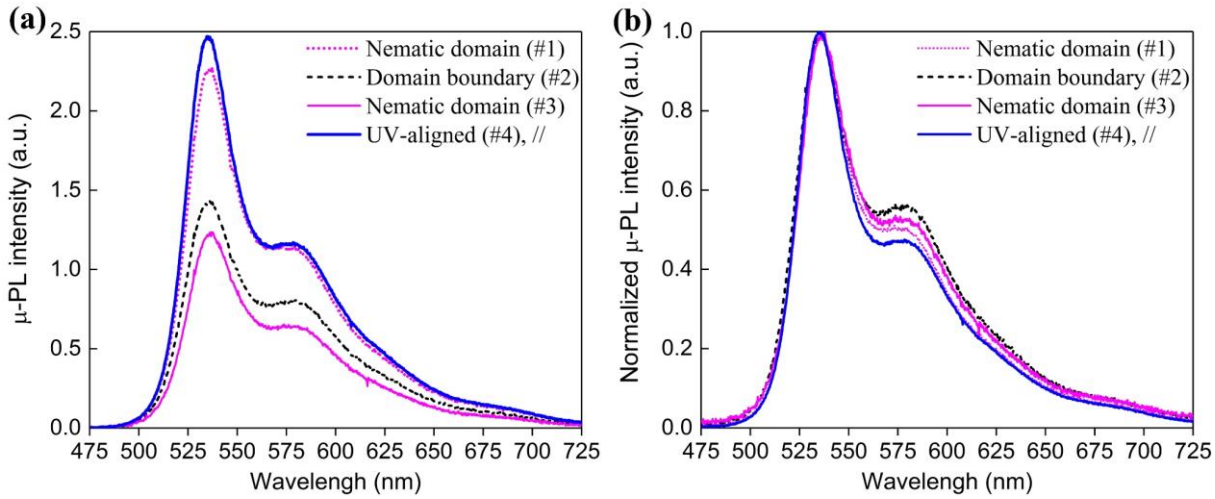

Figure 4.16: (a) Polarised μ-PL spectra and (b) corresponding normalized μ-PL spectra recorded at the four locations labelled in Figure 4.14(b). All polarised μ-PL spectra herein were obtained with the F8BT emission collected with polarisation *parallel* to the transition dipole moment of the SD1-aligned F8BT chains.

By rotating the F8BT emission collection polarisation in the film plane during acquisition of the polarised μ-PL spectra from location #4, the direction of the transition dipole moment of the highly-oriented F8BT chains in the aligned channel is found to lie at ≈20° relative to the SD1-defined chain-alignment direction (see the inset in Figure 4.14(f)). This deviation angle is close to the experimental and computational results of 20° - 22° for the F8BT polymer [35,38].

In contrast to the analogous μ-PL lineshapes recorded from different locations in the nonaligned background and thus the same source of PL emission from the emissive, microstructurally similar polymeric nanocrystals, it is noteworthy that polarisation-dependent PL-spectral separation of the two main vibronic emission transitions is observed for the photoaligned F8BT line. The $PL_{//}$ spectra of an interchain character measured from location #4 closely resembles the vibronically-structured spectra from the nonaligned polydomains (yet with a lower relative weight of the 0-1 vibronic peak, corresponding to a greater Huang-Rhys parameter and more rigid molecular geometry of the aligned F8BT backbones). The $PL_{\perp}$ spectrum from location #4 is relatively featureless and the emission peak that has a relatively low PL intensity is blue-shifted by 10 - 20 nm relative to all other identified 0-1 vibronic PL peaks. This separation of the two orthogonal emissive species may be structurally and energetically enabled by the highly-aligned, closely-packed F8BT backbones by the underlying UV-illuminated SD1 photoalignment layer. The formation of directed BT-to-BT interchain configuration and associated enhancement in the intrachain conjugation is potentially mediated by the dense interchain packing and mitigation of chain entanglements due to the long-range orientational order preserved in the nematic monodomain of F8BT polymer films.

4.6.3 FRET in Nonaligned Glass Films vs Interchain Energy Transfer in Aligned F8BT

Another important indication from all the polarised μ-PL spectral information is that the domain boundary regions exhibit the best resolved 0-1 vibronic transition and the greatest $P_{(0\text{-}1)/(0\text{-}0)}$,

which is thought as a results of enhanced Förster Resonance Energy Transfer (FRET) from the disordered amorphous-phase matrix to the highly-ordered polymeric nanocrystals self-organised in the nonaligned nematic polydomain background. A random distribution of the chain-orientation in/among the polymeric nanocrystal acceptors and highly twisted matrix in the nonaligned nematic polydomains, however, would promote a higher oscillation strength of cross-chain transitions and thus efficient non-radiative interchain FRET funnelling, potentially allowing for the absence of the polarisation-dependent separation between the $PL_{//}$ and $PL_{\perp}$ spectra therein. In addition, the domain boundaries, as an inhomogeneous/interfacial region separating adjacent nematic domains in a polydomain nematic glass film, are supposed to accommodate a relatively higher level of structural/energetic disorder than both the domain interiors and photoaligned monodomains. As the domain boundaries act to smooth the structural heterogeneity between adjacent domains, they can be expected to incorporate a larger fraction of amorphous-phase F8BT or a reduced amount/size of the polymeric nanocrystal inclusions. This increased accommodation of the amorphous chromophoric F8BT could increase PLQE as each polymeric nanocrystal acceptor is peripheralized by relatively more chromophoric donors.

By assuming that the 3D interchain FRET funnelling events occurring in the self-doped host-guest system of F8BT is more efficient to promote the low-energy 0-1 vibronic PL transition than the high-energy 0-0 transition, incorporating higher levels of structurally disordered F8BT could result in greater $P_{(0\text{-}1)/(0\text{-}0)}$ values in the PL spectra. This is consistent with the observation of the nematic domain boundary region (location #2) in Figure 4.14(b). The same PL spectral lineshape change is obtained from a nonaligned 80 nm-thick nematic F8BT film (*Film I*), which demonstrate larger but uniform $P_{(0\text{-}1)/(0\text{-}0)}$, and a slightly blue-shifted, less-defined 0-1 vibronic transition, relative to that from the nonaligned 160 nm background (**Figure 4.17**). This observation in a thinner *Film I* tends to emphasize a higher efficiency of the 3D interchain FRET funnelling with lower energy losses and/or over shorter distances.

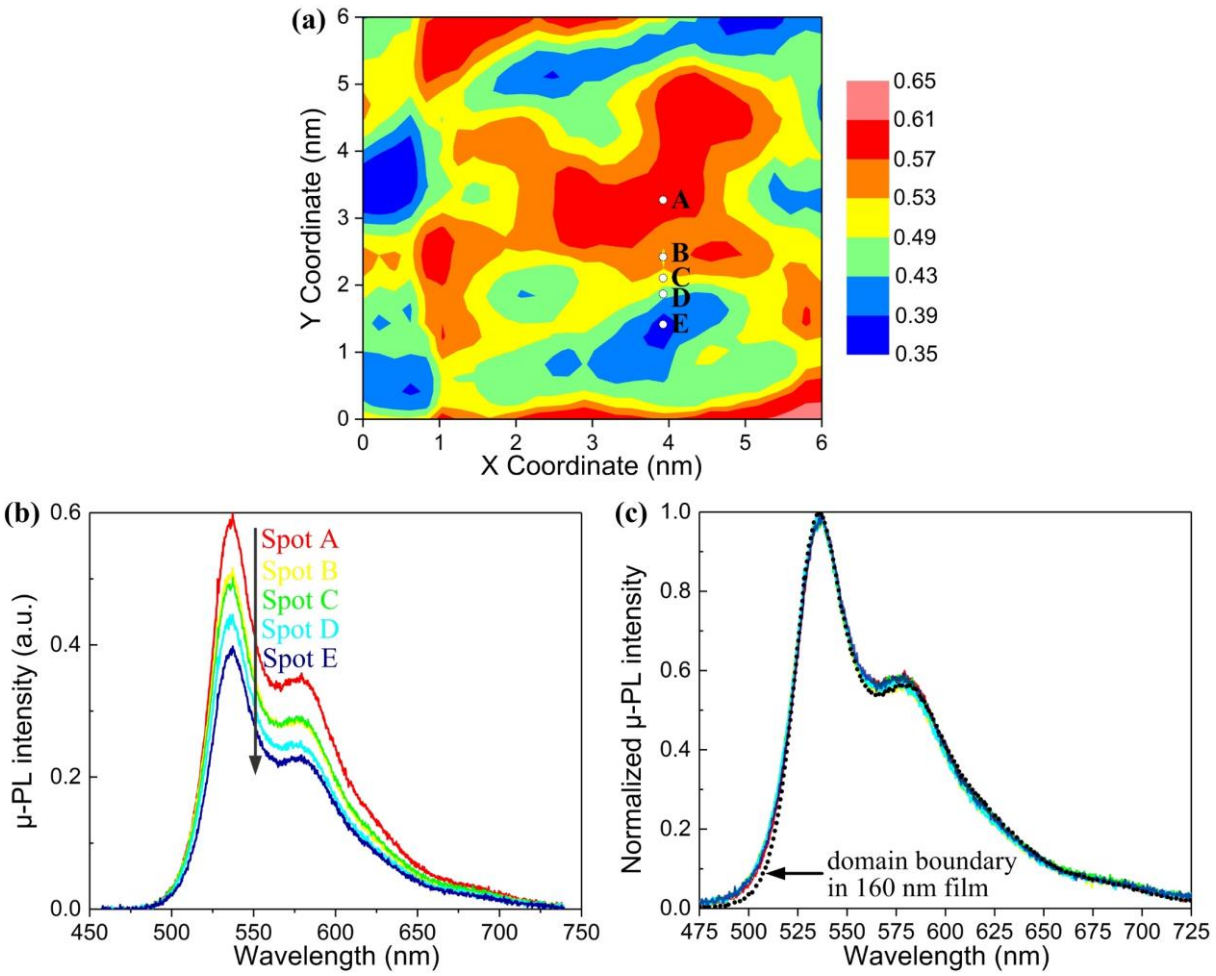

Figure 4.17: (a) A contour plot of polarised μ-PL intensity at the 0-0 vibronic peak for a representative thin (80 nm in thickness, a value commonly used in organic light-emitting diodes) non-aligned F8BT nematic film (*Film I*). (b) Polarised μ-PL spectra and (c) the corresponding normalized spectra collected from the point *A*, *B*, *C*, *D* and *E* labelled in (a). The normalized μ-PL spectrum from the domain boundary in the 160 nm-thick nonaligned F8BT nematic film (the thick black dotted curve) was also plotted in (c) for comparison.

Accordingly, a slight improvement of the PLQE is also confirmed for the nonaligned 80 nm F8BT nematic films, which is thought to be a possible result of a smaller spatially-averaged domain size of the nematic polydomains in this thinner nonaligned F8BT nematic film. The analysis of the ratio $P_{(0\text{-}1)/(0\text{-}0)}$ for different locations across a nematic domain in both the nonaligned 160 nm and 80 nm F8BT nematic films highlights the importance and benefits of fine-tuning the relative weight of the amorphous chromophoric host in the whole F8BT film volume, in term of optimising the resultant photophysical properties of the F8BT films. In this respect, a higher density/fraction of domain boundary regions in the nematic polydomain glass

films appears more desirable to enhance the non-radiative interchain FRET in the amorphous matrix and the PL efficiencies of intrachain emission component.

Calculation of the Förster radius was carried out based on the spectral overlapping between the normalized PL spectrum of amorphous-phase nematic F8BT and the optical absorption spectrum of the nonaligned 160 nm-thick F8BT nematic film, as shown in **Figure 4.18**. This unpolarised PL spectrum for the F8BT nematic glass film is also featureless and analogous to the perpendicular polarised μ-PL spectrum recorded from the aligned F8BT line (Figure 4.14(e)-(f)), although the former PL spectrum becomes broader due to the highly disordered microstructure inherited from the isotropic F8BT melt before quenching. According to the calculation method in Ref. 39 and using our extracted *d*-spacing distance in the polymeric nanocrystals, the Förster radius (R_0) was determined to be 6.9 nm for the nonaligned 160 nm-thick F8BT nematic films, which was then adopted in the estimate of the diffusion length ($=R_0^3/d\text{-spacing}^2$, [40]) as 120 ± 10 nm.

Considering the thickness of active F8BT films that are frequently fabricated in the related electronic and optoelectronic devices lies in a range of 70 nm - 200 nm, this level of diffusion length presents a rather long FRET distance. We attributed this long diffusion length to the condense/close F8BT interchain packing structure and long-range orientational order in the fluorophoric polymeric nano-crystalline acceptor in the nematic mesophase and subsequently the quenched glass film. The value of the interchain diffusion length can be further enhanced in thinner polydomain glass films, due to the reduction in spatially average domain size and the incorporation of a greater fraction of interfacial/disordered regions in a thinner nonaligned nematic glass film (see Section 4.6 as well). As a matter of fact, such an increasing trend in R_0 and FRET funnelling also coincides with the improvement in PLQE obtained in the thinner nonaligned F8BT nematic glass films.

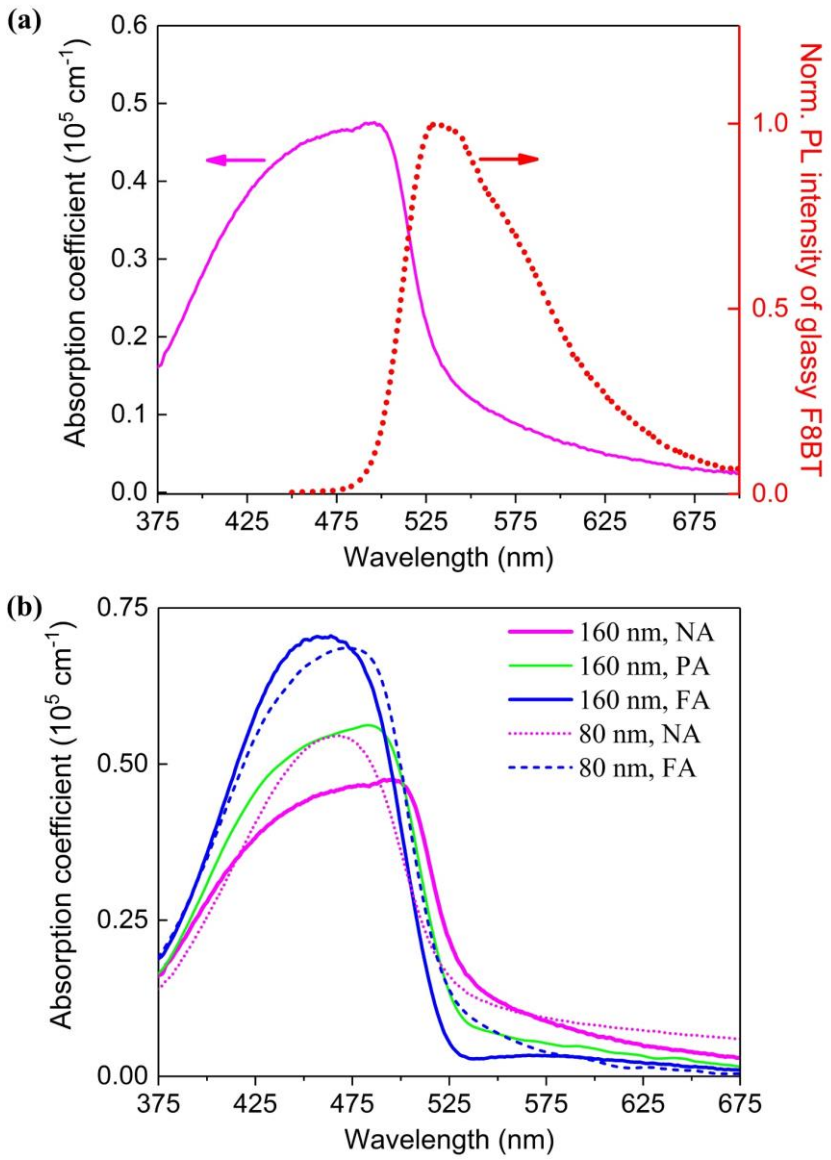

Figure 4.18: (a) Spectral overlap between the normalized PL spectrum of the amorphous-phase nematic F8BT and the absorption spectrum (optical absorption coefficient determined from non-polarised UV-vis absorption measurements) of the nonaligned 160 nm-thick F8BT nematic film (*Film I*). (b) Direct comparison of the absorption spectra in the nonaligned (NA, *Film I*), fully-aligned (FA, *Film II*) and partially-aligned (PA, *Film III*) F8BT nematic films with a thickness of 160 nm or 80 nm.

As a response to the generic formation of self-doped, well-oriented polymeric nanocrystals in the nonaligned F8BT nematic glass films, the broadening and red-shift of the charge-transfer absorption band, alongside the significant scattering tail at longer wavelengths, have been demonstrated in Figure 4.18(b). Although the nonaligned nematic glass films have an attenuated peak absorption, their spectral overlap with the same normalized PL spectra of the amorphous-phase nematic F8BT was enhanced, leading to higher FRET and PLQE

efficiencies in the self-doped guest-host nematic polydomains. To elaborate this in more detail, the optical absorption coefficient spectrum in the 80 nm-thick nonaligned F8BT nematic glass film was found to have a relatively higher peak intensity and an augmented long-wavelength tail, compared with that of the 160 nm-thick nonaligned counterpart. The two aspects would enhance the spectral overlap with the PL spectra of amorphous-phase F8BT and therefore corresponds to more efficient FRET and higher PLQE. The latter increased intensity of the long-wavelength tail (and associated re-absorption) is believed to have originated from either a reduced size of polymeric nanocrystals or a larger fraction of amorphous-phase chains in the 80 nm nonaligned F8BT nematic glass film. Accordingly, its improved absorption strength indicates that a reduction in the film thickness and, concomitantly, chain re-orientation/diffusion results in a confinement of the F8BT backbones so that they face parallel to the film plane, unlike the 3D randomly oriented polymeric nanocrystals formed in the 160 nm-thick counterpart. The same changing trend of both the absorption strength and PLQE still holds for the partial LC alignment or an increasing portion of imperfectly aligned domain regions in the F8BT nematic glass films.

In sharp contrast to the significantly enhanced PLQE and FERE efficiencies in the self-doped guest-host system of the nonaligned nematic glass films, the fully aligned F8BT nematic films of sufficient thickness is dominated by highly oriented extended monodomain with a high polymer crystallinity. It is believed that the energy transfer in the monodomains is largely due to enhanced intrachain conjugation and interchain excitonic migration in the film plane between neighbouring BT units in adjacent F8BT chains. Judging from the dependence of the PLQE on the F8BT alignment quality in Figure 4.12(b), we concluded that the non-radiative FRET over a relatively long lengthscale from the amorphous matrix to the small fraction of fluorophoric polymeric nanocrystals in the polydomains is more efficient than the interchain energy transfer and concomitant radiative interchain recombination in the highly oriented monodomains.

4.7 Domain Size Scaling with Thickness of Nonaligned Nematic Glass Films

Physical tuning of domain boundaries in the F8BT nematic polydomain films complements the photo-patterning of the chain orientation so as to tune the photophysical properties of the F8BT films. **Figure 4.19** showcases the results of a demonstration of domain engineering via systematically varying the thickness of the quenched, nonaligned F8BT nematic films (*Film I*) over a range of 40 nm to 480 nm and its merit in altering the PLQE.

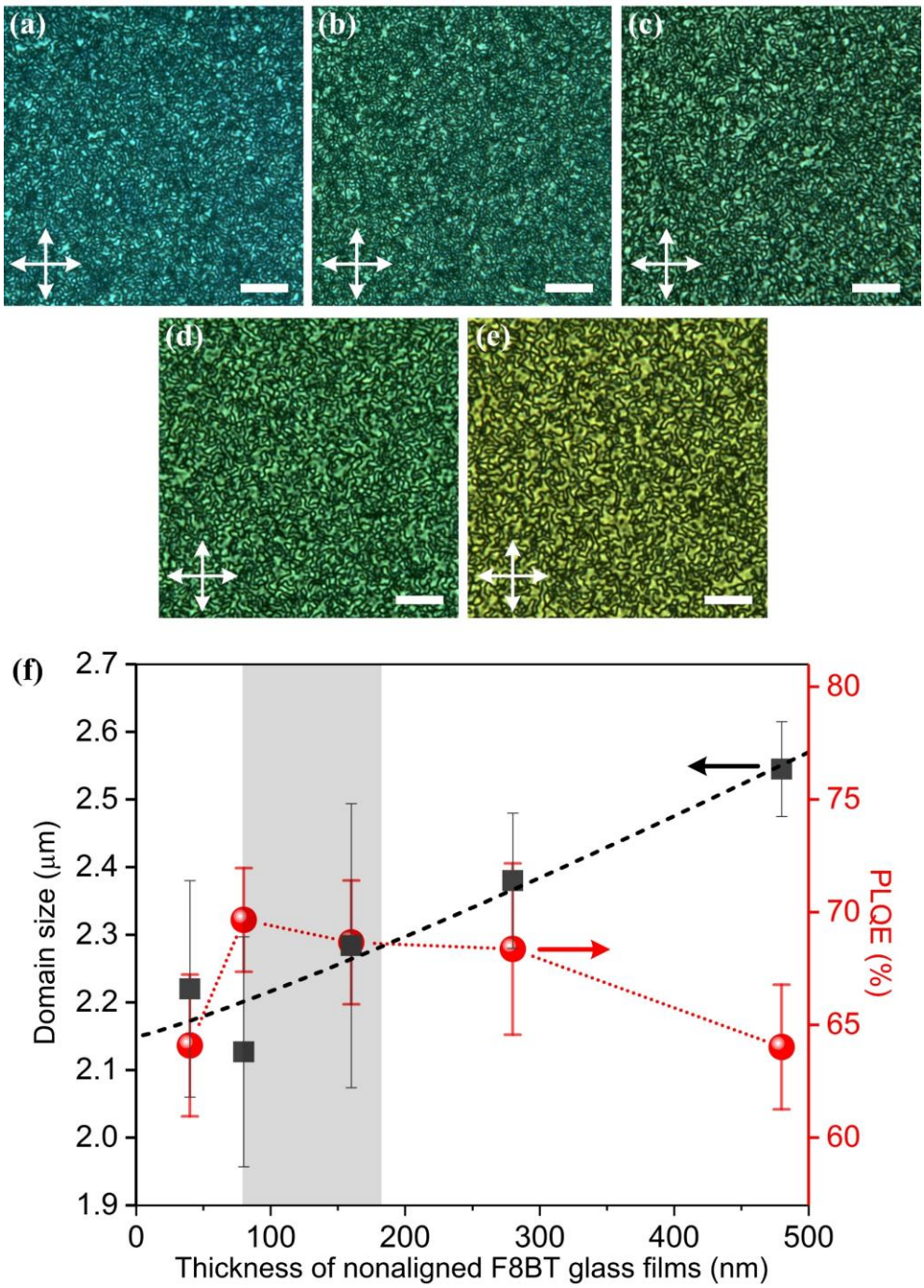

Figure 4.19: (a) - (e) Typical POMs demonstrating a polydomain LC texture observed in the quenched nonaligned F8BT nematic films (*Film I*) coated on a quartz substrate with a film thickness of 40 nm (a), 80 nm (b), 160 nm (c), 280 nm (d) and 480 nm (e), viewed between crossed polarisers as indicated by the two crossed white double-headed arrows. The scale bars in (a) - (e) are 20 μm; the colour change from (a) to (e) corresponds to an increase in retardation in the thicker films. (f) Plots of both the spatially averaged domain size and PLQE as a function of the thickness of the nonaligned nematic F8BT films. The black dashed curve represents the fitting result using the power-law scaling to the dataset for the nematic domain size. The error bars denote a variation in the corresponding data determined from four nonaligned F8BT nematic samples for each film thickness. The shaded rectangle highlights the varying range of the backbone length of the used F8BT.

While a higher PLQE is always demonstrated in a nonaligned F8BT film with smaller nematic domains and thus a larger volume fraction of domain boundaries, Figure 4.19(f) further demonstrates that the increase in the spatially averaged domain size with the film thickness in the nonaligned F8BT nematic polydomain films is nearly linear. Similar size scaling trends have been reported for other LCs, such as the thickness dependence of the lateral size of linear domains in Smectic LCs [41] and defect number density in the typical Schlieren textures of low molar mass nematic LCs [42].

Given the shape irregularity of the polydomain LC texture formed in the nonaligned F8BT nematic glass films, the size of the nematic domains (w) would scale with the film thickness (D) according to a power law, that is, $w \propto D^{H_x/(3-H_y)}$, as a result of a minimization of the energy of the domain bulk against the domain boundary energy [43,44]. H_x and H_y denotes the Hausdorff dimensionality of the irregular F8BT nematic domains along the x-axis and y-axis in the film plane and can be then estimated as $H_x = H_y \approx 1.6$ using the extracted coherence lengths for the nonaligned F8BT nematic film [45]. Taking all together, the scaling of the domain size in the nonaligned F8BT nematic films follows: $w \propto D^{1.14}$, and a fitting result using this power law to the dataset of spatially averaged nematic domain size is illustrated by the black dashed curve in Figure 4.19(f). The minor deviations in fitting the domain size for the nonaligned F8BT nematic

films with thickness <80 nm are likely caused by the enhanced surface confinement of the reorientation of F8BT chains and altered chain-entanglement state in the nematic mesophase in these ultrathin F8BT films [46,47]. These surface limiting factors were not considered in the proposed simple energy minimization model but may result in the formation of polydomain (rather than monodomain) LC textures in sufficiently thin F8BT nematic glass films, even when they were oriented in the nematic phase by a UV-aligned continuous SD1 layer.

4.8 Time-Resolved Solid-State PL Spectra and Lifetime Results

The type of LC textures (polydomain or monodomain) preserved in the SD1-aligned F8BT nematic films is further unveiled to play a deciding role in F8BT emission lifetime and also whether or not the $PL_{//}$ and $PL_{\perp}$ spectra from an F8BT film can be separated. **Figure 4.20**(a) and (b) shows the time-integrated $PL_{//}$ and $PL_{\perp}$ spectra from the fully-aligned F8BT film (by a UV-aligned continuous SD1 layer) with a thickness of 80 nm and 160 nm, respectively. The SD1-aligned 160 nm F8BT nematic films exhibit a monodomain LC texture and a clear polarisation-dependent PL spectral separation, whereas the SD1-aligned 80 nm nematic film displays a polydomain texture (i.e., aligned domains but with unaligned regions) and no clear change in the lineshape for both the $PL_{//}$ and $PL_{\perp}$ spectra. These two distinct cases elucidate a strong structure-property relationship in the SD1-aligned F8BT nematic films: the locked-in LC texture and, most importantly, absence/presence of domain boundaries in the F8BT nematic films dictate the occurrence of polarisation-dependent PL spectral separation.

The excitation laser (a 379 nm laser, pulsed at 10 MHz) for the polarised, time-resolved PL spectra measurements remained linearly polarised parallel to the chain alignment direction in the SD1-aligned F8BT films. The monochromator grating and streak-camera setup allowed for a time range of 20 ns (10K acquisition) and collections of 288 nm emission wavelength range (432 nm - 720 nm) with 6 nm spectral resolution at each time point. F8BT samples and

the collection polariser were rotated in the vertical plane to align the direction of both excitation polarisation and emission collection polarisation; in this way, the emission was collected with polarisation parallel (*//*) or perpendicular ($\perp$) to the excitation polarisation. The collected PL transients were then integrated to record the kinetic traces of different photoemission regions. The lifetime (τ) and rate constants for the radiative decay (k_R) and nonradiative decay (k_{NR}) for the spin-coated non-LC film (*Film 0*), the nonaligned (*Film I*) and fully-aligned (*Film II*) F8BT nematic films are summarized in **Table 4.2** and **Figure 4.21**. The rate constants were calculated based on the equations: $1/\tau = k_R + k_{NR}$, PLQE $= k_R/(k_R + k_{NR})$.

The spin-coated non-LC F8BT film exhibits the shortest lifetime (1.02 - 1.16 ns) and the lowest PLQE, which can be ascribed to a prevalence of the nonradiative decay associated with a highly distorted microstructure. Quenching from the nematic phase increases the intrachain PL lifetime by 30% - 40%, whereas the SD1-mediated uniaxial alignment of the chain orientation does not appear to change the lifetime further since the measured PL emission in both cases is dominated by the efficient intrachain radiative recombination. For all of the SD1-aligned F8BT nematic films, the $PL_{//}$ emission exhibits a slightly longer lifetime than the $PL_{\perp}$ emission. The formation and preservation of a polydomain LC texture in the nematic films, irrespective of the SD1-alignment of the F8BT chain-orientation, effectively suppresses the nonradiative decay/traps in the amorphous-phase F8BT by promoting the non-radiative interchain FRET energy funnelling to enhance the radiative decay of an intrachain charge-transfer character. However, such a suppression is lessened in the photoaligned F8BT nematic monodomain films, where the relative weight of amorphous F8BT is dramatically reduced while emissive interchain fluorescence with a significantly low PLQE is augmented. However, the domain boundaries and associated enhancement in both the amorphous phase fraction and the (nonradiative) interchain energy/exciton migration have been reported to be beneficial in terms of limiting nonradiative defects in other fluorescent LCCP polyfluorene copolymers [48].

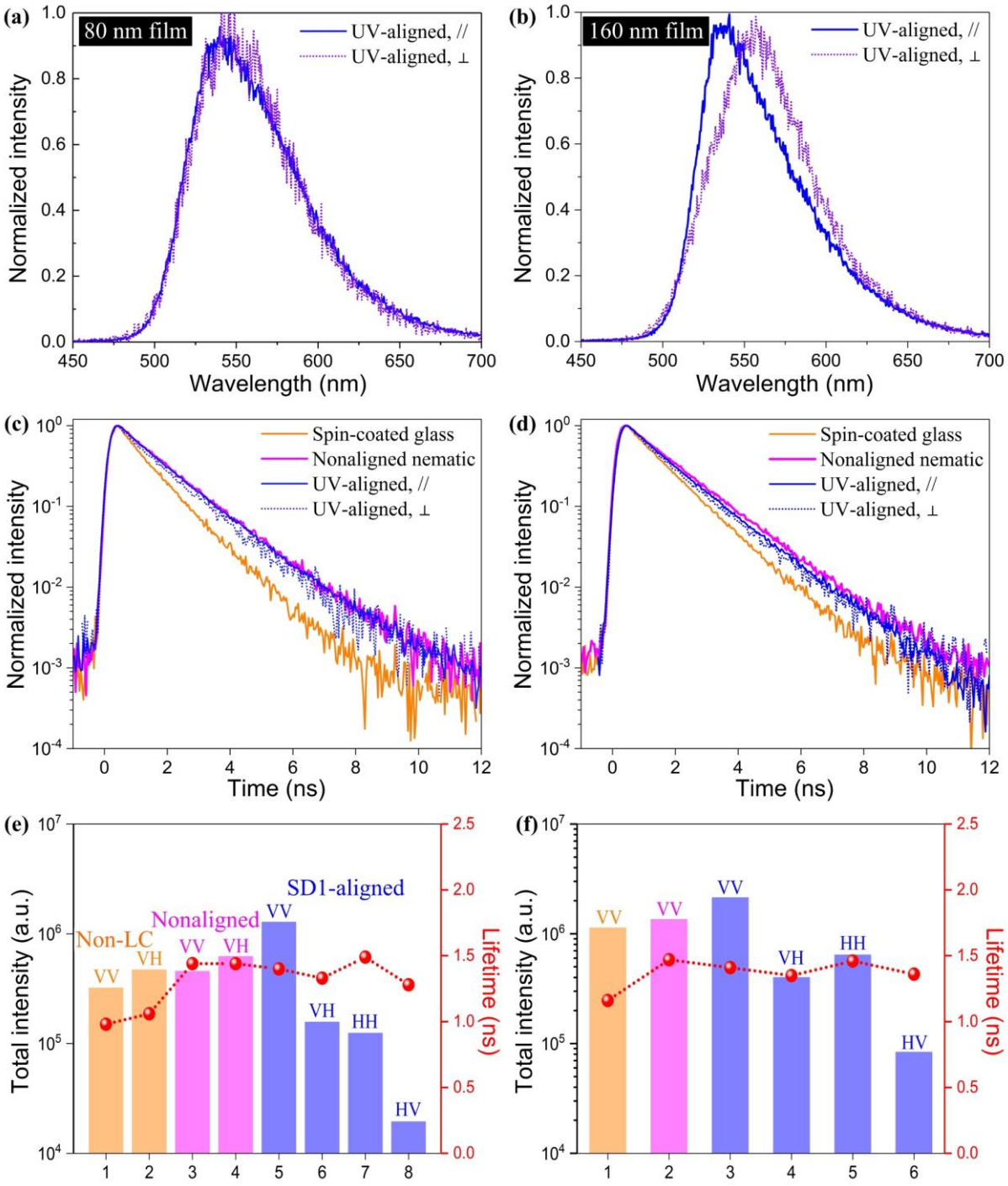

Figure 4.20: (a, b) Areal normalized time-integrated PL spectrum recorded from the fully-aligned F8BT nematic films (*Film II*) with a thickness of 160 nm (a) and 80 nm (b). (c, d) Normalized decay of the total PL intensity from the spin-coated-only (brown, *Film 0*), nonaligned (pink, *Film I*), and fully-aligned F8BT nematic films (blue, *Film II*) recorded using the parallel (the solid blue curve) and perpendicular (the dotted blue curve) configuration, i.e., the excitation polarisation was parallel or perpendicular to the chain alignment direction. All F8BT films are 80 nm in thickness in (c) and 160 nm in (d). (e, f) The total PL intensity (bars) and single exponential fitting lifetime (stars) for the different types of F8BT films with a thickness of 80 nm (e) and 160 nm (f). The excitation laser for polarised PL transients remained linearly polarised along the vertical (*V*) direction in the vertical plane.

The labels used in (e) - (f) are defined as: the first label letter (*V* for vertical, or H for horizontal) represents the chain alignment direction in the aligned F8BT films, and the second label letter (*V* or *H*) for the polarisation of the emission collection.

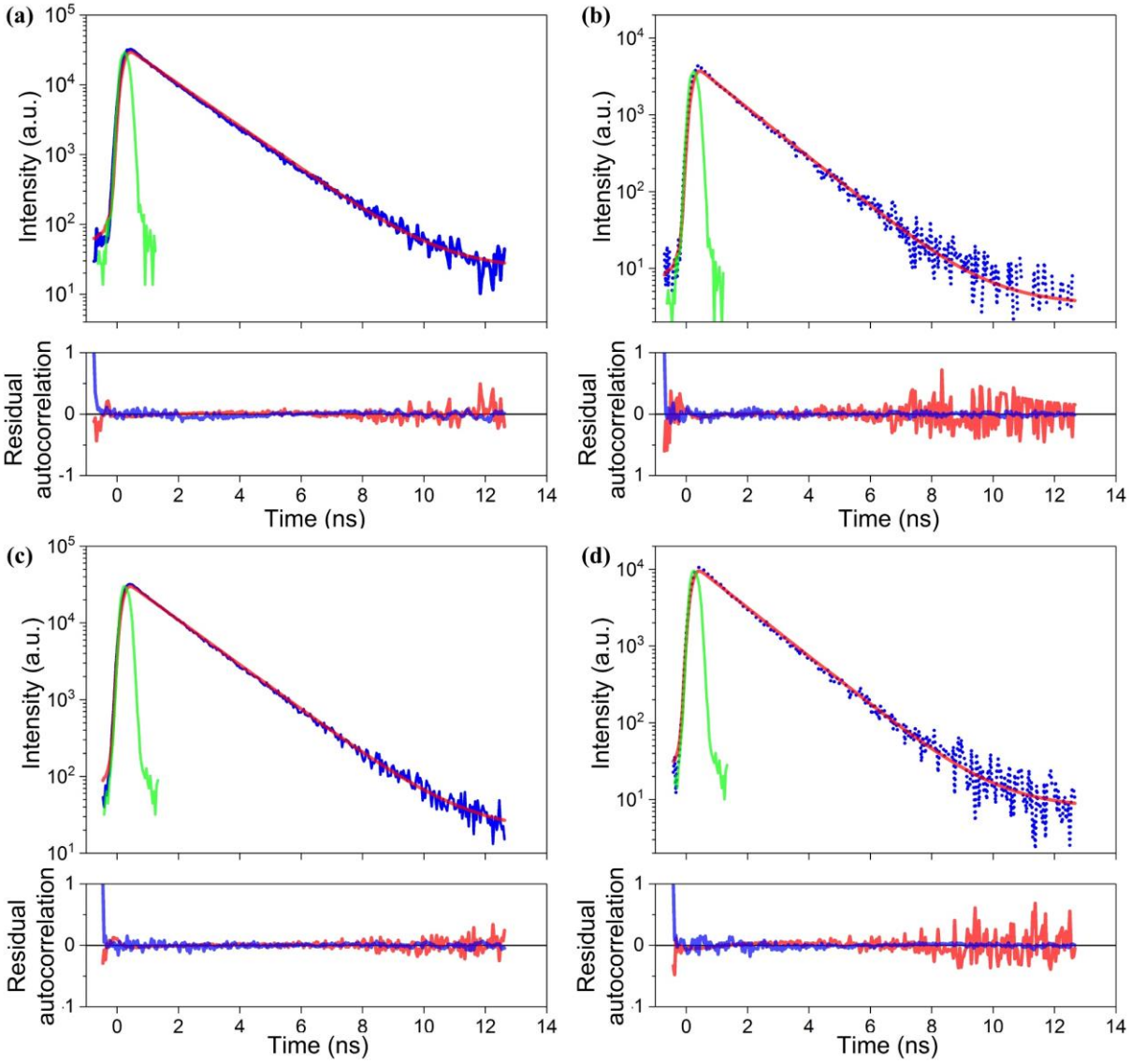

Figure 4.21: (a) Laser-convolved single exponential fitting results of the PL transients from the fully-aligned F8BT nematic film with a thickness of 80 nm (a, b) and 160 nm (c, d). The time-resolved PL detection by the streak camera were excited by the same parallel polarised laser that was aligned to the direction of the alignment of the polymer chains. (a, c) and (b, d) represent the data for the emission collection with light that was aligned parallel or perpendicular to the chain direction, respectively. Our extracted lifetime results at various PL wavelengths indicate that the radiative decay lifetime does not alter with the photon energy in the polarised PL spectra collected from all the measured F8BT film samples.

Table 4.2. Summary of the extracted lifetime (τ) and rate constants for the radiative decay (k_R) and nonradiative decay (k_{NR}) in the spin-coated non-LC F8BT film (*Film 0*) as well as the nonaligned (*Film I*) and fully-aligned (*Film II*) F8BT nematic films.

	80 nm-thick F8BT films			**160 nm-thick F8BT films**		
	Film 0	**Film I**	**Film II**	**Film 0**	**Film I**	**Film II**
LC texture	**Non-LC**	**Poly-domain**	**Aligned domains with unaligned regions**	**Non-LC**	**Poly-domain**	**Mono-domain**
τ **(ns)**	1.02 ± 0.04	1.44 ± 0.04	1.38 ± 0.07	1.16 ± 0.04	1.47 ± 0.04	1.40 ± 0.04
k_R **(10^8 s^{-1})**	2.9 ± 0.1	4.7 ± 0.1	4.4 ± 0.2	3.0 ± 0.1	4.6 ± 0.1	3.6 ± 0.1
k_{NR} **(10^8 s^{-1})**	6.9 ± 0.3	2.2 ± 0.2	2.9 ± 0.3	5.6 ± 0.3	2.1 ± 0.2	3.6 ± 0.3

4.9 Summary

The motivation for the study reported in this Chapter was to investigate the structure-property relationships in the solution-processed light-emitting liquid crystalline conjugated polymers. We report on the use of LC long-range structural ordering and photoalignment of LCCP F8BT chain-orientation to generate different levels of microstructural order (e.g., the order parameter S ≈ 0 - 0.98) in the otherwise structurally disordered spin-coated films. This enables fine-tuning of the chain conformation/orientation, the polymer interchain packing structure and, concomitantly, the photophysical properties of F8BT such as the optical absorption, exciton/energy transfer and photoluminescence efficiencies.

We reveal that the intrinsic long-range orientational order present in the LC mesophase of F8BT facilitates the stabilisation of a minor fraction (5%) of polymeric nanocrystals (identified to have the most extended planar chain conformation, and 3D isotropic coherence lengths of ~14.6 nm) dispersed in a highly disordered amorphous-phase host. This bi-phase texture resembles a bioinspired ‘self-doped’ host-guest system; these LC self-organised F8BT glass films exhibit a polydomain texture that allows record-high PLQE performance via 3D non-radiative host-to-guest FRET funnelling to enable more efficient intrachain PL emission.

The chain orientation in the localised polymeric nanocrystals as the fluorophoric guest inclusions is randomly distributed, evidenced by the smearing of the characteristic GIWAXS ring. These LC self-organised polymeric nanocrystals are thought to have an alternating interchain packing structure and to be most probably responsible for the appearance of the extra lower-energy absorption species and, simultaneously, the domination of the 0-0 vibronic transition in the PL spectra recorded from the nonaligned F8BT nematic polydomain glass films. Compared with the PL efficiencies of 29% - 35% determined for the spin-coated-only non-LC F8BT films, the LC structural self-organisation in the nematic polydomains gives rise to >70% PL efficiencies, which approach the PL efficiency limit of F8BT solutions and are also among the highest values reported for light-emitting LCCP solid-state films. On the contrary, the spin-coated non-LC amorphous films is supposed to energetically favour a highly twisted chain-conformation with a greater population of extremely localised BT-to-BT interactions in order to minimise steric hindrance. Such an extremely disordered F8BT packing structure leads to the absence of long-range structural order, the dominance of a low-energy (0-1) vibronic transition in the PL spectra, and the lowest PLQE values among all the measured F8BT films. In addition, the significantly high degrees of structural disorder in these amorphous F8BT films in the as-prepared state would induce a relatively localised yet strong coupling of the excited state to the ground state and, therefore, shorten the PL emission lifetime.

Within the bi-phase polydomain host-guest system enabled by LC microstructural re-configuration, the spatial energy level differences between the self-organised polymeric nanocrystals and the amorphous-phase matrix drive nonradiative excitonic energy funnelling. The 3D FRET funnels excitation energy from the chromophoric amorphous host onto local highly-oriented nanocrystals, drawing carrier recombination away from traps associated with electronic/energetic disorder and therefore significantly improving the PL intensity and PLQE. This PLQE-enhancement mechanism is in analogous to the ability of adaption of natural light-

harvesting antennas to the temporal sunlight intensity change in the environment, where mechanism of adjusting the number ratio of LH1 complexes to larger LH2 acceptor is adopted to regulate real-time light-harvesting performance.

The relative weight of the amorphous-phase chromophoric host in the nonaligned F8BT nematic film and the radiative interchain PL decay play a key role in determining the PL emission from localised polydomains and the overall PLQE. The spectral results of polarised μ-PL measurements across different locations around the F8BT nematic domains highlight that the PL spectral lineshapes from the Schlieren polydomains and the photoaligned extended monodomain are very similar. The boundary regions by accommodating a greater fraction of amorphous-phase F8BT chains are found to be more favorable than the domain interior, in terms of enhancing the FRET/PL efficiencies, donor/acceptor spectral overlapping and suppressing nonradiative decay. The former suggests that the fluorophoric polymeric nanocrystals, though taking up a very low fraction (~5%) in the nonaligned glass film, literally dedicate the fluorescence behaviour of the polydomain film by making the major fraction of disorder F8BT matrix non-emissive and deactivating traps associated with structural/energetic disorder. Another validation for the self-organised self-doped host-guest behaviour has been showcased by systematically tailoring the polydomains in nonaligned F8BT nematic glass films, via the utilisation of a power-law scaling of the nematic domain size with the film thickness (i.e., a film-thickness modulation of domain boundary fraction in the nematic polydomain glass film). Our best PLQE results are, indeed, obtained from the nonaligned thinner (80 nm-thick) nematic glass films with the smallest domain size among all measured F8BT nematic films.

High-quality uniaxial chain orientation in the photo-aligned F8BT nematic monodomain glass films facilitates the enhancement of the absorption strength parallel to the F8BT chain alignment direction and large anisotropies in both the F8BT packing structure and the polarised

PL intensity. The identified large anisotropy of the in-plane packing structure of F8BT chains, and associated enhancement in the interchain conjugation (and BT-to-BT electronic coupling) and interchain emission, are most probably responsible for the general decrease in the PLQE as a function of the chain-alignment quality (e.g., in terms of optical dichroic ratio presented in Figure 4.12(b)). Strong/long-range electronic coupling and interchain energy transfer are usually accompanied by low PLQE values as they are more likely able to allow the excited states to be tightly bonded as weakly emissive species (e.g., excimer and aggregate) and/or access more nonemissive states before emitting.

Significant improvement in the polymer crystallinity, the intrachain conjugation, and the microstructurally-mediated radiative interchain recombination in the highly-oriented F8BT nematic monodomains result in the polarisation-dependent PL spectral separation of the two orthogonal emission components of distinct characters (Figures 4.11(c) and 4.14(e)), along with the dramatic broadening of the PLE band at both short-and long-wavelengths for the 0-0 vibronic PL transition (Figure 4.11(d)). Although the underlying mechanism for the occurrence of these new phenomena is not well understood, it should be correlated with the competition and efficiency of the intrachain and interchain emissive species in the photo-aligned, condense packed nematic monodomains.

A synergic effect of the LC restructuring, SD1 molecular photo-patterning and ultimately preserving the long-range LCCP orientational order makes it possible to access very highly localised intrachain and interchain states, and to produce significant anisotropies in the charge-carrier mobility [51] and refractive index [52] between the parallel and perpendicular directions to the polymer chain orientation. These huge potentials and the unique photo-patternablity of the SD1-aligned polymer chain-orientations allow for novel and/or performance-improved photonic, charge transporting and optoelectronic devices.

References

[1] G. D. Scholes, G. R. Fleming, A. Olaya-Castro, R. van Grondelle, Lessons from nature about solar light harvesting. *Nature Chem.* **3**, 763 (2011).

[2] S. Kundu, A. Patra, Nanoscale strategies for light harvesting. *Chem. Rev.* **117**, 712 (2017).

[3] G. McDermott, S. M. Prince, A. A. Freer, A. M. Hawthornthwaite-Lawless, M. Z. Papiz, R. J. Cogdell, N. W. Isaacs, Crystal structure of an integral membrane light-harvesting complex from photosynthetic bacteria. *Nature* **374**, 517 (1995).

[4] W. Kühlbrandt, Many wheels make light work. *Nature* **374**, 497 (1995).

[5] S. Scheuring, J.N. Sturgis, V. Prima, A. Bernadac, D. Levy, J. Rigaud, Watching the photosynthetic apparatus in native membranes. *Proc. Natl. Acad. Sci. U.S.A* **101**, 11293 (2004).

[6] B. J. Schwartz, Conjugated polymers as molecular materials: How chain conformation and film morphology influence energy transfer and interchain interactions. *Annu. Rev. Phys. Chem.* **54**, 141 (2002).

[7] J. L. Herek, W. Wohlleben, R. J. Cogdell, D. Zeidler, M. Motzkus, Quantum control of energy flow in light harvesting. *Nature* **417**, 533 (2002).

[8] D. Beljonne *et al.*, Interchain vs. intrachain energy transfer in acceptor-capped conjugated polymers. *Proc. Natl. Acad. Sci. U.S.A* **99**, 10982 (2002).

[9] S. Fratini, M. Nikolka, A. Salleo, G. Schweicher, H. Sirringhaus, Charge transport in high-mobility conjugated polymers and molecular semiconductors. *Nature Mater.* **19**, 491 (2020).

[10] J. A. A. W. Elemans, R. van Hameren, R. J. M. Nolte, Alan E. Rowan, Molecular materials by self-assembly of porphyrins, phthalocyanines, and perylenes. *Adv. Mater.* **18**, 1251 (2006).

[11] P. L. Burn, A. B. Holmes, A. Kraft, D. D. C. Bradley, A. R. Brown, R. H. Friend, R. W. Gymer, Chemical tuning of electroluminescent copolymers to improve emission efficiencies and allow patterning. *Nature* **356**, 47 (1992).

[12] B. K. Yap, R. Xia, M. Campoy-Quiles, P. N. Stavrinou, Donal D. C. Bradley, Simultaneous optimization of charge-carrier mobility and optical gain in semiconducting polymer films. *Nature Mater.* **7**, 376 (2008).

[13] V. I. Klimov *et al.*, Optical gain and stimulated emission in nanocrystal quantum dots. *Science* **290**, 314 (2000).

[14] D. D. C. Bradley, Conjugated polymer electroluminescence. *Synth. Met.* **54**, 401 (1993).

[15] M. R. Wasielewski, Self-assembly strategies for integrating light harvesting and charge separation in artificial photosynthetic systems. *Acc. Chem. Res.* **42**, 1910 (2009).

[16] K. Nakano, K. Tajima, Organic planar heterojunctions: From models for interfaces in bulk heterojunctions to high-performance solar cells. *Adv. Mater.* **29**, 1603269 (2017).

[17] Y. Deng *et al.*, Deciphering exciton-generation processes in quantum-dot electroluminescence. *Nature Commun.* **11**, 2309 (2020).

[18] T. A. S. Doherty *et al.*, Performance-limiting nanoscale trap clusters at grain junctions in halide perovskites. *Nature* **580**, 360 (2020).

[19] J. C. Bolinger, M.C. Traub, T. Adachi, P. F. Barbara, Ultralong-range polaron-induced quenching of excitons in isolated conjugated polymers. *Science* **331**, 565 (2011).

[20] N. Hildebrandt *et al.*, Energy transfer with semiconductor quantum dot bioconjugates: a versatile platform for biosensing, energy harvesting, and other developing applications. *Chem. Rev.* **117**, 536 (2017).

[21] T. Franzl, T. A. Klar, S. Schietinger, A. L. Rogach, J. Feldmann, Exciton recycling in graded gap nanocrystal structures. *Nano. Lett.* **4**, 1599 (2002).

[22] J. Feng, X. Qian, C. Huang, J. Li, Strain-engineered artificial atom as a broad-spectrum solar energy funnel. *Nature Photonics* **6**, 866 (2012).

[23] G. E. Eperon, M. T. Hörantner, H. J. Snaith, Metal halide perovskite tandem and multiple-junction photovoltaics. *Nature Rev. Chem.* **1**, 0095 (2017).

[24] F. Würthner, T. E. Kaiser, C. R. Saha-Möller, J-aggregates: from serendipitous discovery to supramolecular engineering of functional dye materials. *Angew. Chem. Int. Ed.* **50**, 3376 (2011).

[25] F. C. Spano, C. Silva, H-and J-aggregate behavior in polymeric semiconductors. *Annu. Rev. Phys. Chem.* **65**, 477 (2014).

[26] D. Hu, J. Yu, K. Wong, B. Bagchi, P. J. Rossky, P. F. Barbara, Collapse of stiff conjugated polymers with chemical defects into ordered, cylindrical conformations. *Nature* **405**, 1030 (2000).

[27] Y. Shi, P. S. Salter, M. Li, R. A. Taylor, S. J. Elston, S. M. Morris, D. D. C. Bradley, Two-photon laser-written photoalignment layers for patterning liquid crystalline conjugated polymer orientation. *Adv. Funct. Mater.* **31**, 2007493 (2021).

[28] H. Zhang, L. Ma, Q. Zhang, Y. Shi, Y. Fang, R. Xia, W. Hu, D. D. C. Bradley, Azobenzene sulphonic dye photoalignment as a means to fabricate liquid crystalline conjugated polymer chain-orientation-based optical structures. *Adv. Optical Mater.* **8**, 1901958 (2020).

[29] V. G. Chigrinov, V. M. Kozenkov, H. S. Kwok, *Photoalignment of Liquid Crystalline Materials: Physics and Applications*, John Wiley & Sons, West Sussex, England, 2008.

[30] A. M. Donald, A. H. Windle, *Liquid Crystalline Polymers*, Cambridge University Press, Cambridge, 1992.

[31] C. L. Donley, J. Zaumseil, J. W. Andreasen, M. M. Nielsen, H. Sirringhaus *et al.*, Effects of packing structure on the optoelectronic and charge transport properties in poly(9,9-di-n-octylfluorene-alt-benzothiadiazole). *J. Am. Chem. Soc.* **127**, 12890 (2005).

[32] E. Collini, G. D. Scholes, Coherent intrachain energy migration in a conjugated polymer at room temperature. *Science* **323**, 369 (2009).

[33] N. J. Hestand, F. C. Spano, The effect of chain bending on the photophysical properties of conjugated polymers. *J. Phys. Chem. B* **118**, 8352 (2014).

[34] J. M. Winfield *et al.*, Charge-transfer character of excitons in poly [2,7-(9,9-di-n-octylfluorene)(1-*x*)-co-4,7-(2,1,3-benzothiadiazole)(*x*)]. *J. Chem. Phys.* **131**, 035104 (2009).

[35] Q. Zhang *et al.*, Host exciton confinement for enhanced Förster-transfer-blend gain media yielding highly efficient yellow-green lasers. *Adv. Funct. Mater.* **28**, 1705824 (2018).

[36] H. M. Liem, P. Etchegoin, K.S. Whitehead, D. D. C. Bradley, Raman anisotropy measurements: An effective probe of molecular orientation in conjugated polymer thin films. *Adv. Funct. Mater.* 13, 66 (2003).

[37] J. C. de Mello, H. Felix Wittmann, R. H. Friend, An improved experimental determination of external photoluminescence quantum efficiency. *Adv. Mater.* **9**, 230 (1997).

[38] Y. Li, J. B. Lagowski, A multi-step simulation of electron mobility in fluorine-benzothiadiazole conjugated polymer - Case study. *Comput. Theor. Chem.* **977**, 157 (2011).

[39] H. J. Eggimann, F. Le Roux, L. M. Herz, How β-phase content moderates chain conjugation and energy transfer in polyfluorene films. *J. Phys. Chem. Lett.* **10**, 1729 (2019).

[40] X.-H. Jin *et al.*, Long-range exciton transport in conjugated polymer nanofibers prepared by seeded growth. *Science* **360**, 897 (2018).

[41] I. Gryn, E. Lacaze R. Bartolino, B. Zappone, Controlling the self-assembly of periodic defect patterns in smectic liquid crystal films with electric fields. *Adv. Funct. Mater.* **25**, 142 (2015).

[42] T. Ohzono, K. Katoh, C. Wang, A. Fukazawa, S. Yamaguchi, J. Fukuda, Uncovering different states of topological defects in schlieren textures of a nematic liquid crystal. *Sci. Rep.* **7**, 16814 (2017).

[43] G. Catalan *et al.*, Fractal dimension and size scaling of domains in thin films of multiferroic $BiFeO_3$. *Phys. Rev. Lett.* **100**, 027602 (2008).

[44] G. Catalan, J. Seidel, R. Ramesh, J. F. Scott, Domain wall nanoelectronics. *Rev. Mod. Phys.* **84**, 119 (2012).

[45] E. B. Burlakova, A. E. Shilov, S. D. Varfolomeev, G. E. Zaikov (eds.), *Chemical and Biological Kinetics*. New Horizons. Vol. 1. *Chemical Kinetics*, VSP Int. Publ., Leiden-Boston, 2005.

[46] N. Lee, D. Diddens, H. Meyer, A. Johner, Local chain segregation and entanglements in a confined polymer melt. *Phys. Rev. Lett.* **118**, 067802 (2017).

[47] A. Milchev, K. Binder, Linear dimensions of adsorbed semiflexible polymers: What can be learned about their persistence length? *Phys. Rev. Lett.* **123**, 128003 (2019).

[48] M. Ariu, D. G. Lidzey, M. Sims, A. J. Cadby, P. A. Lane, D. D. C. Bradley, The effect of morphology on the temperature-dependent photoluminescence quantum efficiency of the conjugated polymer poly(9,9-dioctylfluorene). *J. Phys.:Condens. Matter.* **14**, 9975 (2002).

[49] R. Xia, G. Heliotis, D. D. C. Bradley, Fluorene-based polymer gain media for solid-state laser emission across the full visible spectrum. *Appl. Phys. Lett.* **82**, 3599 (2003).

[50] S. Milanese, M. L. De Giorgi, Ma. Anni, Determination of the best empiric method to quantify the amplified spontaneous emission threshold in polymeric active waveguides. *Molecules* **25**, 2992 (2020).

[51] H. Sirringhaus *et al.*, Mobility enhancement in conjugated polymer field-effect transistors through chain alignment in a liquid-crystalline phase. *Appl. Phys. Lett.* **77**, 406 (2000).

[52] F. Le Roux, R. A. Taylor, D. D. C. Bradley, Enhanced and Polarization-Dependent Coupling for Photoaligned Liquid Crystalline Conjugated Polymer Microcavities. *ACS Photonics* **7**, 746 (2020).

Chapter 5

Direct Laser Writing of Photoalignment Layers for Spatially-Patterned Liquid Crystalline Conjugated Polymers

The previous chapters have demonstrated the feasibility of spatial patterning of the alignment of the polymer chains in liquid crystalline conjugated polymers using a combination of SD1 photoalignment layers, UV-exposure and photomasks. However, the alignment patterns that are fabricated are predetermined by the characteristics of the mask whist the spatial resolution is typically limited to several micrometres. In this Chapter, a two-photon direct laser writing (DLW) technique is employed, for the first time, which demonstrates a maskless photoalignment approach that enables bespoke patterns and submicron resolution to be achieved in liquid crystalline conjugated polymers (LCCPs) when deposited on to the two-photon laser-written SD1 photoalignment layers. This fine pattern resolution of the LCCP chain-orientation/conformation is of great importance for prototyping a variety of photonic and optoelectronic structures. DLW using ultrashort pulsed lasers and aberration correction provide unique and fascinating opportunities in terms of unlocking the full potential of the photoalignment technique and subsequently improving the orientation quality in both the photoalignment and the light-emitting LCCP layers. This new photoalignment technology explored in this Chapter is particularly promising for high-resolution, high quality and on-demand spatial patterning of the physical structure of multifunctional LCCPs and other related organic semiconductors.

5.1 Introduction

Direct laser writing (DLW) with ultrafast lasers has become a powerful technique for the versatile structural modification and precise 3D microfabrication of a wide range of photo-responsive materials [1]. In particular, non-linear two-photon laser writing technique has been utilised to sculpturing various functional photonic structures such as ultracompact multi-lens objectives [2] and 3D waveguides in diamond [3], as well as producing high-resolution spatial-patterning in the chemical mixtures of photo-polymerisable polymers [4] and low molecular weight LCs [5]. However, this promising two-photon DLW has yet been explored for locally orienting the photoalignment commanding layers and therefore creating on-demand alignment patterns in the SD1 films.

For the work in this Chapter, we reported the first time use of the two-photon DLW technique as a maskless photoalignment approach to produce bespoke alignment patterns and submicron resolution in both SD1 photoalignment layers and LCCP films deposited on to the laser-written photoalignment layers. When the ultrashort infrared pulses are focused onto the surface of a photoalignment layer, the electric field at the focus can be sufficient to trigger the instantaneous absorption of two photons of half the energy by the chromophores in the photoalignment layer (e.g. SD1). The highly nonlinear nature of this two-photon absorption process means that the rate depends nonlinearly on the intensity, which leads to smaller voxels in the focal plane [6,7] compared with that obtained using single photon illumination (as-shown in **Figure 5.1**). In this work, the objective is to apply DLW to photoalignment layers in order to align liquid crystal conjugated polymers. Using two-photon laser writing leads to a reduction in the excited material volume in the SD1 photoalignment layer so that alignment only takes place within a very small volume, which leads to a high spatial resolution of the alignment of the SD1 molecules in the substrate plane.

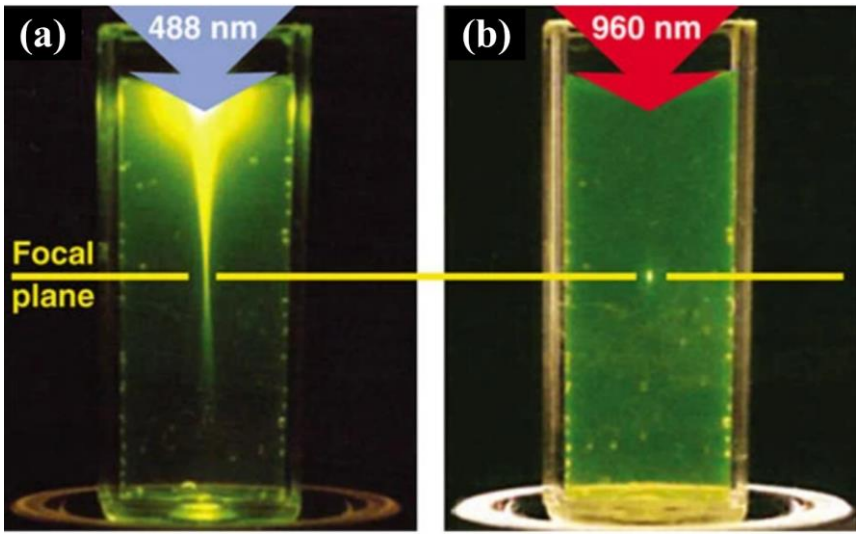

Figure 5.1: Localization of the excitation of fluorescein by two-photon absorption. (a) Single-photon excitation by focused light (488 nm; 0.16 NA). (b) Two-photon excitation using focused (0.16 NA) femtosecond pulses of 960-nm light. Images were reproduced from [7].

For the work in this thesis, an ultrafast DLW system is used that includes adaptive optics elements, which allow for facile spatiotemporal modulation of the phase and amplitude of the writing beam [8]. Optical aberrations occur when the writing beam propagates through a non-uniform distribution of the refractive index, which introduces a spreading out of the intensity in the focal plane [9]. In the absence of any correction, aberrations degrade the beam focusing resolution from the ideal diffraction limit. Adaptive phase compensation methods such as pre-programming a liquid crystal (LC) spatial light modulator (SLM) enables aberration correction to be applied so as to reduce the size of the focal region of the laser beam [8,10]. A combination of the nonlinear nature of two-photon absorption and the adaptive aberration correction can therefore significantly enhance the spatial pattern resolution in the laser-written SD1 alignment, which is subsequently transferred to a patterning of the chain-orientation in an overlying liquid crystal conjugated polymer (LCCP) film.

Utilising the DLW technique to achieve photoalignment could lead to further benefits. For example, it would be possible to reconfigure the pattern design by programming the motion of the sample stage relative to the laser focus, enabling a greater degree of photo-patterning

flexibility [11]. Using a high-precision 2D translation stage on which the photoalignment layer (SD1)-coated substrate is placed, it would be possible to produce arbitrary 2D alignment patterns by trimming a bi-directional raster of the DLW scanned lines. This would potentially negate the need for the design and fabrication of a photomask, which is a necessity for spatial patterning when polarised UV-illumination is employed, as described in the previous chapters.

After the laser writing process has been conducted, heating to the nematic LC phase would enable the laser-written SD1-alignment patterns to be transferred to an overlying LCCP film thereby resulting in the long-range orientational ordering of the polymer chains. Furthermore, the integration of laser-written photoalignment patterns in stacked multilayers of alternating SD1 and LCCP films could potentially give rise to high-resolution 3D control over more complicated photoalignment networks, and hence potentially facilitate the fabrication and/or performance improvement of LCCP-based optical circuits.

The photoalignment direction and pattern resolution of the long-range orientational order of SD1 molecules and subsequently the LCCP chains are dictated by the spatial distribution of the laser focus intensity and polarisation. In this work, the ultrafast DLW facility enables the wavefront and polarisation of the ultrashort laser pulses to be tuned. Previous research has shown that it is possible to generate multiple foci simultaneously using reflective SLMs displaying computer-generated holograms [10,12]. Moreover, a well-controlled spatial distribution of the laser focal intensity and polarisation [3] would enable sophisticated photoalignment patterns to be written with ultrahigh resolution, such as birefringence vortices and 2D organic microcavities. This powerful capability would unlock new potential applications for photoaligned LCCPs. In the following, the use of laser writing to structure photoalignment layers so as to align the polymer chains in LCCPs is demonstrated.

5.2 Aberration-Corrected Two-Photon Laser Direct Writing

5.2.1 The Experimental Setup

The experimental setup for laser writing of a photoalignment layer is schematically shown in **Figure 5.2**. The laser source was a titanium sapphire ultrafast oscillator (Spectra Physics Maitai) with a central wavelength of 785 nm and a pulse repetition rate of 80 MHz. The pulse duration at the sample was 250fs. The laser was linearly polarised and the power was attenuated via a reflective variable neutral density (ND) wheel. The beam from the laser was expanded to fill the back aperture of a high numerical aperture (NA) microscope objective lens. Aberration correction was applied with the use of a computer-programmable liquid crystal SLM, positioned prior to the objective lens, which generated the conjugate phase of the distorted focus in the absence of any correction. This ensured that the system was able to produce a diffraction-limited laser spot at the SD1 layer.

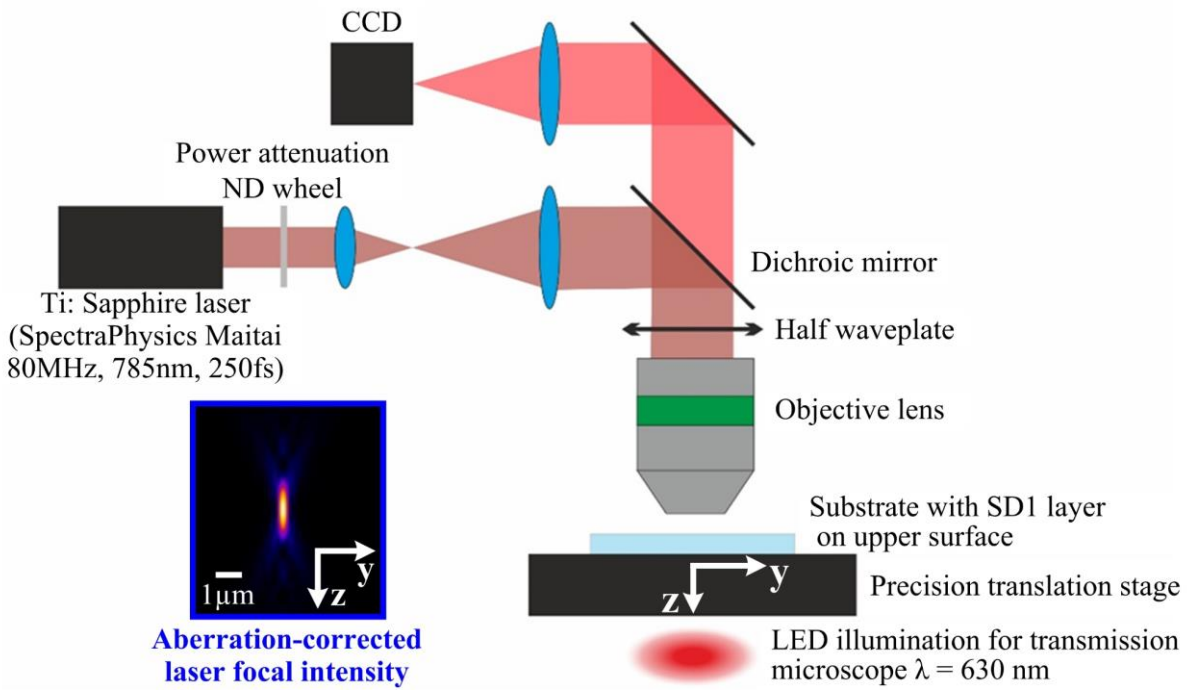

Figure 5.2: The optical setup for two-photon laser direct writing of a photoalignment layer. The insert (extracted from [13]) on the bottom left is a side-viewed image demonstrating the stimulated spatial distribution of the laser focal intensity of this setup inside diamond based on a Fourier optics model within Hecht software.

The SD1 photoalignment layer was mounted beneath the objective lens on a 3D stack of high precision positioning stages (Aerotech ABL10100 (*x*-*y*) with ± 50 nm repeatability and ANT-95 (*z*)). The desired alignment patterns were written by means of translating the substrate relative to the fixed laser focus. A rotatable half waveplate was positioned above the objective lens to control the direction of the polarisation at the sample, and hence the resulting alignment direction of the SD1 layer. The average laser power used for photoalignment was measured using a thermal power meter placed just before the objective lens. An LED (λ = 630nm) positioned beneath the sample provided illumination for a transmission microscope for real time monitoring of the sample during the laser writing process. A dichroic mirror positioned above the objective lens separated the light from the laser and the LED, with the LED light being directed onto a CCD detector.

5.2.2 Key Laser-Writing Parameters

The key factors that are of importance in terms of dictating the pattern resolution and photoalignment quality include:

- **Numerical aperture of the focusing objective lens**

  The spot size in the focus plane of the femtosecond pulsed infrared laser is limited by 0.5 λ / NA = 392.5 nm / NA, hence highlighting that in principle a greater NA objective leads to a greater focusing resolution. The inset in Figure 5.2 shows the spatial distribution of the laser focal intensity obtained with an SLM-corrected 1.4 NA lens in the DLW system. Although the focal spot displayed a characteristic elongation along the out-of-plane (*z*) direction, the full width at half maximum (FWHM) of the focal spot size in the substrate plane (*x*-*y* plane) remained of the order of 250 - 300 nm, which tallies with the theoretically predicted resolution of ~280 nm. Additionally, it should be noted that a higher NA objective lens introduces a larger degree of polarisation distortion in the focal plane [8]. As a result,

adopting too high NA lenses in the two-photon DLW can also risk inducing an unexpected laser polarisation distortion; extra polarisation compensation, in this case, will be needed in order to enable fine control over the focal polarisation of the two-photon laser.

- **Laser power and polarisation**

  The collective reorientation process of the SD1 molecules takes place when the absorbed photon energy in a specific area of the photoalignment layer overcomes the energy barrier between the final highly oriented state and the initial non-aligned configuration. Exceeding this excitation threshold demands sufficiently high laser power with appropriate polarisation direction. As discussed previously, the polarisation direction/distribution at the focus of the laser writer not only defines the ultimate molecular orientation upon completion of the laser-written photoalignment in an SD1 layer, but also has a huge impact on the resulting LC alignment in the SD1-oriented LCCP film. The relative angles between the first and second laser writing process of the SD1 photoalignment can result in different LC alignments and the presence of LC defects in the quenched LCCP glass film. Rewriting with the DLW using an orthogonal polarisation to that used in the previous photoalignment process can result in the formation of defect lines at the intersection between regions of alignment that are orthogonal to one another (also see Section 5.4). Laser rewriting with a polarisation that is not orthogonal to the previous case can result in a continuous variation of the localised chain-orientation at the border of the most recent written pattern.

- **Writing speed**

  The translation speed of the sample relative to the laser focus plays an opposite role to laser power in terms of influencing the absorbed energy by a specific area in the SD1 layer. Assuming all other factors are fixed, a higher writing speed reduces the number of ultrashort pulses irradiated on a specific region in the SD1 layer, which means that the occurrence of

laser-written SD1-alignment is most probably impossible when the writing speed becomes too high to allow the laser excitation to overcome the energy barrier.

- **The separation between adjacent scanning lines**

  The photoalignment quality and pattern resolution of DLW is reliant on the uniformity of the laser writing of a photoalignment layer. In order to ensure continuous coverage of bi-directional laser scanned lines, the separation of the adjacent scanned lines cannot be less than the width of the laser-written lines. Otherwise, the non-written region between neighbouring lines is likely to produce a different LC texture or chain-alignment direction in the corresponding regions in the resulting overlying LCCP glass film.

By taking full advantage of both the tunable laser-writing parameters and the rewritablity of the photoalignment in the SD1 layers, there exist many combinations of writing parameters that can be used for patterning the SD1/LCCP orientation with a high degree of resolution. For example, it is possible to combine macroscopic UV-prealignment of a clean SD1 background with subsequent highly localised laser-written realignment using different polarisation states relative to that of the polarised UV-alignment for enabling complicated chain-orientation patterns in the quenched LCCP films.

Alternatively, multi-step laser re-writing of a photoalignment layer with distinct laser polarisation directions could be particularly useful in terms of tailoring the in-plane distribution of the LCCP chain orientation towards on-demand alignment patterns. As long as the SD1-alignment is spatially patterned, there are a variety of LC materials that could then be aligned using this method and that would be of interest in a wide range of photonic and optoelectronic applications. In this respect, the LC materials parameters (e.g., molecular weight, polydispersity), as well as the LC device structure and critical dimension (e.g., the thickness of

the LC cells and LCCP films) are also limiting factors in terms of the achievable pattern resolution and alignment quality in the SD1-aligned LCs.

5.3 Laser Writing and Rewriting of Photoalignment Layers

In this work, two-photon laser photo-patterning was carried out either by direct writing of a non-aligned SD1 layer or by rewriting of an SD1 layer that had been previously uniformly aligned using polarised UV-illumination. For the *laser-written photoalignment* as schematically shown in **Figure 5.3,** the two-photon laser beam (λ = 785 nm) was tightly focused onto the pristine non-aligned SD1 layer so as to locally align the SD1-molecules. The substrate with the photoalignment layer on it was translated relative to the laser focus using a high-precision *x-y* stage enabling a bespoke alignment pattern on-demand. Two-photon absorption of ultrashort laser pulses by the SD1 chromophores results in highly localised reorientation and/or *cis-trans* isomerization of the SD1 molecules, leading to micron- and nano-scale resolution of the spatial pattern in the SD1 layer and the overlying LCCP glass film.

The rewritablity of the SD1 photoalignment allows for multi-step alignment/pattern in the same SD1 alignment layer and the correspondingly oriented LCCP glass film. For example, a novel combination of spatially uniform alignment using polarised UV-LED-illumination and spatially patterned micron-scale alignment using two-photon laser writing is demonstrated in **Figure 5.4**. Initially, linearly polarised UV-LED light (λ = 365 nm) is shone onto an SD1 film to initiate uniform alignment across the whole substrate. Subsequently, it is feasible to employ the two-photon laser writing to locally re-configure the SD1-alignment. Adjusting the polarisation direction of the writing laser (shown at 90° orientation in Figure 5.4) relative to that used to uniformly align the background using UV illumination, as well as controlling the beam spot size, laser power and scan speed allows generation of bespoke alignment patterns.

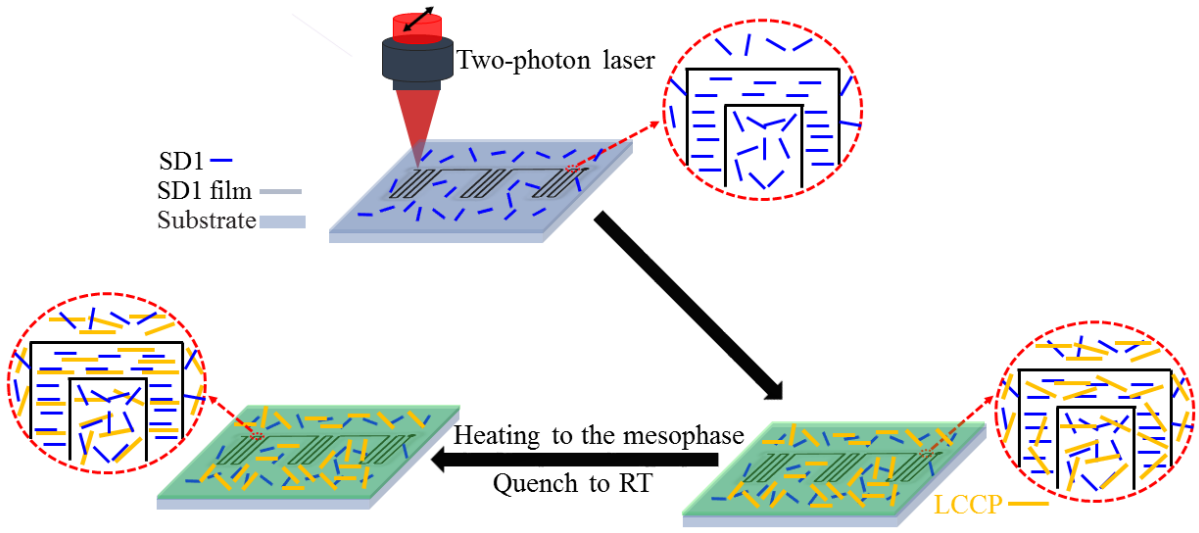

Figure 5.3: Schematic illustration of the procedure employed for the *direct two-photon laser writing* of a non-aligned SD1 photoalignment layer for patterning the polymer chain-orientation in an overlying LCCP glass film. Local regions of the pristine SD1 layer are DLW-aligned; a LCCP film is then deposited onto the laser-patterned SD1 layer and heated to 265 °C (isotropic melt) before slow cooling into the nematic liquid crystal phase, where the polymer chains become oriented along a direction defined by the SD1 molecular orientation. The LCCP main-chains and associated optical transition dipole moment orientations are frozen-in by rapid quenching to room temperature to form a nematic glass film.

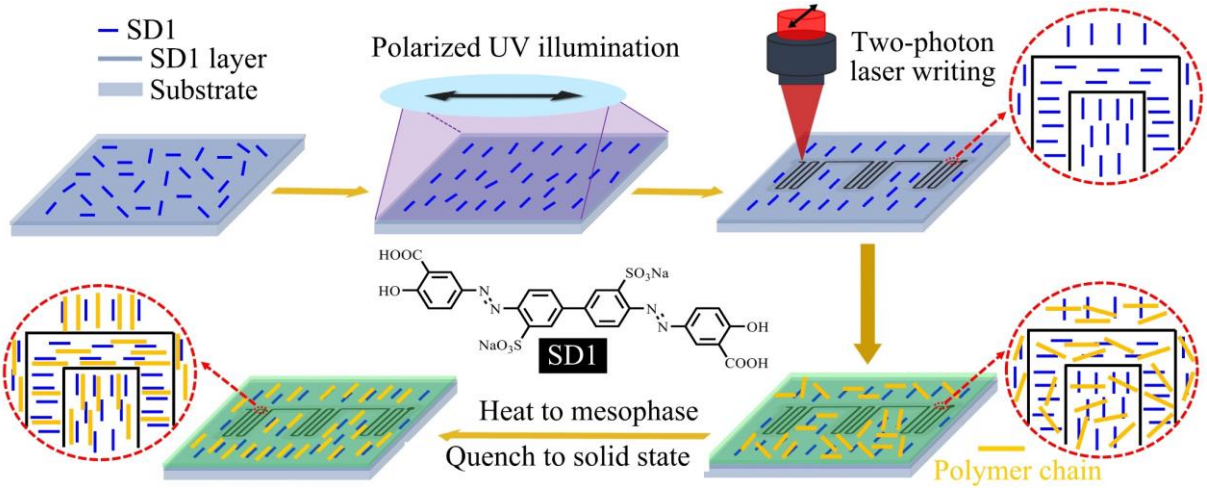

Figure 5.4: Schematic illustration of the procedure employed for the *direct two-photon laser re-writing* of uniformly prealigned SD1 photoalignment layer by polarised UV exposure, which is subsequently used for patterning the polymer chain-orientation in an overlying LCCP glass film. The polarisation of the two-photon laser writer for the rewritten alignment is shown to be perpendicular to that of the linear polarised UV illumination used for uniaxial SD1-alignment prior to the locally laser-rewritten SD1-alignment.

Adjusting the polarisation direction of the writing laser relative to that used either for the uniform UV-alignment of the background or during a step before the laser-written SD1-alignment, allows the SD1 orientation and/or in-plane 2D distribution to be manipulated in the photoalignment layer. Subsequently, the alignment pattern in the photoaligned SD1 layers can be transferred to an LCCP glass film that is deposited on top of the alignment layer by entering the nematic LC phase, which exists at elevated temperatures. The use of the nematic LC mesophase enables the alignment written into the SD1 photoalignment layer to be communicated through the bulk of the LCCP film. The process of heating up to the nematic LC phase followed by quenching was carried out in an inert atmosphere in order to avoid the occurrence of any unwanted oxidation in the LCCP layer.

The lower two panels of Figure 5.4 schematically demonstrate the LCCP chain-orientation process, in which a UV/laser-aligned SD1 layer is used to orient an LCCP film by making use of the inherent long-range orientational order present in the nematic mesophase of an LCCP. The LCCP film is first spin-coated on top of the photo-patterned SD1 layer. Alignment of the polymer chains in the LCCP layer was achieved using a Linkam THMS600 hot stage with 0.1 ºC resolution. The SD1/LCCP bilayer was then heated at 20 °C min^{-1} slightly above the temperature for the isotropic phase (e.g., 265 °C for F8BT, 200 °C for PFO), before it was slowly cooled at 3 °C min^{-1} to a temperature that lies in the middle of the temperature range of the nematic phase (e.g., 247 - 250 °C for F8BT, 170 °C for PFO) and held there for 10 min. Subsequently, the bilayer sample was rapidly quenched to room temperature by transferring the sample from the hot stage onto a copper bar. This quenching step prevents crystallization and thereby “freezes-in” the SD1-mediated ordering of the LCCP polymer backbones, yielding a highly oriented nematic glass film.

5.4 Examples of Laser-Written Alignment Patterns

In order to initially identify appropriate values of the key writing parameters, and also to demonstrate the feasibility of two-photon DLW for photoalignment of low molar mass LCs and LCCPs, experiments involving laser (re)writing of SD1 photoalignment layers were carried out. These photoaligned substrates were then used to align the LC director in low molar mass nematic LC mixtures (E7) in glass cells as well as the polymer chain orientation in PFO and F8BT LCCP films. The bright-state and dark-state as observed on a crossed polariser optical microscope (POM) of the resulting LC-alignment are demonstrated in **Figures 5.5** and **5.6**, in which the patterning is exemplified by a group of separated lines and concentric circles.

At first, two-photon laser-rewritten photoalignment was adopted to fabricate a group of 50 μm-long lines that were written into the SD1 alignment layer with a 0.5 NA objective lens over a range of laser powers (from 5 mW to the maximum available of 35 mW) and writing speeds (i.e., substrate displacement rates, ranging from 5 μm s^{-1} to 50 μm s^{-1}). The orientation of the incident laser polarisation was at 90° with respect to the polarisation of the UV light source used to align the sample before the laser writing process. A laser-rewritten SD1 substrate was then paired with a uniformly UV-aligned SD1 substrate to assemble a 2 μm-thick glass cell, which was then capillary filled with the nematic LC mixture E7. The UV-aligned orientations on the two SD1-coated substrates were configured to be parallel to one another. Therefore, after the laser writing process, which results in lines that exhibit an orthogonal alignment, this leads to twisted configuration for regions defined by the laser-written lines.

Figure 5.5(a) shows no evidence of a laser-written line in the laser patterned regions of the nematic LC cell when the laser power was too low and/or the writing speed was too high. See, for example, the results when a power of 5 mW was used. Increasing the laser power for a fixed writing speed appears to lead to thicker and more obvious lines. Alternatively, increasing

the writing speed for a fixed power appears to result in a reduction in the linewidth of the laser-written lines. The threshold power for successful two-photon laser writing of a layer of SD1 that has initially been aligned using UV illumination appears to relate to the writing speed, as can be seen in the figure. Higher writing speeds appear to require higher laser powers to overcome the energy barrier for SD1 molecular realignment. For example, the laser power required when using a scanning speed of 50 µm s^{-1} is greater than 25 mW, whereas a lower power threshold of 10 mW power is sufficient when a scan speed of 10 µm s^{-1} is used.

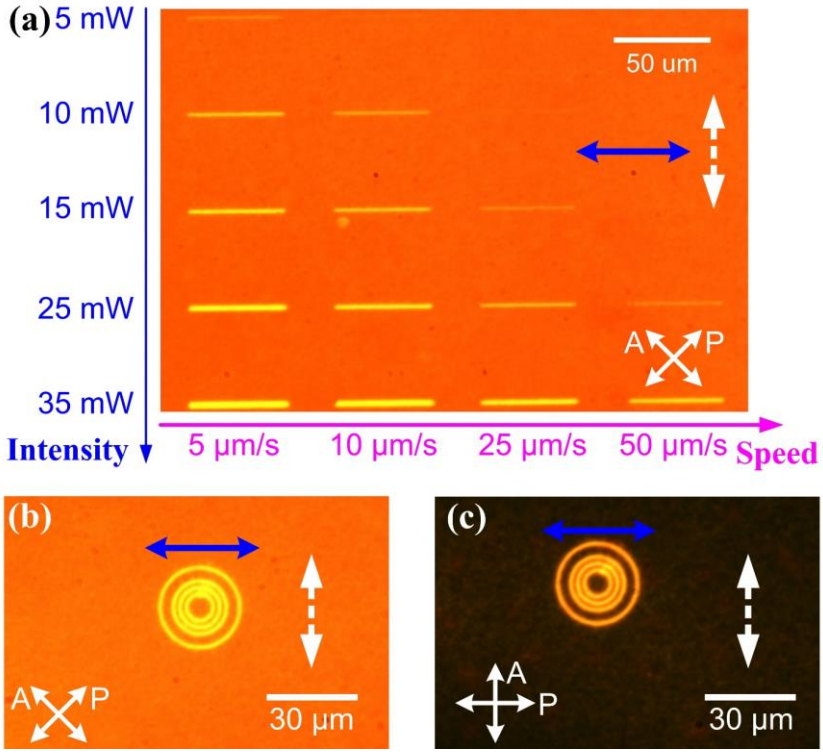

Figure 5.5: POM images demonstrating laser-written alignment patterns formed in a nematic E7-filled glass cell of 2 µm thickness, which was homogeneously aligned by a pair of UV-aligned SD1 layers (~7 nm in thickness) spin-coated from 1 mg/ml SD1 solution in anhydrous 2-methoxyethanol. The solid blue double-headed arrows indicate the laser-patterned alignment directions, while the alignment directions for the UV-aligned background are denoted by the double-headed dashed white arrows. The double-headed solid white arrows denote the orientations of the transmission axes of the polariser and analyser.

Figure 5.5(b) and (c) demonstrate the bright-state and dark state POM images, respectively, of three separate concentric circles in a nematic LC cell, in which the circles were

formed by the laser-writing of a pattern in the SD1 layer using a power and scanning speed of 25 mW and 10 µm s^{-1}, respectively. Before the laser writing of the circles, the SD1 layer had been illuminated with UV light to form a uniform orientation of the photoalignment layer. The POM images show that the colour of the laser-written circles in the LC cell changes from red to yellow when the cell is rotated relative to the crossed polariser/analyser pair. Simultaneously, the UV-aligned background changes from bright (red) to dark. The fact that the circles can be seen regardless of whether there is a bright or dark state is indication of the twisted nature of the alignment of the LC in the glass cell corresponding to the regions consisting of a UV-induced alignment on one substrate and an orthogonal laser written alignment on the opposite substrate. From the images, the width of the three circles was estimated to be 1.5 - 2 µm, corresponding to a pattern resolution that is much better than the best achievable resolution that is typically enabled using photomasked UV-alignment.

For the laser-written 1D diffraction pattern in **Figure 5.6**(a) and (b), which are composed of 40 lines with 5 µm periodicity that were laser written into an SD1 layer, a series of lines are clearly visible in a 100 nm-thick PFO film that has been deposited directly onto the SD1 layer. Here it can be seen that the alignment written into the SD1 layer has been communicated through the bulk of the PFO (LCCP) film when the nematic LC phase has been accessed through thermal treatment and this alignment has been locked-in through the quenching process. In contrast to a clear trace of the laser-patterned 1.5 µm-thick lines in the bright-state POM image, the dark-state POM shows a rather less resolved line pattern, together with substantial nonuniformities in the UV-aligned background. This may be indicative of non-uniform chain-orientation in the UV-aligned PFO region or a significant fraction of not well-oriented PFO backbones. Although the laser-writing parameters are not optimised at this stage, neither property is ideal for high-quality LCCP orientation and high-resolution spatial patterning.

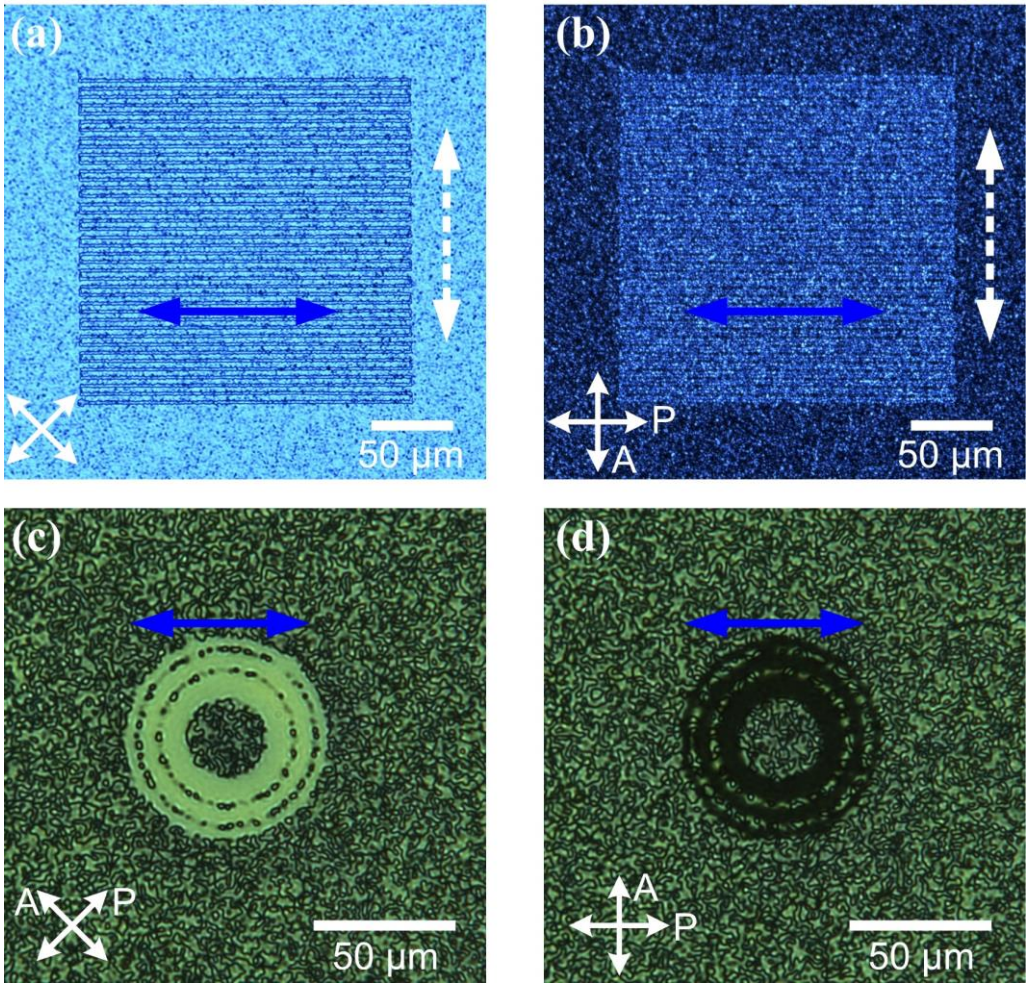

Figure 5.6: POM images demonstrating laser-written alignment patterns formed in SD1 layers (~7 nm in thickness) used to thermotropically orient a layer of 100 nm-thick PFO (a, b) and 165 nm-thick F8BT (c, d) nematic glass films on top of the SD1 layer. The solid blue double-headed arrows indicate the laser-patterned alignment directions, while in the laser-aligned patterns in (a) - (b) the alignment directions for the UV-aligned background are denoted by the double-headed dashed white arrows. The double-headed solid white arrows denote the orientations of the transmission axes of the polariser and analyser.

LCCP films of the polyfluorene, F8BT, were spin-coated on top of a photoaligned SD1 substrate to investigate the photoalignment quality and pattern resolution of the DLW technique. Two-photon laser writing of a spin-coated pristine SD1 layer was conducted with a laser power of 25 mW, 10 µm s^{-1} writing speed, and 1 µm separation of adjacent laser written lines. This time three concentric rings with inner diameters of 30 µm, 50 µm, and 70 µm as well as thicknesses of 8 µm, 4 µm, and 2 µm, respectively, were laser-written into the pristine SD1 layer. Following this, a 165 nm-thick F8BT nematic film was deposited on top of the SD1 layer

and then heated to access the nematic LC phase to induce an alignment of the polymer chains, as determined by the features written into the underlying SD1 layer. POM images of the bright and dark state are shown in Figure 5.6(c) and (d), respectively. These images show a clear indication of the uniformity of the alignment of the F8BT polymer chains in the circular patterns. The dimensions of the three laser-written F8BT circles in the two POM images remain consistent with the dimensions selected in our two-photon laser-writing process. In addition, the non-aligned F8BT background significantly reduces both the spatial-pattern resolution and the overall birefringence contrast due to the existence of randomly oriented polymer backbones. The next step is to consider ways to improve the resolution of the spatial patterning.

5.5 Spatial Pattern Resolution in LCCPs

An advantage of the two-photon laser writing process is the potential for rapid prototyping of complex LCCP structures at high resolution. Experiments were carried out to optimise the writing parameters and improve the pattern resolution and chain-orientation quality in F8BT nematic glass films. Laser-induced SD1-realignment was performed on uniformly aligned SD1 layers that had been prealigned using UV illumination. For this study, a range of writing powers and speeds were considered. Different focusing optics were used, with 0.5 and 0.95 NA lenses (Zeiss 20× or Olympus 50×) yielding theoretically predicted focal spot sizes of 0.8 μm and 420 nm full width at half maximum (FWHM), respectively.

Results are shown in **Figure 5.7** for two different orientations (90° and 45°) of the incident laser beam polarisation relative to the UV light polarisation used for the uniform SD1 prealignment. From inspection of Figure 5.7(a), there is clearly different LC textures in the laser-written F8BT stripes at 90° and 45° alignment relative to the background. The former shows distinct non-uniformity with clear Schlieren textures.

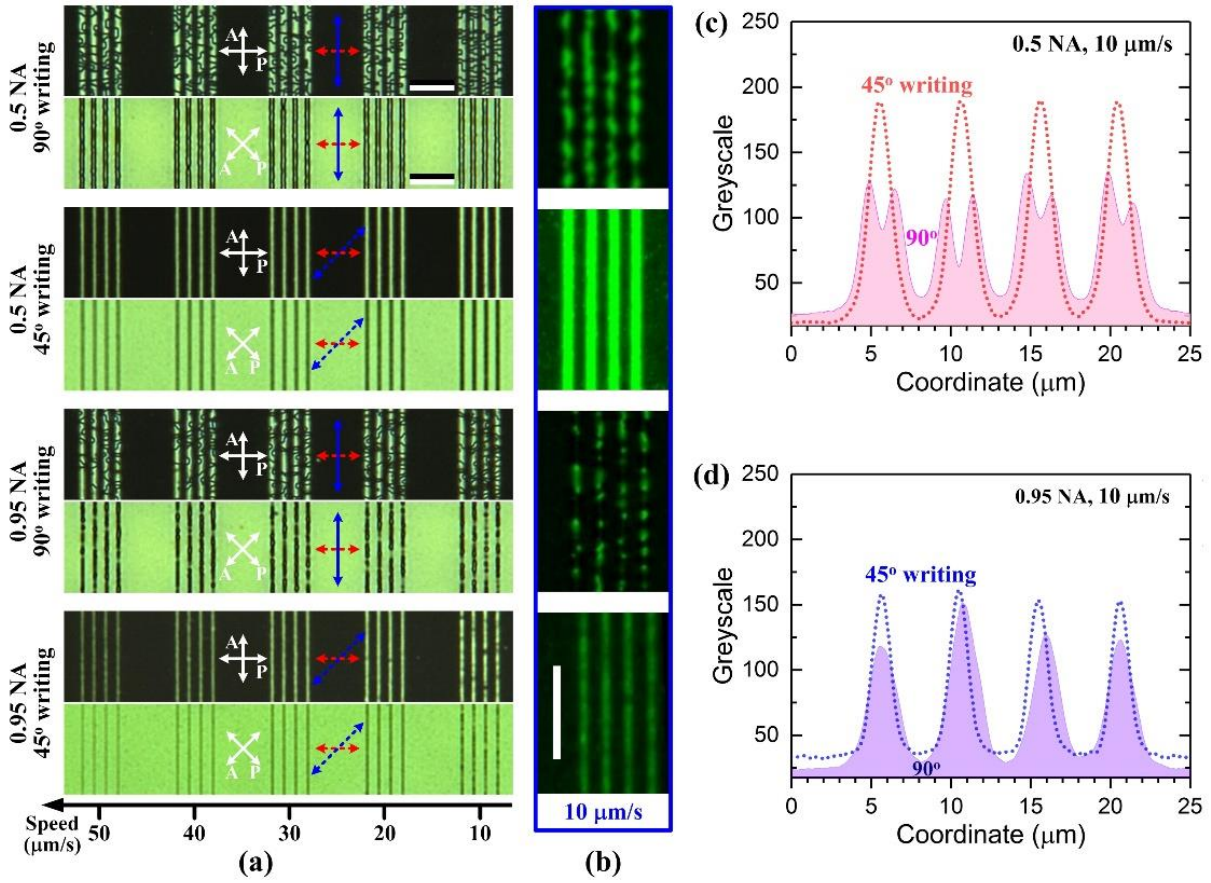

Figure 5.7: Optimisation of the resolution of laser written lines in an SD1 layer and the subsequent alignment of the polymer chains in an F8BT film deposited on top of the SD1 layer. (a) Crossed-polariser microscope images for F8BT oriented on groups of laser-rewritten SD1 lines at 5 μm separation intervals in a UV-prealigned uniform SD1 background. The horizontal scale bars are 20 μm. The top two panels (each with dark and bright states for the background) were written using the 0.5 NA and the bottom two with the 0.95 NA objective lens. The writing speed used for each set of lines is shown by the axis at the bottom of the (a). Results are presented for polarisations of the rewriting laser that are either at 90° (solid double-headed blue arrow; 1st and 3rd panes) or 45° (dashed double-headed blue arrow; 2nd and 4th panes) relative to the UV-alignment of the background (dashed double-headed red arrows). (b) Polarised confocal fluorescence images of the four laser-written F8BT lines with 10 μm s^{-1} rate. The vertical white scale bar in the lowest fluorescence image is 20 μm. (c - d) Plot of the extracted greyscale for the four laser-written F8BT lines with 10 μm s^{-1} speed and 0.5 NA (c) and 0.95 NA (d) objective lens as a function of the horizontal coordinate. Dashed lines are for the 45° alignment whereas as the solid filled lines are for a 90° orientation between the UV aligned background and the laser written lines.

Within Figure 5.7(a), disclination lines are visible throughout the 90° writing sample and these remain black between cross-polarisers for all azimuthal sample orientations. Such LC defects arise only for the 90° writing case, since when the LCCP is heated into its nematic phase there is a degeneracy between the two possible orientations of the director at the border of the laser written regions of SD1 and the UV aligned background, leading to the formation of $\lambda = ½$ disclinations. For the 45° writing case, this degeneracy is lifted such that there is no defect formation and uniformly aligned lines with higher resolution are achievable.

The different LC textures in the images for the 90°- and 45°-written F8BT lines manifest distinct light-emitting properties. Polarised confocal fluorescence images (Figure 5.7(b)) of the four laser-written SD1 lines with 10 μm s^{-1} writing speed were recorded when a black state occurs in the background by adjusting the analyser polarisation for F8BT emission or the maximum fluorescence intensity in the case of the 45°-written lines. The defect lines appear to break, in an irregular way, the spatial continuity of the fluorescence detected in the 90°-written F8BT lines, whereas the lifting of the degeneracy in the 45°-written lines is accompanied by a well-defined and uniform emission intensity. These observations emphasize the benefits of the non-orthogonal two-photon laser writing process with regard to a prealigned background in terms of enhancing the spatial pattern resolution and chain-alignment tunability/uniformity in the oriented LCCP films.

The extracted greyscale profiles for all of the groups of the four laser-written lines created using a 10 μm s^{-1} scanning speed as well as the 0.5 and 0.95 NA focusing objective lenses are plotted in Figures 5.7(c) and (d), respectively. These profiles were used to compare the spatial variation of the defect lines, pattern resolution, and photoalignment quality enabled by two-photon laser writing with the same laser power and writing speed. Compared to the 90° laser-written lines observed in F8BT, the 45°-rewritten lines display a much sharper variation and more reproducible peak intensity in their greyscale profiles, corresponding to a higher spatial

pattern resolution and larger contrast in the birefringence of the F8BT layer between the laser-written lines and the UV-prealigned background. In contrast to the existence of only one greyscale peak for each 45°-rewritten F8BT line, most 90°-rewritten F8BT lines created using the 0.5 NA objective lens were characterised by two intensity peaks and also a broadened width, which was due to the presence of LC defect lines on both edges of the laser written line. The thickness of the F8BT defect-line stipes on each edge is estimated to be 0.6 - 0.9 μm, which is equivalent to a line broadening of 1.2 -1.8 μm across the 90°-rewritten F8BT line.

It is noteworthy that each of the two greyscale peaks observed in a 90°-rewritten F8BT line intersects with the greyscale profile of the corresponding 45°-rewritten line. This implies that for the two laser writing orientations the F8BT LC optical textures resemble each other in the central region of the various laser-rewritten F8BT lines using the same 0.5 NA focusing objective lens. In other words, when ruling out the defect-line broadening effect in the 90°-rewritten F8BT line with the 0.5 NA objective lens, the intensity profiles in the 90°- and 45°-rewritten F8BT lines are very similar to each other. However, the laser-written F8BT lines using the 0.95 NA objective lens become much thinner than the ones written using the 0.5 NA lens. This linewidth reduction would allow direct contact and then a merging of the disclination lines that initialize and grow from the two different edges of a 90°-written F8BT line. Consequently, isolated micro-regions with a high degree of irregularity in terms of the shape are stabilised in the F8BT alignment by the laser-written SD1 layer using the 0.95 NA objective lens, which is also evidenced by the discontinuous fluorescent pattern in the third panel of Figure 5.7(b).

The LC degeneracy-induced defect-line regions not only broaden the 90° laser written F8BT linewidth, but they also result in a decrease in the maximum greyscale intensity and the lack of a well-defined peak. It is shown in **Figure 5.8** that, in contrast to the nearly identical peak intensity for the 45°-written continuous F8BT lines measured for the same writing speed,

there are significant and random fluctuations in the maximum greyscale in the lines that are written with an alignment that is at 90° to the background. Moreover, the greyscale minima for the 90° written lines, which exhibit the $\lambda = ½$ disclinations, are still higher than the uniform greyscale intensity extracted from the dark-state in the UV-aligned background. The greyscale minima (the regions between the laser written lines) for the lines written at 45° relative to the UV-aligned background does decrease to the level in the background region, though the peak intensity of the former decreases linearly as the writing speed increases from 10 μm s^{-1} to 50 μm s^{-1}, together with a reduction in the linewidth.

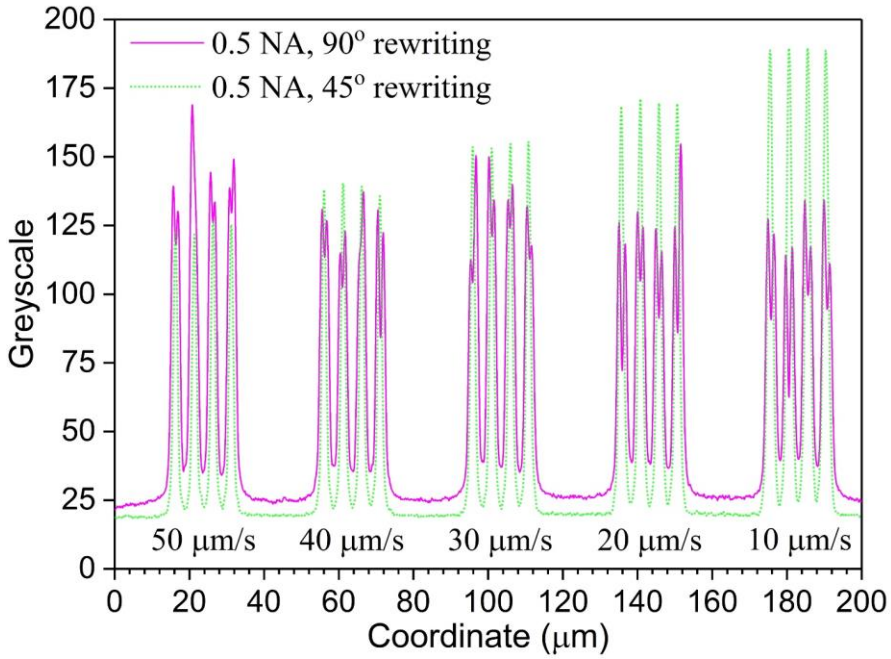

Figure 5.8: The extracted greyscale as a function of the horizontal coordinate for the groups of lines that are laser written at either 90° (the dark-state POM image in the first panel of Figure 5.7(a)) or 45° (the dark-state POM image in the second panel of Figure 5.7(a)) to the UV-aligned background. The results were obtained using a 0.5 NA objective lens and 5 different writing speeds.

Taking all of the information obtained from the greyscale plots and the polarised fluorescence images, we can see that the non-orthogonal laser writing condition appears to yield a higher spatial pattern resolution, a larger birefringence contrast as well as better pattern

reproducibility. In contrast, the 90° laser written F8BT lines exhibit irregular shapes but higher fluorescence intensity relative to the UV-aligned background, which is oriented along an orthogonal direction to that of the laser written lines.

Extraction of the greyscale profiles for all of the laser-rewritten F8BT lines in Figure 5.7(a) and averaging them over each set of four laser written lines with the same writing parameters yields the FWHM values, which are plotted in **Figure 5.9** as a function of writing speed and laser power. Decreasing the laser power and/or increasing the writing speed are effective in reducing the linewidth of the laser-aligned F8BT lines. Whether this is due to secondary (scattered and/or reflected) light interactions with the SD1 layer that leads to a broadening of the region exposed by the illumination requires further investigation. Additionally, as expected, the patterning resolution is higher for the F8BT lines written with a smaller laser spot size. The minimum FWHM linewidth for the 45° laser written lines using the 0.95 NA objective was determined to be less than 1 μm. This linewidth determined herein is somewhat larger than the theoretically predicted laser spot size (420 nm FWHM), which is possibly a consequence of the existence of certain in-plane distances required for F8BT director reorientation in the nematic phase, as dictated by the elasticity of the F8BT nematic film.

It should be noted that some of the extracted linewidths in Figure 5.7 are close to the diffraction-limited resolution of our crossed-polarised optical microscope and, therefore, the actual linewidth may indeed be lower than the ≈ 1 μm value determined here. In the future, the use of instrumentation with higher resolution capabilities such as polarised scanning transmission X-ray microscopy [14] or scanning nanodiffraction in transmission electron microscopy [15] might be useful techniques for obtaining a more accurate estimation of the laser-rewritten pattern resolution. Irrespectively, the resolution limit demonstrated here is still substantially smaller than that using the non-laser-based, photomasked UV alignment process.

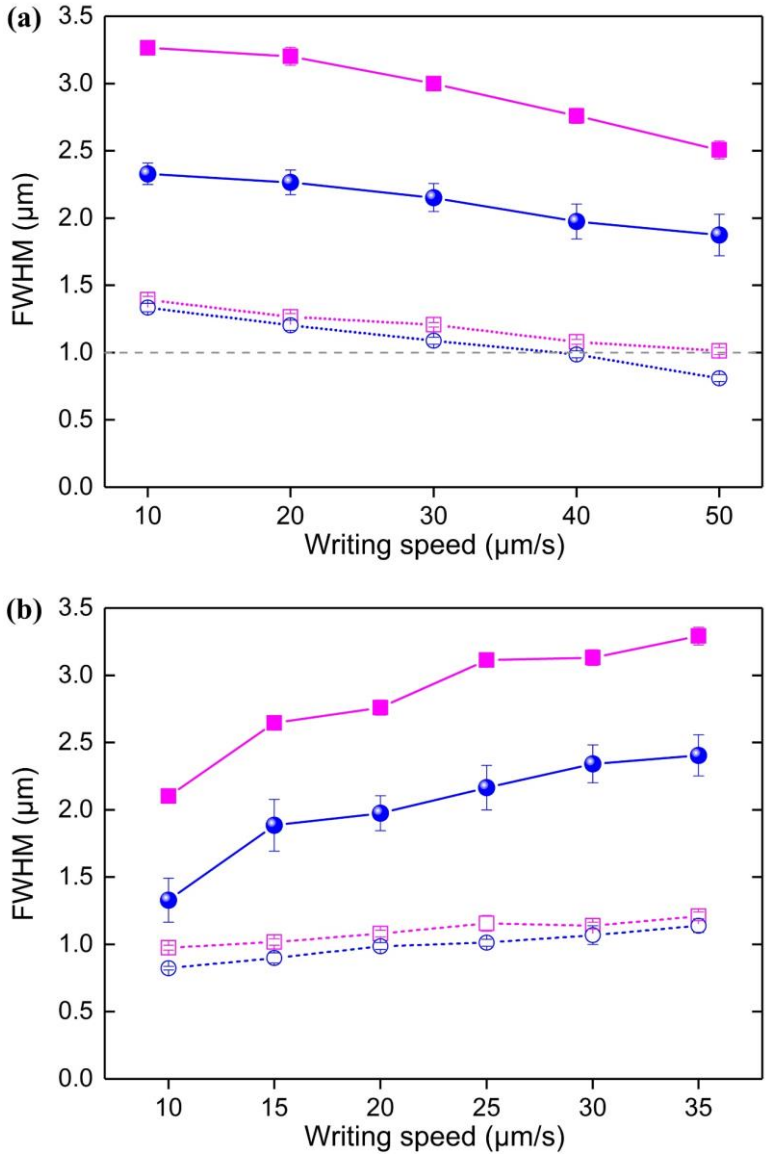

Figure 5.9: The extracted FWHM as a function of laser writing speed for a fixed laser power (a) and laser power for a fixed writing speed (b). Results are shown for two different objective lens numerical apertures (NA = 0.5, red squares; 0.95, blue circles) and laser polarisations relative to the background uniform UV-alignment (90° laser-writing, filled symbols; 45° laser-writing, open symbols). The horizontal dash-dotted line in (a) highlights a 1 μm FWHM.

5.6 Fabrication of 2D Patterns of Aligned LCCPs

Two-photon laser writing with photoalignment layers enables rapid prototyping of advanced LC and LCCP configurations and the fabrication of sophisticated 2D alignment patterns with high resolution. On top of bi-directional rastering of laser-written lines/circles, the key laser-

writing parameter for enabling uniform 2D SD1-alignment patterns is to adopt an appropriate separation distance between adjacent computer-controlled scanning steps. This would require the scanning line separation to exceed the laser-written linewidth in an SD1 photoalignment layer. Although the determined spatial F8BT pattern resolutions for two-photon DLW, as plotted in Figure 5.6, can provide guidance for selecting the laser scanning separation, it is imperative to get rid of the defect-line broadening effect that has been observed for the 90°-written LCCP lines.

Experiments were performed to study the influence of the LC defect line and the separation of the laser written lines on the uniformity of two-photon laser-written photoalignment. Laser writing of ten consecutive 10 µm-long lines in a uniform, but orthogonally UV-prealigned SD1 background, using the same writing parameters, i.e., the maximum laser power of 35 mW, a writing speed of 10 µm s^{-1} and two NA (0.5 and 0.95) objective lenses, but with three different scanning line separations (0.5 µm, 1 µm, and 2 µm) was implemented. The bright-state and dark-state LC textures observed following the deposition of a 165 nm-thick F8BT film onto the laser written SD1 photoalignment layer are presented in **Figure 5.10**. As before, the LCCP was heated to the nematic LC phase in order to communicate the alignment of the molecules in the SD1 layer to the polymer chains in the overlying F8BT layer. It is clear that different LC textures are visible in the 0.5 and 0.95 NA lens-focused-laser written stripes using a 2 µm scanning line separation. For example, the stripe written using the 0.5 NA objective lens shows random discontinuous F8BT defect lines, whereas the defect lines merge into a continuous Schlieren texture across the laser-written stripes when the 0.95 NA objective lens was used. Given the same number of laser-written lines in the two oriented F8BT stripes, a much higher fraction of the defect-line regions exists in the F8BT stripe written with the 0.95 NA objective lens, which is indicative of a thinner linewidth for the corresponding laser-written SD1 lines. The presence of F8BT defect lines in both types

of laser written stripes indicates that the laser pattern SD1-alignment resolution using the 0.5 and 0.95 NA objective lens are < 2 µm, which is in accord with the FWHM linewidth identified in the laser-written F8BT lines using a laser beam polarisation at a non-orthogonal angle to that used for the UV-alignment of background.

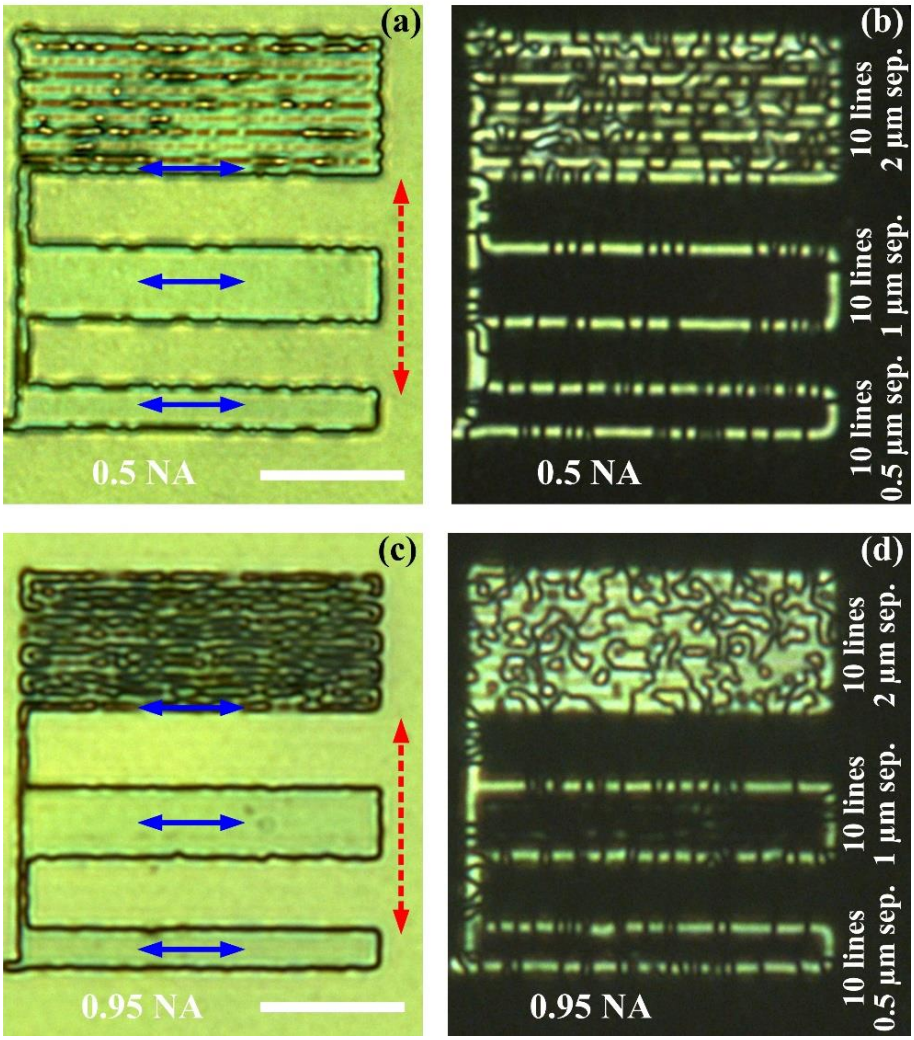

Figure 5.10: Crossed-polariser POM images of the resultant LC optical texture of an F8BT nematic glass film spin-coated onto a laser-patterned SD1 layer. In this case, three 50 µm-long stripes with ten consecutive lines were laser written using a polarisation that was orthogonal to the background (the solid blue double-headed arrows represent the chain-alignment direction for the laser written regions whereas the dashed double-headed red arrows represent the chain-alignment direction in the UV-aligned background). The laser writing parameters were laser power of 35 mW, writing speed of 10 µm s^{-1}, and two NA (0.5 and 0.95) objective lenses but with three different scanning line separation distances (sep. = 0.5 µm, 1 µm, and 2 µm). The horizontal white scale bars in (a) and (c) represent a length of 20 µm.

Laser writing of the SD1 layer with the maximum laser power, the 0.5 NA objective lens, and scanning line separation of 1 and 0.5 μm was shown to be able to produce a high-quality F8BT monodomain pattern in the laser-written stripes, leading to the determination of a laser pattern resolution of 1 - 2 μm in the locally patterned SD1 layer. For the case of laser writing of the SD1 layer using the 0.95 NA objective lens, a clear and uniform chain-orientation pattern appeared only when the scanning line separation was reduced to ~0.5 μm, confirming that the achievable laser-written SD1-alignment using this objective lens is slightly larger than the theoretically predicted limit of 420 nm.

This serves as an important extension regarding the determination of the two-photon laser spatial pattern resolution presented in Figure 5.9, in which the resolution results were likely underestimated, particularly for the 45°-written F8BT lines due to the fact that they were estimated to be close to the diffraction-limited resolution of ≈ 1 μm value for our crossed-polarised optical microscope. Considering that the pattern resolution extracted from the 90° laser-written F8BT using the 0.5 NA lens was determined to be 1 - 2 μm in comparison to its theoretically predicted limit of 0.8 μm, we believe that the two-photon excitation threshold for the SD1 photoalignment may be slightly lower than the half-maximum focal intensity of the ultrafast laser used in our DLW system.

5.7 Tailoring Chain-Orientation in Laser-Aligned F8BT

The two-photon DLW experimental setup allows for a large degree of flexibility in terms of fine-tuning the in-plane chain-orientation in bespoke 2D LCCP alignment patterns. The direction of the laser polarisation can be rotated azimuthally by adjusting the half waveplate. Uniform laser-aligned 100 μm × 100 μm squares in SD1 layers were (re)written with a bi-directional raster scan using a 0.5 NA objective lens, 35 mW power, 10 μm s^{-1} writing rate and

1 µm scanning line separation, as well as different laser polarisation directions in the plane of the SD1 substrate. Polarised confocal fluorescence (FL) images of the laser-aligned F8BT squares were then recorded for various orientations of the analyser used to select the polarisation of the emitted light from the F8BT layer. This enables the FL intensity to be determined for different orientations of the analyser, which probes the orientation of the transition emission dipole moments of the oriented F8BT polymer chains in the different laser written squares relative to the UV-aligned background.

Crossed-polariser POM images are shown in **Figure 5.11**(a) and (b) for three differently oriented 100 µm × 100 µm F8BT squares that have been fabricated by writing square patterns into the SD1 photoalignment layer. Polarised optical micrographs were recorded with the samples placed between a crossed polariser/analyser pair to reveal the orientational order in the laser-pattern induced F8BT nematic glass state resulting in birefringence of the F8BT film. The excellent laser writability and tunability of the molecular orientation in the SD1 photoalignment layer is clearly revealed.

The POM images and polarised FL intensity images for the three square patterns emphasize the quality and uniformity of the F8BT orientation in the laser-written SD1 layer and subsequently the alignment in the overlying F8BT film. Monodomain F8BT orientation is observed within all three of the laser-written squares. The laser-pattern induced contrast in the image between the 45° laser-written F8BT square and the other two squares appears noticeably high in Figure 5.11(a) and (b), whereas the laser pattern resolution as well as the optical and FL intensity contrast in the laser-written squares relative to the non-aligned F8BT background are significantly reduced because the background consists of randomly oriented polymer chains with respect to the polarisation of the analyser.

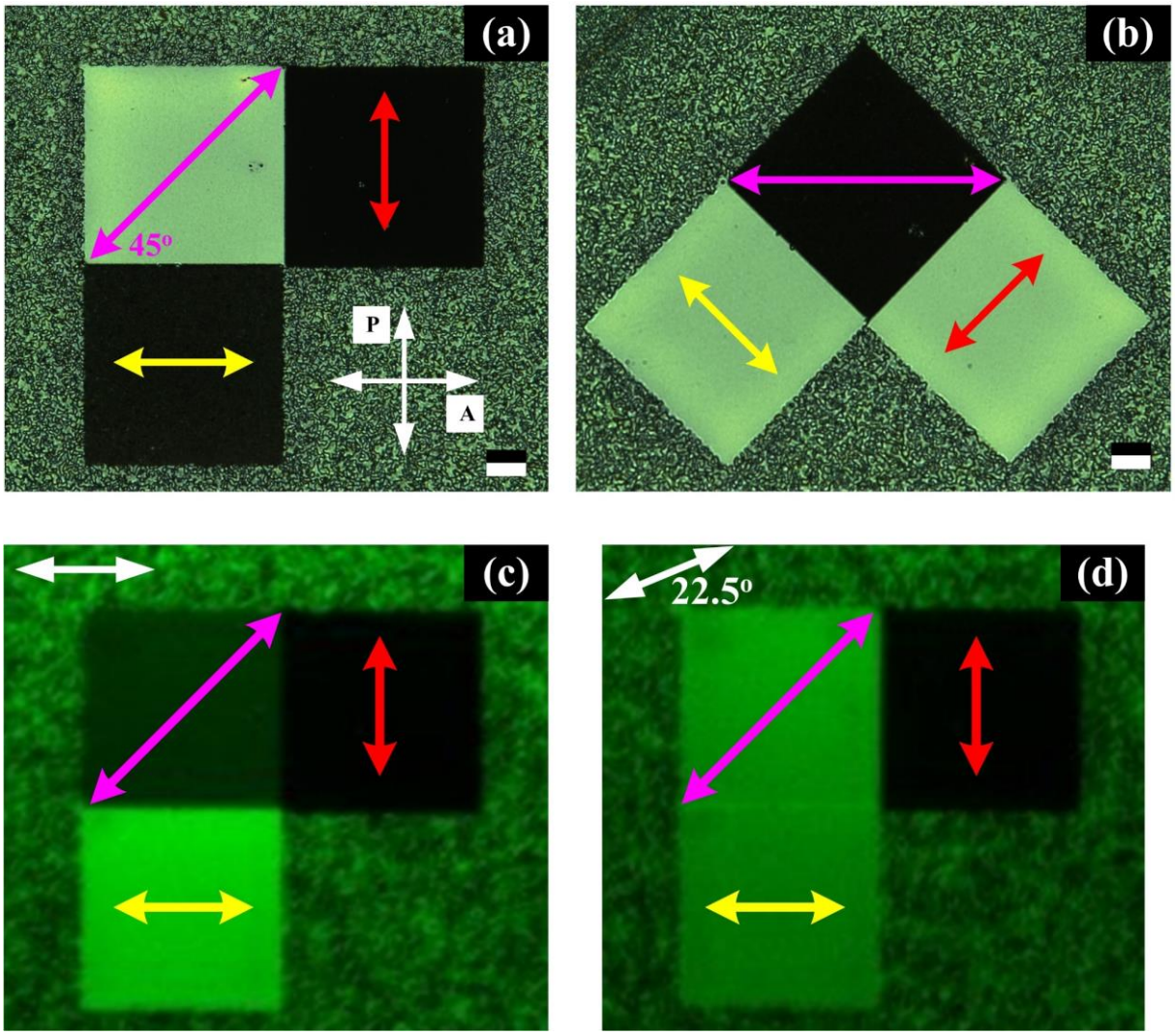

Figure 5.11: (a - b) Crossed-polariser POM images and (c - d) polarised FL intensity images of three squares that have been written with a laser polarisation that is aligned at different orientations. An F8BT film of 165 nm in thickness has been deposited onto the SD1 layer (spin-coated from 1 mg/ml SD1 solution) and heated to the nematic phase to transfer the alignment in the SD1 layer to the overlying F8BT film. The resulting F8BT chain-orientation in the three separate squares are indicated by the yellow, red, and pink double-headed arrows in the images. A dark state is observed when the orientation of the polymer chains is parallel to either the polariser or analyser whereas a bright state is observed when it is at 45° to the axes of the polariser (P) and analyser (A). The FL images were obtained for an excitation wavelength of 450 nm with an unpolarised excitation source. The double headed white arrows show the orientation of the analyser used to select the polarisation of the collected emitted light. The scale bars in (a) and (b) are 20 µm.

There is clear correlation between the polarised light emission intensity and the designed F8BT alignment direction and in turn the orientation of the transition emission dipole moment. In Figure 5.11(c) the squares reveal a dark, intermediate, or bright PL state when the analyser polarisation direction (indicated by the white arrows) is either orthogonal (red arrow), at 45° (pink arrow) or parallel (yellow arrow) to the orientation of the F8BT chain axis, respectively. In Figure 5.11(d) the analyser is rotated by 22.5° whilst keeping the substrate orientation fixed. As a result, the angle of the analyser to the F8BT polymer chains in the squares (indicated by the pink and yellow arrows) is 22.5° in both cases, thereby yielding the same relatively bright state, and 67.5° for the square indicated by the double-headed red arrow, yielding a relatively dark state. This indicates that the orientation of the polymer transition emission dipole moment is parallel to the two-photon laser-induced F8BT chain-orientation direction.

In order to enhance the FL intensity contrast and compare the polarised light-emitting properties for an LCCP that has been aligned by the two-photon laser writing process with respect to the UV-aligned background, two 100 μm × 100 μm F8BT squares were aligned in the nematic phase by the corresponding laser-written SD1 squares using 45° and 90° laser polarisation orientations relative to that used for the uniform UV-prealignment of the background. Polarised confocal FL images of the two differently oriented F8BT squares against the UV-aligned background are shown in **Figure 5.12**. The FL intensity contrast between the laser-written F8BT squares and the uniform UV-aligned background appears significantly enhanced in comparison to the case in a non-aligned background (Figure 5.11), though the contrast between the two squares here is comparable to the laser-written counterparts. These impressive results emphasize the huge potential of using laser- and UV-aligned LCCP patterns to create polarised emission patterns or a grey scale in the FL intensity by tuning the relative orientation between the photoaligned chain axis and the analyser polarisation. When rotating the analyser polarisation about an azimuthal direction, emissive LC defect lines are visible at

the boundary between the 90°-written F8BT square and the orthogonally UV-oriented background. However, there is no defect-line emission observed at the boundaries between the 90°-written and 45°-written F8BT squares, as well as between the 45°-written square and the background. This is in accordance with the director degeneracy origin of the disclination lines.

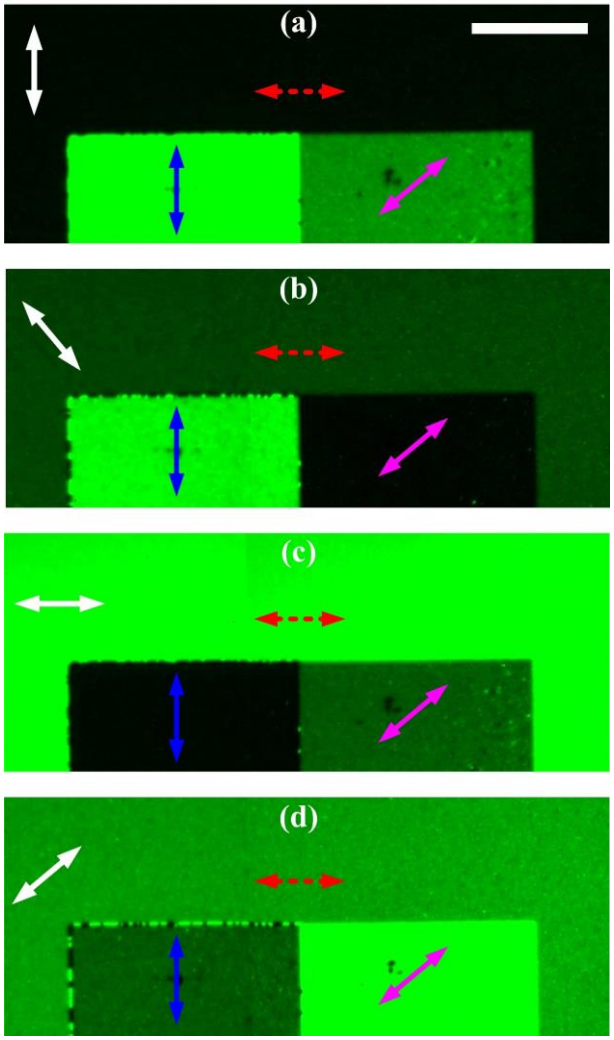

Figure 5.12: Polarised FL intensity images of the two-photon laser-rewritten alignment squares against the UV-aligned background in the same quenched nematic glass F8BT film. The resulting 90° and 45° F8BT chain-orientation directions are indicated by the blue and pink double-headed arrows, respectively, for the two separate squares, while the F8BT chain-orientation direction in the background is denoted by the dashed double-headed red arrows. The FL emission from the UV-prealigned and laser-rewritten alignment patterns of the nematic F8BT was obtained using an excitation wavelength at 450 nm with an unpolarised excitation source. The white arrows show the orientation of the analyser used to select the polarisation of the collected emission light, i.e., at 0° in (a), 45° in (b), 90° in (c), and 135° in (d) to the vertical direction. The scale bar in (a) is 50 µm.

Another important finding from Figure 5.12 lies in that, unlike the two-photon laser-written squares, the angular variation in the FL intensity in the UV-aligned background (compare Figure 5.12(b) and (d)) is not perfectly symmetric with respect to the horizontal analyser polarisation. This observation may be indicative of an off-axis orientation of the associated transition dipole moment relative to the UV-aligned chain-axis direction.

5.8 Summary

In summary, two-photon direct laser (re)writing of SD1 photoalignment layers using an ultrafast Ti:sapphire laser (785 nm, 250 fs, 80 MHz) has been proposed and demonstrated, for the first time, to create patterned chain-orientation structures in quenched LCCP films. The key writing parameters include the laser power, writing speed, laser written line separation and the NA of the focusing objective lens. These parameters have been systematically studied to optimise the laser spatial-pattern resolution as well as the photoalignment quality and uniformity. A combination of the highly localised laser-rewritten alignment with uniform UV-alignment has exhibited the unique potential to enable high-quality LCCP alignment and submicron-scale spatial pattern resolution that is very close to the theoretically predicted diffraction-limited focusing resolution, i.e., d = 392.5 nm / NA for our two-photon laser writing system. This newfound LCCP-orientation and spatial-pattern method based on ultrafast DLW is expected to advance the fabrication of more sophisticated photonic and optoelectronic devices based on multifunctional LCCPs.

Laser (re)written patterns inscribed into SD1 photoalignment layers are enabled by scanning the film sample relative to the focused laser beam, which leads to sub-micron lateral resolution when the laser writing conditions are optimised, e.g., laser power 10 - 20 mW and scanning speed 40 - 50 μm s^{-1}. Spatial patterning can either be performed by laser writing on an unexposed SD1 film or writing into an SD1 film that has been pre-aligned by uniform

exposure to a polarised UV light source. Higher contrast is achieved for polarised confocal FL images when the laser writing is into a prealigned SD1 photoalignment layer as the ordering of the background produces a highly uniform signal against which the laser written pattern clearly stands out. Two-photon laser-(re)written and UV-aligned F8BT nematic monodomains may have different relative orientations between the transition emission dipole moment and the photo-aligned direction of the F8BT chain-orientation. The two orientations largely remain parallel to each other for the ultrafast two-photon laser-(re)written F8BT, whereas they appear to be at a certain angle for the UV-aligned F8BT polymer chains.

Laser rewriting can be also done using a range of different relative angles between the pre-alignment direction and the laser-writing polarisation. When the laser polarisation is selected to be orthogonal to the UV pre-alignment direction, there is a well-defined transition zone that consists of $\lambda = ½$ disclination lines due to the associated degeneracy between two equally probable director orientations in the nematic LC phase. These defect-line regions display a typical Schlieren LC texture and broaden the linewidth in the resulting LCCP alignment pattern border (e.g., 1.2 - 2 μm for the laser-written F8BT lines using the 0.5 NA objective lens), hence significantly degrading the laser pattern resolution and the photoalignment uniformity. For 45° rewriting, however, the director degeneracy that causes this transition zone is lifted and there is no defect formation. As a consequence, 45° rewriting consistently gives rise to narrower lines for a variety of writing parameters. Also, by adopting the appropriate laser writing parameters, such as employing a combination of non-orthogonal polarisation relative to the background, the maximum laser power, a writing rate of 10 μm s^{-1} and 0.5 NA objective lens, and laser scanning line separation of 1 μm, is feasible for prototyping high-quality, defect-free LCCP alignment with bespoke in-plane alignment patterns.

In terms of the limit of the laser-written linewidth (or chain-pattern resolution) for the different orientations of the laser polarisation relative to that for the polarised UV-aligned regions, there are three factors that should be considered: (i) the patterning resolution currently available for our two-photon laser writing setup is limited by the positioning resolution of our translation stage (~50 - 100 nm) and the diffraction limit; (ii) from a materials point of view, a limiting factor could be the contour length of the LCCP backbone, which is likely to lie in the range of 10 - 20 nm as found from our grazing-incidence wide-angle X-ray scattering measurements for F8BT (see Chapter 4) or the coupled gel permeation chromatography and light scattering measurements for PFO [16]; and (iii) chain entanglement may also play an important role in essentially limiting the spatial patterning resolution that can be achieved in the quenched LCCP glass films.

References

[1] A. Courvoisier, M. J. Booth, P. S. Salter, Inscription of 3D waveguides in diamond using an ultrafast laser. *Appl. Phys. Lett.* **109**, 031109 (2016).

[2] T. Gissibl, S. Thiele, A. Herkommer, H. Giessen, Two-photon direct laser writing of ultracompact multi-lens objectives. *Nat. Photonics* **10**, 554 (2016).

[3] A. Courvoisier, M. J. Booth, P. S. Salter, Inscription of 3D waveguides in diamond using an ultrafast laser. *Appl. Phys. Lett.* **109**, 031109 (2016).

[4] G. Stoychev, A. Kirillova, L. Ionov, Light-responsive shape-changing polymers. *Adv. Optical Mater.* **7**, 1900067 (2019).

[5] C. C. Tartan, J. Sandford O'Neill, P. S. Salter, J. Aplinc, M. J. Booth, M. Ravnik, S. M. Morris, S. J. Elston, Read on demand images in laser-written polymerizable liquid crystal devices. *Adv. Optical Mater.* **6**, 1800515 (2018).

[6] M. Farsari, B. N. Chichkov, Materials processing: two-photon fabrication. *Nature Photon.* **3**, 450 (2009).

[7] W. R Zipfel, R. M Williams, W. W. Webb, Nonlinear magic: multiphoton microscopy in the biosciences. *Nature Biotechnology* **21**, 1369 (2003).

[8] P.S. Salter, M. J. Booth, Adaptive optics in laser processing. *Light Sci. Appl.* **8**, 110 (2019).

[9] B. Sun, P. S. Salter, C. Roider, A. Jesacher, J. Strauss, J. Heberle, M. Schmidt, M. J. Booth, Four-dimensional light shaping: manipulating ultrafast spatiotemporal foci in space and time. *Light Sci. Appl.* **7**, 17117 (2018).

[10] S. Hasegawa, Y. Hayasaki, Polarisation distribution control of parallel femtosecond pulses with spatial light modulators. *Opt. Express* **21**, 12987 (2013).

[11] Y. C. Chen, B. Griffiths, L. Weng, et al., Laser writing of individual nitrogen-vacancy defects in diamond with near-unity yield. *Optica* **6**, 662 (2019).

[12] M. J. Booth, M. A. A. Neil, R. Juškaitis, T. Wilson, Adaptive aberration correction in a confocal microscope. *Proc. Natl. Acad. Sci. USA* **99**, 5788–7086 (2002).

[13] P. S. Salter, M. J. Booth, A. Courvoisier, D. A. J. Moran, D. A. MacLaren, High resolution structural characterisation of laser-induced defect clusters inside diamond. *Appl. Phys. Lett.* **111**, 081103 (2017).

[14] B. A. Collins, J. E. Cochran, H. Yan, E. Gann, C. Hub, R. Fink, C. Wang, T. Schuettfort, C. R. McNeill, M. L. Chabinyc, H. Ade, Polarised X-ray scattering reveals non-crystalline orientational ordering in organic films. *Nat. Mater.* **11**, 536 (2012).

[15] C. J. Takacs, N. D. Treat, S. Krämer, Z. Chen, A. Facchetti, M. L. Chabinyc, A. J. Heeger, Remarkable order of a high-performance polymer. *Nano Lett.* **13**, 2522 (2013).

[16] M. Grell, D. D. C. Bradley, X. Long, T. Chamberlain, M. Inbasekaran, E. P. Woo, M. Soliman, Chain geometry, solution aggregation and enhanced dichroism in the liquid crystalline conjugated polymer poly (9, 9 ‐ dioctylfluorene). *Acta Polymerica* **49**, 439 (1998).

Chapter 6

A Comparison of the UV Illuminated and Laser Written Photoalignment Techniques

Systematic tuning of the physical structure of LCCPs allows for fine control over their desired electronic and optical properties. Chain orientation via LC alignment facilitated by high-quality photoalignment of an SD1 layer (as shown in the previous chapters) allows access to fundamental light-emission and optical anisotropies. The associated modification of the emission polarisation and refractive index offers great potential for the fabrication and performance improvement of a rich range of photonic and optoelectronic structures. It has been demonstrated in Chapter 5 that optimisation of the two-photon laser power and writing speed allows alignment features to be achieved with linewidths down to ~ 1 μm and ~ 0.5 μm when using objectives with 0.5 and 0.95 NA, respectively. Furthermore, as shown in the previous chapters, adopting the appropriate fabrication parameters for either UV-alignment or laser (re)writing enables rapid prototyping of bespoke chain-orientation patterns with fine features.

These remarkable LCCP photoalignment results arise from the combined benefits of a highly localised nonlinear two-photon absorption of the ultrafast infrared laser pulses and macroscopic one-photon UV-alignment in the structurally anisotropic SD1 chromophores. As observed in the work in this Chapter, these different photoalignment techniques appear to lead to distinct SD1 molecular structures, which then result in different microstructures of the overlying LCCP film and subsequent photophysical properties after polymer chain orientation

through the nematic LC phase. This Chapter was prepared mainly based on the first/second journal paper in the publication list but with more analyses and discussions, with the aim of further studying the molecular structure-property relationship by directly comparing the photoalignment quality and polarised light-emitting properties for F8BT nematic glass films deposited on either laser written or UV illuminated photoalignment layers.

6.1 Photoalignment Quality and Polarised Light Emission

6.1.1 Sample Preparation

For this study, SD1 was spin-coated from 1 mg/ml SD1 solutions in anhydrous 2-methoxyethanol (≥ 99.8%) as an ultra-thin (<7 nm) photoalignment layer onto Spectrosil substrates. If not exposed to linearly polarised light (either from the UV light source or the two-photon laser beam), the film exhibited no evidence of long-range orientational order, as identified by the lack of macroscopic ordering of the polymer chains in the F8BT polymer layer when coated onto an unaligned SD1 and quenched from the nematic phase. In contrast, linearly polarised light from a Thorlabs CS2010 UV-curing LED system (λ_p = 365 nm) results in the long molecular axis of the photo-alignable SD1 molecules orienting in the plane of the substrate along a direction that is orthogonal to the excitation polarisation [1]. The photoalignment of the SD1 films is a rewritable process, which allows different in-plane alignment patterns to be written into the same layer. As has been shown in Chapter 5, it is feasible to first uniformly align the SD1 layer using polarised UV light before realigning certain areas of the SD1 layer using the two-photon laser rewriting process. The two-photon laser (re)writing of a spin-coated-only (non-aligned) or UV-prealigned SD1 substrate of the St. Cross College Oxford crest pattern was implemented with optimised laser writing parameters of 0.5 NA (Zeiss 20×) focusing objective lens, 35 mW laser power, 10 μm s^{-1} writing speed, and 1 μm separation distance between adjacent scanning lines. The laser-(re)written chain-orientation directions in the resulting overlying F8BT nematic glass films after heating and quenching from the nematic

phase (~165 nm F8BT layer thickness) were realised by adjusting the polarisation direction of the writing laser (e.g., at 90° or 35°) relative to that used to align the uniform background with linearly polarised UV illumination.

6.1.2 Alignment Quality of Photoaligned F8BT Nematic Glass Films

Polarised optical absorption spectra for the F8BT films on either a non-aligned SD1 layer or on a uniformly UV illuminated SD1 are demonstrated in **Figure 6.1** after heating and quenching from the nematic LC phase at 247 °C. The optical absorption dichroic ratio at the long-wavelength peak was found to be 12.6 ± 0.3, corresponding to an order parameter of $S = 1$. This perfect value of the order parameter for an F8BT film aligned on an SD1 photoalignment layer that has been pre-aligned using polarised UV light, has been estimated based on the parallel ($A_{//}$) and perpendicular ($A_{\perp}$) components of the absorbance using $S = [(A_{//} - A_{\perp}) / (A_{//} + 2\,A_{\perp})] / [(3\cos^2\beta - 1)/2]$, where the dipole-moment off-axis angle β of F8BT was taken as 22° [2].

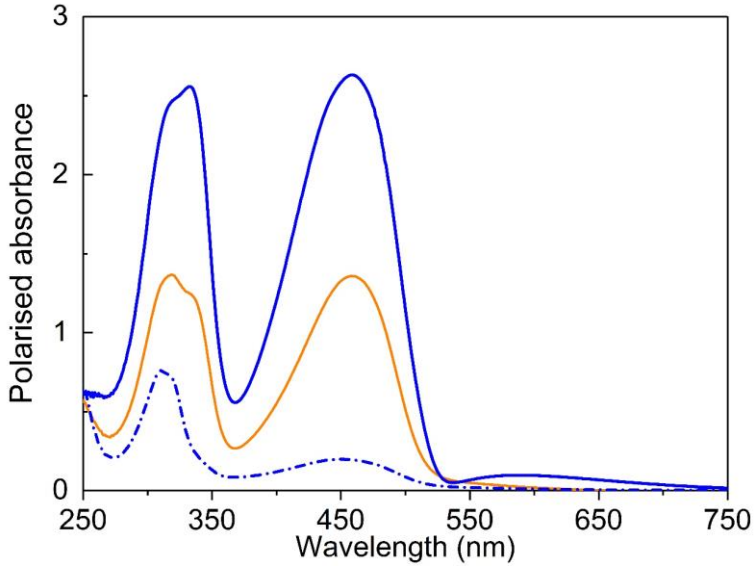

Figure 6.1: Polarised absorbance spectra for an F8BT film aligned on an SD1 photo-alignment layer that was exposed to polarised-UV-light before the deposition of the F8BT layer. Spectra are shown for both parallel (solid blue line) and perpendicular (dashed blue line) incident polarisations, relative to the polymer chain orientation direction. Also shown (orange solid line) is the spectrum recorded for unpolarised light for a 165 ± 5 nm-thick pristine F8BT film spin-coated onto a non-aligned SD1 substrate. This non-aligned F8BT film has the same thickness as the oriented film so as to allow a direct comparison.

The uniformity of the F8BT film aligned via the nematic LC phase and the associated reduction in optical scattering and enhancement in the refractive index along the alignment direction are evident from the long-wavelength interference fringe seen in the $A_{//}$ spectrum in Figure 6.1. Laser rewriting a pattern into a pre-aligned SD1 layer enhances the absorption contrast and reduces the polydomain defects, which is highly desirable for many device applications. We didn't show the polarised optical absorption spectra of the laser-written F8BT, as it is unrealistic to rely on this photoalignment technique to create uniform SD1-alignment across a sufficient region for a reliable UV-vis absorption spectral measurement due to the difficulty related with two-photon laser focus. Note that the largest F8BT monodomain pattern that we have succeeded to fabricate with DLW is 500 μm × 500 μm, however, an extended area of several mm^2 of SD1 and LCCP alignment is actually needed in the UV-vis setup we used.

A direct comparison of the photoalignment quality for the case when the pattern of a College crest was written into the SD1 layer along a direction that was at 90º relative to the UV-aligned background is shown in **Figure 6.2**. The results show the microscope images for the resulting F8BT film that has been deposited onto the photoalignment layer and subsequently heated to and quenched from the nematic phase. We can see that the average intensity in the bright-state greyscale transmission intensity for the laser-written F8BT crest is slightly larger by ~7% - 9% than that recorded from the F8BT film over the UV-aligned background. The dark-state transmitted intensities, on the other hand, are nearly identical. This would indicate either a slightly larger order parameter in the laser-rewritten crest or a certain deviation angle between the direction of optical transition dipole moment of oriented F8BT and the polymer backbone for the F8BT film on top of the UV-aligned background. As the order parameter for the UV-aligned F8BT approaches unity, the latter hypothesis regarding off-axis dipole moment orientation appears to be more plausible. Additionally, the width of the transition zone between the laser-rewritten and UV-aligned F8BT regions was estimated to be ~1.7 - 2.5 μm.

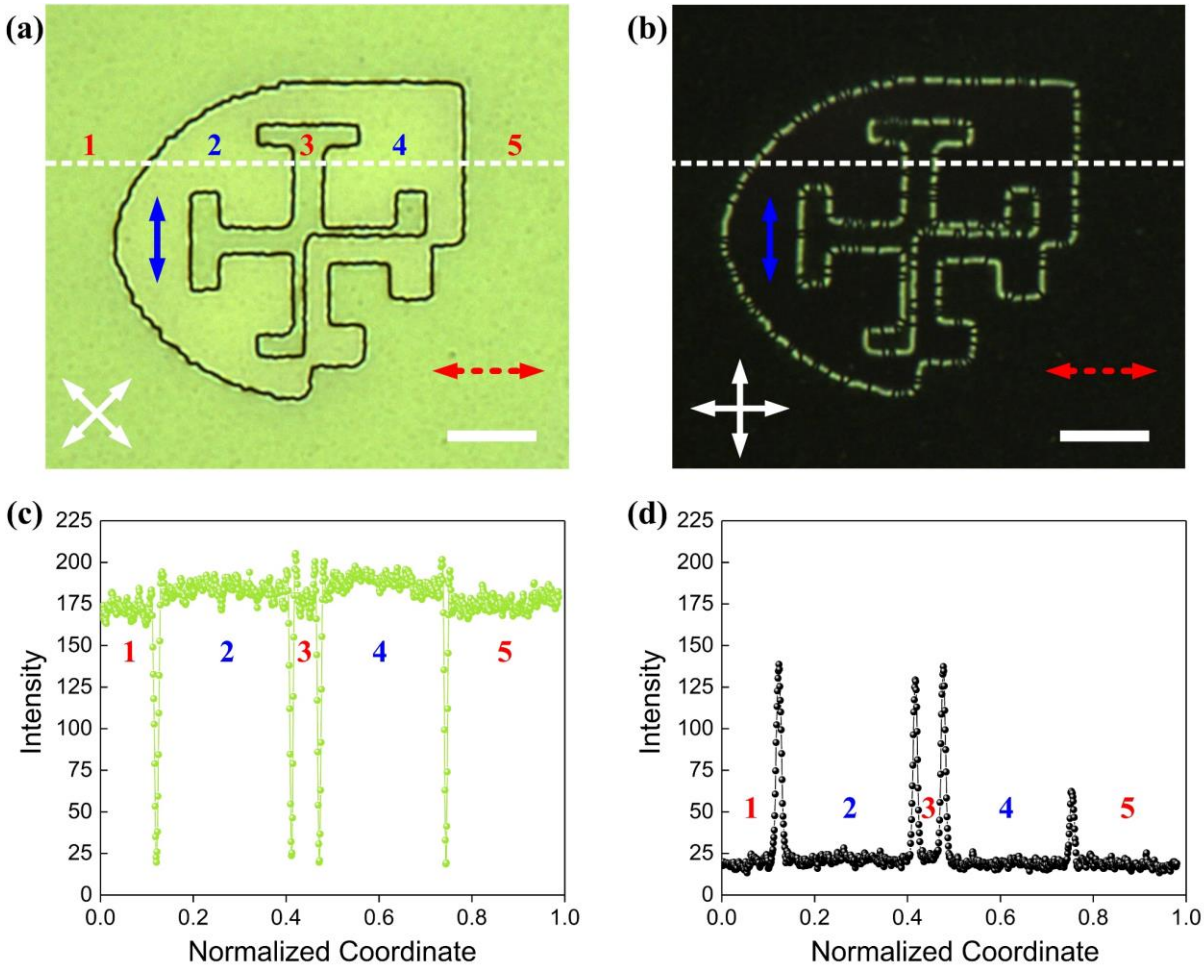

Figure 6.2: Comparison of the resultant alignment quality achieved in an F8BT film that has been aligned by either a laser written region in the SD1 in the form of a College crest or the surrounding UV-aligned regions. The orientation of the polymer chains in the region defined by the College crest are at 90º to the alignment of the polymer chains in the F8BT film directly above the UV aligned SD1 layer. POM images for the bright (a) and dark states (b) are presented along with the corresponding greyscale profiles in (c) and (d), respectively, which have been extracted along the white-dashed horizontal lines in (a) and (b). The double headed white arrows in (a) and (b) represent the orientations of the polariser and analyser. Regions #1, #3 and #5 in (a) represent the areas of the F8BT film that are directly above the UV-aligned background with the chain-orientation denoted by the dashed red arrows, whereas regions #2 and #4 correspond to the region of the F8BT film that sits directly on top of the laser written crest in the SD1 alignment layer. The laser writing was carried out with a polarisation orientation of the laser that is at 90º to the UV-prealigned background. The horizontal white scale bars in (a) and (b) are 20 µm.

6.1.3 Polarised Fluorescence from Photoaligned Patterns in F8BT Films

Polarised optical micrographs shown in **Figure 6.3**(a) and (b) were recorded with the samples placed between a crossed polariser/analyser pair, demonstrating the orientational order and concomitant optical contrast arising from the quenched F8BT nematic glass phase above the

laser-written St Cross College crest pattern against the regions of F8BT aligned using UV illumination of the SD1 layer.

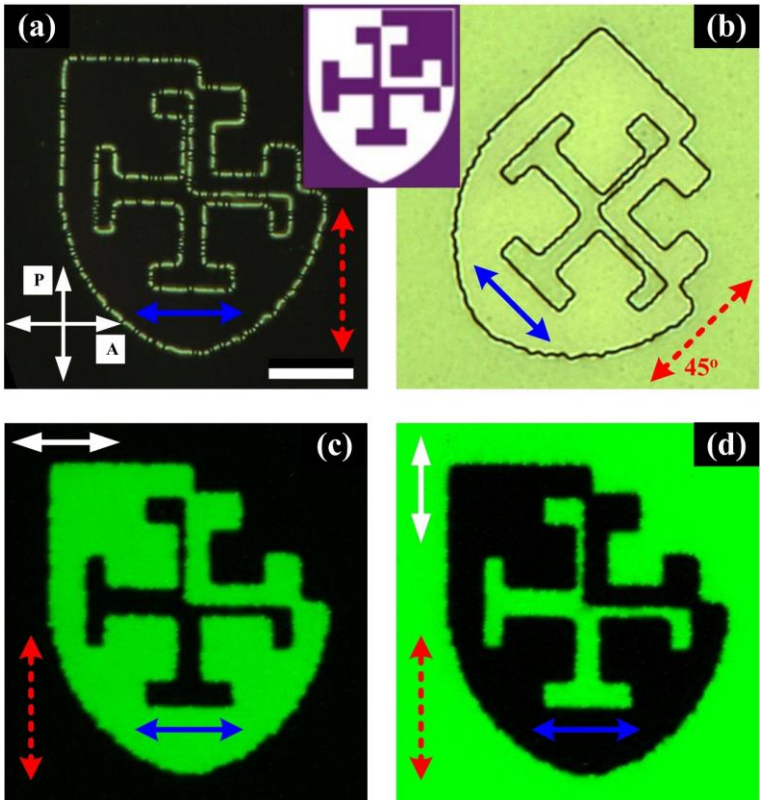

Figure 6.3: (a - b) Polarised optical micrographs and (c - d) Polarised FL intensity images demonstrating the photoalignment quality and polarised light emission for an F8BT film on the 90°-rewritten crest pattern and the UV-aligned background in the same F8BT nematic glass film. The double-headed white arrows in (a) denote the polarisation directions of the crossed polariser and analyser pairs, labelled, respectively, P and A. (b) was recorded by azimuthally rotating the sample by 45º from (a) while fixing the positions of the crossed polarisers. The crest pattern is based on the St. Cross College, Oxford crest (see inset) and was laser written on a UV-prealigned SD1 film with a polarisation direction that was at 90º relative to the UV-oriented background. The double-headed blue and dashed red arrows show, respectively, the orientation of the polymer chains in the crest and the background. Polarised FL intensity images were obtained for an excitation wavelength of 450 nm with an unpolarised excitation source. The doubled-headed white arrows show the orientation of the analyser used to select the polarisation of the emitted light. The scale bars in (a) is 20 µm.

Results are presented for F8BT films on both laser-rewritten and UV-aligned regions of the SD1 layer (Figure 6.3) as well as on top of a nonaligned SD1 (**Figure 6.4**). The excellent writability and rewritablity of the SD1 photoalignment layer are clearly demonstrated by a

combination of the highly localised two-photon laser rewriting and uniform UV-prealignment. The POM images show a dark state when the chain orientation direction (defining the optic axis) is parallel to the transmission axis of either the polariser or analyser, resulting in no transmission between crossed polarisers. Conversely, when the orientation of the polymer chains is at 45° to the transmission axes of the polariser/analyser then a bright transmissive state is observed. For the case of the crest that appears in the F8BT film, the visibility of the pattern only arises because of a transition region between the two orthogonal orientations of the polymer chains, which appears as a bright state in Figure 6.3(a) and a dark state in Figure 6.3(b). This is because the local orientation of the polymer chains in the transition zone is intermediate between the two orthogonal orientations in the crest and the surrounding background.

High quality monodomain F8BT orientation is observed in all of the polarised optical micrographs, which can readily extend over cm^2 areas for the macroscopically aligned background. Due to the inherent director degeneracy caused by the orthogonal laser rewriting, a discontinuous transition zone between the F8BT oriented on the UV-aligned SD1and the F8BT oriented on the crest pattern is clearly visible in Figure 6.3(a) and (b). This region maps the transmission in two orthogonally oriented monodomain regions and as a consequence shows a LC optical texture consisting of defect lines in the F8BT alignment. Polarised fluorescence (FL) intensity images for the crest against the F8BT film on the UV-aligned background further emphasize the quality of the F8BT film orientation for the two photo-alignment techniques. Figure 6.3(c) and (d) show the corresponding FL contrast for the highly oriented F8BT polymer chains on the laser-rewritten SD1 crest pattern for the case where the analyser and crest pattern orientations are parallel and orthogonal, respectively. In the parallel orientation case, the FL intensity in the F8BT crest is maximum (bright state), and in the orthogonal case minimum (dark state). The presence of LC defects at the boundary of the 90°-rewritten F8BT crest pattern induces rough borders in the polarised FL images, alongside a certain degree of uncontrolled or complicated emissive states at the disclination lines.

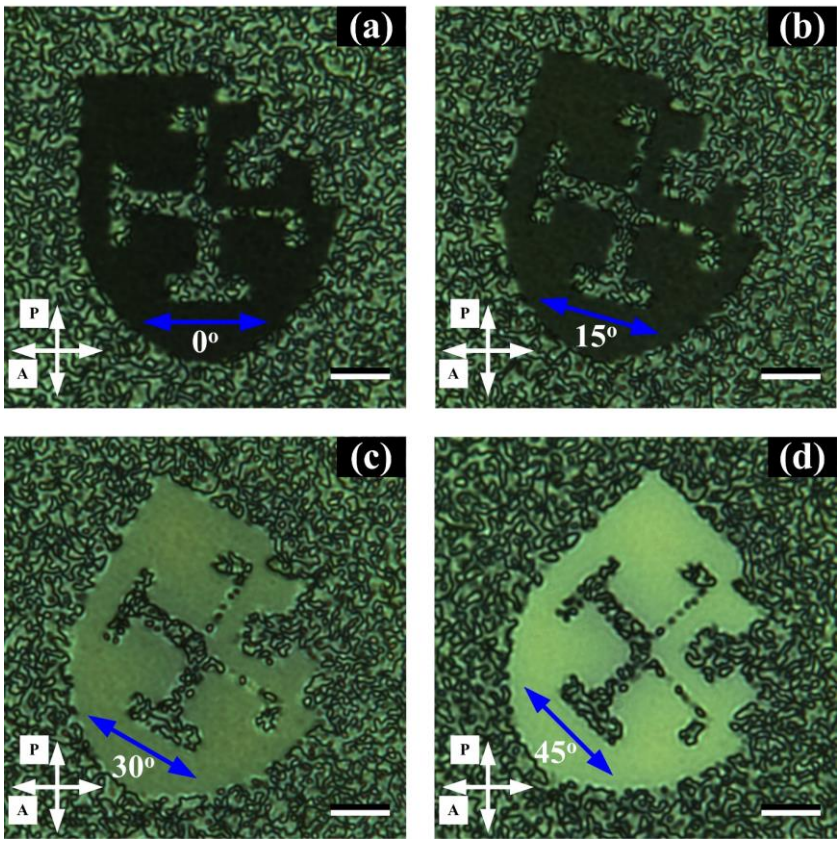

Figure 6.4: Polarised optical micrographs (viewed between crossed polariser (P, vertical doubled headed white arrow) and analyser (A, horizontal white double-headed arrow)) of an F8BT film (165 nm thickness) aligned on a laser written region of the SD1 photoalignment layer in the form of a crest pattern. This pattern was written into a non-aligned SD1 layer of ~3.5 nm thickness. The orientation of the F8BT polymer chains in the film (after heating to and quenching from the nematic phase) is indicated in each image by a double-headed solid blue arrow. The numerical values next to these arrows are the angles subtended between the chain axis and the analyser polarisation direction. The horizontal scale bar in the bottom right of each image is 20 μm.

Examples of polarised optical micrographs for F8BT films oriented on the crest patterns written in nonaligned SD1 are shown in Figure 6.4, in which the Schlieren texture evident in the background to the crest pattern is as expected for a non-aligned polydomain nematic glass, in contrast to the highly oriented monodomain in the F8BT crest pattern created from laser-written alignment. The polydomain-to-monodomain interfacial region leads to a loss of fidelity in the alignment pattern because, in this case, the background includes birefringence from polymer chains that randomly align with the transmission axis of the analyser. Consequently, the pattern resolution and birefringence contrast appear significantly reduced.

Both polarised optical micrographs and polarised FL images of a 35°-written F8BT crest compared with the alignment of an F8BT film on a UV-aligned background are shown in **Figure 6.5**. In this exemplar case, the director degeneracy that arises in the nematic phase is lifted and, thus, a continuous and smooth transition zone separating the 35°-rewritten crest pattern and the background is formed. The uniform linewidth of this continuous transition zone considerably improves the spatial pattern resolution and better reproduces the sharp features on the pattern border than the orthogonally laser-rewritten crest.

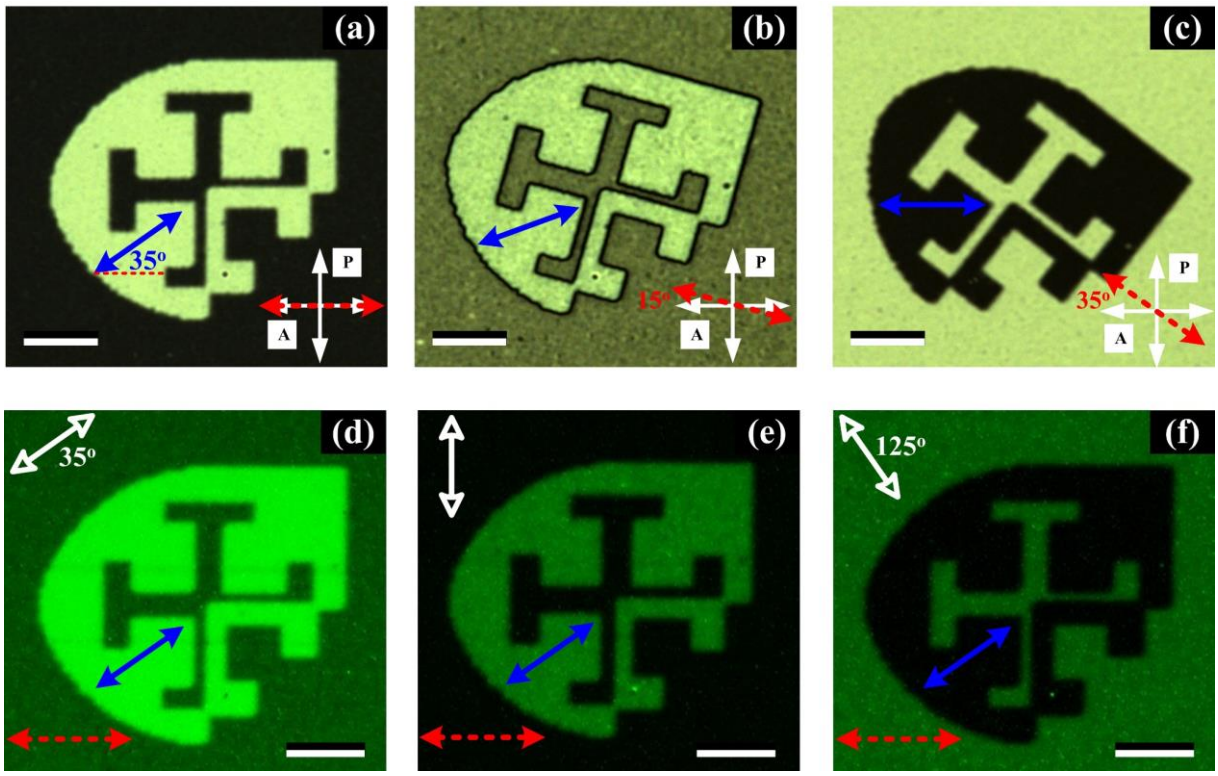

Figure 6.5: (a - c) Polarised optical micrographs and (d - f) Polarised FL intensity images of a F8BT film aligned on regions of SD1 that have been either laser written in the form of a crest pattern or have been uniformly illuminated using UV light. The orientation of the polymer chains in the regions of the F8BT film defined by the crest are at 35° to the orientation of the polymer chains of the F8BT film above the UV-illuminated SD1 regions. The FL intensity images were acquired by changing the relative angle between the transmission axis (white arrows) of the analyser and the orientation of the polymer chains in the surrounding background regions (dashed red arrow). Images (d), (e), and (f) were recorded for relative angles 35°, 90°, and 125°, corresponding to an emission collection polarisation that is parallel in (d), at 55° in (e) and orthogonal in (f), respectively, to the chain alignment direction in the laser-rewritten crest (dashed blue arrow). The horizontal scale bar in each image is 20 µm.

The contrast in the FL and optical textures showcased in this Section highlight the fine tunability of the light emission polarisation in the photoaligned fluorescent LCCPs and the generation of emission intensity greyscales by adjusting the chain orientation relative to the orientation of the transmission axis of the analyser.

6.2 Polarised Micro-PL Spectra from Photoaligned F8BT

In addition to the polarised fluorescence intensity maps recorded from F8BT films aligned over regions of SD1 that were prepared using either two-photon laser writing and/or UV illumination, a detailed photoluminescence spectroscopy study was conducted to elucidate the light-emitting properties of the highly oriented F8BT nematic films that have been created using the three different photoalignment methods: 1) polarised UV illumination only, 2) laser writing into a nonaligned SD1 film, or 3) laser rewriting of an SD1 layer that had already been illuminated with polarised UV light. Polarised micro-PL (μ-PL) characterisation (see Figure 2.4 and Section 2.6 for the optical layout and measurement details of the μ-PL spectral mapping) including location-dependent PL spectra and integrated PL intensity maps have been carried out with respect to the same F8BT nematic glass film with the laser-(re)written crest pattern and the UV-aligned background. A frequency-doubled femtosecond Ti:sapphire laser (100 fs pulses at 76 MHz) operating at 405 nm was used as the excitation source. The laser was focused on the top surface of an F8BT film by a 100× objective with a numerical aperture of 0.7. The spot size of the incident laser beam focused on the sample was ~1 μm in diameter.

Examples of μ-PL maps recorded using different combinations of the laser excitation polarisation and the orientation of the transmission axis of the analyser are shown in **Figures 6.6 and 6.7**, where the integrated spectral intensity for each case is plotted both as a 2D colour-coded image and a 3D rendered image. The μ-PL scanning step size was set as 1 μm in both in-plane directions. These total intensity images were obtained when the excitation polarisation

was aligned parallel to the F8BT chain orientation in the crest (i.e., along the *y*-axis, or orthogonal to the F8BT chain orientation in the background) as well as the analyser polarisation parallel to the excitation for Figure 6.6 and perpendicular thereto for Figure 6.7(a) and (b). As a result, the polarisation configuration in Figure 6.6 (in Figure 6.7(a) and (b)) results in a high (low) intensity recorded for the anisotropic emission in the laser-aligned crest and a lower (higher) intensity from the UV-aligned background. The map from the F8BT layer atop a nonaligned SD1 background is, as expected, independent of the analyser orientation as there is no preferential alignment of the polymer chains among micro-domains. Once again, the F8BT aligned by the crest that was written into the SD1 layer after the UV-induced alignment of the entire SD1 layer demonstrates a considerably higher pattern resolution than that obtained when the laser was used to write the crest directly into the photoalignment layer without the initial alignment step using polarised UV illumination.

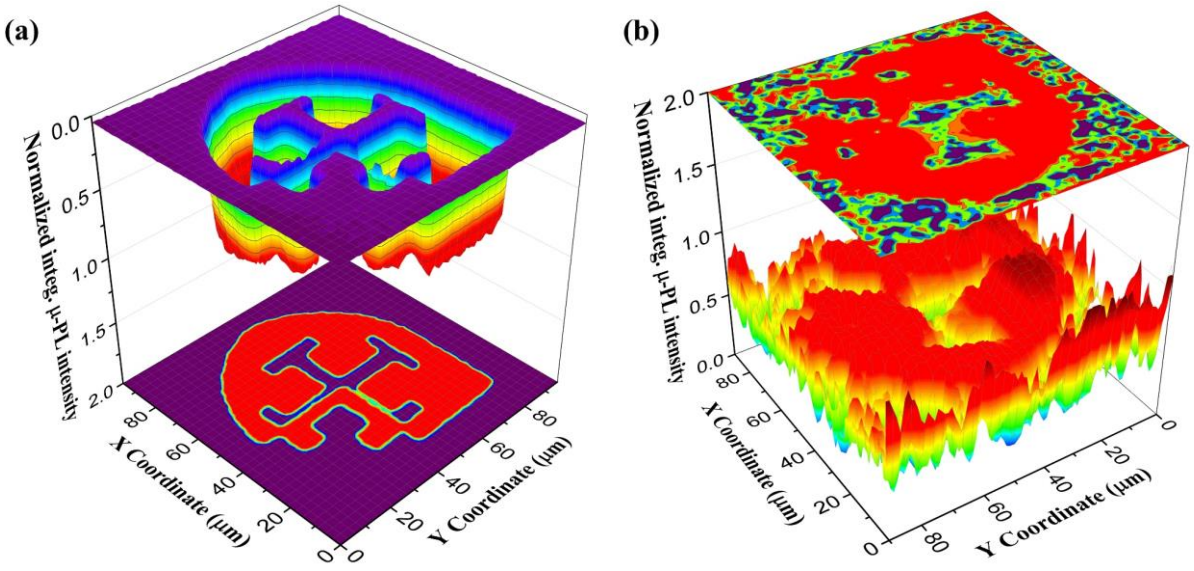

Figure 6.6: Spectrally integrated μ-PL intensity maps of (a) from a layer of F8BT aligned over a crest pattern that was laser written into an SD1 photoalignment layer. The background represents the initial alignment that was achieved using polarised UV illumination (which is at 90º to the alignment in the crest) and (b) the laser-written crest into a non-aligned SD1 layer. Both intensity maps have been normalized to the maximum emission intensity in each case. For both cases, the excitation polarisation and the analyser polarisation were aligned along the *y*-axis, which is parallel to the orientation of the F8BT polymer chains in the laser-rewritten and laser-written crests and, thus, perpendicular to that in the UV-aligned background.

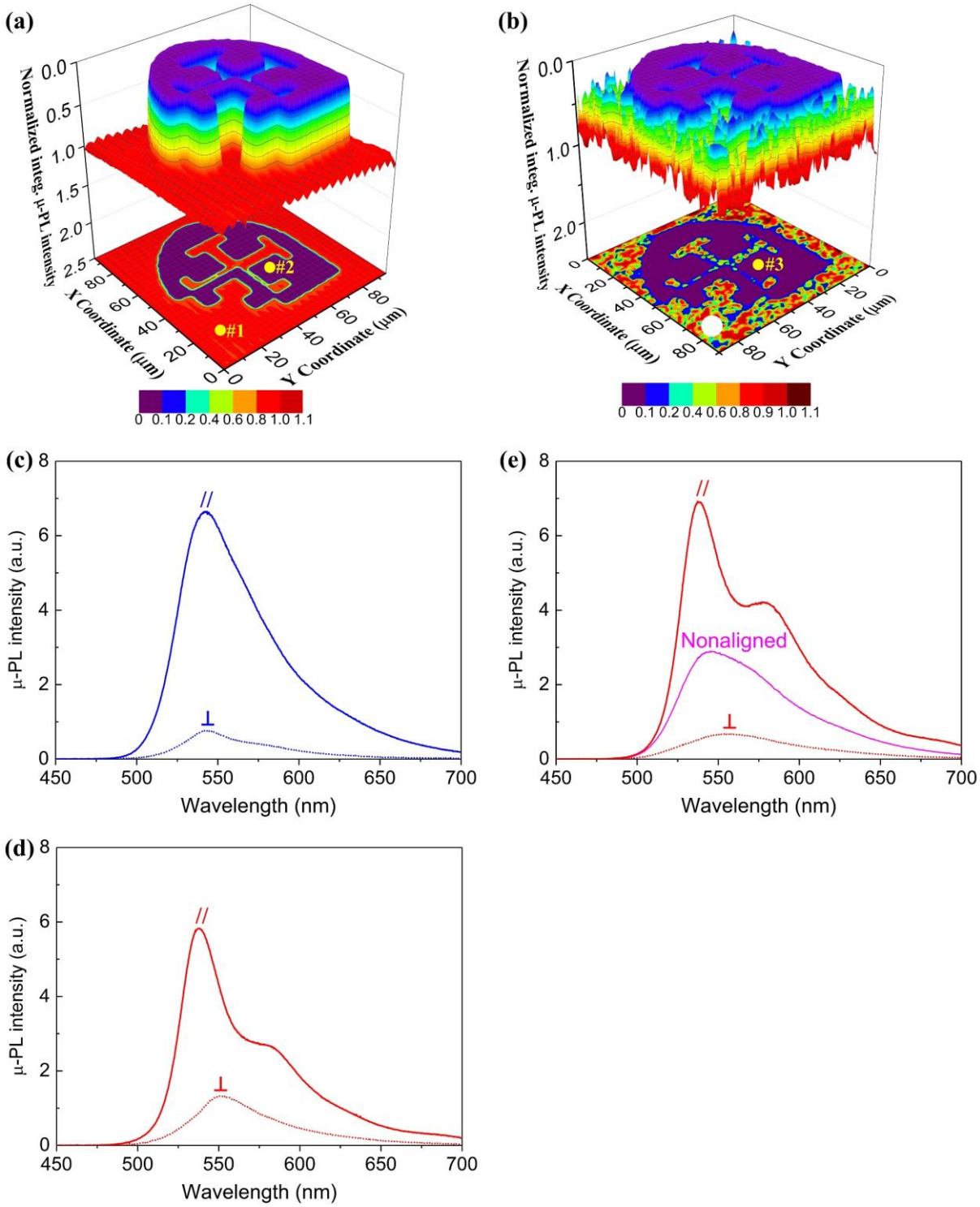

Figure 6.7: (a - b) Micro-PL maps of spectrally integrated PL intensity and (c - e) Selected μ-PL spectra for different locations on F8BT films with the laser-written and 90°-rewritten alignment crest patterns. Intensity maps normalized to the maximum emission intensity in each case are shown where the background was (a) aligned with UV illumination and (b) nonaligned. For (a), the excitation polarisation and the PL collection polarisation were aligned along the *x*-axis, which is orthogonal to the orientation of the F8BT polymer chains in the laser-rewritten crest and parallel to the UV-aligned background. For (b), the excitation was along the *y*-axis (chain axis direction in the laser-written crest) and the analyser polarisation was along the *x*-axis. The small undulation in the intensity for the UV-aligned background is

considered to be an experimental artefact. PL spectra are shown for: (c) location #1 in (a); (d) location #2 in (a); and (e) location #3 in (b) along with the spectrum from a nonaligned F8BT region highlighted by the large white dot (bottom corner in the 2D intensity map of (b), at which the μ-PL spectra recorded from a 10 μm × 10 μm non-aligned F8BT region were averaged). For each location, the excitation polarisation was rotated to align along the chain orientation direction and the PL spectra were collected with the analyser both parallel and perpendicular to this excitation polarisation. For the spectrum of the nonaligned F8BT, the excitation was along the *y*-axis and the analyser polarisation was along the *x*-axis.

In Figures 6.6(a) and 6.7(a), the crest pattern was laser written into an SD1 layer that had already been prealigned using polarised UV illumination. The alignment of the F8BT polymer chains in the crest was set to be at 90° relative to that obtained for the regions of F8BT aligned by the UV-illuminated background. In Figures 6.6(b) and 6.7(b) the SD1 layer was not aligned before laser writing the crest pattern. All images highlight the uniformity in the laser-patterned alignment over extended areas and also the significant benefit in laser rewriting of uniformly UV-aligned SD1. The transition region seen in Figures 6.2 and 6.3 is also evident in the 2-D colour-coded image in Figures 6.6(a) and 6.7(a), showing intermediate PL intensity of more or less halfway between the uniform background and the laser-rewritten crest intensities.

Figure 6.7(c)-(e) display the μ-PL spectra recorded from different specific locations marked in Figure 6.7(a) and (b). In each case, the 405 nm excitation source was polarised parallel to the orientation of the polymer chains and the emission from F8BT was separated using an analyser to reveal the components polarised parallel ($PL_{//}$) and perpendicular ($PL_{\perp}$) to the chain axis. Figure 6.7(c) shows the spectra recorded for F8BT oriented on a UV-aligned SD1 region that had not been subjected to laser rewriting (location #1, Figure 6.7(a)). From the UV-aligned F8BT spectra, the peak wavelengths for $PL_{//}$ and $PL_{\perp}$ occur at 543 ± 1 nm, with a weak shoulder at ~ 580 nm in the $PL_{\perp}$ spectrum indicating the possibility that the transition emission dipole moment orientation of the UV-aligned F8BT polymer chains is not perfectly parallel to the chain alignment direction. The PL anisotropy at 543 nm is found to be $PL_{//} / PL_{\perp}$

≈ 9. The corresponding emission spectra recorded with the laser excitation polarised perpendicular (⊥) to the polymer chains are shown in **Figure 6.8(a)**; no spectral differences are evident but, as expected, weaker emission results because of the weaker alignment between the excitation beam polarisation and the absorption dipole moment orientation for F8BT [2-3].

The anisotropy in the PL emission spectra for an F8BT film that was aligned using the laser rewriting process on the UV-aligned SD1 background is shown in Figure 6.7(d). In this case the excitation polarisation was rotated to be aligned along the chain axis in the F8BT film aligned by the laser rewritten crest. The main peak at λ = 538 nm in the $PL_{//}$ is at a slightly shorter wavelength than for the UV-aligned case (λ = 544 nm), whilst that for $PL_{\perp}$ (552 nm) is at a slightly longer wavelength (*c.f.* 543 nm). A second, weaker peak (at 580 nm) is also evident in the $PL_{//}$. The PL anisotropy at the main $PL_{//}$ peak (λ = 538 nm) is $PL_{//} / PL_{\perp}$ = 6.5. The corresponding PL emission spectra recorded with excitation polarised perpendicular to the polymer chains are shown in Figure 6.8 (b); again, no spectral differences are evident and, as before, weaker emission results.

The polarised PL spectra in Figure 6.7(e) are for F8BT aligned on a crest region (location #3 in Figure 6.7(b)) that was laser written onto a nonaligned SD1 layer. They closely resemble the spectra shown in Figure 6.7(d), except that the emission anisotropy is larger and the peak at 580 nm in $PL_{//}$ is more defined here. The PL anisotropy ratio at λ = 538 nm (parallel emission peak) is $PL_{//} / PL_{\perp}$ = 13, which is notably bigger than that recorded for the UV-aligned SD1 case (Figure 6.7(c)) and the laser rewritten crest in the UV-aligned background (Figure 6.7(d)). Values for the integrated PL anisotropy, on the other hand, are found to be $\int PL_{//} / \int PL_{\perp}$ = 10.1, 8.4, and 4.1 for UV alignment, laser writing in a nonaligned background, and laser rewriting in a UV-aligned background, respectively. Also shown in Figure 6.7(e) is the nonaligned PL spectrum from an F8BT film following heating and quenching for a location atop a nonaligned

SD1 layer; the spectrum peaks at 546 nm and generally matches the PL spectra previously reported for nonaligned F8BT and other dialkylfluorene-benzothiadiazole containing conjugated molecules [3-6].

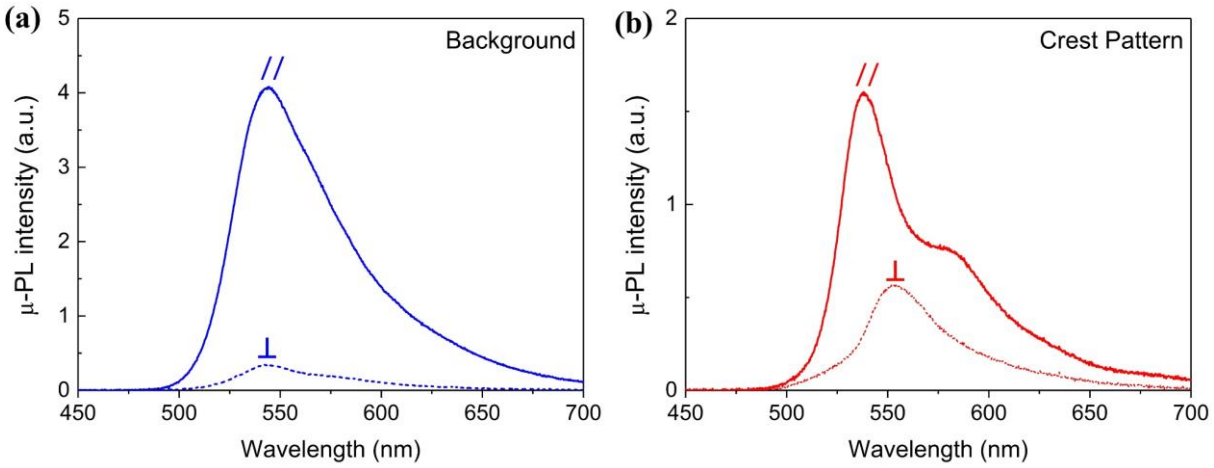

Figure 6.8: Micro-PL spectra for F8BT on (a) the laser written crest and (b) the UV-aligned background. In both cases, the two-photon laser excitation used to trigger the PL was linearly polarised orthogonal to the orientation of the polymer chains and spectra are shown for PL emission polarised both along the chain direction ($PL_{//}$) and perpendicular to it ($PL_{\perp}$). The anisotropy ratios at the peaks in their respective $PL_{//}$ spectra are 12.3 at 544 nm for (a) and 5.3 at 538 nm for (b). The $PL_{\perp}$ spectra peak at 543 nm and 554 nm, respectively, for (a) and (b).

Direct two-photon laser writing of the SD1 photoalignment layer thereby emerges as a promising method for spatial patterning of the oriented LCCP films. In addition, the alterations in the spectral characteristics point to a significant change in the F8BT microstructure when oriented on laser (re)written SD1 alignment layers. Assuming a single emission species with the different spectral features part of the same vibronic progression, the change between UV-aligned and laser-(re)written SD1 would be indicative of lower inhomogeneous broadening (increased resolution of the second peak) and higher molecular structural order in the laser-written F8BT crest pattern, together with a smaller Huang-Rhys parameter (greater relative weight in the first (0-0) vibronic transition) in the laser-rewritten crest; the latter generally arises from a more rigid molecular geometry [7]. This is not, however, in agreement with previous discussions of the PL spectral features in F8BT for which a model has been proposed that has

two distinct emissive species, resulting from differing chain-packing motifs. The relative weighting of spectral components then depends on inter-chain, inter-BT unit contacts with an increase in direct BT to BT contact increasing the strength of the longer wavelength feature [8].

Comparing the cases when the laser writing is either into a nonaligned SD1 layer or one that has been aligned initially using UV illumination, we note that the smaller polarisation ratio observed for the latter seems to signal a reduction in the overall degree of F8BT chain orientation atop the laser rewritten SD1 and/or an increase in the off-axis component of the corresponding transition dipole moment. The latter possibility is an interesting topic for future study, which could be investigated using polarised absorption and Raman anisotropy measurements [2,9]. The combination of UV-alignment followed by two-photon laser writing will not cause any oxidative damage to the F8BT film as these steps are taken prior to coating the polymer film and performing a single thermal annealing cycle that is the same for all samples. It might be, however, that the SD1 layer is susceptible to photooxidative damage leading to a reduced ability to generate subsequent alignment of F8BT. Further discussion on this point will be made in the following sections, where we would propose that a subsequent two-photon laser rewriting/realignment of the UV-prealigned SD1 probably increase the relative weighting of randomly oriented F8BT chains in the laser-rewritten F8BT nematic glass films, relative to the disorder formed in both UV-aligned and laser-written F8BT.

From the PL spectra presented in Figures 6.7 and 6.8, while also referring to **Figure 6.9** which plots all spectra in a normalized peak intensity format for closer comparison, we can make some general observations. The spatially averaged PL emission from the F8BT layer atop a nonaligned SD1 layer is, as expected, independent of the analyser orientation and similar to many published spectra for spin-coated F8BT films [8]. The emissive excited state of F8BT is

reported to have significant charge transfer character which will likely lead to shifts in the spectral position that is dependent on packing density and the local dielectric environment [10].

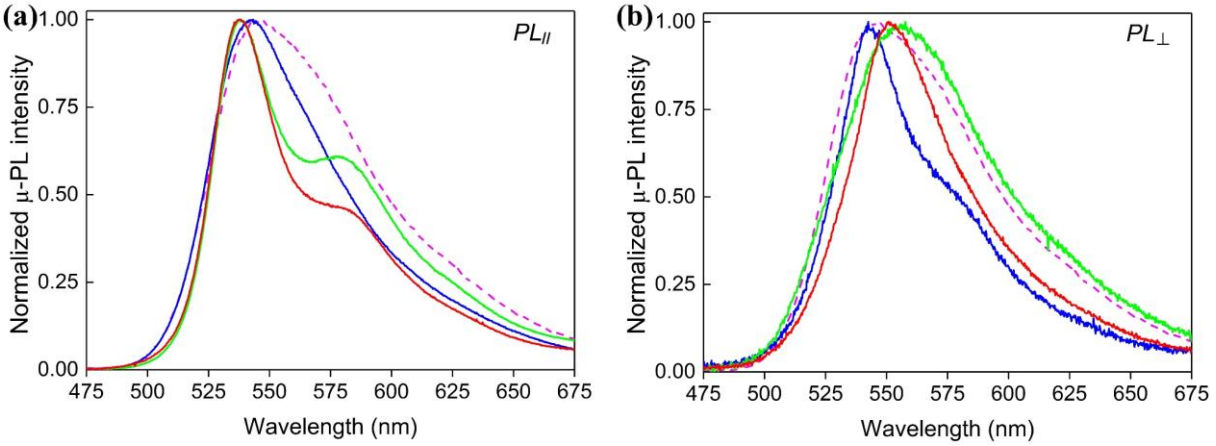

Figure 6.9: Peak normalized µ-PL spectra for F8BT annealed and quenched on top of a crest-pattern that was laser rewritten on a nonaligned (solid green line) and a uniformly UV-aligned (solid red line) SD1 film. Also shown are the spectra for F8BT annealed and quenched on top of a non-patterned UV-aligned (solid blue line) and a non-aligned (dashed pink line) SD1 film. Spectra are shown for (a) parallel ($PL_{//}$) and (b) perpendicular ($PL_{\perp}$, polarised emission relative to the chain orientation direction). In both cases, the spectra were obtained using an excitation polarisation that was parallel to the chain orientation direction.

The PL from the F8BT film on a UV-aligned SD1 layer (Figure 6.9, blue line) exhibits a narrower spectral linewidth than that from nonaligned films for both emission polarisation components. In addition, the $PL_{\perp}$ emission spectrum for the F8BT on a UV-aligned SD1 layer shows the resolution of a weak shoulder at 580 nm. The F8BT PL spectra from the laser-rewritten SD1 on a UV-aligned background (Figure 6.9, red line) differs in that the resolution of a second peak/shoulder at 580 nm appears in the $PL_{//}$ spectra (compared to the $PL_{\perp}$ component for the case of the UV-aligned sample), whereas the $PL_{\perp}$ spectra is relatively featureless, peaking at ≈ 552 nm. The $PL_{//}$ spectrum for the laser-written crest in the nonaligned background (Figure 6.9, green line) is similar to that seen for the crest in the UV-aligned background (albeit with more definition in the peak/shoulder at 580 nm), the spectrum recorded for the $PL_{\perp}$ component is rather broader, although still relatively featureless.

6.3 Polarisation-dependent PL Spectral Separation of Two Orthogonal Emissive Species

Figure 6.10 shows the normalized PL spectra for an F8BT film aligned on a two-photon-laser written region of SD1 and on the surrounding UV aligned SD1 background. Again, the orientation of the chains defined by the crest are at 90º to the surrounding regions. These results were recorded with the excitation polarisation and emission light that is polarised either parallel or perpendicular to the photoaligned chain axis. All polarised spectra highlight different vibronic structures of the anisotropic emission from the F8BT regions on laser-(re)written and UV-aligned SD1, with the laser (re)written F8BT crests exhibiting a well-defined $PL_{//}$ spectra with a clear secondary peak/shoulder at 580 nm and a noticeable red-shift of the $PL_{\perp}$ spectrum. However, no such redshift is observed for the PL emission from the UV-aligned F8BT background and, furthermore, the weak appearance of a second peak at 580 nm is visible in the $PL_{\perp}$ spectrum, rather than the $PL_{//}$ spectral component. Another finding from Figure 6.10 is that the PL spectral line shape of photoaligned F8BT is essentially determined by the relative emission collection polarisation orientation (Pol_{Em}) to the chain axis, while the peak intensity of the vibronic transitions is reliant on the relative angle between the excitation polarisation (Pol_{Ext}) and the F8BT chain alignment direction.

Such polarisation-dependent PL spectral separation phenomenon between two orthogonal emissive components is also identified in **Figure 6.11** for the two-photon-laser 35°-rewritten F8BT crest with Pol_{Ext} and Pol_{Em} parallel and orthogonal to the chain orientation in the UV-aligned background, leaving Pol_{Ext} and Pol_{Em} aligned at 35° or 55° relative to F8BT backbone in the 35°-rewritten crest in order to detect intermediate imaging contrast. Once again, the two spectra detected with Pol_{Em} = 35° exhibit the dominant first vibronic PL peak at 538 nm and a resolved secondary peak/shoulder at 580 nm, whereas the two red-shifted spectra recorded with Pol_{Em} = 55° peaking at 547 nm are broad and featureless.

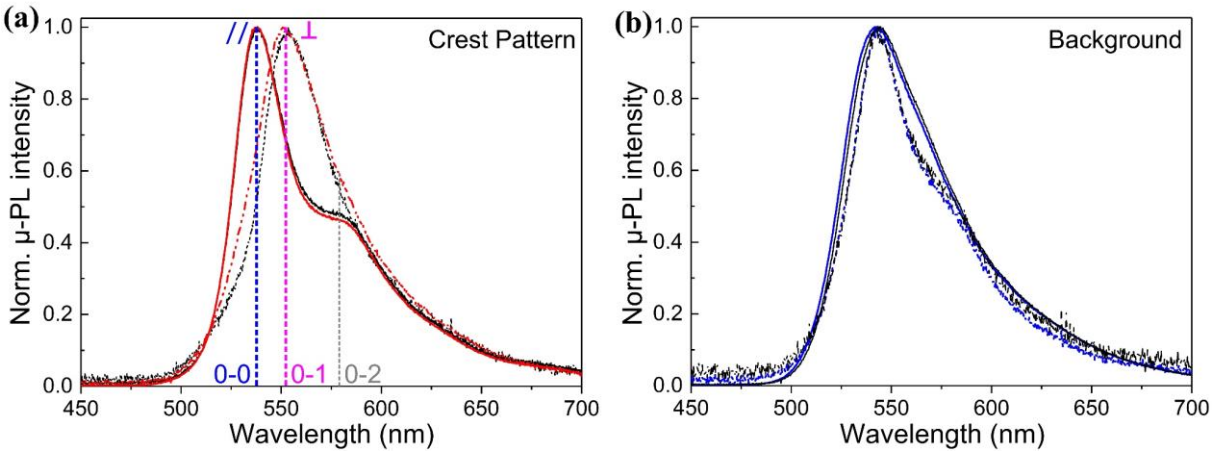

Figure 6.10: Peak normalized µ-PL spectra of F8BT aligned on a crest pattern that was laser written into the SD1 layer (a) and the UV-aligned background (b) that is at 90° to the orientation of the polymer chains in the crest. The results were recorded with four combinations of the excitation polarisation and emission collection polarisation. Solid lines are for emission polarised parallel (//) to the polymer chains, with excitation either parallel (red line in (a); blue line in (b)) or perpendicular (black line in (a) and (b)). Dashed lines are for emission polarised orthogonal (⊥) to the chain direction, with excitation either parallel (red dashed line in (a); blue dashed line in (b)) or perpendicular (black dashed line in (a) and (b)). The three vertical dashed lines in (a) mark wavelength of the 0-0, 0-1, and 0-3 vibronic PL peaks.

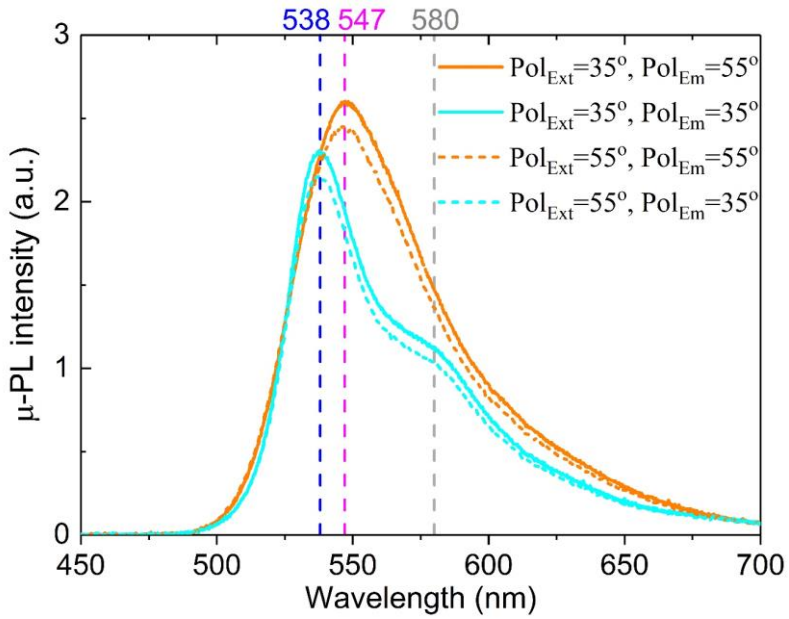

Figure 6.11: µ-PL spectra collected from F8BT aligned on a crest that was written into the SD1 layer such that the orientation of the polymer alignment is at 35° with respect to the background alignments. Results are presented for four combinations of the laser excitation polarisation used to trigger PL (Pol_{Ext}) and the PL collection polarisation (Pol_{Em}). In this case, both Pol_{Ext} and Pol_{Em} were still along the *x*-axis or *y*-axis, which makes the two polarisation directions to be at 35° or 55° relative to the laser-induced chain alignment in the crest.

Taking all of the PL spectral information into account leads to the conclusions (i) that the resulting F8BT film microstructure is significantly dependent on how the SD1 layer is aligned, reflecting the different microstructuring and/or molecular alignment of SD1 by the macroscopic one-photon UV exposure and the highly localised excitation of ultrashort two-photon laser pulses; (ii) that non-parallel excitation polarisation (e.g., the cases of 35° or 55° excitation of F8BT emission relative to the photo-aligned chain axis) reduces the spectral red-shift of the laser writing aligned F8BT to 9 nm between the 35° and 55° collected PL spectra from 14 nm between the $PL_{//}$ and $PL_{\perp}$ spectrum in the 90°-rewritten F8BT crest; and (iii) that whilst the spectra do appear to have contributions from two emissive species, as reported in the literature [5], these are not spectrally separated as previously assumed. What is observed here, most clearly in Figures 6.7(d) and 6.8(b), is that one species gives rise to a vibronically-structured emission with clearly resolved PL peaks at ~ 538 and ~ 580 nm (*c.f.* the $PL_{//}$ spectrum in Figure 6.7(d)) and the other species gives rise to an unstructured, red-shifted emission (c.f. the $PL_{\perp}$ spectrum in Figure 6.7(d)) peaking in this case at ~ 552 nm.

The use of polarised detection helps to separate the two emissive species, and the location and height of their PL peaks are keenly reliant on the relative orientation between the F8BT chain alignment and the emission detection polarisation or excitation polarisation, respectively. These observations suggest that the second emissive PL component may have a more inter-chain character. The literature explanation of two F8BT emissive states depending on the relative orientation of F8 and BT units in neighbouring chains does not fully align with these observations; if nothing else, the existence of a vibronic structure has not been included within that description. The existence of two overlapping emission contributions makes analysis of the anisotropies more difficult, especially since, as surmised here, it may be that one of the species has a more inter-chain, orthogonally polarised, character.

6.4 Linearly Polarised PL of Photoaligned F8BT

The occurrence of the red-shifted $PL_{\perp}$ spectrum and the polarisation-dependent PL spectral separation in F8BT that has been aligned using two-photon laser (re)writing into an SD1 layer, as well as the absence of both of these features in the UV-aligned F8BT most probably correlate with different F8BT film microstructures. In particular, the peak intensity in the $PL_{//}$ spectrum of the UV-aligned F8BT background recorded with the laser excitation polarised perpendicular ($\perp$) to the F8BT polymer chains (Figure 6.8) is considerably higher in comparison with the corresponding $PL_{\perp}$ spectrum for laser 90°-rewritten F8BT crest, though the former exhibits the highest integrated PL anisotropy and possibly the highest molecular structural order as well. This noticeable difference would be indicative of distinct relative orientations of the transition emission dipole moment with respect to the chain alignment direction in the UV- and laser-aligned F8BT films.

Figure 6.12 displays a polar plot of the peak normalized µ-PL intensity at 543 nm for the UV-aligned F8BT background in (a) and of the integrated µ-PL intensity for the 90°-rewritten F8BT crest in (b), both as a function of the angle between the emission collection/analyser polarisation and the chain alignment direction (defining 0° in the two polar plots) in the two types of highly oriented F8BT. All deconvoluted µ-PL spectra in Figure 6.12 were recorded at the same location with an excitation polarisation parallel to the chain orientation and during 360° rotation of the analyser polarisation angle with a step size of 10°. The normalized PL intensity for the UV-aligned F8BT is found to reach a maximum at an analyser polarisation angle of ~21°, whereas the strongest (smallest) total intensity in the laser-rewritten F8BT crest occurs for the parallel (right-angle) analyser polarisation angle with respect to the polymer chain alignment direction.

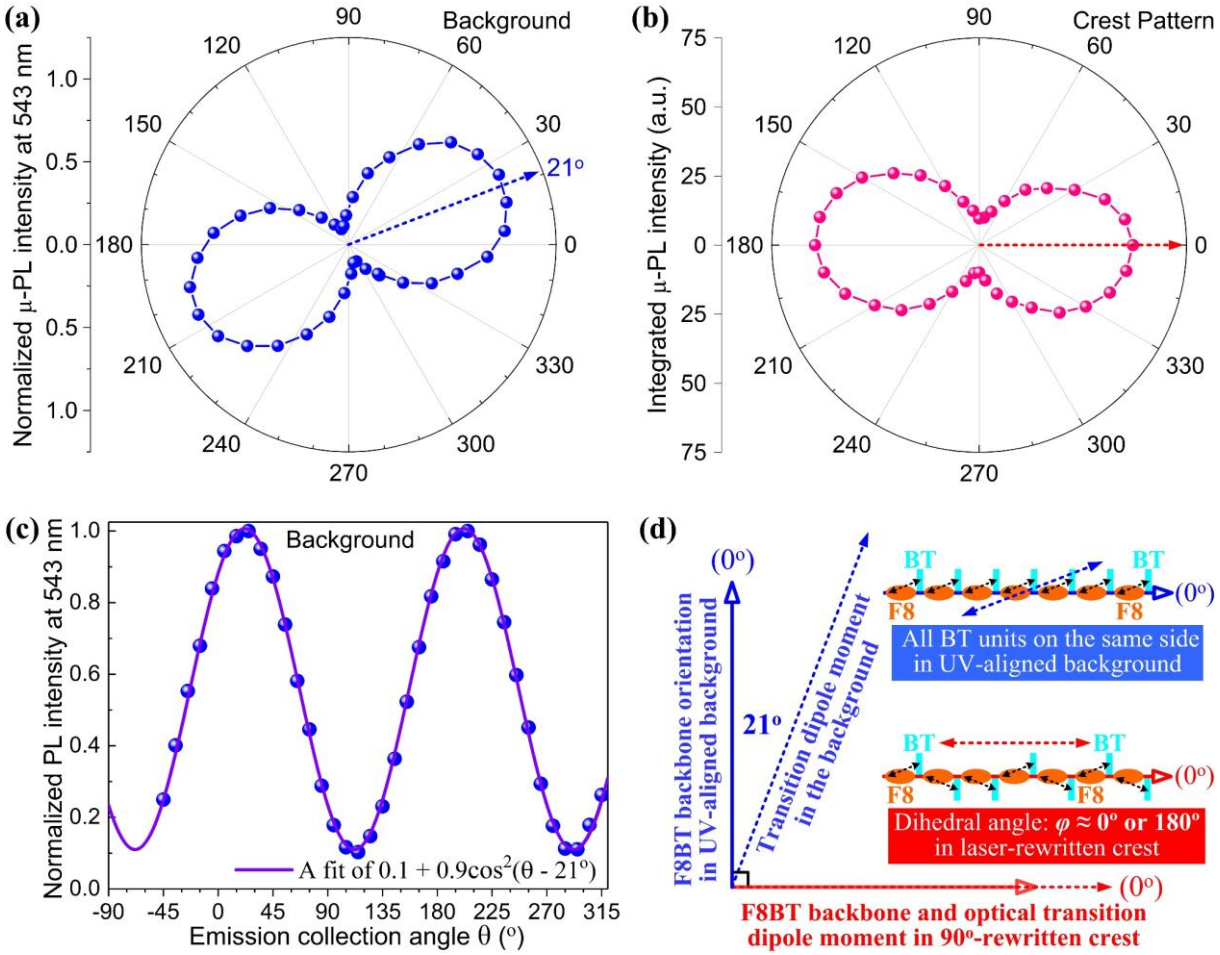

Figure 6.12: Polar plot of (a) peak normalized μ-PL intensity for F8BT regions aligned on the UV exposed SD1 layer and (b) integrated μ-PL intensity for the regions of F8BT aligned using the laser writing process with a polarisation that is at 90° to the UV aligned regions. All μ-PL spectra were recorded at the same location with parallel excitation polarisation (to the chain alignment direction) for a 360° azimuthal rotation of the analyser transmission axis in increments of 10°. (c) Cosine-square function fitting of the peak normalized μ-PL intensity for the F8BT aligned on the UV-aligned background. (d) Schematic illustration of the inferred F8 unit positions relative to the BT unit along the chain axis and concomitant emission dipole moment orientations (thin dashed lines) relative to the chain axis (defining 0°; denoted by thick solid lines) in the laser-rewritten F8BT crest and the UV-aligned background. The black dashed arrows mark the emission dipole orientation of the F8BT monomer. Intermolecular torsion and chain bending were not considered here for simplicity.

The angular variation of the peak normalized μ-PL intensity for the UV-aligned background was further shown in Figure 6.12(c) following a 21° right-shifted cosine-square function with respect to the analyser polarisation angle. This highlights a linearly polarised

emission feature in the highly oriented F8BT background that was aligned using a UV illumination of the SD1 before heating to and quenching from the nematic LC phase. The integrated PL intensity in the laser 90°-rewritten F8BT crest pattern, on the other hand, cannot be well fitted by a cosine-square function (not shown), through it still demonstrates a periodic angular change with a periodicity of 180° and the maximum/minimum intensity located at the parallel and right-angle analyser polarisation. This different would point to the possibility of the existence of a significantly more complicated vibronic PL structure and/or different chain conformations and interchain packing for the F8BT polymer chains oriented at the nematic phase by the highly localised ultrafast two-photon laser (re)written SD1 and UV-aligned SD1.

Based on the information about the angular variation in the PL intensity, different chain-conformations and emission transition dipole moment orientations relative to the F8BT chain alignment direction are proposed and schematically illustrated in Figure 6.12 (d) for the laser-rewritten and UV-aligned F8BT configurations. The main difference in the chain-conformation lies in how the BT units are positioned relative to the F8 units, in terms of variation of the dihedral angle (φ) between the two units along the backbone. Assuming the planar F8 units are aligned parallel to the plane of the oriented F8BT nematic film, the single Carbon-Carbon bond linking the adjacent F8 and BT unit allows a certain degree of freedom for the two units to rotate relative to each other. As a result, the φ variation is a key factor that gives rise to the concomitant F8BT planarity and intrachain/interchain exciton coherence length. For the two-photon laser-aligned F8BT polymer chains, a random switching between $\varphi = 0°$ and $\varphi = 180°$ along the backbone is able to cancel out any off-axis component of the emission dipole moment relative to the chain axis, leading to the two being parallel to each other. For the UV-aligned F8BT, considering that our determined off-axis angle $\beta = 21°$ of the emission dipole moment relative to the chain axis is nearly equivalent to the theoretically predicted and experimentally measured value of $\beta = 22°$ [2,11,12], all BT units, in this case, are most probably located on

the same side of the backbone with all φ remaining close to 0°. It is noteworthy that these proposed F8BT chain conformations also accord to the corresponding PL spectra recorded with Pol_{Ext} and Pol_{Em} parallel to the direction of optical transition dipole moment of oriented F8BT.

In order to complement the polarised PL spectra recorded with Pol_{Ext} and Pol_{Em} along a direction that is either parallel or orthogonal to the chain axis orientation (presented in Figures 6.7(c), 6.8(a)), additional µ-PL spectra of the UV-aligned F8BT background detected with Pol_{Ext} parallel to the direction of optical transition dipole moment (i.e., at $\beta = 21°$ relative to the chain axis of the UV-aligned F8BT polymer chains) and Pol_{Em} aligned parallel ($PL_{//,dipole}$) and perpendicular ($PL_{\perp,dipole}$) to Pol_{Ext} are shown in **Figure 6.13**.

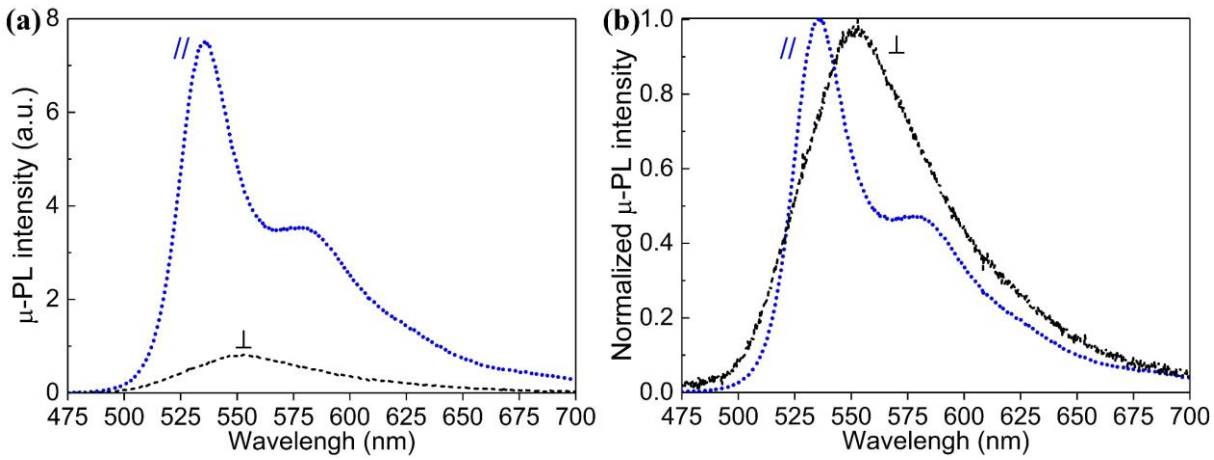

Figure 6.13: Polarised µ-PL spectra of the UV-aligned F8BT background, detected with Pol_{Ext} parallel to the emission dipole moment direction as well as Pol_{Em} parallel (//) to Pol_{Ext} and perpendicular (⊥) thereto.

The $PL_{//,dipole}$ spectrum of the UV-aligned F8BT background exhibits two well-defined vibronic bands peaking at 536 nm and 582 nm. Unlike the $PL_{\perp}$ spectrum of the UV-aligned background detected with Pol_{ext} parallel and Pol_{Em} perpendicular to the chain axis (see Figure 6.7(c)), the red-shifted $PL_{\perp,dipole}$ spectrum appears featureless and shows no clear resolution of a second peak/shoulder at ~580 nm. This slightly broader $PL_{\perp,dipole}$ spectrum is mainly responsible for the reduced integrated PL anisotropy in the same regions of F8BT that have

been aligned with UV illumination from $\int PL_{//} / \int PL_{\perp} = 10.1$ to $\int PL_{//,dipole} / \int PL_{\perp,dipole} = 7.3$. The PL anisotropy at the 0-0 vibronic peak between the $PL_{//,dipole}$ and $PL_{\perp,dipole}$ spectrum, however, is enhanced to ~12 in comparison with the value of ~9 obtained between the $PL_{//}$ and $PL_{\perp}$ spectrum. Besides, polarisation-dependent separation of the $PL_{//,dipole}$ and $PL_{\perp,dipole}$ spectrum is manifest in the UV-aligned F8BT background. In contrast to the same change trend of PL intensity/anisotropy experienced by the laser-aligned F8BT during an azimuthal rotation of Pol_{Ext} and Pol_{Em}, the integrated PL anisotropy and PL peak anisotropy in the UV-aligned F8BT undergo an opposite change trend with rotational Pol_{Ext} and Pol_{Em}, which may be a consequence of the off-axis orientation of the transition dipole moment for the later photoalignment case.

6.5 Polarisation-dependent Vibronic Progressions

Ultrafast, locally two-photon laser (re)written F8BT manifests with different polarisation-dependence of the PL spectra with these of the macroscopically, uniformly UV-aligned F8BT. Vibronic progression for the polarised μ-PL spectra was implemented in order to study the angular distribution of the relative weighting of the identified vibronic PL bands. Multiple-Gaussian-peak fitting results for the well-defined $PL_{//}$ spectrum and the red-shifted $PL_{\perp}$ spectrum recorded for the laser 90°-rewritten F8BT crest (with parallel Pol_{Ext}) are presented in **Figure 6.14**. It can be seen that multi-peak fitting with three Gaussian peaks (i.e., the identified 0-1 and 0-2 vibronic peak at 552 nm and 580 nm, and a higher-order (0-3) vibronic peak corresponding to the long-wavelength tail/background) appears to explain the structure of the $PL_{\perp}$ spectrum, while a four-peak (together with the 0-0 vibronic peak at 538 nm) fitting curve is required to accurately reproduce the $PL_{//}$ spectrum. These multi-peak fits were performed by fixing the peak locations so as to investigate the best-fitted height and spectral area at each vibronic peak. The same data fitting method was used to best fit all other PL spectra that were collected at the same location in the rewritten F8BT crest for a 360° rotation of Pol_{Em} relative to the chain orientation using a step size of 10°.

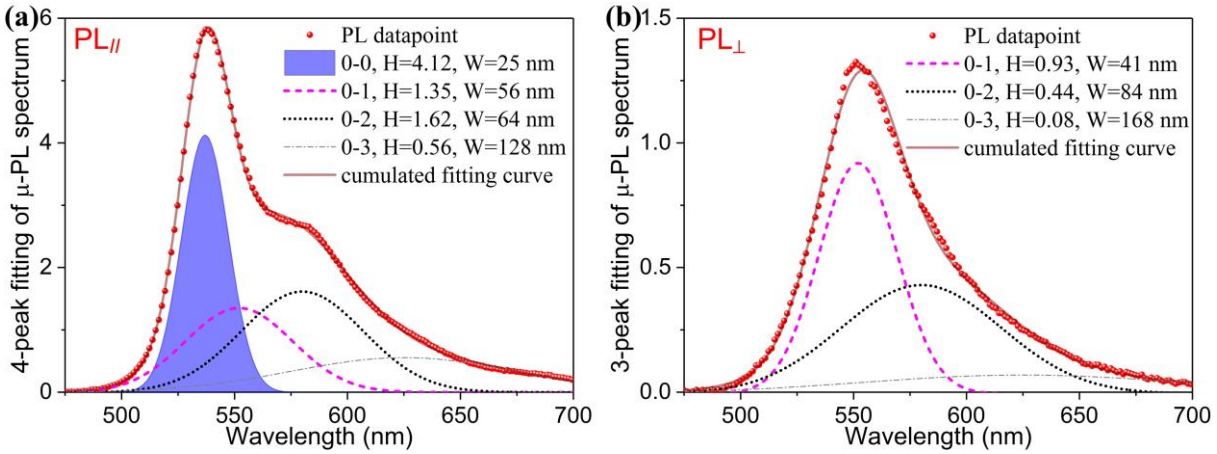

Figure 6.14: Multiple-peak fitting for the $PL_{//}$ spectrum (a) and the red-shifted $PL_{\perp}$ spectrum (b) for the aligned F8BT crest pattern by a laser re-written SD1 commanding layer. The laser rewriting was carried out with a polarisation that was aligned at 90° to the SD1 alignment induced by the bulk UV illumination. The deconvolution of each PL spectrum was implemented using the multiple peak fit tool in Origin software with fixing the equally separated locations of the 0-0, 0-2 and 0-3 vibronic PL peaks at 538 nm, 580 nm and 622 nm, respectively, whereas the 0-1 vibronic transition centred at 552 nm is used to correspond to a different origin of the μ-PL emission. The letter H and W appearing in the figure legend of (a) and (b) denote the fitted height and FWHM of the corresponding Gaussian peaks, both of which were set free in the process of simultaneous multi-peak fitting in order to accommodate the related inhomogeneous spectral line broadening effects.

The different angular variations of the spectral area fractions of the main vibronic PL transitions are shown in **Figure 6.15(a)** as polar plots as a function of the angle between Pol_{Em} and the chain orientation. For instance, the relative weighting of the vibronic bands in the $PL_{//}$ spectrum was plotted at 0° analyser polarisation angle and the $PL_{\perp}$ spectrum at 90°. The variation in the angular areal fraction of the 0-0 vibronic emission band appears linearly polarised for all analyser polarisation angles with the greatest weight and the thinnest line-width occurring for a parallel polarisation orientation (i.e., along the F8BT chain alignment direction) and a zero fraction at orthogonal polarisation angle. The higher-order (0-2 and 0-3) vibronic transitions exhibit nearly a circle-shaped angular variation in the polar plot, indicating a non-polar character. The 0-1 vibronic transition shows an elliptical plot with the greatest (smallest) weight occurs at 90° (0°) polarisation angle. These dissimilar variations imply that the whole emission is contributed from a non-polarised component and a strong linearly polarised PL component whose polarisation is perpendicular to the F8BT chain alignment direction; the non-polarised PL component likely originate from amorphous phase F8BT chains.

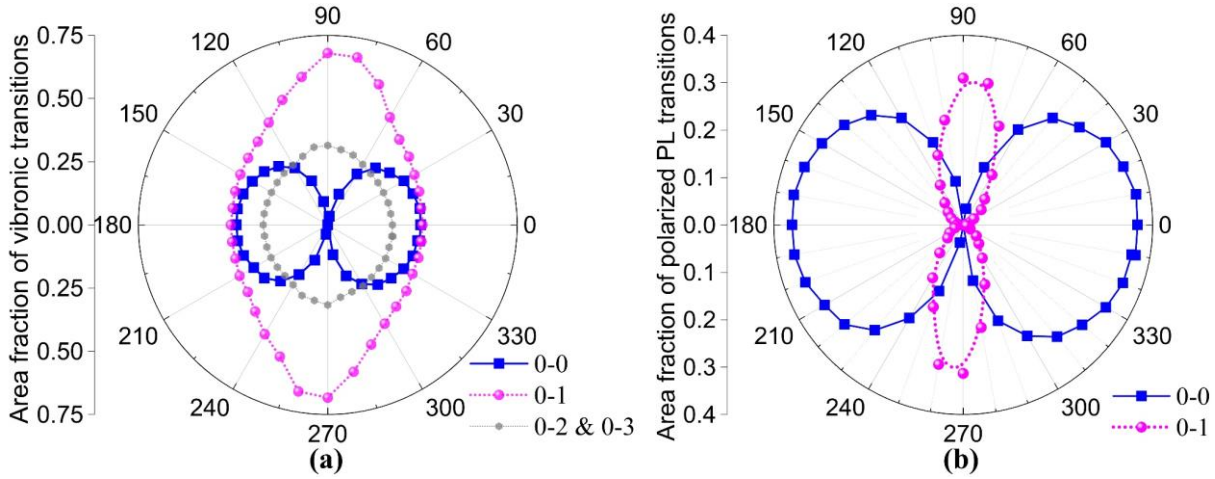

Figure 6.15: (a) Polar plot of the spectral area fraction of the vibronic transitions in the polarised µ-PL spectra as a function of the relative angle between Pol_{Em} and the chain orientation. The PL spectra were detected at the same location in the two-photon laser 90°-rewritten F8BT crest with parallel excitation polarisation and recorded whilst Pol_{Em} was rotated 360° relative to the chain orientation in step sizes of 10°. (b) The corresponding polar plot of the spectral area fraction of the polarised vibronic PL components in the µ-PL spectra.

For the $PL_{//}$ spectrum, both the areal fractions of the 0-0 and 0-1 vibronic transition in the integrated PL intensity are determined to be ~37 %, which, together with the relative weight of the other two higher-order vibronic transitions of ~26%, resembles a Poisson distributed vibronic progression with the number occurrence of 1 in the framework of Franck-Condon principle [13]. The non-polar PL feature exhibited by the 0-1, 0-2 and 0-3 vibronic components corresponds to the presence of randomly oriented F8BT chains in the laser-rewritten crest (i.e., the overall crystallinity in the crest is <100%) and infers distinct origins between these non-polarised longer-wavelength vibronic transitions and the highly linearly polarised 0-0 vibronic transition along the polymer alignment direction. Based on the identical faction of ~37% for both the non-polar and polarised PL components at the 0-1 vibronic peak in the $PL_{\perp}$ spectrum, the fraction of parallelly oriented F8BT chains in the laser-written F8BT crest is determined to be 74%, because the total PL intensity ratio between the contribution from non-aligned F8BT in the $PL_{//}$ spectrum (Figure 6.14(a)) and the $PL_{\perp}$ spectrum (Figure 6.14(b)) is estimated as 2.84. Furthermore, a PLQE value of ~10% is extracted for the perpendicular polarised interchain light emission based on the requirement of 74% amorphous F8BT (PLQE = 29% - 35%) to produce

the same intensity of the 0-1 vibronic PL transition in the $PL_{\perp}$ spectrum as 26% highly-oriented F8BT, together with the obtained polarised absorption strength of the two F8BT phases.

When a right-angle analyser polarisation was used, the PL contribution of the linearly polarised 0-0 vibronic band reduces according to a Cosine-squared function. As the weight of the broad higher-order vibronic transitions remains constant, the gradually reduced areal fraction of the first allowed (0-0) transition adds exactly to the weight of the second allowed but orthogonally polarised vibronic transition, as demonstrated in Figure 6.15(b). The dominant PL component of the highly oriented F8BT chains alters from the emissive intrachain species to the low-energy interchain species and yields a continuous red-shift of the PL spectrum. As the PL spectra of the spatially averaged non-aligned nematic F8BT chains are independent of angle relative angle of the transmission axis of the analyser, the intensity difference between the $PL_{//}$ spectrum and the $PL_{\perp}$ spectrum ($PL_{//}$ - $PL_{\perp}$) recorded at the same location with fixed excitation polarisation can be utilised to remove the emission component of the non-aligned F8BT content, hence providing insight of the vibronic PL structure originating purely from the highly oriented F8BT chains by photoalignment. **Figure 6.16** shows the $PL_{//}$ - $PL_{\perp}$ spectrum subtracted for the laser 90°-rewritten F8BT crest. The $PL_{//}$ - $PL_{\perp}$ spectrum for F8BT aligned using laser writing into an SD1 layer that had been illuminated with UV light was compared with the μ-PL spectra from the nonaligned nematic F8BT region with the same film thickness (shown in Figure 6.7(e)). The $PL_{//}$ - $PL_{\perp}$ spectrum of the laser-rewritten F8BT crest exhibits a significantly enhanced 0-0 vibronic transition and also a slightly reduced PL band that exists exactly between the wavelengths of the 0-1 and 0-2 vibronic peak. The former PL intensity enhancement dictated by the well-defined $PL_{//}$ spectrum of the highly oriented F8BT polymer chains is potential manifestation of emission from J-aggregate structures (a head-to-tail chain orientation that optically allows the 0-0 vibronic PL transition) of emissive intrachain species [13,14]. The suppressed 0-1 PL intensity supports a more H-like aggregate feature that prevents the 0-0 optical transition due to the side-to-side interactions, as shown in the $PL_{\perp}$ spectrum.

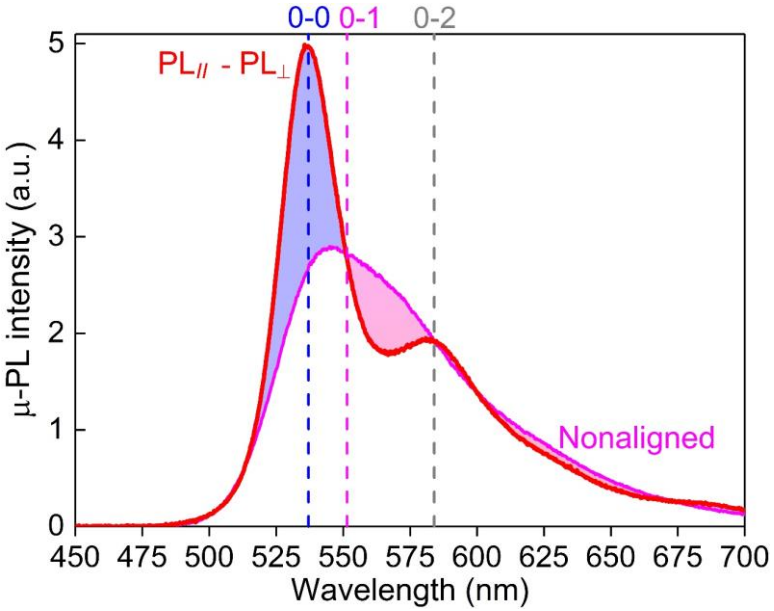

Figure 6.16: The $PL_{//}$ - $PL_{\perp}$ spectrum subtracted for the F8BT on laser written SD1 that was written with a polarisation such that the chain alignment was at 90° relative to the UV alignment. Both the $PL_{//}$ and $PL_{\perp}$ spectra were detected with parallel excitation polarisation but parallel (//) and perpendicular ($\perp$) analyser polarisation relative to the chain alignment direction in the crest.

The enhanced PL intensity of the longer-wavelength semi-band of the 0-0 vibronic transition in the well-defined $PL_{//}$ spectrum (relative to the nonaligned F8BT emission) and the reduced intensity of the shorter-wavelength semi-band of the 0-1 vibronic transition in the $PL_{\perp}$ spectrum countervail with each other, yielding near equal intensity on both $PL_{//}$ - $PL_{\perp}$ spectrum and nonaligned F8BT spectrum at the 0-1 vibronic peak. This is also consistent with the multi-peak μ-PL spectral fitting results that emphasize mutual transfer between the areal fractions of the linearly polarised intrachain 0-0 vibronic transition and the polarised component of the interchain 0-1 vibronic transition. The same counteracting mechanism can be also responsible for the spectral intersection at the 0-2 vibronic peak. Furthermore, it is found that the long-wavelength spectral tails in the two spectra in Figure 6.16 are in close proximity, implying that the PL behaviour of the higher-order vibronic transitions are not very sensitive to F8BT chain alignment and aggregation state, which well corresponds to their non-polar PL character previously indicated based on the spectral vibronic progression results.

6.6 Comparison of Alignment Quality and Proposed Chain Conformations

The degree of orientation of the F8BT polymer chains and the vibronic structure present in the PL spectra from the aligned F8BT films/patterns appear to be dictated by (i) how the SD1 layer has been photoaligned (e.g., via macroscopic UV illumination and/or highly localised two-photon ultrafast laser (re)writing), (ii) the concomitant structural order of the SD1-aligned F8BT polymer chains, and (iii) how the polarised PL spectra are detected, that is, the direction of the transmission axis of the analyser (Pol_{Ext} or Pol_{Em}) relative to the chain axis and the emission dipole moment orientation. We observe that the polarised PL spectra for the two-photon laser aligned F8BT films appear to have two orthogonal components possibly resulting from emissive intrachain and interchain species. Under fixed excitation laser beam polarisation and power, the strongest (weakest) total PL intensities for the laser-rewritten F8BT crest seem to occur when the analyser is set to an angle of 0° (90°) corresponding to the well-defined $PL_{//}$ spectrum (red-shifted, featureless $PL_{\perp}$ spectrum). The orientation of the optical transition dipole moment in the highly oriented F8BT polymer chains which have been aligned by an SD1 layer that has been exposed to UV illumination, on the other hand, appears to occur at an angle of 21° relative to the aligned chain axis. This could complicate the polarised PL spectral information for the UV-aligned F8BT films: when Pol_{Ext} and Pol_{Em} were aligned parallel or orthogonal to the chain axis, the polarisation-dependent PL spectral separation between the $PL_{//}$ and $PL_{\perp}$ spectrum did occur but without clear red-shift in the PL peak location; however, the red-shift in peak wavelength as well as the $PL_{//}$ and $PL_{\perp}$ spectral separation were observed when the emission are detected with a rotational Pol_{Em} from parallel (the $PL_{//,dipole}$ spectrum) to perpendicular (the $PL_{\perp,dipole}$ spectrum) to the direction of emission dipole moment along which the Pol_{Ext} is aligned as well. Therefore, a more reliable direct comparison of the chain-orientation quality in F8BT regions aligned by two-photon laser-(re)written SD1 and UV-aligned SD1 requires special consideration of the different emission dipole moment orientations with respect to the photoaligned chain axis.

High-quality orientation of the polymer chains of F8BT can lead to well-resolved vibronic PL lines. The well-defined $PL_{//}$ spectra recorded for both the laser written and 90°-rewritten F8BT crests, together with the vibronic structured $PL_{//,dipole}$ spectrum observed for the UV-aligned background in the same F8BT nematic glass film, can provide a reliable comparison of the F8BT alignment quality. As the crystallinity in the photoaligned F8BT nematic films is inevitably less than 100%, the three well-defined spectra should include certain non-polar emission contributions arising from the unaligned, randomly oriented F8BT polymer chains. Because of the polarisation-independent feature of the emission of amorphous-phase F8BT polymer chains [3,11], the $PL_{//,dipole}$ - $PL_{\perp,dipole}$ spectrum for an oriented F8BT film/region should be dictated by the radiative vibronic electronic transitions of the photoaligned F8BT polymer chains. As thus, the ratio between the total intensity of this $PL_{//,dipole}$ - $PL_{\perp,dipole}$ spectrum and that of the obtained $PL_{//,dipole}$ spectrum can be thought as a measure of the degree of crystallinity achieved in the photoaligned and quenched F8BT glass films.

Making use of the integrated PL intensity ratio of the $PL_{//}$ to $PL_{\perp}$ spectra recorded at the same location in both laser-written and 90°-rewritten F8BT crests as well as the $PL_{//,dipole}$ and $PL_{\perp,dipole}$ spectrum for the UV-aligned background, the crystallinity in the laser written, laser-rewritten, and UV-aligned F8BT regions was calculated to be 88%, 76%, and 86%, respectively. Such crystallinity change trend is consistent with the PL peak intensity anisotropies of 13, 6.5, and 12 for these three cases, respectively. Moreover, a relation between the three F8BT crystallinity levels hold, that is, 76% (laser-written F8BT) ≈ 86% (UV-aligned F8BT) × 88% (laser-written F8BT). This equation suggests that the structural disorder (e.g., molecular tilt, oxidative damage) in a multi-step photoaligned SD1 layer is an accumulated result of the induced molecular disorder in every step of photo-alignment and, subsequently, can be detrimental to the chain orientation quality in an overlying F8BT film in the nematic phase.

The different vibronic structural features observed in the $PL_{//,dipole}$ - $PL_{\perp,dipole}$ spectrum presented in **Figure 6.17** for the laser-written, laser-rewritten, and UV-aligned F8BT regions can also be correlated with the as-shown inferred F8BT chain conformations. Although the three $PL_{//,dipole}$ - $PL_{\perp,dipole}$ spectra exhibit very similar vibronic lines, they differ significantly in the PL intensity ratio between the first (peaking around 538 nm) and second (peaking around 580 nm) vibronic transition (R_{PL}), which is commonly expressed as $R_{PL} = N_{coh} / \lambda^2$ where $N_{coh,}$ is the exciton coherence length and λ is the Huang-Rhys factor [15].

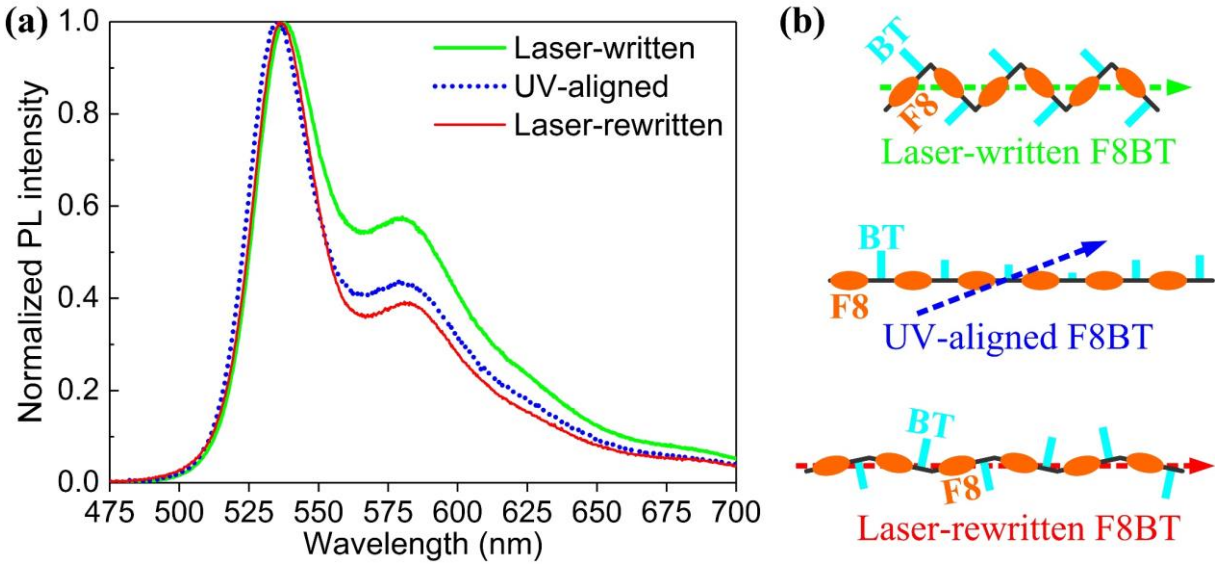

Figure 6.17: (a) The extracted $PL_{//,dipole}$ - $PL_{\perp,dipole}$ spectrum obtained for the two-photon laser-written F8BT crest (solid green line), the laser 90°-rewritten F8BT crest (solid red line), and the UV-aligned F8BT background (dashed blue line). (b) Schematic illustration of the proposed chain conformations for the three different types of photoaligned F8BT. The dashed one-headed arrow (blue, green, and brown for UV-aligned F8BT, laser-written F8BT, and laser-rewritten F8BT, respectively) indicate the emission dipole moment orientation in each case. The solid black lines denote the bending of the F8BT backbone. The non-uniform length of the BT unit bars along the UV-aligned F8BT chain axis schematically demonstrates a small variation of the dihedral angle.

The F8BT crest created from laser writing demonstrates the lowest R_{PL} ratio, which means a shorter intrachain coherence length (or a greater Huang-Rhys factor, i.e. a softer F8BT nematic glass film) that generally indicates a lower chain-planarity and/or a larger degree of microstructural distortions such as chain-segment kinks. As the two-photon laser-written F8BT

exhibits the highest PL peak anisotropy and a collinear alignment of the emission dipole orientation with the chain axis, it is proposed and schematically illustrated in Figure 1.17(b) that the concomitant chain conformation is characterised by the lowest intermolecular torsion and the greatest extent over which random kinks of the backbone segments occurs around the chain axis in the film plane, probably due to a random variation in the dihedral angle between 0° or 180°. Substantial chain-segment kinks would effectively shorten the conjugation length of the F8BT backbone and also soften the glass film [16], hence enhancing the Huang-Rhys factor and inhomogeneously broadening the vibronic line width [17].

For the UV-aligned F8BT, the position of the BT units most probably occurs on one side of the backbone such that the direction of the spatially averaged emission dipole moment remains parallel to the molecular transition dipole moment orientation of an F8BT monomer, both deviating from the chain axis by ~21° - 22°. This linear chain-conformation can diminish chain-segment kinks and, thus, extend/stiffen the F8BT polymer chains, which in turn leads to a more rigid molecular geometry and improves the exciton coherence length along the backbone direction, in line with a more condensed interchain packing structure and possibly a strong interchain excitonic coupling. These molecular features can be correlated with the blue-shifted $PL_{//,dipole}$ spectrum (by 2-3 nm) and slightly wider separation between the first and second vibronic lines. However, it should be stressed that the rather structured $PL_{//,dipole}$ spectrum for the UV-aligned monodomain only displays an intermediate R_{PL} ratio (i.e., still lower than the ratio for the laser-rewritten F8BT), which suggests the existence of nonnegligible molecular disorder in the UV-aligned F8BT. This may be related to a random but small variation in the dihedral angle along the F8BT chain axis (see also the GIWAXS pattern in Figure 4.4(c)). Although the high-quality F8BT alignment enabled by UV-aligned SD1 largely orientates the F8BT chains laying in the proximity of the film plane, the collective SD1 reorientation excited by polarised macroscopic UV illumination for a relatively long period may result in a small but

random tilt angle of the UV-aligned SD1 molecules. Such SD1 rotation may then cause the long F8BT backbones to undergo a small intermolecular torsion between >100 constituent molecules, particularly in the nematic phase. This feature is, in fact, consistent with the enhanced $PL_{//,dipole}$ peak intensity observed for the UV-aligned background, compared with that observed for both the laser-written and laser-rewritten F8BT crests, as a result of combined effects of linear chain-conformation and chain tilling that tend to induce a more condense interchain packing structure.

Carrying out two-photon laser rewriting following UV pre-alignment of SD1 may, however, restrict the UV-excited SD1 tilting in the photoalignment layer, due to the highly localised and ultrafast nature of the two-photon absorption. The overlying F8BT film tends to inherit the migrated interchain distortions and an extended molecular geometry along the chain axis after thermotropic alignment and quenching. The collective benefits of the reduced degrees of chain-bending and -tilting potentially causes the laser-rewritten F8BT crest to exhibit the most rigid/planar molecular geometry (smallest Huang-Rhys factor) and an enhanced coherence length, which also substantiates the greatest R_{PL} ratio predicated from Figure 6.17.

6.7 Disclinations and High PL Anisotropy for 90°-Rewritten 2D Alignment Patterns

Laser rewriting of an SD1 photoalignment layer takes advantage of both localised ultrafast two-photon laser writing and macroscopic UV-alignment in terms of enabling submicron pattern resolution and high emission anisotropy in the oriented LCCP films. For this process, the relative polarisation orientation of the uniform UV-prealignment to the subsequent laser rewriting polarisation becomes a limiting factor in determining the director degeneracy that causes the formation of LC disclination lines in the transition zone and highlights the importance of polarisation engineering of the emission anisotropy between adjacent polymer alignment patterns. This calls for experimentation of the spatial variation of the PL anisotropy across LCCP patterns that have been aligned using different methodologies.

A combination of high-resolution POM and FL imaging with the high-resolution µ-PL spectral intensity scanning of the 90°- and 35°-rewritten F8BT crests against UV-aligned background has been carried out to distinguish the different optical and emissive properties in the photoaligned patterns. For comparison, the crossed-polariser POM image and polarised confocal FL images of the two laser-rewritten F8BT crest patterns are demonstrated in **Figure 6.18**. As expected, the borders of the two crests in Figure 6.18(a) exhibit different optical texture: those of the 90°-rewritten F8BT crest illustrate a very thin defect line that has an irregular shape and is embedded in a continuous thicker white transition line, whereas the 35°-rewritten crest exhibits only a continuous thick black border (also see Figure 6.5(b)).

Figure 6.18(b) presents a direct comparison of the integrated PL profile of the 90°- and 35°-rewritten F8BT crest as a function of the coordinate along a horizontal scanning line (location marked in Figure 6.18(a)), which showcases the fascinating benefits of combining macroscopic UV-alignment and high-resolution two-photon laser rewriting. The integrated PL anisotropy, in this case, between the laser-written F8BT crest and the orthogonally UV-aligned F8BT background varies between 12 and 15, which becomes significantly higher than the integrated PL anisotropy of 4.1 obtained for the $PL_{/\!/}$ to $PL_{\perp}$ spectra of the same crest and of 7.3 - 10.1 for the UV-aligned background. This is because, this time, it is the $PL_{/\!/}$ spectrum of the laser-rewritten F8BT and the $PL_{\perp}$ spectrum of the UV-aligned F8BT that dictates the emission anisotropy; the latter has remarkably reduced PL intensity as it was excited with a laser beam with right-angle polarisation. Emission in the 35°-rewritten F8BT crest shown in Figure 6.18(b), however, exhibits much lower PL anisotropies (~5) relative to the background emission due to off-axis excitation and analyser orientation. In addition, the µ-PL scanning results demonstrate the width of the transition zone separating the crest patterns and the background is ~5 µm, which is thicker by 2 -3 µm than the linewidth determined from the polarised microscope images in Figure 6.2. This is sensible when considering the inherent broadening of the µ-PL

scanning line by the excitation laser spot size (~ 1 μm in diameter) on both sides of the scanned transition zone.

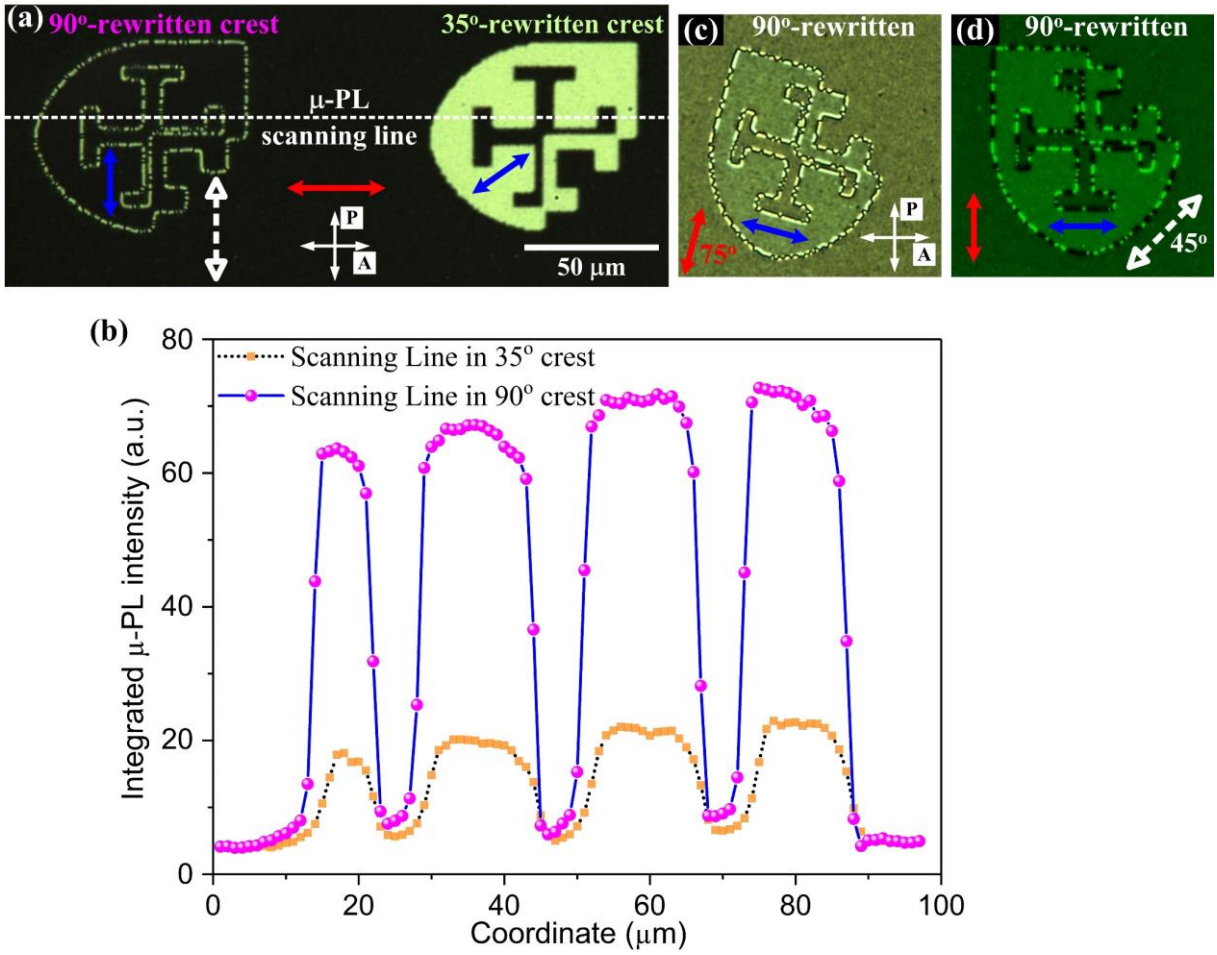

Figure 6.18: (a) Crossed-polariser POM image of 165 nm-thick F8BT films that are aligned on layers of SD1 that have been prealigned with UV illumination and then subjected to laser writing to create the College crest pattern. The two cases are for a laser polarisation that is at 35°- and 90° to the alignment induced by the UV illumination process. The crests have been written into the same F8BT nematic film. Also shown is the μ-PL scanning line location in the two F8BT crests, with the excitation polarisation and analyser polarisation (dashed white double-headed arrow) parallel to the chain orientation (the vertical solid blue double-headed arrow) in the 90°-rewritten crest. The chain orientation in the UV-aligned background is denoted by the solid red double-headed arrows. The transmission axes for the polariser (P) and the analyser (A) are denoted by the solid double-headed white arrows. (b) Plot of the integrated μ-PL intensity scanned for the two crests vs the horizontal coordinate. (c) POM image and (d) Polarised confocal image of the 90°-rewritten F8BT crest with the analyser polarisation (dashed white arrow) at 45° relative to the chain orientation in the crest.

6.8 Summary

In conclusion, this chapter presents a study on the molecular structure-property relationship in highly oriented F8BT that have been aligned using either two-photon laser-(re)written and/or one-photon UV illumination of an SD1 photoalignment layer. It is suggested that different chain-conformations are most probably formed in the laser- and UV-aligned F8BT nematic films, which essentially limits the best achievable absorption and emission anisotropies enabled by the highly localised ultrafast laser writing technique and the macroscopic polarised UV alignment. In particular, the relative orientation of the photoaligned chain axis and the concomitant transition emission dipole moment differs in photoaligned F8BT films that have been prepared using the different processes. The evidence obtained elucidates that the chain axis and the transition dipole moment are parallel for the F8BT patterns prepared using laser writing, whereas for the UV-aligned F8BT regions they are at angle of ~21° relative to each other. As a result, making use of the polarisation degree of freedom for PL excitation and detection, together with multi-step rewriting of spatial features oriented at different angles relative to each other, has been demonstrated as an effective method to fine-tune the vibronic emission structure and optical/photophysical anisotropies in a photoaligned LCCP pattern.

The UV-aligned F8BT nematic monodomain glass films exhibit ultrahigh optical order parameters of ~1 as well as integrated PL anisotropies of 7.3 - 10.1 and PL peak anisotropies of 9 - 12 at the first vibronic peak, which is dependent on how the PL excitation and detection polarisation is aligned relative to the chain axis or emission dipole moment orientation. The F8BT regions on top of laser written SD1 display the highest PL peak anisotropy of 13. The two-photon laser rewriting of SD1 alone was found to yield the lowest emission anisotropies, i.e., 6.5 and 4.1 in terms of the PL peak anisotropy and integrated PL anisotropy, respectively. However, the latter anisotropy increases to 12 - 15 when comparing the PL intensity in the laser-written F8BT with that in the UV-aligned background. These anisotropy values

correspond well to the estimated degrees of crystallinity in the three types of photoaligned F8BT. Using the spectral area ratio between the well-defined $PL_{//,dipole}$ spectrum and the featureless $PL_{\perp,dipole}$ spectrum as a measure of crystallinity, we determine the overall crystallinity in the UV-aligned, laser-written, and laser-rewritten F8BT to be 86%, 88%, and 76%, respectively, suggesting an accumulation of the structural disorder induced by each process of laser/UV-realignment into the oriented F8BT pattern. This high crystallinity for the UV-aligned F8BT nematic monodomain film is similar to the estimation from the GIWAXS results (Chapter 4).

Polarisation-dependent PL spectral separation between the vibronically structured $PL_{//,dipole}$ spectrum and the red-shifted $PL_{\perp,dipole}$ spectrum occurs in all three types of highly oriented F8BT monodomains. The angular variation of the PL spectral area fraction of the polarised PL spectra as a function of the analyser transmission angle suggests that the parallel polarised component of the $PL_{//,dipole}$ spectrum is dominated by the linearly polarised first (0-0) vibronic transition with an intrachain character, whilst an interchain emission peaking at ~552 nm and with a significantly reduced PLQE (estimated as ~10%) contributes largely to the $PL_{\perp,dipole}$ spectrum. It is additionally found that the rather structured $PL_{//,dipole}$ spectra in the UV-aligned, laser-written, and laser-rewritten have distinct vibronic structures. For example, the spectrum for the two-photon laser-written F8BT crest pattern exhibits the lowest R_{PL} ratio, i.e., the PL intensity ratio between the 0-0 vibronic peak and the peak at ~580 nm. We ascribed this low ratio to a possible chain conformation with a significant zig-zag type kinks of adjacent backbone segments and all F8 and BT units remaining parallel to the film plane, which would considerably inhibit the π-conjugation and exciton coherence. The UV-aligned F8BT, on the other hand, is expected to possess the most extended linear chain-segment geometry, with all BT units located at the same side of the chain axis but a small variation of the dihedral angle based on the GIWAXS pattern. The two-photon laser-rewritten F8BT shows the highest R_{PL} ratio, as a possible result of a synergic effect of an enhanced planarity of F8BT and a lowered degree of chain bending/kinks across the F8BT backbone.

References

[1] V. G. Chigrinov, V. M. Kozenkov, H. S. Kwok, *Photoalignment of Liquid Crystalline Materials: Physics and Applications*, John Wiley & Sons, West Sussex, England, 2008.

[2] H. M. Liem, P. Etchegoin, K.S. Whitehead, D. D. C. Bradley, Raman anisotropy measurements: An effective probe of molecular orientation in conjugated polymer thin films. *Adv. Funct. Mater.* **13**, 66 (2003).

[3] H. Zhang, L. Ma, Q. Zhang, Y. Shi, Y. Fang, R. Xia, W. Hu, D. D. C. Bradley, Azobenzene sulphonic dye photoalignment as a means to fabricate liquid crystalline conjugated polymer chain-orientation-based optical structures. *Adv. Optical Mater.* **8**, 1901958 (2020).

[4] M. Grell, M. Redecker, K. Whitehead, D. D. C. Bradley, M. Inbasekaran, E.P. Woo, Monodomain alignment of thermotropic fluorene copolymers. *Liquid Crystals* **26**, 1403 (1999).

[5] R.B. Fletcher, D.G. Lidzey, D. D. C. Bradley, M. Bernius, S. Walker. Spectral properties of resonant-cavity, polyfluorene light-emitting diodes. *Appl. Phys. Lett.* **77**, 1262 (2000).

[6] C. R. Belton *et al.*, Location, location, location - strategic positioning of 2, 1, 3 - benzothiadiazole units within trigonal quaterfluorene - truxene star - shaped structures. *Adv. Funct. Mater.* **23**, 2792 (2013).

[7] M. Ariu, M. Sims, M. D. Rahn, J. Hill, A. M. Fox, D. G. Lidzey, M. Oda, J. Cabanillas-Gonzalez, D. D. C. Bradley, Exciton migration in -phase poly(9,9-dioctylfluorene). *Phys. Rev. B* **67**, 195333 (2003).

[8] C.L. Donley, J. Zaumseil, J.W. Andreasen, M. M. Nielsen, H. Sirringhaus, R. H. Friend, J. S. Kim, Effects of packing structure on the optoelectronic and charge transport properties in poly(9,9-di-n-octylfluorene-alt-benzothiadiazole). *J. Am. Chem. Soc.* **127**, 12890 (2005).

[9] M. C. Gather, D. D. C. Bradley, An improved optical method for determining the order parameter in thin oriented molecular films and demonstration of a highly axial dipole

moment for the lowest energy π - π^* optical transition in poly(9,9 - dioctylfluorene-co-bithiophene). *Adv. Funct. Mater.* **17**, 479 (2007).

[10] J. M. Winfield, A. Van Vooren, M. J. Park, D. H. Hwang, J. Cornil, J. S. Kim, R. H. Friend, Charge-transfer character of excitons in poly [2, 7-(9, 9-di-n-octylfluorene)(1- x)-co-4, 7-(2, 1, 3-benzothiadiazole)(x)]. *J. Chem. Phys.* **131**, 035104 (2009).

[11] Q. Zhang, J. Liu, Q. Wei, X. Guo, Y. Xu, R. Xia, L. Xie, Y. Qian, C. Sun, L, Luer J. Cabanillas-Gonzalez, D. D. C. Bradley, W. Huang, Host exciton confinement for enhanced Förster - transfer - blend gain media yielding highly efficient yellow - green lasers. *Adv. Funct. Mater*. **28**, 1705824 (2018).

[12] Y. Li, J. B. Lagowski, A multi-step simulation of electron mobility in fluorine-benzothiadiazole conjugated polymer - case study. *Comput. Theor. Chem.* **977**, 157 (2011).

[13] F. C. Spano, C. Silva, H-and J-aggregate behavior in polymeric semiconductors. *Annu. Rev. Phys. Chem.* **65**, 477 (2014).

[14] N. J. Hestand, F.C. Spano, Expanded theory of H- and J-molecular aggregates: the effects of vibronic coupling and intermolecular charge transfer. *Chem. Rev.* **118**, 7069 (2018).

[15] H. Yamagata, 2013, *The effects of vibronic coupling on the photophysics of π-conjugated oligomers and polymers*. PhD Thesis, Temple University, Philadelphia.

[16] D. Hu, J. Yu, K. Wong, B. Bagchi, P. J. Rossky, P. F. Barbara, Collapse of stiff conjugated polymers with chemical defects into ordered, cylindrical conformations. *Nature* **405**, 1030 (2000).

[17] T. Adachi, J. Vogelsang, J. M. Lupton, Chromophore bending controls fluorescence lifetime in single conjugated polymer chains. *J. Phys. Chem. Lett.* **5**, 2165 (2014).

[18] R. Steyrleuthner, M. Schubert, I. Howard *et al.*, Aggregation in a high-mobility n-type low-bandgap copolymer with implications on semicrystalline morphology. *J. Am. Chem. Soc.* **134**, 18303 (2012).

Chapter 7

Concluding Remarks and Outlook

7.1 Conclusions

The aim of this thesis was to study and optimise potential polymer alignment methods that are able to simultaneously enable high-quality chain orientation and high-resolution spatial patterning of liquid crystalline conjugated polymers (LCCPs). In this thesis, the unique benefits and effectiveness of using photoalignment for orienting light-emitting conjugated polymer films that exhibit a nematic LC phase have been demonstrated. In contrast to conventional mechanically rubbed-polyimide alignment layers that are not stable in the LC-phase temperature range of LCCPs, this thesis demonstrates that the photoalignment layers could provide sufficient high-temperature thermal stability at temperatures as over 300 °C and induce record-high quality of polymer chain orientation over extended LCCP monodomain films.

By making use of the long-range orientational order present in the nematic mesophase, photoalignment layers have been shown in this thesis to provide excellent photo-rewritablity and -patternablity for creating planar chain orientation (patterns) in LCCPs such as the highly fluorescent F8BT conjugated copolymer. Photo-aligned/patterned F8BT films are found to exhibit highly oriented monodomains with uniform alignment, a record-high structural ordering in terms of almost a 100% order parameter and polymer crystallinity of 73% - 86%. In addition, non-aligned F8BT nematic polydomain glass films, which consist of a self-organised bi-phase mixture of a minor fraction of ordered polymeric nanocrystals dispersed in a randomly oriented

amorphous-phase matrix, show the highest photoluminescence (PL) efficiency among all types F8BT films that we have investigated. This is believed to be due to a prevalence of efficient intrachain radiative recombination taking place in the highly oriented polymeric nanocrystals and 3D non-radiative FRET that funnels excitonic energy from the amorphous phase host to the fluorophoric LCCP nanocrystal guest over >100 nm diffusion length.

In order to further improve the chain-orientation pattern resolution of 2 - 4 μm achieved by making use of a facile photo-masked UV illumination process, a two-photon direct laser writing (DLW) technique has been employed for the first time to inscribe bespoke planar photoalignment patterns with submicron features in both non-aligned and UV-prealigned photoalignment layers. The alignment written into the photoalignment layer was then transferred to the overlying LCCP layer via the LC phase alignment, which is then frozen-in to form a solid glass film after rapid quenching from the nematic phase. Linearly polarised photoluminescence (PL) emission and high PL polarisation ratios were observed from the photo-aligned F8BT glass films on either a photoalignment layer that had been illuminated uniformly with UV light or locally aligned using an ultrafast two-photon laser written pattern in the photoalignment layer. Results indicate that the two-photon femtosecond laser writing improves the resolution of the photoalignment technique to yield submicron pattern resolution and gives rise to higher PL anisotropies in the resultant LCCP monodomains. Moreover, we found that UV alignment and laser writing produce different F8BT film microstructures, as determined by notable differences in the micro-PL spectra. The polarisation-dependent PL spectral separation between two orthogonal interchain and interchain emissive components is also identified in the photoaligned F8BT nematic glass films. These anisotropic PL spectra provide information on the emissive intrachain/interchain excited states that complements previous studies on the structure-property relationship in non-oriented conjugated polymers.

In the first chapter, a background on π-conjugated polymers and LC-alignment is given. It has been emphasized that the optical, electronic and optoelectronic properties of polymeric semiconductors are dictated by their intrachain/interchain interactions and the configurations of the chemical motifs and physical structure. As the solution-processed polymer films usually exhibit a polydomain or amorphous structure with significant structural/energetic disorder, a combination of the LC-phase long-range orientational order and the emergent photoalignment technology has been proposed to facilitate easy and low-cost manufacture of the favourable highly oriented extended LCCP monodomains. Photoalignment was introduced in this chapter along with its potential for both high-quality alignment and high resolution patterning of LCCPs.

The second chapter contains a detailed introduction of the operating principle and benefits of different experimental techniques for characterising the alignment quality and the spatial dependence of the structure/properties in photo-aligned/pattered LCCP films. It is explained how GIWAXS diffraction patterns can be used to reveal the order parameter, the mean interchain/interchain spacing, the interchain packing structure, the effective conjugation length, and the overall crystallinity in different types of LCCP samples. Crossed polarising optical microscopy is effective for imaging the LC optical texture with ≈1-2 μm resolution, whilst polarised optical spectral measurements are useful to investigate the order parameter and the intrachain/interchain chromophoric and emissive species. Moreover, the effectiveness of polarised confocal fluorescence microscopy for spatially resolving the polarisation components of the fluorescence and the contrast in the intensity for light emission from polydomains or monodomain LCCP film is described. In addition, μ-PL mapping is introduced as a powerful technique for providing spectral information about both the PL intensity and spectrum at a given point on an LCCP film, hence enabling the PL spectral information to be collected at different locations in a photo-patterned LCCP film.

In the third chapter, the photoalignment material used throughout this thesis, SD1, is presented as a solution (water)-processable, non-luminescent, high-temperature (>300 °C) stable, and optically (re)writable material for providing uniform chain-orientation and high-resolution spatial definition of the ordering in quenched LCCP glass films. A linearly polarised UV illumination process has been explored and optimised to photo-align the SD1-coated glass substrates. These UV-aligned SD1 commanding layers are demonstrated as a better homogeneous alignment layer than the standard rubbed-PI alignment layer, in terms of enabling higher order parameters and better high-temperature thermal stability in low molar mass nematic E7 glass cells. It is then found that continuous SD1 layers are fabricated when the concentration of the SD1 solution is > 0.5 mg/mL, whereas SD1 discontinuously covers the substrate when solution concentrations of <0.1 - 0.25 mg/mL are used. The UV-alignment process has also been optimised in terms of maximising the F8BT alignment quality with the same thickness. Optimised UV-aligned SD1 photoalignment layer has been identified as the ones that are spin-coated using the 0.5 mg/mL SD1 solution (3 - 4 nm in thickness) and then UV-illuminated for 5 min, which results in almost 100% order parameter in the photoaligned F8BT overlying films. By engineering the F8BT thickness we show that highly aligned polymer chains (>10 dichroic ratios) are obtained for the F8BT glass films with thicknesses in the range of 100 to 300 nm, which are similar to the film thicknesses commonly used in a rich range of device structures. A spatial chain-pattern resolution of 2 - 4 μm is determined from our patterning resolution test where a standard 1951 US Air Force Resolving Power Test Target was used as the photo-mask to pattern the polarised UV alignment of the SD1 layer, which was subsequently used to orient the overlying F8BT nematic glass films. Moreover, the effectiveness of an indirect photoalignment method for aligning polymer blend films is showcased by an SD1-aligned 90 wt% F8BT:10 wt% copolymer Red-F binary blend film, which emitted highly polarised red-light due to the alignment of the polymer chains of non-LC Red-F guest by the SD1-oriented F8BT polymer chains in the nematic phase of the F8BT host.

In the fourth chapter, the microstructure-property relationship in different F8BT LCCP films is systematically investigated by fine tuning the order parameter ranging from 0 to ~1 through making use of the LC long-range orientation order and the photoalignment technology explored in Chapter 3. Four types of F8BT films are considered: 1) a spin-coated pristine non-LC (amorphous) film used as the reference sample; 2) a non-aligned nematic polydomain glass film; 3) a fully photoaligned monodomain glass film; and 4) a partially photoaligned polydomain glass film. These different films were prepared in order to characterise their different chain-orientation quality, polymer packing structure, and photophysical properties such as the light absorption and emission, excitonic energy transfer, photoluminescence efficiencies, and amplified spontaneous emission behaviours. The amorphous reference film in the as-prepared state showed no obvious GIWAXS pattern and therefore the absence of long-range structural order, due to a highly twisted chain-conformation with a greater population of extremely localised BT-to-BT interactions in order to minimise steric hindrance. This highly disordered polymer packing structure leads to a dominance of the low-energy (0-1) vibronic transition in the PL spectra, the lowest PLQE of 29% - 35%, and the shortest PL emission lifetime among all the measured F8BT films. On the contrary, the GIWAXS images recorded from the non-aligned F8BT nematic polydomain film visualise a smearing of the characteristic diffraction ring stemming from an ~5% fraction of the locally self-organised polymeric nanocrystals that act as low-energy fluorophoric inclusions dispersed in the highly disordered amorphous-phase matrix. These LC-phase self-organised F8BT nanocrystals and the surrounding amorphous-phase matrix resemble a self-doped host-guest system in the nonaligned polydomain nematic glass film. Such bi-phase material system gives rise to an extra-long-wavelength bandgap-edge absorption state and a scattering tail in the optical absorption spectrum. The well-dispersed fluorophoric polymeric nanocrystals dictate the film PL behaviours by maximising the intrachain radiative recombination over coherent non-radiative FRET funnelling from the amorphous chromophoric matrix, alongside exhibiting >70% PLQE

values that approach the PL efficiency limit of F8BT solutions. The prevalence of the non-emissive amorphous-phase F8BT matrix and deactivated traps associated with disorder/defects in nonaligned F8BT nematic polydomain glass film produces a record-high PLQE for the LCCP solid-state films. These self-organised polymeric nanocrystals are then proposed to have an alternating interchain packing structure, in which the separated F8BT backbones and significantly suppressed BT-to-BT close contacts leads to a dominance of the high-energy (0-0) transition band in the PL and PLE spectra. Analogously, the polarised μ-PL measurements recorded across different locations in the nonaligned nematic polydomain background highlight that the domain boundary regions, where a relative higher fraction of amorphous-phase F8BT polymer chains is accommodated, are more favorable than the domain interior in terms of enhancing the FRET and PL efficiencies.

The most important finding of Chapter 4 is the high-quality unidirectional chain orientation achieved in the fully photoaligned F8BT nematic monodomain films, where the absorption strength parallel to the F8BT alignment direction is significantly enhanced, together with large anisotropies in both the F8BT packing structure and polarised PL intensity ratios. The considerable enhancement in the polymer structural order in the plane of the substrate and in the interchain exciton/energy transfer in the highly oriented F8BT nematic monodomains also causes anisotropic GIWAXS patterns, polarisation-dependent PL spectral separation of the two orthogonal emissive excited states, as well as a dramatic broadening of the PL excitation band at both short-and long-wavelengths for the dominant 0-0 vibronic PL transition. We ascribe these striking photophysical phenomena to the long-range orientational ordering of F8BT chains “locked-in” from the SD1-aligned nematic mesophase, which makes it possible to access highly localised states and establish an interconnected molecular network with enhanced intrachain conjugation and long-range interchain electronic coupling pathways.

In the fifth chapter, two-photon direct laser (re)writing of SD1 photoalignment layers using an ultrafast Ti:sapphire laser (785 nm, 250 fs, 80 MHz) has been used, for the first time, to create patterned chain-orientation structures in the quenched LCCP glass films. The key writing parameters including the laser power, writing speed, laser written line separation and the NA of the focusing objective lens, have been comprehensively studied to optimise the laser spatial-pattern resolution as well as the photoalignment quality and uniformity. A combination of the highly localised laser-rewritten alignment with uniform UV-alignment has exhibited the unique benefit to enable high-quality LCCP alignment and submicron-scale spatial pattern resolution, which is very close to the theoretically predicted diffraction-limited focusing resolution for our two-photon laser writing system. Spatial patterning is performed by laser writing on an unexposed SD1 film or writing into an SD1 film that has been pre-aligned by uniform exposure to a polarised UV light source. Higher contrast is achieved for polarised confocal fluorescence images when the laser writing is into a prealigned SD1 photoalignment layer, as the ordering of the background produces a highly uniform signal against which the laser written pattern stands out. It has been demonstrated that laser rewriting can be done using different relative angles between the pre-alignment direction and the laser-writing polarisation. When the laser polarisation is selected to be orthogonal to the UV pre-alignment direction, there is a well-defined transition zone that consists of $\lambda = ½$ disclination lines due to the associated degeneracy between two equally probable director orientations in the nematic LC phase. These defect-line regions display a typical Schlieren LC texture and broaden the linewidth in the resulting LCCP alignment pattern border, hence significantly degrading the laser pattern resolution and the photoalignment uniformity. For 45° rewriting, however, the director degeneracy that causes this transition zone is lifted and there is no defect formation.

In the sixth chapter, a series of experiments are carried out to investigate the molecular structure-PL property relationship in highly oriented F8BT that had been aligned using either

two-photon laser-(re)written and/or one-photon UV illumination of an SD1 photoalignment layer. Different chain-conformations are identified in the ultrafast two-photon laser- and UV-aligned F8BT nematic films to essentially limit the best achievable absorption and emission anisotropies enabled by these two photoalignment approaches. In particular, the relative orientation of the photoaligned chain axis and the concomitant optical transition dipole moment differs for the laser- and UV-aligned F8BT films: the two are parallel for the F8BT patterns prepared using laser writing, but at angle of ~21° relative to each other for the UV-aligned F8BT regions. As a result, making use of the polarisation degree of freedom for PL excitation and detection, together with multi-step laser rewriting of the spatial features oriented at different angles relative to each other, has been highlighted as an effective method for fine-tuning the vibronic PL structure and optical/electrical anisotropies in the photoaligned LCCP.

While the UV-aligned F8BT nematic glass films exhibit an order parameter of ~100% and PL peak anisotropies of 9 - 12 at the first vibronic peak, the F8BT regions on top of laser written SD1 display the highest PL peak anisotropy. Although the two-photon laser rewriting of SD1 alone yielded the relatively low PL peak anisotropy of 6.5 in the oriented F8BT, this anisotropy increases to 12 - 15 when comparing the PL intensity in the laser-rewritten F8BT monodomain pattern with that in the UV-prealigned background. These anisotropy values remain consistent with the estimated degrees of crystallinity in the three types of photoaligned F8BT film - 86%, 88%, and 76%, for the UV-aligned, laser-written, and laser-rewritten F8BT, respectively. It is noteworthy that this calculated crystallinity for the UV-aligned F8BT is close to the crystallinity level of 73% estimated based on its GIWAXS pattern presented in Chapter 4. Once again, the polarisation-dependent PL spectral separation between the vibronically structured, parallel-polarised $PL_{//}$ spectrum and the red-shifted perpendicular-polarised $PL_{\perp}$ spectrum is observed in all three types of photoaligned F8BT monodomains. It is further shown that the highly efficient (intrachain) emissive excited state with >70% PLQE is responsible for

the linearly polarised first (0-0) vibronic transition, whereas the interchain character of the polarised longer-wavelength radiative decay dominates the $PL_{\perp}$ spectrum and results in a significantly reduced PLQE of ~10%. Moreover, we elucidate that the rather structured $PL_{//}$ spectra in all UV-aligned, laser-written, and laser-rewritten F8BT films have distinct vibronic structures, suggesting different chain conformations and interchain packing structures. The emission spectrum for the laser-written F8BT crest pattern exhibits the lowest relative weight in the 0-0 vibronic transition in the parallel polarised μ-PL spectra, which was ascribed to a softer chain conformation possibly with a significant zig-zag kinked backbone segments while the F8 and BT units remain parallel to the film plane. The UV-aligned F8BT, on the other hand, is expected to possess a more extended linear chain geometry with all BT units located at the same side of the chain axis but still a small variation in the dihedral angle associated with the overall chain bending, in line with the observed (010) diffraction arc in the perpendicular configured GIWAXS pattern. Finally, the two-photon laser-rewritten F8BT monodomain pattern shows the highest relative weight in the 0-0 vibronic transition (i.e., the smallest Huang-Rhys parameter) due to the enhanced chain planarity and dramatically suppressed chain bending.

7.2 Future Work and Outlook

The first piece of future work has been started by the author at Oxford University with some preliminary measurements on the impact of high-quality chain orientation on the amplified stimulated emission (ASE) properties for the different F8BT films. Photo-excitation stripes (i.e., a stripe-shaped air/F8BT/quartz slab) were created using a cylindrical lens and an adjustable slit to focus the excitation beam into a narrow stripe of dimension of 100 μm × 4 mm. The spontaneously emitted photons are amplified as they are waveguided within an optically pumped ASE stripe with a Q-switched Nd:yttrium-aluminum-garnet laser (355 nm wavelength, emitting 8.1 *ns* pulses at a repetition rate of 10 Hz). The energy of the laser pulses was tuned from 1 nJ to 750 nJ by a set of calibrated neutral density filters. The emission signal from the

photoexcited F8BT stripes were collected at one end of the ASE stripe with a fiber-coupled grating spectrometer equipped with a charge coupled device detector. For an ASE measurement of the photo-aligned F8BT film, the edge-collected emission was acquired by aligning the SD1-aligned chain-orientation direction at various angles relative to the polarisation direction of the excitation laser beam. Among the four combinations of the beam polarisation and chain orientation used for the 0°-aligned F8BT nematic film, our preliminary ASE tests suggest that the strongest ASE spectral line-narrowing occurred around the 0-1 vibronic transition when the F8BT chain orientation was aligned parallel to the excitation polarisation and perpendicular to the ASE stripe length (see **Figure 7.1** for the measurement configuration). This configuration is reasonable since it corresponds to the maximum excitation absorption and, simultaneously, an alignment of the effective waveguiding along with the in-plane propagation direction of the spontaneously emitted photons in the SD1-aligned F8BT monodomain films.

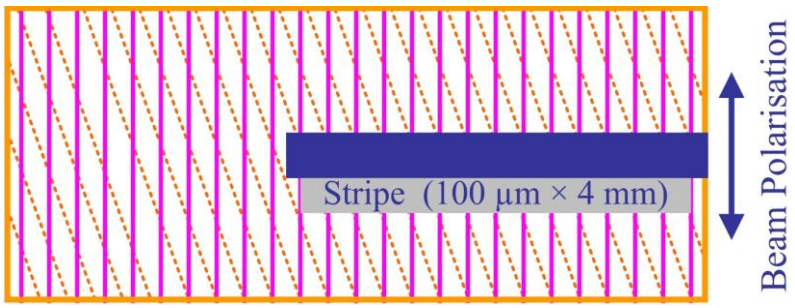

Figure 7.1: Illustration of the configuration used for the ASE measurements of all F8BT films.

Our preliminary ASE stripe (100 μm × 4 mm) measurements were carried out on the fully photoaligned F8BT monodomain films with different orientations (e.g., 0°, 10°, 20°, 30°, 45° and 90°) between the chain alignment direction and the stripe length in order to elucidate the chain orientation effect on the ASE properties. As a comparison, the nonaligned nematic polydomain and spin-coated non-LC F8BT films with the same thickness were also photo-excited using the same stripe configuration. **Figure 7.2** compares the distinct ASE spectral line narrowing behaviours recorded from various 190 nm-thick F8BT films including 0°, 10°, 20°, 30°, 45° and 90°-oriented nematic monodomain glass films, as well as the spin-coated

amorphous reference film and nonaligned polydomain nematic glass film. A fourfold reduction in the ASE threshold fluence down to 15 ~ 16 μJ/cm^2 is identified in the 0^o- and 10^o-aligned F8BT stripes, compared with a threshold of ~60 μJ/cm^2 determined for the non-LC reference F8BT film and no clear ASE line-narrowing in the non-aligned F8BT nematic polydomain glass film at the maximum pump energy. Our preliminary ASE results also confirm ~four times increase in both the optical net gain and stimulate-emission cross-section for the 0^o/10^o-aligned F8BT stripes relative to the spin-coated reference stripe. These encouraging ASE results highlight the huge potential of photoaligned LCCP films for polymer lasers/cavities and fluorescent concentrators.

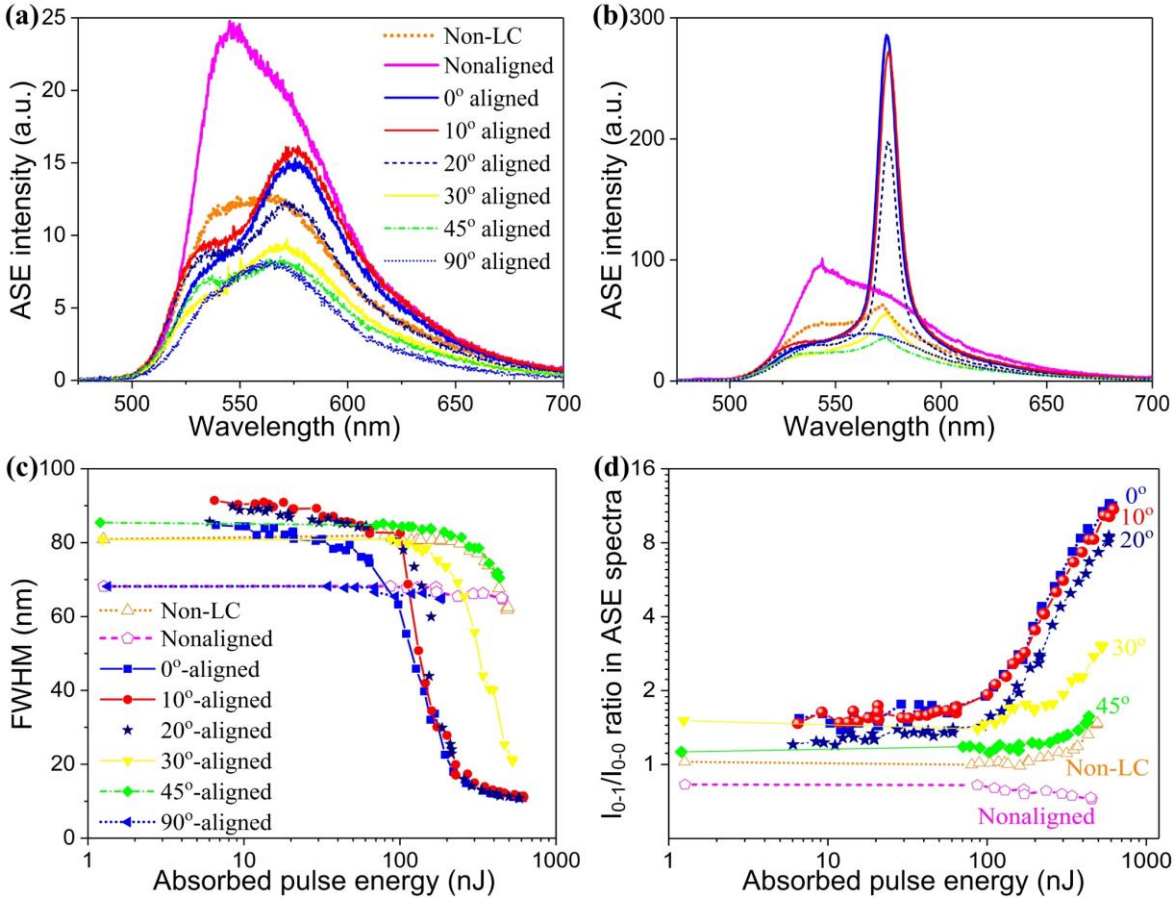

Figure 7.2: The ASE spectral line-narrowing behaviours measured in different types of F8BT films. (a - b) Edge-collected ASE spectra from all measured F8BT ASE stripes photoexcited at an absorbed pulse energy of 50 nJ (a) that is lower than the identified ASE threshold energy and of 450 nJ exceeding the ASE threshold (b). The absorbed pulse energy dependence of (c) the full width at half maximum (FWHM) and (d) the binary logarithm of the emission peak intensity ratio between the 0-1 (peaking at ~570 nm) to 0-0 (at ~538 nm) vibronic peaks, $I_{0\text{-}1}/I_{0\text{-}0}$ ratio, in the corresponding ASE spectra in all measured F8BT stripes.

The short-term research can also include to further study some important speculations involved in this thesis, which can be exemplified by (*i*) the mechanistic understanding of highly efficient nonradiative 3D FRET funnelling excitonic energy from the amorphous host to the local highly-oriented polymeric nanocrystals as the low-energy fluorophoric guest dispersed in the self-doped F8BT nematic polydomain glass films (Chapter 4), and (*ii*) super-resolution microstructural and spectral characterisation of the different chain conformations, interchain packing structures, and the competitive emissive intrachain/interchain species generated in the different types of F8BT films (Chapter 5), alongside the associated molecular configuration in the photoaligned SD1 commanding layers. For the former case, simultaneous spatially resolved and time-revolved/delayed light absorption/transfer/emission measurements of an identical region selected in an F8BT film of different types are useful to distinguish between the distinct light emission and energy transfer mechanisms (e.g., FRET, interchain and intrachain energy transfer), and to provide information on the oscillating strength, polarisation, lifetime and decay dynamics of the competitive emissive excited electronic states in fluorescent LCCPs. In order to study the LCCP chain conformations and interchain packing as well as the correlated phase transition and/or crosslinking in the photo-aligned SD1 layers, solid-state nuclear magnetic resonance and high resolution microstructural imaging techniques such as high-resolution scanning tunneling microscope, polarised scanning transmission X-ray microscopy are feasible.

In addition, the short-term research activities can be devoted to further improving the spatial patterning resolution of photoalignment, ideally down to the nanoscale, by coupling with other techniques such as polarised 1D/2D optical interference patterns, photolithography and electron beam lithography. It is reasonable to use multi-beam interference patterns, such as the stripe interface pattern enabled by Lloyd's mirror two-beam interference, to photo-align/pattern the SD1 alignment layer with a 100-200 nm pattern resolution. Other more sophisticated optical

interference systems and in-plane patterning techniques endow extra flexibility in terms of fine-tuning the shape, critical dimension and oversize of the resultant photoalignment patterns.

Moreover, the two photoalignment techniques presented in this thesis is supposed to be versatile for orienting and spatial patterning other LCCPs, and deposited molecular semiconductors whose chemical structure is similar to the photoalignment layer material. As a medium-term research project, UV-aligned and/or photo-patterned SD1 commanding layers can be utilised to direct the molecular/chain alignment in solution-processed high-mobility LCCP films or a small molecular organic thin-film fabricated from thermal (or vacuum) evaporation, chemical vapour deposition, or physical vapour deposition.

In the long-term perspective, high-quality polymer alignment brings high structural order to the otherwise disordered amorphous/polydomain films, which would allow us to access highly localised states and fundamental optical/electrical anisotropy. Highly oriented and/or spatially patterned extended polymer monodomains with submicron- to nano-scale features could enable easy and fine tuning of the refractive index distribution, oriented optical transition dipole moment and polarised light emission, large charge-carrier mobility anisotropy and electronic/ionic conductivity, and enhanced spatiotemporal coherence of the excitation energy transfer or photon emission/amplification. This creates an exciting new platform for the fabrication of novel photonic/optoelectronic devices, meta-materials, optical routing, fluorescent concentrating, and quantum coherent light-harvesting and quantum-engineering systems based on polymeric or small-molecular semiconductors. Along these lines, topics for the long-term study encompass: *i*) Investigating the use of spatial patterning of high quality chain-orientation in conjugated polymers for enabling fundamental optical anisotropies and associated refractive modification, which could offer great potential for the design and fabrication of completely planar optical cavities/waveguides, holograph, integrated optical

circuits/computing, and meta-structures/materials. *ii*) The presented photoalignment technique is applicable to induce high quality alignment of a wide range of liquid-crystalline conjugated polymers such as high-mobility polymer systems and, thus, expected to offer new opportunities to access the most deeply trapped electron transport physics and create high spatiotemporal quantum coherence by inducing high polymer crystallinity and eliminating disorder defects. *iii*) The self-doping approach by fine-tuning the physical structure that has been explored in this thesis, working together with external chemical/molecular doping methods, could bring structural order for enabling the performance improvement of a rich range of functional devices such as artificial photosynthesis structures, polymer thin-film transistors, organic spintronics, thermoelectrics and bioelectronics. *iv*) Bringing high coherence to the otherwise disordered organic semiconductors in order to investigate the feasibility of polymer-based coherent quantum information/engineering science and biomimetic energy conversion devices. *v*) Freestanding and photo-aligned/patterned organic semiconducting films as an active but flexible emissive/absorbing/transporting layer in a variety of energy-harvesting, solid-state lighting and biomedical applications can be lifted by immersing the readily photo-aligned SD1/organic bilayer into an orthogonal solvent such as water or ethanol. *vi*) Our preliminary experimental results highlight the possibility of directly photo-aligning LCCP chain orientation via one-step UV-alignment of LCCP/SD1 blend films, which would remove the requirement of thermotropic LCCP alignment in the nematic phase and therefore avoid any high-temperature degradation of the desired properties. *vii*) Use of a photo-aligned/patterned molecular host to introduce indirect orientation of other functional guests in a blend/composite film so as to extend the applications of the explored photoalignment technology into other scientific and technological frontiers.